October 17, 1995

CONTRACT NAS8-38856

# Structural Damage Prediction and Analysis for Hypervelocity Impact

# Formation and Description of Debris Clouds Produced by Hypervelocity Impact - UDR-TR-95-46

*LOCKHEED MARTIN*

# FORMATION AND DESCRIPTION OF DEBRIS CLOUDS
# PRODUCED BY HYPERVELOCITY IMPACT

By
Andrew J. Piekutowski
University of Dayton Research Institute
300 College Park Avenue
Dayton, Ohio 45469-0182

October 1995

Prepared for

# TABLE OF CONTENTS

# TABLE OF CONTENTS
## (Concluded)

# LIST OF ILLUSTRATIONS

# LIST OF ILLUSTRATIONS
## (Continued)

# LIST OF ILLUSTRATIONS
## (Continued)

# LIST OF ILLUSTRATIONS
## (Continued)

# LIST OF ILLUSTRATIONS
## (Continued)

# LIST OF ILLUSTRATIONS
## (Continued)

# LIST OF ILLUSTRATIONS
## (Continued)

# LIST OF ILLUSTRATIONS
## (Continued)

# LIST OF ILLUSTRATIONS
## (Continued)

# LIST OF ILLUSTRATIONS
## (Continued)

# LIST OF ILLUSTRATIONS
## (Continued)

# LIST OF ILLUSTRATIONS
## (Concluded)

# LIST OF TABLES

# DEFINITION OF SYMBOLS

| Symbol | Definition |
|---|---|
| $c, c_0$ | Speed of sound |
| $D$ | Diameter of projectile |
| $d$ | Nominal fragment diameter (after Grady, [23]) |
| $d_f$ | Equivalent diameter of large central fragment |
| $d_h$ | Average diameter of hole in bumper |
| $d_m$ | Martin's diameter of a spall-shell fragment |
| $\tilde{d}_m$ | Median Martin's diameter of spall-shell fragments |
| $H$ | Height of large central fragment |
| $K_c, K_{Ic}$ | Critical stress intensity factor or fracture toughness of projectile |
| $L$ | Length of center-element fragments |
| $M_C$ | Total mass of material in center element |
| $M_S$ | Total mass of material in spall shell |
| $m$ | Mass of projectile |
| $m_b, m_p$ | Computed mass of bumper and projectile in front element |
| $m_f$ | Computed mass of large central fragment |
| $N_F$ | Number of spall fragments in fields used in sampling procedure |
| $N_T$ | Total number of fragments in spall shell |
| $P$ | Pressure |
| $P_H$ | Hugoniot pressure |
| $R_0$ | Radius of projectile |
| $s$ | Nominal fragment diameter (after Grady, [24]) |
| $T$ | Thickness of large central fragment |
| $t$ | Bumper thickness |
| $U$ | Shock velocity |

# DEFINITION OF SYMBOLS
## (Concluded)

| Symbol | Definition |
|--------|-----------|
| $u_p$ | Particle velocity in material behind shock |
| $V$ | Volume |
| $V_0$ | Impact velocity |
| $V_{AXIAL}$ | Axial velocity of a point or pair of points in debris cloud, measured parallel to shot-line axis |
| $V_{CP,P}$ | Velocity of collision point in projectile reference frame |
| $V_{CP,T}$ | Velocity of collision point in target reference frame |
| $V_{CTR}$ | Velocity of center of arc defining shell of spall fragments |
| $V_{DIAMETRAL}$ | Expansion velocity of opposing points in debris cloud, measured normal to shot-line axis |
| $V_f$ | Velocity of large central fragment |
| $V_H$ | Hugoniot volume |
| $V_n$ | Velocity of a point in debris cloud (n = 1 to 10) |
| $V_r$ | Radial expansion velocity of spall-shell fragments |
| $V_S$ | Threshold velocity for formation of spalled region at the rear surface of a spherical projectile |
| $W$ | Width of large central fragment and center-element fragment |
| $x$ | Distance from front of bumper to leading edge of debris cloud |
| $\dot{\varepsilon}$ | Strain rate, approximated as $V_r/R_0$ |
| $\rho$ | Density |
| $\tau$ | Time after impact |
| $\tau_n$ | Time of exposure of radiograph with respect to impact (n = 1 to 4) |

# ACKNOWLEDGMENT

# SECTION I. INTRODUCTION

Since astronomers first envisioned sending craft and travelers into space, they have expressed concern for the protection of spacecraft from the accidental impact of meteoroids. They realized that spacecraft with walls thick enough to absorb the impact of a meteoroid would be impractical and considered alternate forms of wall construction. In 1947, Whipple [1] described the operation of a double-wall system that could be used to provide the required protection. A thin, sacrificial outer sheet, known as a bumper or shield, would completely disintegrate the meteoroid upon impact, forming a debris cloud composed of meteoroid and bumper fragments. The debris cloud would disperse as it moved across a short standoff space toward the inner or pressure wall of the spacecraft. The inner wall would be somewhat thicker than the bumper and resist the impact of the cloud of meteoroid and bumper debris, thus protecting the contents of the spacecraft. Use of this simple shield-and-wall construction (or Whipple-bumper system) permitted a significant reduction in the weight of the spacecraft.

As interest in space travel by manned and unmanned vehicles became a national priority, numerous investigations of a wide variety of hypervelocity impact phenomena were undertaken. See, for example, the proceedings of the seven Hypervelocity Impact Symposia held between 1955 and 1964 [2-8] and the AIAA Hypervelocity Conference held in 1969 [9]. A number of the studies described in these proceedings and other contemporary references were executed to evaluate performance of spacecraft shield systems. Although many materials and projectile shapes were used to simulate micrometeoroids, aluminum spheres were used as simulants in a significant fraction of the shield studies. Determination of the ballistic limit of a shield, optimization of a shield against a specific threat, and/or development of design criteria were the usual purposes for most test programs. Occasionally, radiographs or high-speed photographs of "typical"

debris clouds produced during the tests were presented with test results. Only rarely were quantitative descriptions of the debris clouds given and when descriptions were provided, they were not systematic (i.e., did not describe changes in the debris-cloud morphology as a result of changes in impact velocity, bumper thickness, etc.). Results of the studies presented in [10-14] are representative of these earlier works.

Aluminum spheres continue to be used in shield studies as simulants of orbital-debris fragments [15-18]. This report critically examines the aluminum sphere/thin aluminum sheet (projectile/bumper) interaction occurring during hypervelocity impact and the debris clouds produced as a result of this interaction. Although the impact velocities of the tests described in this report are well below the closing velocities of debris fragments with spacecraft, they do represent the state of the art in current test capabilities. Detailed understanding of the impact process at these reduced velocities is essential when extending the results of the reduced-velocity tests to estimate the response of spacecraft walls to impacts occurring at velocities high enough to completely melt and vaporize the fragment and the impacted area of the shield. It is the author's hope that the data presented in this report will be used to validate the adequacy of computational techniques that must be used to evaluate shield performance for the range of impact conditions that are beyond current test capabilities. Every effort was made to provide detailed and high-quality, quantitative data, and to make the presentation of test results, analysis, and discussion of test results as relevant to the formation of debris clouds as possible. The effect (pass/fail) of the impact of the debris cloud on a rear wall was a secondary consideration. However, descriptions of the damage patterns produced on the witness plates used for the tests are provided.

A portion of the analysis presented in this report was done with support provided by NASA Marshall Space Flight Center (NAS 8-38856) on Subcontract A71447 with Martin Marietta Manned Space Systems. Results of a set of 43 tests are presented in

2

detail. This set of 43 tests consisted of: (1) six tests performed specifically to examine debris-cloud formation as part of the funded analytical effort; (2) two tests performed for McDonnell Douglas; and (3) 35 tests supported by the Office of the Director of the University of Dayton Research Institute (UDRI). Where appropriate, limited results of other tests performed at UDRI are also presented. The data obtained from the 35 UDRI tests were incidental to the main objective of the gun firings — evaluation of gun loading conditions, dynamic testing of instrumentation, determination of exact loading conditions for tests where impact velocity was critical, etc. Use of a bumper sheet, witness plate, and flash x-rays was all that was required to obtain the data presented in this report.

In the tests, two aluminum alloys were used for the projectiles and three aluminum alloys were used for the thin bumper sheets. A detailed listing of the projectile diameter and material, and bumper-sheet thickness and alloy is given in Section II for each test. Sufficient test data were available to permit an evaluation of the effect of bumper-thickness-to-projectile-diameter ratio ($t/D$), impact velocity, scale, and material on the debris-cloud formation process. The evaluation focused on tests using thinner bumper sheets but was limited in terms of the range of data for each set of test parameters and the number of tests (usually one) at each set of test conditions. The analyses and discussions represent an interpretation of the formation of debris clouds that was based on the data available at the time the report was prepared. Sufficient data were available to permit determination of trends and reasonable speculation on behavior in those regions where data were not available.

Several types of data were obtained. Measurements taken from multiple-exposure, orthogonal-pair flash radiographs permitted determination of the velocity of a number of characteristic "points" in the debris cloud, fragment sizes, fragment-size distributions, and sufficient data to allow a user of this report to reconstruct the debris cloud in terms of shape and position as a function of time after impact. Measurements

3

were also made of the hole in the bumper sheet and of the damage pattern produced on witness plates placed downrange of the bumper. A complete listing of data available for each test is tabulated at the end of Section II.

Radiographs and a description of selected debris clouds produced by the normal impact of a sphere with a single-sheet bumper are presented in Section III. In Section IV, results of an analysis of the projectile fragments in the debris cloud are presented and discussed for a number of tests. Results of bumper-hole diameter measurements and micrographs of sections of representative bumper sheets are presented in Section V.

A model for the projectile-bumper interaction which occured during hypervelocity impact is presented in Section VI. The model described the processes leading to the formation of the various debris-cloud elements. Distribution of mass in the debris cloud and within the debris-cloud elements is discussed. A method for estimating the state of material in the debris cloud is developed and used to estimate the properties of debris clouds formed by impacts at velocities high enough to produce aluminum vapor. The estimated debris-cloud properties are qualitatively compared with debris clouds produced by the impacts of cadmium spheres with cadmium sheets. Impact velocities for the cadmium tests ranged from velocities which produced only solid fragments to velocities which produced considerable vaporization of the cadmium sphere and bumper. Finally, a description of shock propagation in the bumper is given. The model presented in Section VI is based on observations, measurements, and analysis of data presented in Sections III, IV, and V. For some readers, Sections III, VI, and V will serve only as sources for data and may not be relevant to their interests. A quantitative description and discussion of the damage patterns produced on the witness plates used for the tests is presented in Section VII. In Sections VIII, IX, and X, the limited results of tests with multi-component shields, oblique impacts, and nonspherical projectiles, respectively, are presented.

# SECTION II. EXPERIMENTAL MATERIALS AND PROCEDURES

All tests described in this report were performed in the UDRI Impact Physics Laboratory using the 50/20 mm, two-stage, light-gas gun shown in Figure 1. Impact velocity determinations were made with use of four laser-photodetector stations installed at various locations along the flight path of the projectile. Passage of the projectile
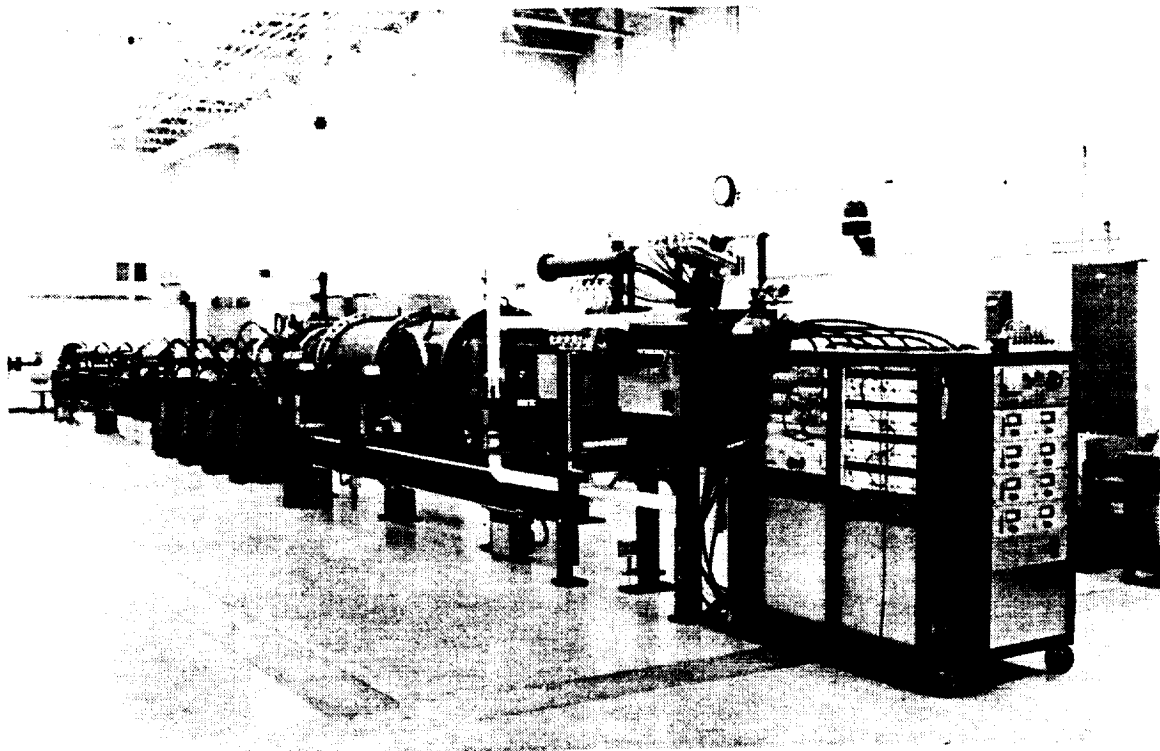


Figure 1. View of University of Dayton Research Institute 50/20 mm, two-stage, light-gas gun. View is from instrumentation/target chamber end of range.

through a laser beam directed into each photodetector produced a momentary drop in the output signal of the photodetector. Measurement of the time between the electrical pulses formed as the projectile moved downrange permitted the computation of the projectile velocity between any pair of laser-photodetector stations. Accuracy of the impact

velocity determination was better than ± 0.5 percent. A detailed listing of the materials used in the tests and a description of the experimental procedures is given in the remainder of this section.

# A. Materials

Three diameters of 2017-T4 aluminum spheres (6.35 mm, 9.53 mm, and 12.70 mm) were used as projectiles for the tests. A test employing a 12.70-mm-diameter, 1100-O aluminum sphere was also performed. Various thicknesses of 1100-O, 2024-T3, and 6061-T6 aluminum sheets, ranging from 0.25 mm to 4.80 mm, were used as bumpers. Bumper-sheet thickness, shot number, and projectile weight (centered under thickness and shot number) are shown for each projectile diameter and alloy in Table 1. The shot number given in Table 1 uniquely identifies each test. Shot number and/or $t/D$ ratio will be used as the index for the sorting of tabulated data presented in this report.

A witness plate was placed approximately 38 cm downrange of the bumper for each test. The large spacing between the bumper and the witness plate permitted several flash radiographs of the debris cloud to be made as the cloud traversed the space between the plates. In addition, it allowed the debris to disperse sufficiently to isolate individual fragments in the x-ray view taken just before the cloud struck the witness plate.

Four thicknesses of 6061-T651 aluminum plate and one thickness of 2219-T81, 2219-T87, and 5456-H116 aluminum sheet were used as witness plates. The witness plates were merely used to record the damage pattern produced by the impact of the debris cloud; the posttest condition of the plate was not relevant to the test objectives. However, when selecting a witness plate, every attempt was made to use a plate that was thick enough to withstand the impact (avoiding a large blowout-type failure) and capable of providing a good record of the damage pattern. Two-inch-thick hardwood planks were

# TABLE 1

## MATERIALS USED IN DEBRIS-CLOUD TESTS

To avoid any error through conversion to metric units, bumper thicknesses are presented in the units in which they were measured. Typical measurement error was ± 0.0001 inch. Projectile weights are shown below the sheet thickness and shot number and are given in grams.

*Sheet thickness, shot number, and projectile weight are shown for each combination of materials*

| Bumper Alloy | Projectile Diameter and Alloy | | | |
| --- | --- | --- | --- | --- |
| | *6.35 mm  2017-T4* | *9.53 mm  2017-T4* | *12.70 mm  2017-T4* | *12.70 mm  1100-O* |
| **Single-Sheet Bumper - Normal Impact** | | | | |
| **1100-O** | 0.0120  4-1318<br>0.3726 | 0.0119  4-1290<br>1.2752 | | |
| **2024-T3** | | 0.0200  4-1282<br>1.2748<br>0.0200  4-1284<br>1.2752 | 0.0199  4-1281<br>3.0002<br>0.0799  4-1357<br>3.0006 | |
| **6061-T6** | 0.0125  4-1449<br>0.3729 | 0.0097  4-1392<br>1.2750<br>0.0097  4-1395<br>1.2752<br>0.0097  4-1715<br>1.2751<br>0.0183  4-1360<br>1.2754<br>0.0184  4-1394<br>1.2755<br>0.0183  4-1428<br>1.2750<br>0.0184  4-1433<br>1.2748<br>0.0183  4-1744<br>1.2754<br>0.0233  4-1359<br>1.2753<br>0.0233  4-1633<br>1.2753<br>0.0315  4-1287<br>1.2751<br>0.0315  4-1289<br>1.2753<br>0.0315  4-1621<br>1.2754<br>0.0315  4-1622<br>1.2757<br>0.0314  4-1631<br>1.2754<br>0.0314  4-1632<br>1.2754 | 0.0233  4-1358<br>3.0009 | 0.0234  4-1601<br>2.9175 |

7

## TABLE 1 (Concluded)
## MATERIALS USED IN DEBRIS-CLOUD TESTS

To avoid any error through conversion to metric units, bumper thicknesses are presented in the units in which they were measured. Typical measurement error was ± 0.0001 inch. Projectile weights are shown below the sheet thickness and shot number and are given in grams.

*Sheet thickness, shot number, and projectile weight are shown for each combination of materials*

| Bumper Alloy | Projectile Diameter and Alloy | | | |
|---|---|---|---|---|
| | 6.35 mm 2017-T4 | 9.53 mm 2017-T4 | 12.70 mm 2017-T4 | 12.70 mm 1100-O |
| **Single-Sheet Bumper - Normal Impact** | | | | |
| 6061-T6 | 0.0381 4-1283<br>1.2751 | | | |
| | 0.0495 4-1722<br>1.2751 | | | |
| | 0.0505 4-1716<br>1.2750 | | | |
| | 0.0610 4-1291<br>1.2752 | | | |
| | 0.0630 4-1717<br>1.2754 | | | |
| | 0.0875 4-1351<br>1.2754 | | | |
| | 0.0876 4-1352<br>1.2754 | | | |
| | 0.0875 4-1718<br>1.2750 | | | |
| | 0.0875 4-1719<br>1.2750 | | | |
| | 0.0875 4-1720<br>1.2745 | | | |
| | 0.1590 4-1353<br>1.2756 | | | |
| | 0.1892 4-1721<br>1.2755 | | | |
| **Multiple-Sheet Bumper - Normal Impact** | | | | |
| 1100-O | 0.0120 (2 sheets) 4-1285<br>1.2752 | | | |
| | 0.0118 (2 sheets) 4-1286<br>1.2754 | | | |
| | 0.0118 (2 sheets) 4-1288<br>1.2749 | | | |
| | 0.0119 (5 sheets) 4-1292<br>1.2752 | | | |
| **Single-Sheet Bumper - Oblique Impact** | | | | |
| 2024-T3 | 0.0200 (30°) 4-1301<br>1.2752 | | | |
| 6061-T6 | 0.0450 (45°) 4-1303<br>1.2751 | | | |

8

used as witness plates for four tests. Wood was used for these tests to minimize damage to the x-ray film which occurred when heated ejecta fragments (from the witness plate) come to rest on the x-ray-film cassettes. Foam blocks and rags were used, without witness plates, for five tests in which the projectiles were recovered.

## B. Procedures

1. Test Setup. All but two of the tests were performed with the bumper normal to the range center line. The thinner bumpers were 10.8 cm square and were securely taped to a 3.18-mm-thick, 15.2-cm-square aluminum frame that had an 8.9-cm-square opening cut in its center. The thicker (1 mm or greater) bumpers were 15.2 cm square and were held at their corners by screws passing through the sheets into appropriate support posts. The bumper sheets used for the oblique tests were taped to the same frame used to hold the bumpers for the normal-impact tests. However, the frame was attached to a fixture that could be rotated to obtain the desired oblique impact angle. The witness plates for all tests were supported by a framework that extended from the rear wall of the target chamber.

2. Multiple-Exposure, Orthogonal-Pair Flash Radiography. Four pairs of fine-source, soft, flash x-rays were used to observe the projectile and debris cloud. The x-ray heads were accurately positioned on the target chamber to provide simultaneous, orthogonal views of the debris clouds. A typical test setup is shown in Figure 2. Field Emission Model 2772, 180 kV dual pulsers and Scandiflash 150 kV remote tubeheads (Model XT 150) with soft x-ray adapters and 1-mm-diameter sources were used to produce the radiographs. The x-ray tubeheads were positioned so that the source-to-object (range center line) distance was 64 cm. Kodak Direct Exposure Diagnostic Film
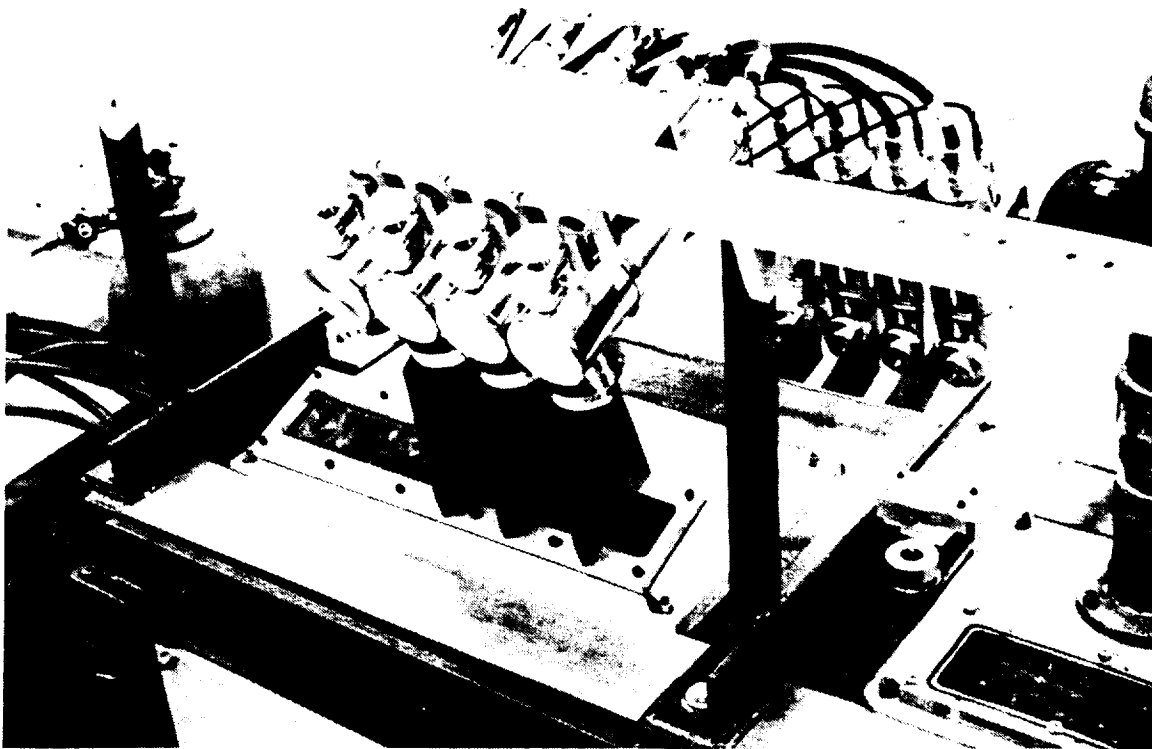
Figure 2. View of target chamber showing multiple orthogonal pairs of flash x-ray heads, chamber windows, and shielding.
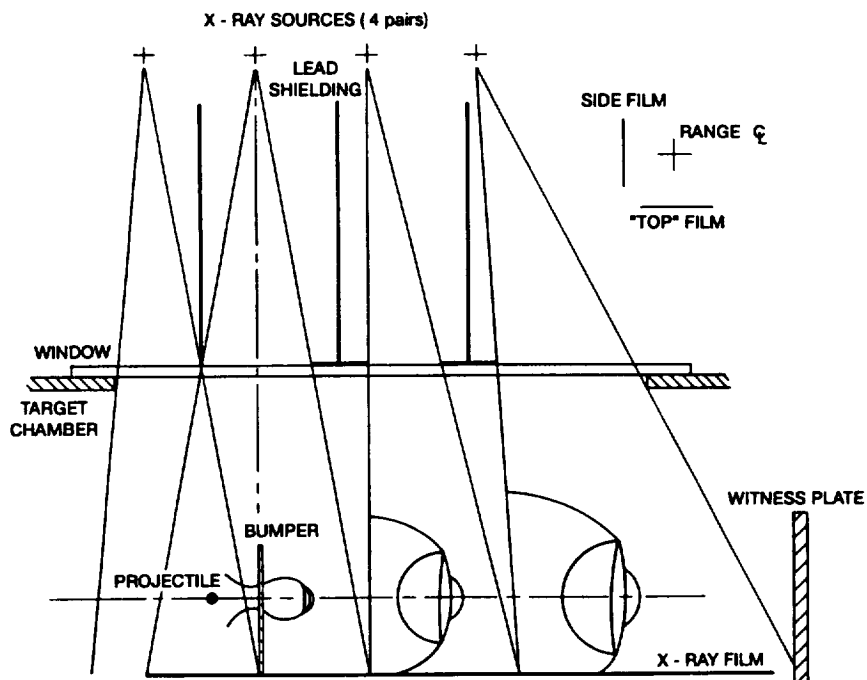


Figure 3. Setup used to obtain multiple-exposure, orthogonal-pair, flash radiographs of debris clouds.

(Cat 154 2463) was placed in a paper film cassette. The side and top film cassettes were positioned about 9.6 cm from the range center line using a film-holding fixture attached to the target-chamber floor.

Details of the shielding used to produce the multiple-exposure radiographs are illustrated in Figure 3. The first pair of x-ray heads was used to view and record the position of the projectile a few microseconds before impact. This view verified projectile integrity and permitted an accurate determination of the time after impact for the various views taken of the debris cloud after its formation. Normally, the first two debris-cloud views were taken when the leading edge of the cloud was about 4 cm and 12 cm downrange of the bumper. The two pairs of x-ray heads used to produce these views were positioned directly above and 7.87 cm downrange of the bumper. The fourth pair of x-ray heads was fired when the debris cloud was about 30 cm downrange of the bumper. The delay in firing this pair of heads allowed the cloud to expand and permitted a more detailed examination of the cloud structure. The fourth pair of x-ray heads was positioned 15.8 or 31.5 cm downrange of the bumper to provide oblique (approximately 13 degrees from normal) or normal views of the cloud, respectively.

A pair of multiple-exposure, flash-radiograph prints, obtained using the setup shown in Figures 2 and 3, is presented in Figure 4. Three features of this pair of radiographs require further explanation. First, the pre-impact view of the sphere and the ejecta veil generated by the impact were double-exposed in the first panel of the films. When prints of the radiographs were prepared for presentation in this report, the exposure of the film was carefully controlled during printing to bring out detail in the ejecta veil and to provide a background of about the same contrast level as for the single-exposed views. Second, the fourth pair of x-ray heads was positioned so that the side head (prefix "S" in shot number) was 31.5 cm downrange of the bumper and produced a normal view

S4-1359

T4-1359
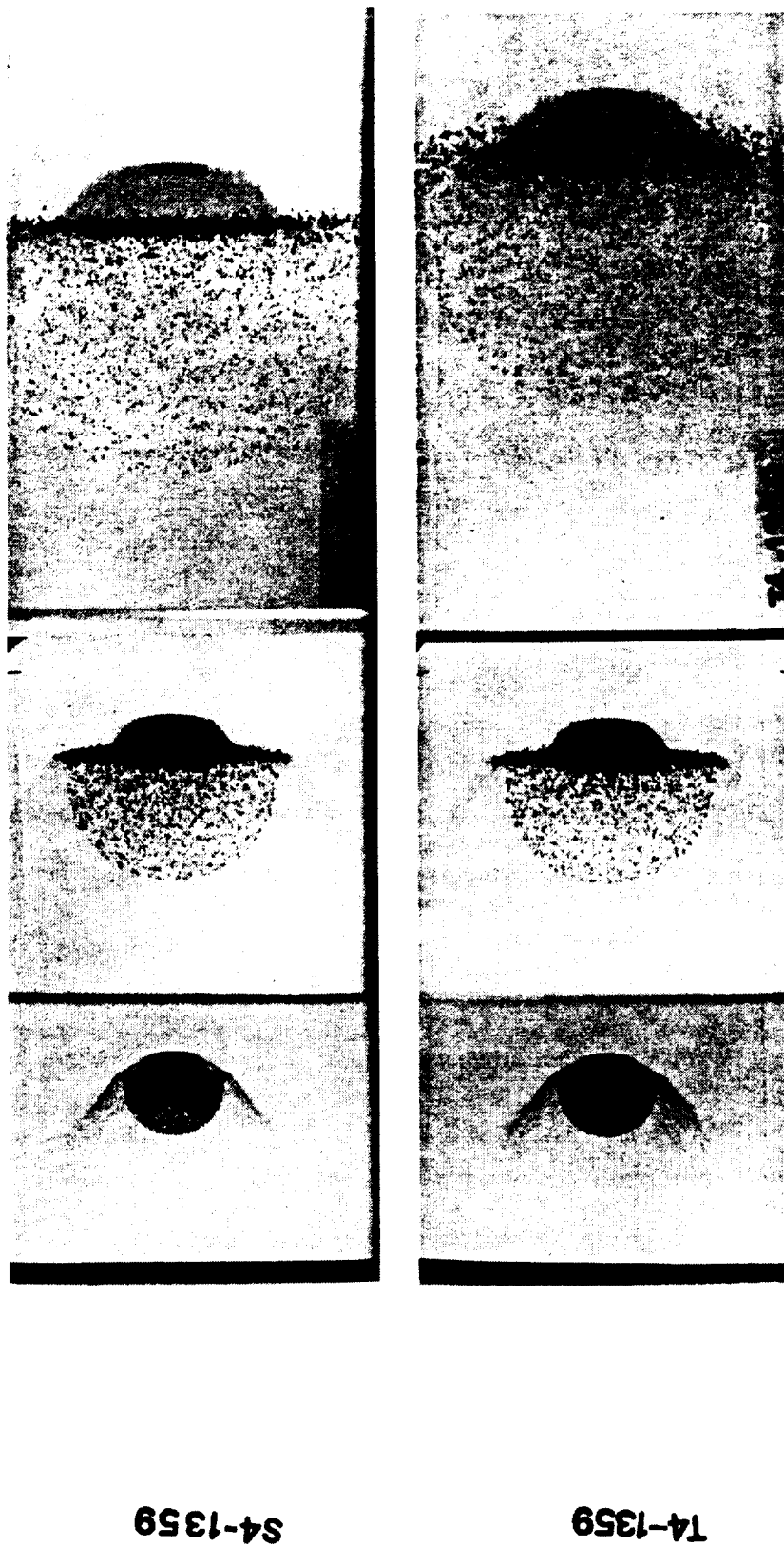
Figure 4. Sample pair of multiple-exposure radiographs. Note that the fourth view (extreme right) in the upper radiograph was made with the x-ray head moved downrange to provide a normal view of the debris cloud. The fourth view in the lower radiograph was made with the x-ray head positioned as shown in Figure 3 to obtain an oblique view of the debris cloud. The pre-impact portion of both radiographs is double exposed to provide a view of the projectile and the ejecta veil which is formed after impact. During printing of the radiographs presented elsewhere in this report, the density of the double-exposed region was adjusted to match the density of the single-exposed region.

12

of the debris cloud. The top head (prefix "T") was positioned 15.8 cm downrange of the bumper to produce an oblique view of the cloud. In other tests, these heads were placed to obtain two oblique views or two normal views. Finally, the largest available size of direct-exposure film was 8 x 10 inches. In order to "cover" the space between the bumper and the witness plate (as well as provide the pre-impact view), two pieces of film (one 4 x 10 inches and one 4 x 8 inches) were placed in an acetate film holder and the assembly was inserted in a standard 4-1/2 x 17 inch paper film cassette. A short piece of fine copper wire was placed along the upper and lower edges of the acetate film holder in the region where the pieces of film overlapped. When the film was exposed, the shadows of the wires left on each piece of film precisely indicated the relative position of the two pieces of film, thus facilitating joining of the prints of each for data analysis purposes.

3. Data Reduction. Data were obtained from three sources — the radiographs, the hole left in the bumper, and the damage pattern on the witness plate. The radiographs were used to determine axial and radial velocities of a number of characteristic elements of the debris clouds. The position of each point in each of the debris-cloud views was measured and adjusted for film magnification. The adjusted or true distances were divided by the time between x-ray exposures to obtain the velocity of the point. The fourth or late-time view was also used to determine the dimensions of the large central fragment in the debris cloud and for the fragment size and size-distribution analyses. Specific details of the measurements are presented as the data are introduced in Sections III and IV.

The diameter of the hole left in the bumper sheet was carefully measured using an optical comparator. Measurements were taken parallel and perpendicular to the rolling direction of the sheet stock. Eight of the bumpers had a section of the bumper and the lip region removed, mounted, and the cross section microscopically examined. Results of the hole-diameter measurements and a discussion of the findings of the microscopic examination are given in Section V.

Identifiable structures in the damage patterns, which were produced on the front and rear of the witness plates, were measured using a scale. The results and interpretation of these measurements are found in Section VII.

A tabulation of the various types of data available for each test is given in Table 2. Shown in the table are the number of flash x-ray views made for each test. As noted, only two post-impact views were made for some of the tests. In some instances, debris velocities were limited to one or two points in the cloud. In others, the velocities of up to twelve points (or pairs of points) were determined. Dimensions of three types of fragments were obtained for many of the tests. Bumper-hole diameters were recorded for all but one of the tests. Witness-plate damage-pattern measurements were obtained for all but twelve of the tests. Finally, sponsorship of the individual tests is also noted in Table 2.

An index was provided at the end of the report to assist the reader in locating radiographs, photographs of bumper sheets and witness plates, etc., used in the various figures presented in the report. The index is accessed with use of the shot number.

## TABLE 2

## TYPES OF DATA AVAILABLE FOR EACH TEST

Dash indicates data were not available. Formal identification of sponsors
for the tests listed in the table is given at the end of the table.

| Shot Number | Radiographs, Number of views[a] | Debris Velocity | Fragment Sizes[b] | Bumper-Hole Diameter | Witness-Plate Damage | Sponsor |
|---|---|---|---|---|---|---|
| | | | Single-Sheet Bumper - Normal Impact | | | |
| 4-1281 | 3 | x | L | x | x | UDRI |
| 4-1282 | 2 | x | -- | x | x | UDRI |
| 4-1283 | 3 | x | L | x | x | UDRI |
| 4-1284 | 3 | x | L | x | x | UDRI |
| 4-1287 | -- | -- | -- | x | x | UDRI |
| 4-1289 | 3 | x | C, L, S | x | x | MMMSS/MSFC |
| 4-1290 | 3 | x | L | x | x | McDD/JSC |
| 4-1291 | 3 | x | L | x | x | MMMSS/MSFC |
| 4-1318 | 3 | x | L | x | x | UDRI |
| 4-1351 | 2 | -- | -- | x | -- | UDRI |
| 4-1352 | 2 | x | L (Est.) | x | x | UDRI |
| 4-1353 | 2 | x | -- | x | x | UDRI |
| 4-1357 | 3 | x | L | x | x | UDRI |
| 4-1358 | 3 | x | C, L, S | x | x | UDRI |
| 4-1359 | 3 | x | C, L, S | x | x | MMMSS/MSFC |
| 4-1360 | 3 | x | C, L, S | x | x | MMMSS/MSFC |
| 4-1392 | 3 | x | L | x | x | UDRI |
| 4-1394 | 3 | x | C, L, S | x | x | UDRI |
| 4-1395 | 3 | x | C, L, S | x | x | UDRI |
| 4-1428 | 3 | x | L | x | x | UDRI |
| 4-1433 | 3 | x | C, L, S | x | x | UDRI |
| 4-1449 | 3 | x | L | x | x | UDRI |
| 4-1601 | 3 | x | C, L, S | x | x | UDRI |
| 4-1621 | 3 | x | C, L, S | x | x | UDRI |
| 4-1622 | 3 | x | L, S | x | x | UDRI |
| 4-1631 | 3 | x | L | x | -- | UDRI |
| 4-1632 | 3 | x | L | x | -- | UDRI |
| 4-1633 | 3 | x | L | x | -- | UDRI |
| 4-1715 | 3 | x | L | x | -- | UDRI |
| 4-1716 | 3 | x | C, L, S | x | x | UDRI |
| 4-1717 | 3 | x | L | x | x | UDRI |
| 4-1718 | 1 | -- | L | x | -- | UDRI |
| 4-1719 | 1 | -- | L | x | -- | UDRI |
| 4-1720 | 3 | x | L | x | -- | UDRI |
| 4-1721 | 3 | x | L | x | -- | UDRI |
| 4-1722 | 3 | x | L | x | -- | UDRI |
| 4-1744 | 3 | x | C, L, S | x | x | UDRI |

[a] Shown are number of post-impact views of debris cloud. All radiographs have a pre-impact view of projectile. Soft x-rays were used for all shots except 4-1281.

[b] C = Center-element fragment, L = Large central fragment, S = Spall fragment.

TABLE 2 (Concluded)

## TYPES OF DATA AVAILABLE FOR EACH TEST

Dash indicates data were not available. Formal identification of sponsors
for the tests listed in the table is given at the end of the table.

| Shot Number | Radiographs, Number of views[a] | Debris Velocity | Fragment Sizes[b] | Bumper-Hole Diameter | Witness-Plate Damage | Sponsor |
|---|---|---|---|---|---|---|
| | | Multiple-Sheet Bumper - Normal Impact | | | | |
| 4-1285 | -- | -- | -- | x | x | UDRI |
| 4-1286 | 3 | x | L | x | x | UDRI |
| 4-1288 | 3 | x | L | x | x | UDRI |
| 4-1292 | 3 | -- | -- | x | x | McDD/JSC |
| | | Single-Sheet Bumper - Oblique Impact | | | | |
| 4-1301 | 2 | x | -- | x | x[c] | MMMSS/MSFC |
| 4-1303 | 3 | x | x[d] | x | x[c] | MMMSS/MSFC |

[a] Shown are number of post-impact views of debris cloud. All radiographs have a pre-impact view of projectile. Soft x-rays were used for all shots except 4-1281.

[b] C = Center-element fragment, L = Large fragment, S = Spall fragment.

[c] Plates are shown in Section IX. Detailed measurements of the damage pattern were not made.

[d] Limited measurements were made of selected fragments in the debris cloud.

## IDENTIFICATION OF SPONSORS

| Listing in Table | Formal Name of Sponsor |
|---|---|
| MMMSS/MSFC* | Martin Marietta Manned Space Systems/ Marshall Space Flight Center |
| McDD/JSC* | McDonnell Douglas Space Systems Company/ Johnson Space Center |
| UDRI | University of Dayton Research Institute, Office of the Director |

* Work at UDRI was done under subcontract or purchase order with first-listed sponsor. Second-listed sponsor was the center issuing the prime contract.

# SECTION III.  DESCRIPTION OF DEBRIS CLOUDS

## A.  Major Debris-Cloud Features and Elements

Two views of a debris cloud are presented in Figure 5 to illustrate the three major features of the cloud.  First, an ejecta veil, consisting almost entirely of bumper fragments, was ejected from the impact or front side of the bumper.  Second, an expanding bubble of bumper debris formed on the rear side of the bumper.  Finally, there was a significant structure composed of projectile debris located inside and at the front of the external bubble of bumper debris.  This internal structure was composed of a front, center, and rear element.  For a 6.70 km/s impact, the front element consisted of finely divided,
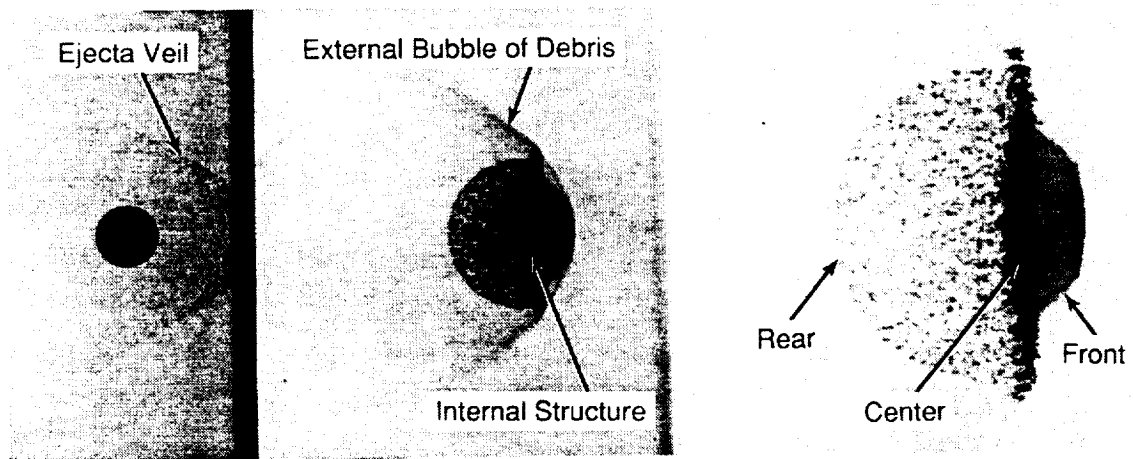


Figure 5.  Morphological features and elements of a debris cloud produced by an impact at 6.70 km/s.  Note that the ejecta veil and projectile are a double exposure in this figure and in all radiographs presented in this report.

molten droplets of bumper and projectile.  The disk-like center element was composed of a large number of solid slivers, comma-shaped, and/or chunky pieces of fragmented projectile.  This element also contained a single large chunky projectile fragment that was located at the center of the disk and on the debris-cloud center line.  A central fragment was observed in all debris clouds where the $t/D$ ratio was less than 0.2, and was most

17

clearly observed in the late-time view of the debris cloud. This central fragment represented the most severe threat to rear wall integrity [19]. The bulk of the post-impact projectile mass appeared to be concentrated in the center element. The rear element of the structure was a hemispherical shell of fragments spalled from the rear surface of the sphere. The internal structure of the debris cloud, shown in Figure 5 and subsequent figures, was the most significant feature of the debris cloud in terms of potential for rear-wall damage. In this report, the term "debris cloud" is synonymous with "internal structure."

In the remainder of this section, radiographs of debris clouds from selected tests will be presented. Where appropriate, radiographs of tests not presented in this section are shown in subsequent sections of the report. The radiographs presented in this section were selected because they provided a visual record of the effect a change in $t/D$ ratio and/or impact velocity had on the debris-cloud shape. An index to the radiographs used in the figures presented in this report is located at the end of this document.

The effect of a change in the $t/D$ ratio on debris-cloud morphology is shown in Figure 6 for eight $t/D$ ratios. All debris clouds shown in this figure were produced by the impact of a 9.53-mm-diameter, 2017-T4 aluminum sphere with a 6061-T6 aluminum sheet at an impact velocity of 6.70 km/s, $\pm$ 0.08 km/s. As shown in Figure 6, $t/D$ ratios for the tests ranged from 0.026 to 0.424. In addition to a significant expansion of the internal structure of the debris cloud, the following changes in internal-structure morphology occurred as the $t/D$ ratio was increased and impact velocity was held constant: (1) the diameter of the disk-like center element increased, began to "bend over" at a $t/D$ of 0.084, and formed a flat-bottomed bowl at $t/D$ = 0.163; (2) radial expansion of the hemispherical shell of spall fragments at the rear of the internal structure increased; and (3) the size of fragments in the center and rear element decreased. In contrast to the growth of the center and rear element, the front element of the cloud did not change significantly in size, shape (a truncated cone), or radiographic density until the $t/D$ ratio was greater than 0.102.

**t/D = 0.026**

4-1395
t = 0.246 mm
6.70 km/s

**t/D = 0.049**

4-1360
t = 0.465 mm
6.62 km/s

**t/D = 0.062**

4-1359
t = 0.592 mm
6.78 km/s

**t/D = 0.084**

4-1289
t = 0.800 mm
6.68 km/s
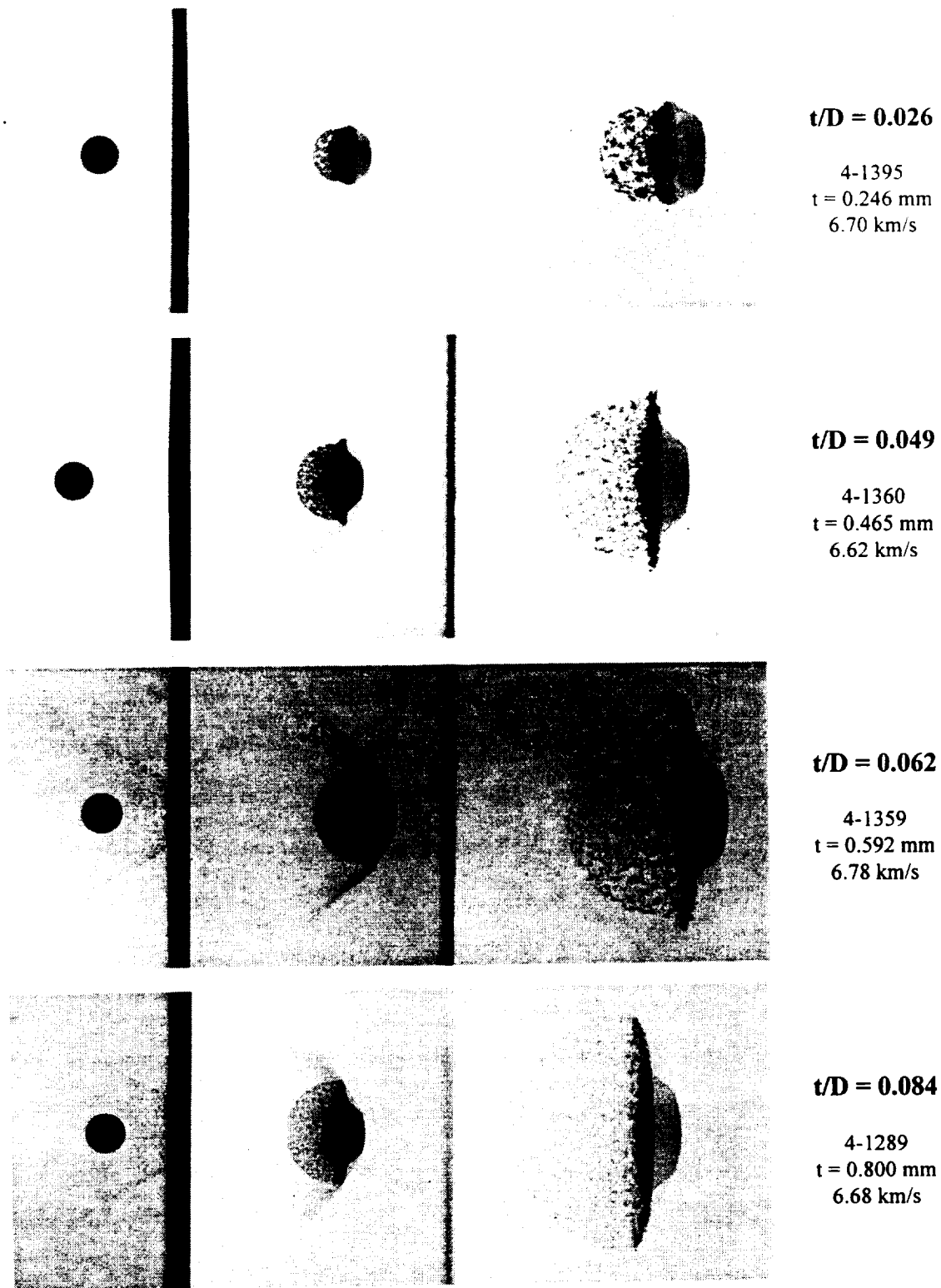
Figure 6.  Views of debris clouds produced by the impact of 9.53-mm-diameter,2017-T4
aluminum spheres with 6061-T6 aluminum sheets.  Sheet thickness was varied
and impact velocity was held constant.

19

t/D = 0.102

4-1283
t = 0.968 mm
6.72 km/s

t/D = 0.163

4-1291
t = 1.549 mm
6.71 km/s

t/D = 0.234

4-1352
t = 2.225 mm
6.64 km/s

t/D = 0.424

4-1353
t = 4.039 mm
6.68 km/s
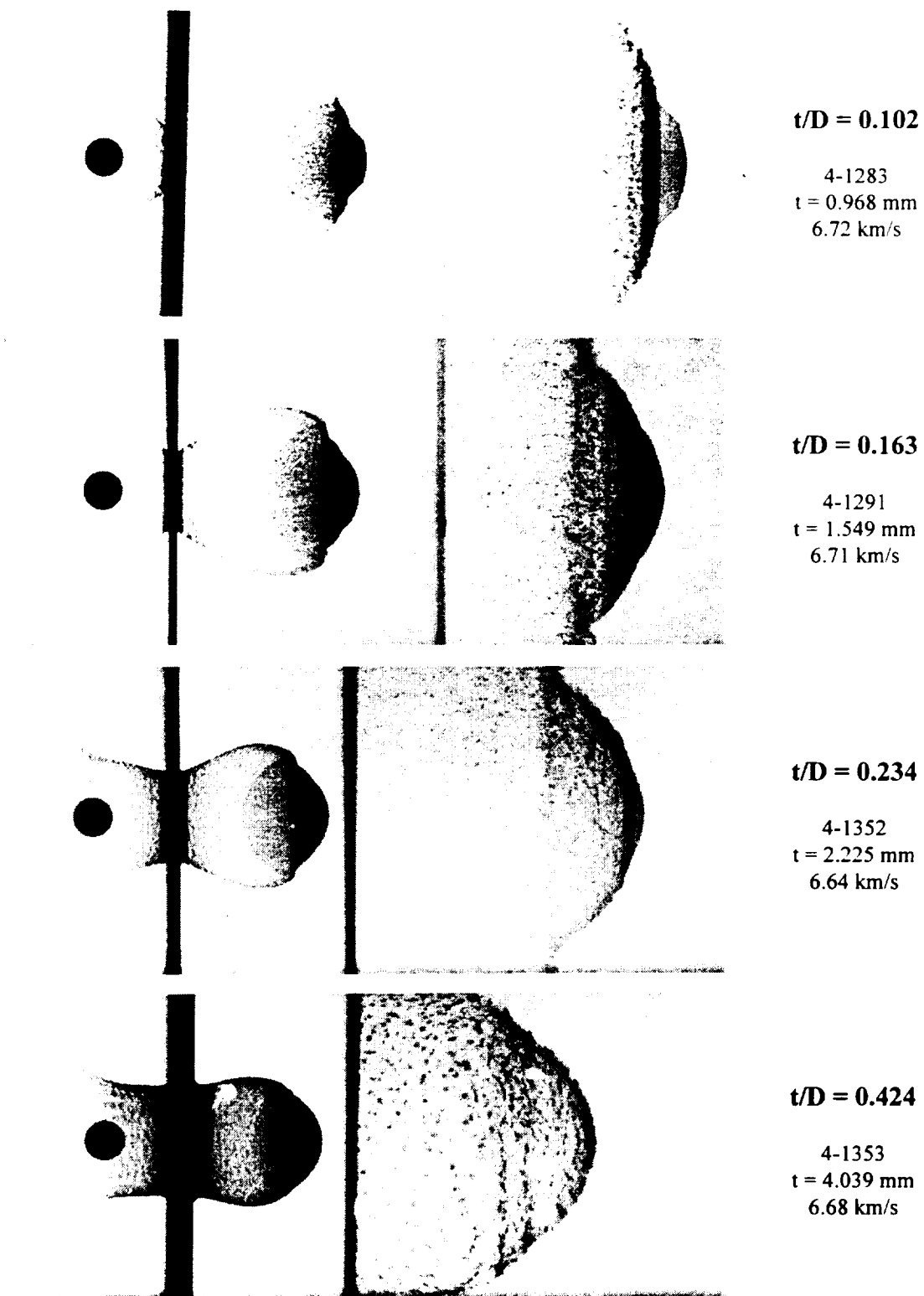
Figure 6. (Concluded). Views of debris clouds produced by the impact of 9.53-mm-diameter, 2017-T4 aluminum spheres with 6061-T6 aluminum sheets. Sheet thickness was varied and impact velocity was held constant.

20

At $t/D$ ratios of 0.163 and 0.234, this element was a spherical sector; it did not exist when the $t/D$ ratio was 0.424. The relatively constant radiographic density of the front element for the lower $t/D$ ratios was noteworthy when compared to the varying radiographic density of the external bubble of debris and the ejecta veil for these same tests. As the $t/D$ ratio increased, a significantly larger fraction of the bumper became involved in the formation of the external bubble of debris.

The effects of a change in impact velocity on debris-cloud morphology are shown in Figure 7 for tests with a constant $t/D$ ratio of 0.049. In all five tests, 9.53-mm-diameter, 2017-T4 aluminum spheres and 0.465-mm-thick, 6061-T6 aluminum sheets were used. Although not visible in the photographic reproduction of the radiograph for the test at 3.77 km/s, the post-impact-view radiographs from this test show a narrow region of reduced density just inside the rear surface of the sphere. A spall failure (shown in more detail in Section VI) developed inside the rear surface of the sphere, increased its radius and formed a shell that remained attached to the sphere. A slight flattening of the front of the sphere and a small piece of bumper that moved downrange slightly faster than the flattened sphere was also observed for this test. As impact velocity increased, fragmentation of the sphere and an increase in the axial and diametral expansion of the internal structure was observed. A small front element was clearly evident when the impact velocity reached 5.45 km/s. Further development of the front element occurred as impact velocity was increased to 6.62 km/s and 7.38 km/s. The limited data available for a series of $t/D$ = 0.084 tests also indicated that development of the debris cloud followed the same processes identified for the $t/D$ = 0.049 tests. However, the changes observed for the $t/D$ = 0.084 tests occurred at lower impact velocities than for the $t/D$ = 0.049 tests.

Subtle changes in debris-cloud properties were observed when the projectile material was changed from 2017-T4 aluminum to 1100-O aluminum. These changes

**3.77 km/s**
4-1428

**4.71 km/s**
4-1433

**5.45 km/s**
4-1394

**6.62 km/s**
4-1360

**7.38 km/s**
4-1744
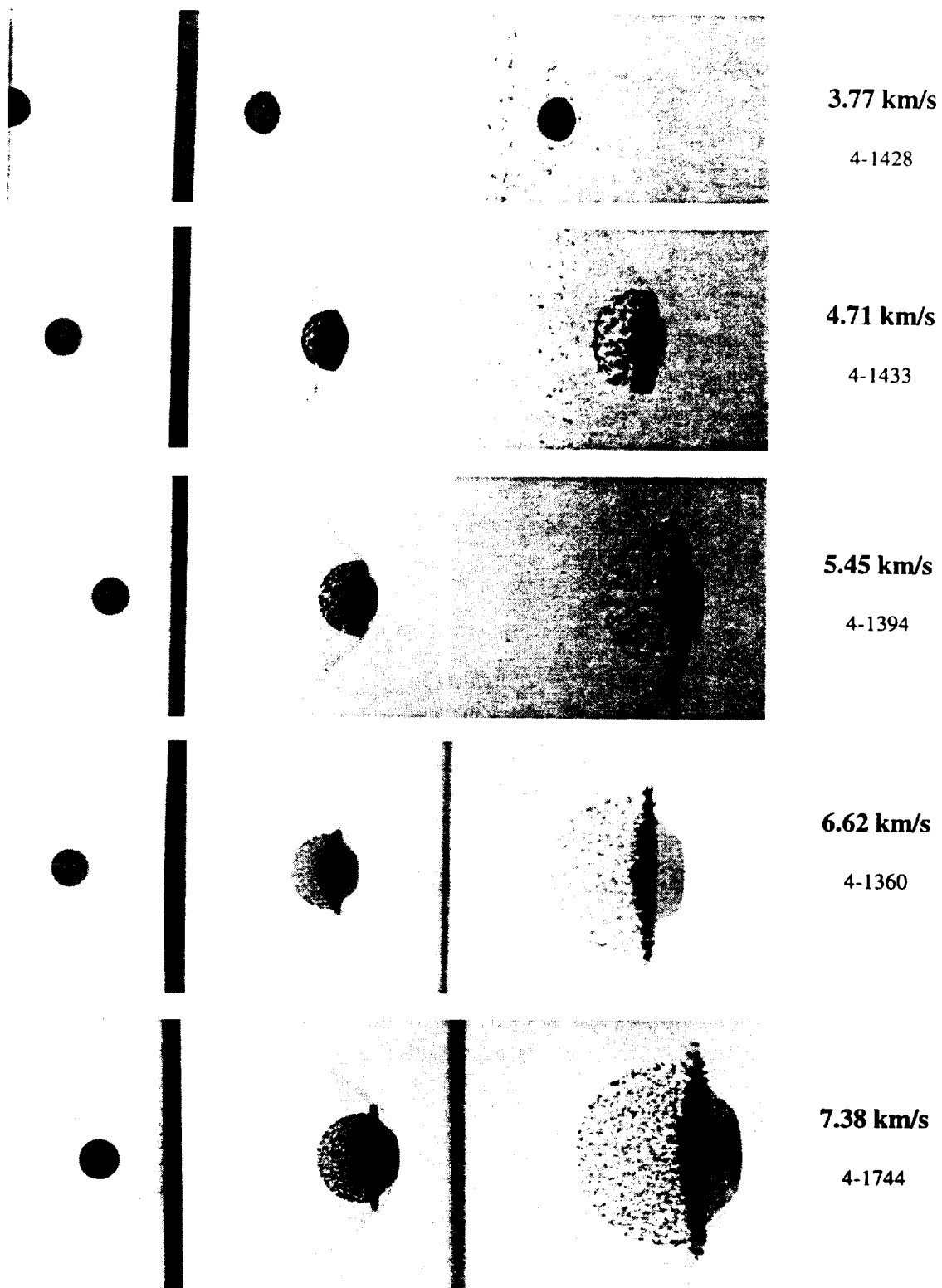
Figure 7. Views of debris clouds produced by impact of 9.53-mm-diameter, 2017-T4 aluminum spheres with 6061-T6 aluminum sheets. Impact velocity was varied and *t/D* ratio was held constant at 0.049.

were not readily apparent when viewing the radiographs and are treated more thoroughly in Section IV. Use of other bumper materials, 1100-O and 2024-T3 aluminum, did not measurably affect debris-cloud shape or characteristics.

# B. Analysis of Radiographs

All usable radiographs from tests included in this report were analyzed. Readily identifiable features and locations in the debris clouds were assigned point numbers as shown in Figure 8. Axial and radial positions and velocities of each of these points, with respect to the debris-cloud center line, and the radial expansion velocity of the hemispherical shell of projectile spall fragments was determined. Use of the fine-source, soft x-rays and direct-exposure film produced radiographs in which fragments as small as 0.25 mm could be seen and measured. Accurate positioning of the x-ray heads and use of a common reference point for measurements taken from the radiographs permitted specific debris-cloud positions to be determined to within ± 0.25 mm or better. Rotation of individual fragments at critical measurement points produced most of the "error" encountered when determining the location of these points. The time between firing of the pairs of flash x-rays was determined to within ± 0.1 μs. Accordingly, velocities of material at measurement points could be determined to within ± 0.1 km/s or better. For those cases in which test results for two nearly identical test conditions were available, agreement between measured values was excellent.

Several comments regarding notation in the following tables and figures are in order. Measurements of points ① through ④ were made along the debris-cloud center line, referenced to the front surface of the bumper. Six points in Figure 8, ⑤ through ⑩
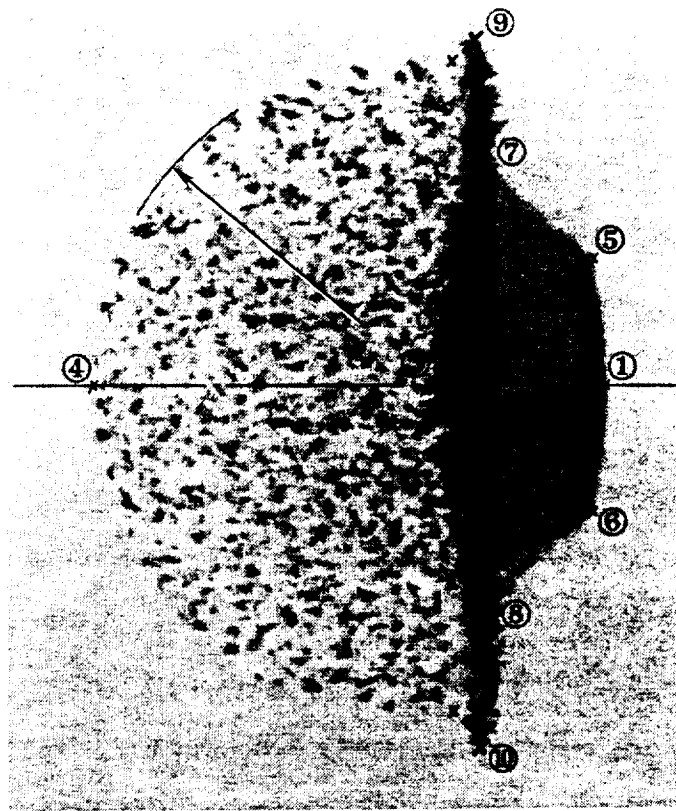
Figure 8. Points used when making measurements of debris-cloud features.

inclusive, are points for which two sets of measurements were taken; (1) axial distance from the front surface of the bumper and (2) distance between points, measured normal to the debris-cloud center line. These measurements were used, with appropriate timing information, to determine axial and diametral velocities of these points or pairs of points, respectively. Axial distances and velocities were denoted when the points were separated by a comma. Diametral distances and velocities were denoted when the points were separated by a dash. The radius of an arc defining the perimeter of the shell of spall fragments and the position of the center of this arc (on the debris-cloud center line) were also measured when appropriate. Finally, the distance from the front surface of the bumper to the rear of the large central fragment was measured.

The measurements taken from the film were adjusted to account for parallax and for the magnification of the shadow of the debris cloud resulting from the placement of the x-ray source, object (debris cloud), and film. Appropriate corrections were applied to all measured values before further computational work was performed on the data.

Three post-impact views of the debris clouds were made to provide for correlation of the debris velocities between any two of the measurement points and to determine (in the event the velocities failed to agree) the magnitude of any accelerative forces acting on the debris-cloud structure. Analysis of the radiographs of all tests shown in Table 2 indicated that the post-impact flight of debris-cloud material was ballistic (i.e., did not accelerate). In some tests, evidence of drag due to the slight atmospheric pressure in the range was noted in the behavior the front element. An ambient range pressure of 8 to 10 mm Hg of nitrogen was used to aerodynamically separate the sabot from the projectile and may have affected the flight of the leading edge of the debris cloud.

The timing of the flash x-ray exposures (shown with respect to impact) and a listing of adjusted distances taken from the *second view* of the debris cloud are presented in Table 3. Only data from normal-impact, single-sheet bumper tests are included in this table. As shown in Table 2, flash radiographs were not available for four of the tests because of failure of the x-rays to fire (Shot 4-1287) or improper timing of the x-ray exposures (Shots 4-1351, 4-1718, and 4-1719). The distances shown in Table 3 can be used with the time after impact of the exposure, $\tau_3$, and the velocities of the measured points (given later in this section) to reconstruct the shape of the debris cloud for any time after impact. The distances shown are averages of the values measured from the side and top views, but are accurate to within ± 0.25 mm (0.01 inch). In some instances, the values may vary somewhat more as a result of rotation of fragments or asymmetry of the element.

## TABLE 3

## POSITIONS OF VARIOUS POINTS, DIAMETERS, AND RADII
## MEASURED IN SECOND VIEW OF DEBRIS CLOUD ($\tau_3$)

Times are in microseconds (± 0.1 µs) and distances are in inches (± 0.01 in)
Distances have been adjusted for parallax and film magnification.

| Shot Number | $\tau_1$ | $\tau_2$ | $\tau_3$ | $\tau_4$ | 1 | 2 | 3 | 4 | 5,6 | 7,8 | 9,10 | Center |
|---|---|---|---|---|---|---|---|---|---|---|---|---|
| | | *Time of X-Ray Exposures With Respect to Impact* $\tau = 0$ *at Impact* | | | | | *Distance From Front Surface of Bumper* | | | | | |
| **Projectile - 6.35-mm-diameter, 2017-T4 aluminum sphere. Nominal mass - 0.373g.** | | | | | | | | | | | | |
| 4-1318 | -3.5 | 5.9 | 19.1 | 43.6 | 5.04 | 4.80 | 4.66 | 3.93 | 5.00 | 4.80 | 4.75 | 4.58 |
| 4-1449 | -3.1 | 6.5 | 17.8 | 38.8 | 5.16 | 4.89 | 4.71 | 3.92 | 5.13 | 4.88 | 4.83 | 4.67 |
| **Projectile - 9.53-mm-diameter, 2017-T4 aluminum sphere. Nominal mass - 1.275g.** | | | | | | | | | | | | |
| 4-1282 | -4.0 | 6.4 | 24.3 | --- | 6.31 | 5.96 | 5.80 | 4.78 | 6.26 | 5.96 | 5.92 | 5.75 |
| 4-1283 | -3.1 | 7.3 | 20.4 | 42.2 | 5.24 | 5.00 | 4.83 | 3.45 | 5.16 | 4.95 | 4.64 | 4.76 |
| 4-1284 | -4.0 | 0.9 | 19.5 | 44.9 | 5.05 | 4.78 | 4.58 | 3.78 | 5.02 | 4.79 | 4.73 | 4.56 |
| 4-1289 | -3.4 | 6.9 | 19.9 | 45.4 | 5.19 | 4.93 | 4.77 | 3.57 | 5.13 | 4.90 | 4.76 | 4.70 |
| 4-1290 | -3.6 | 6.7 | 19.8 | 45.3 | 5.33 | 5.05 | 4.80 | 4.28 | 5.29 | 5.04 | 4.98 | 4.84 |
| 4-1291 | -3.1 | 7.2 | 20.3 | 28.8 | 5.02 | 4.81 | 4.73 | 2.98 | --- | 4.77 | --- | 4.64 |
| 4-1352 | -3.5 | 6.6 | 20.9 | --- | 4.83 | 4.73 | --- | 2.67 | --- | 4.69 | --- | 4.29 |
| 4-1353 | -1.7 | 8.4 | 22.6 | --- | 4.36 | --- | --- | --- | --- | --- | --- | --- |
| 4-1359 | -3.2 | 8.2 | 21.3 | 44.8 | 5.63 | 5.33 | 5.13 | 4.08 | 5.58 | 5.33 | 5.24 | 5.04 |
| 4-1360 | -4.2 | 7.2 | 20.3 | 43.8 | 5.24 | 4.98 | 4.75 | 3.97 | 5.22 | 4.96 | 4.92 | 4.72 |
| 4-1392 | -4.4 | 6.0 | 19.0 | 44.4 | 5.01 | 4.74 | 4.49 | 4.08 | 4.99 | 4.76 | 4.67 | 4.56 |
| 4-1394 | -3.6 | 9.3 | 25.7 | 53.8 | 5.41 | 5.28 | 5.06 | 4.44 | 5.40 | 5.27 | 5.20 | 5.12 |
| 4-1395 | -3.4 | 6.9 | 19.9 | 43.4 | 5.41 | 5.10 | 4.85 | 4.40 | 5.37 | 5.09 | 5.05 | 4.88 |
| 4-1428 | -12.3 | 6.7 | 29.0 | 68.7 | 4.15 | 4.11 | --- | 3.76 | --- | --- | 4.02[a] | --- |
| 4-1433 | -6.7 | 9.2 | 27.9 | 61.5 | 5.02 | 5.02 | 4.70 | 4.34 | --- | --- | 4.89[a] | 4.89 |
| 4-1621 | -6.9 | 9.1 | 29.2 | 64.2 | 5.06 | --- | 4.73 | 4.02 | --- | --- | 4.78 | 4.89 |
| 4-1622 | -5.1 | 15.2 | 40.6 | 84.9 | 6.08 | --- | 5.42 | 4.96 | --- | --- | 5.59 | 5.73 |
| 4-1631 | -8.2 | 12.3 | 38.0 | 82.7 | 5.09 | --- | 4.79 | 4.50 | --- | --- | 4.99 | 5.09 |
| 4-1632 | -6.1 | 16.2 | 44.2 | 93.1 | 5.62 | 5.59 | --- | --- | --- | --- | --- | --- |
| 4-1633 | -6.3 | 14.9 | 41.4 | 87.4 | 5.68 | 5.62 | --- | --- | --- | --- | --- | --- |
| 4-1715 | -6.4 | 9.7 | 29.7 | 64.6 | 5.38 | 5.33 | --- | 4.97 | --- | --- | --- | --- |
| 4-1716 | -5.7 | 10.3 | 30.3 | 65.3 | 5.21 | --- | --- | 3.82 | --- | 4.87 | 4.67 | 5.24 |
| 4-1717 | -5.4 | 9.8 | 28.9 | 62.1 | 5.12 | --- | --- | 3.53 | --- | 4.73 | 4.49 | 5.14 |
| 4-1720 | -12.6 | 18.4 | 59.8 | 130.0 | 4.68 | --- | --- | 4.35 | --- | --- | 4.33 | --- |
| 4-1721 | -12.1 | 30.1 | 94.7 | 204.7 | 5.23 | 5.17 | --- | 4.97 | --- | --- | --- | --- |
| 4-1722 | -19.8 | 7.9 | 44.8 | 107.4 | 4.04 | 3.97 | --- | 3.66 | --- | --- | --- | --- |
| 4-1744 | -2.9 | 7.5 | 19.6 | 41.6 | 5.83 | 5.37 | 5.22 | 4.26 | 5.77 | 5.45 | 5.41 | 5.12 |
| **Projectile - 12.70-mm-diameter, 2017-T4 aluminum sphere. Nominal mass - 3.000g.** | | | | | | | | | | | | |
| 4-1281 | -8.4 | 2.9 | 17.0 | 36.0 | 4.39 | 4.12 | 3.83 | 3.27 | 4.37 | 4.11 | 4.06 | 3.87 |
| 4-1357 | -4.8 | 7.5 | 21.6 | 31.4 | 4.97 | 4.79 | --- | 2.96 | --- | 4.76 | --- | 4.71 |
| 4-1358 | -4.6 | 7.4 | 21.2 | 46.0 | 5.16 | 4.92 | 4.61 | 3.92 | 5.13 | 4.89 | 4.83 | 4.66 |
| **Projectile - 12.70-mm-diameter, 1100-O aluminum sphere. Nominal mass - 2.918g.** | | | | | | | | | | | | |
| 4-1601 | -4.3 | 7.5 | 21.4 | 46.5 | 5.36 | 5.11 | 4.84 | 3.96 | 5.34 | 5.07 | 5.03 | 4.81 |

[a] Points ⑨ and ⑩ as defined did not develop. Measured points similar to points behind ⑨ and ⑩ in Figure 8.

## TABLE 3 (Concluded)

## POSITIONS OF VARIOUS POINTS, DIAMETERS, AND RADII
## MEASURED IN SECOND VIEW OF DEBRIS CLOUD ($\tau_3$)

Times are in microseconds (± 0.1 μs) and distances are in inches (± 0.01 in)
Distances have been adjusted for parallax and film magnification.

| Shot Number | $\tau_1$ | $\tau_2$ | $\tau_3$ | $\tau_4$ | 5-6 | 7-8 | 9-10 | Shell Radius | Large Fragment[b] |
|---|---|---|---|---|---|---|---|---|---|
| | Time of X-Ray Exposures With Respect to Impact $\tau = 0$ at Impact | | | | Diameter of Cloud | | | | |
| **Projectile - 6.35-mm-diameter, 2017-T4 aluminum sphere. Nominal mass - 0.373g.** | | | | | | | | | |
| 4-1318 | -3.5 | 5.9 | 19.1 | 43.6 | 0.54 | 0.93 | 1.46 | 0.66 | 4.67 |
| 4-1449 | -3.1 | 6.5 | 17.8 | 38.8 | 0.60 | 1.13 | 1.66 | 0.76 | 4.73 |
| **Projectile - 9.53-mm-diameter, 2017-T4 aluminum sphere. Nominal mass - 1.275g.** | | | | | | | | | |
| 4-1282 | -4.0 | 6.4 | 24.3 | --- | 0.75 | 1.29 | 2.13 | 0.97 | 5.80 |
| 4-1283 | -3.1 | 7.3 | 20.4 | 42.2 | 0.80 | 1.21 | 2.67 | 1.31 | 4.84 |
| 4-1284 | -4.0 | 0.9 | 19.5 | 44.9 | 0.64 | 1.05 | 1.75 | 0.79 | 4.58 |
| 4-1289 | -3.4 | 6.9 | 19.9 | 45.4 | 0.76 | 1.15 | 2.23 | 1.13 | 4.77 |
| 4-1290 | -3.6 | 6.7 | 19.8 | 45.3 | 0.61 | 0.99 | 1.17 | 0.56 | 4.84 |
| 4-1291 | -3.1 | 7.2 | 20.3 | 28.8 | --- | 2.21 | --- | 1.67 | 4.73 |
| 4-1352 | -3.5 | 6.6 | 20.9. | --- | --- | 0.94 | --- | 1.61 | --- |
| 4-1353 | -1.7 | 8.4 | 22.6 | --- | --- | --- | --- | --- | --- |
| 4-1359 | -3.2 | 8.2 | 21.3 | 44.8 | 0.71 | 1.17 | 2.19 | 0.96 | 5.13 |
| 4-1360 | -4.2 | 7.2 | 20.3 | 43.8 | 0.62 | 1.12 | 1.73 | 0.75 | 4.75 |
| 4-1392 | -4.4 | 6.0 | 19.0 | 44.4 | 0.54 | 0.89 | 0.91 | 0.46 | 4.49 |
| 4-1394 | -3.6 | 9.3 | 25.7 | 53.8 | 0.47 | 0.76 | 1.38 | 0.67 | 5.08 |
| 4-1395 | -3.4 | 6.9 | 19.9 | 43.4 | 0.59 | 0.96 | 0.99 | 0.48 | 4.86 |
| 4-1428 | -12.3 | 6.7 | 29.0 | 68.7 | --- | --- | 0.40[a] | --- | --- |
| 4-1433 | -6.7 | 9.2 | 27.9 | 61.5 | --- | --- | 1.01[a] | 0.54 | 4.70 |
| 4-1621 | -6.9 | 9.1 | 29.2 | 64.2 | --- | --- | 1.63 | 0.86 | 4.76 |
| 4-1622 | -5.1 | 15.2 | 40.6 | 84.9 | --- | --- | 1.32 | 0.76 | 5.42 |
| 4-1631 | -8.2 | 12.3 | 38.0 | 82.7 | --- | --- | 1.08 | 0.60 | 4.79 |
| 4-1632 | -6.1 | 16.2 | 44.2 | 93.1 | --- | --- | --- | --- | 5.32 |
| 4-1633 | -6.3 | 14.9 | 41.4 | 87.4 | --- | --- | --- | --- | 5.62 (Front) |
| 4-1715 | -6.4 | 9.7 | 29.7 | 64.6 | --- | --- | --- | --- | --- |
| 4-1716 | -5.7 | 10.3 | 30.3 | 65.3 | --- | 1.63 | 2.79 | 1.43 | 5.00 |
| 4-1717 | -5.4 | 9.8 | 28.9 | 62.1 | --- | 1.70 | 2.93 | 1.60 | 4.94 |
| 4-1720 | -12.6 | 18.4 | 59.8 | 130.0 | --- | --- | 1.20 | --- | --- |
| 4-1721 | -12.1 | 30.1 | 94.7 | 204.7 | --- | --- | --- | --- | --- |
| 4-1722 | -19.8 | 7.9 | 44.8 | 107.4 | --- | --- | --- | --- | --- |
| 4-1744 | -2.9 | 7.5 | 19.6 | 41.6 | 0.72 | 1.40 | 2.04 | 0.86 | 5.22 |
| **Projectile - 12.70-mm-diameter, 2017-T4 aluminum sphere. Nominal mass - 3.000g.** | | | | | | | | | |
| 4-1281 | -8.4 | 2.9 | 17.0 | 36.0 | 0.58 | 1.05 | 1.38 | 0.61 | 3.83 |
| 4-1357 | -4.8 | 7.5 | 21.6 | 31.4 | --- | 1.22 | --- | 1.75 | --- |
| 4-1358 | -4.6 | 7.4 | 21.2 | 46.0 | 0.63 | 1.11 | 1.65 | 0.75 | 4.61 |
| **Projectile - 12.70-mm-diameter, 1100-O aluminum sphere. Nominal mass - 2.918g.** | | | | | | | | | |
| 4-1601 | -4.3 | 7.5 | 21.4 | 46.5 | 0.68[c] | 1.15[c] | 1.65 | 0.84 | 4.88 |

[a] Points ② and ⑩ as defined did not develop. Measured points similar to points behind ③ and ⑨ in Figure 8.
[b] Measurement is to rear of large central fragment, except for Shot 4-1633.
[c] Oval cross section. Ratio of major axis to minor axis = 9:8. Average diameter shown.

# C. Results and Discussion

The results of the measurements and computations made to determine the post-impact velocity of the various debris-cloud features are presented in Table 4. The effects of a change in $t/D$ ratio and/or impact velocity on the velocities of the axial measurement points of the debris cloud, the axial and diametral velocities of the front element, the axial and diametral velocities of the disk-like center element, and the radial expansion velocity of the spall-shell fragments are presented, in that order.

Discussion of the data presented in Table 4 will focus on the results of two series of tests: (1) tests with an impact velocity of approximately 6.70 km/s and all $t/D$ ratios and (2) tests with varying impact velocities but at a $t/D$ ratio of 0.049. Results of a third but smaller series of tests, with varying impact velocities and a $t/D$ ratio of 0.084, were available but were not included in the discussion, primarily to keep the figures less cluttered. Qualitatively, however, the data from the $t/D = 0.084$ series exhibited the same trends observed in the $t/D = 0.049$ series. In general, the figures presented in this section will show that all debris clouds expanded, both axially and radially, as $t/D$ ratio and impact velocity were increased.

In Figure 9a, the normalized axial debris-cloud velocities for points ①, ②, and ④ are shown to decrease as $t/D$ ratio is increased. Point ③ was omitted from this figure because its behavior was similar to point ② and its inclusion in Figure 9 would not add significantly to the data presented. The velocities of points ② and ③ are very close to or may be the velocity of the center of mass of the debris cloud. The observed decrease in velocity of these points is not surprising since the mass of bumper involved in the collision increased with increasing $t/D$ ratio. Conservation of momentum would require, therefore, that the velocity of the center of mass of the debris cloud decrease accordingly. The velocity of point ②, as shown in Figure 9b, is nearly constant, as would be expected

# TABLE 4

## NORMALIZED DEBRIS-CLOUD VELOCITY DATA

Velocity data have been normalized by dividing the various measured velocities by the impact velocity of the test. Unless noted otherwise, all bumpers were 6061-T6 aluminum sheet.

| Shot Number | $\frac{l}{D}$ | Impact Velocity, (km/s) | $V_1/V_0$ | $V_2/V_0$ | $V_3/V_0$ | $V_4/V_0$ | $V_{5,6}/V_0$ | $V_{7,8}/V_0$ | $V_{9,10}/V_0$ |
|---|---|---|---|---|---|---|---|---|---|
| Projectile - 6.35-mm-diameter, 2017-T4 aluminum sphere. Nominal mass - 0.373 g. | | | | | | | | |
| 4-1318 | 0.048[a] | 6.64 | 1.002 | 0.970 | 0.970 | 0.825 | 0.999 | 0.970 | 0.963 |
| 4-1449 | 0.050 | 7.23 | 1.019 | 0.978 | 0.965 | 0.819 | 1.014 | 0.974 | 0.971 |
| Projectile - 9.53-mm-diameter, 2017-T4 aluminum sphere. Nominal mass - 1.275 g. | | | | | | | | |
| 4-1715 | 0.026 | 4.67 | 0.985 | 0.978 | 0.978 | 0.978 | --- | --- | --- |
| 4-1392 | 0.026 | 6.54 | 1.032 | 0.997 | 0.988 | 0.907 | 1.026 | 0.994 | 0.992 |
| 4-1395 | 0.026 | 6.70 | 1.030 | 0.991 | 0.985 | 0.901 | 1.015 | 0.984 | 0.984 |
| 4-1290 | 0.032[a] | 6.67 | 1.018 | 0.982 | 0.974 | 0.877 | 1.013 | 0.978 | 0.974 |
| 4-1428 | 0.049 | 3.77 | 0.966 | 0.958 | --- | 0.958 | --- | --- | 0.960[b] |
| 4-1433 | 0.049 | 4.71 | 0.970 | 0.970 | 0.970 | 0.904 | --- | --- | 0.965[b] |
| 4-1394 | 0.049 | 5.45 | 0.982 | 0.971 | 0.972 | 0.866 | 0.982 | 0.971 | 0.964 |
| 4-1360 | 0.049 | 6.62 | 1.012 | 0.980 | 0.977 | 0.826 | 1.010 | 0.976 | 0.968 |
| 4-1744 | 0.049 | 7.38 | 1.031 | 0.966 | 0.963 | 0.804 | 1.024 | 0.978 | 0.977 |
| 4-1282 | 0.053[c] | 6.58 | 1.002 | 0.962 | 0.970 | 0.809 | 0.997 | 0.960 | 0.959 |
| 4-1284 | 0.053[c] | 6.58 | 0.997 | --- | 0.968 | 0.805 | 0.994 | 0.960 | 0.954 |
| 4-1633 | 0.062 | 3.65 | 0.951 | 0.950 | --- | --- | --- | --- | --- |
| 4-1359 | 0.062 | 6.78 | 1.001 | 0.968 | 0.966 | 0.785 | 0.997 | 0.968 | 0.954 |
| 4-1632 | 0.084 | 3.47 | 0.928 | 0.928 | --- | --- | --- | --- | --- |
| 4-1631 | 0.084 | 3.64 | 0.937 | --- | 0.934 | 0.887 | --- | --- | 0.931 |
| 4-1622 | 0.084 | 3.84 | 0.935 | --- | 0.935 | 0.864 | --- | --- | 0.927 |
| 4-1621 | 0.084 | 4.62 | 0.950 | --- | 0.939 | 0.814 | --- | --- | 0.924 |
| 4-1289 | 0.084 | 6.68 | 0.986 | 0.960 | 0.968 | 0.734 | 0.970 | 0.962 | 0.931 |
| 4-1283 | 0.102 | 6.72 | 0.973 | 0.955 | 0.948 | 0.696 | 0.960 | 0.942 | 0.882 |
| 4-1722 | 0.132 | 2.54 | 0.906 | 0.893 | 0.893 | 0.893 | --- | --- | --- |
| 4-1716 | 0.135 | 4.71 | 0.934 | --- | --- | 0.732 | --- | 0.896 | 0.858 |
| 4-1291 | 0.163 | 6.71 | 0.939 | 0.915 | 0.928 | 0.596 | --- | 0.916 | --- |
| 4-1717 | 0.168 | 4.96 | 0.915 | --- | --- | 0.673 | --- | 0.861 | 0.818 |
| 4-1720 | 0.233 | 2.44 | 0.816 | 0.811 | 0.811 | 0.811 | --- | --- | 0.784 |
| 4-1352 | 0.234 | 6.64 | 0.893 | 0.894 | --- | 0.536 | --- | 0.892 | --- |
| 4-1353 | 0.424 | 6.68 | 0.793 | --- | --- | --- | --- | --- | --- |
| 4-1721 | 0.504 | 2.23 | 0.623 | 0.623 | 0.623 | 0.623 | --- | --- | --- |
| Projectile - 12.70-mm-diameter, 2017-T4 aluminum sphere. Nominal mass - 3.000 g. | | | | | | | | |
| 4-1281 | 0.040[c] | 6.46 | 1.012 | 0.981 | 0.977 | 0.851 | 1.011 | 0.975 | 0.972 |
| 4-1358 | 0.047 | 6.26 | 1.003 | 0.981 | 0.978 | 0.851 | 1.007 | 0.975 | 0.970 |
| 4-1357 | 0.160[c] | 6.38 | 0.934 | 0.918 | --- | 0.610 | --- | 0.914 | --- |
| Projectile - 12.70-mm-diameter, 1100-O aluminum sphere. Nominal mass - 2.918 g. | | | | | | | | |
| 4-1601 | 0.047 | 6.37 | 0.998 | 0.972 | 0.972 | 0.810 | 0.997 | 0.968 | 0.967 |

[a] 1100-O aluminum bumper.

[b] Points ⑨ and ⑩, as defined, did not develop. Measured points were similar to points behind ⑨ and ⑩ in Figure 8.

[c] 2024-T3 aluminum bumper.

29

## TABLE 4 (Concluded)

## NORMALIZED DEBRIS-CLOUD VELOCITY DATA

Velocity data have been normalized by dividing the various measured velocities by the impact velocity of the test. Unless noted otherwise, all bumpers were 6061-T6 aluminum sheet.

| Shot Number | $\dfrac{t}{D}$ | Impact Velocity, (km/s) | Diametral Debris-Cloud Velocities $V_{5\text{-}6}/V_0$ | $V_{7\text{-}8}/V_0$ | $V_{9\text{-}10}/V_0$ | $\dfrac{V_r}{V_0}$ | $\dfrac{V_{CTR}}{V_0}$ |
|---|---|---|---|---|---|---|---|
| Projectile - 6.35-mm-diameter, 2017-T4 aluminum sphere. Nominal mass - 0.373 g. | | | | | | |
| 4-1318 | 0.048[a] | 6.64 | 0.081 | 0.140 | 0.247 | 0.111 | 0.937 |
| 4-1449 | 0.050 | 7.23 | 0.094 | 0.178 | 0.271 | 0.133 | 0.943 |
| Projectile - 9.53-mm-diameter, 2017-T4 aluminum sphere. Nominal mass - 1.275 g. | | | | | | |
| 4-1715 | 0.026 | 4.67 | --- | --- | --- | 0 | --- |
| 4-1392 | 0.026 | 6.54 | 0.075 | 0.122 | 0.115 | 0.064 | 0.966 |
| 4-1395 | 0.026 | 6.70 | 0.079 | 0.124 | 0.122 | 0.063 | 0.966 |
| 4-1290 | 0.032[a] | 6.67 | 0.082 | 0.130 | 0.153 | 0.079 | 0.960 |
| 4-1428 | 0.049 | 3.77 | --- | --- | --- | 0 | 0.960 |
| 4-1433 | 0.049 | 4.71 | --- | --- | 0.117[b] | 0.070 | 0.974 |
| 4-1394 | 0.049 | 5.45 | 0.042 | 0.097 | 0.185 | 0.095 | 0.963 |
| 4-1360 | 0.049 | 6.62 | 0.084 | 0.137 | 0.254 | 0.118 | 0.944 |
| 4-1744 | 0.049 | 7.38 | 0.089 | 0.186 | 0.290 | 0.127 | 0.935 |
| 4-1282 | 0.053[c] | 6.58 | 0.088 | 0.152 | 0.281 | 0.131 | 0.942 |
| 4-1284 | 0.053[c] | 6.58 | 0.085 | 0.131 | 0.272 | 0.128 | 0.932 |
| 4-1633 | 0.062 | 3.65 | --- | --- | --- | --- | --- |
| 4-1359 | 0.062 | 6.78 | 0.099 | 0.143 | 0.327 | 0.142 | 0.922 |
| 4-1632 | 0.084 | 3.47 | --- | --- | --- | --- | --- |
| 4-1631 | 0.084 | 3.64 | --- | --- | 0.126 | 0.082 | 0.972 |
| 4-1622 | 0.084 | 3.84 | --- | --- | 0.161 | 0.109 | 0.990 |
| 4-1621 | 0.084 | 4.62 | --- | --- | 0.249 | 0.152 | 0.970 |
| 4-1289 | 0.084 | 6.68 | 0.102 | 0.141 | 0.364 | 0.187 | 0.921 |
| 4-1283 | 0.102 | 6.72 | 0.114 | 0.149 | 0.443 | 0.208 | 0.900 |
| 4-1722 | 0.132 | 2.54 | --- | --- | --- | 0 | --- |
| 4-1716 | 0.135 | 4.71 | --- | 0.210 | 0.446 | 0.225 | 0.958 |
| 4-1291 | 0.163 | 6.71 | --- | 0.161 | --- | 0.283 | 0.873 |
| 4-1717 | 0.168 | 4.96 | --- | 0.222 | 0.464 | 0.254 | 0.931 |
| 4-1720 | 0.233 | 2.44 | --- | --- | 0.106 | --- | --- |
| 4-1352 | 0.234 | 6.64 | --- | 0.081 | --- | 0.268 | 0.807 |
| 4-1353 | 0.424 | 6.68 | --- | --- | --- | --- | --- |
| 4-1721 | 0.504 | 2.23 | --- | --- | --- | --- | --- |
| Projectile - 12.70-mm-diameter, 2017-T4 aluminum sphere. Nominal mass - 3.000 g. | | | | | | |
| 4-1281 | 0.040[c] | 6.46 | 0.077 | 0.146 | 0.212 | 0.091 | 0.941 |
| 4-1358 | 0.047 | 6.26 | 0.081 | 0.128 | 0.224 | 0.104 | 0.954 |
| 4-1357 | 0.160[c] | 6.38 | --- | 0.135 | --- | 0.293 | 0.903 |
| Projectile - 12.70-mm-diameter, 1100-O aluminum sphere. Nominal mass - 2.918 g. | | | | | | |
| 4-1601 | 0.047 | 6.37 | 0.080 | 0.114 | 0.215 | 0.119 | 0.928 |

[a] 1100-O aluminum bumper.

[b] Points ⑨ and ⑩, as defined, did not develop. Measured points similar to points behind ⑨ and ⑩ in Figure 8.

[c] 2024-T3 aluminum bumper.
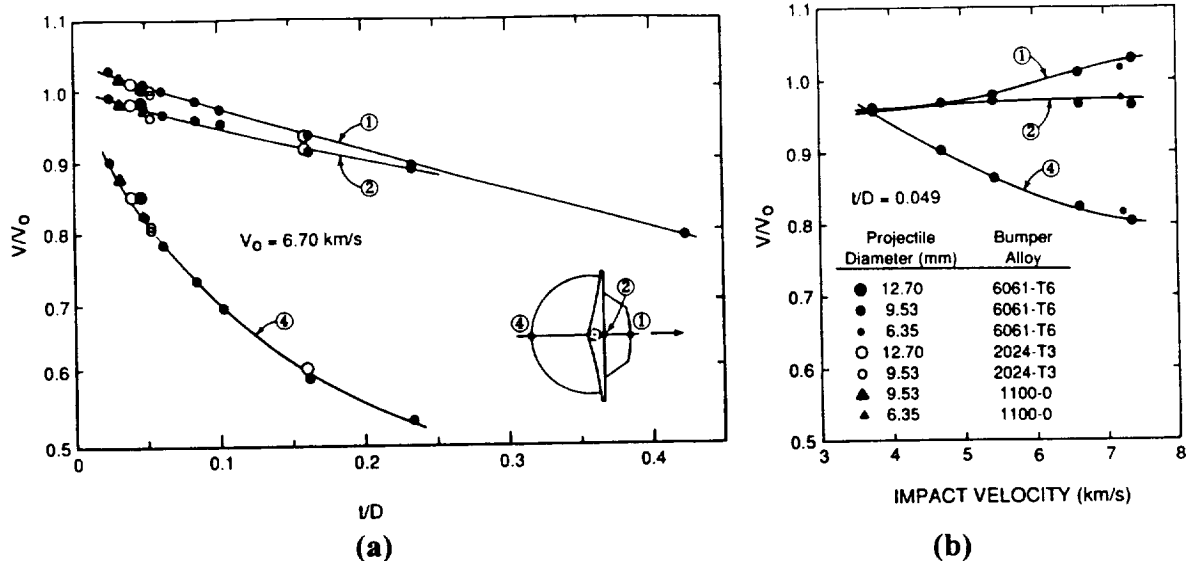
Figure 9. Normalized velocity of selected on-axis measurement points in the debris cloud versus $t/D$ ratio and impact velocity.

since the $t/D$ ratio is constant. However, the sudden increase in the velocity of point ① in Figure 9b is noteworthy and will be discussed in more detail in Section VI.

Normalized axial and diametral velocities of points ⑤, ⑥, ⑦, and ⑧ are presented in Figure 10. As $t/D$ ratio increased in Figure 10a, the axial velocity of all four points decreased, in keeping with the decrease in the velocity of the center of mass of the debris cloud. Points ⑤ and ⑥ ceased to be distinct when the front element changed from a truncated-cone shape to a spherical sector at a $t/D$ ratio between 0.10 and 0.16. The diametral velocity of points ⑦ and ⑧ increased slightly to a maximum at a $t/D$ ratio of 0.16 to 0.17, then decreased rapidly until the front element disappeared ($t/D > 0.23$). The opposite behavior of these points was observed when the $t/D$ ratio was held constant and impact velocity increased. The axial velocity of points ⑤ and ⑥ increased; however, little or no change in the axial velocity of points ⑦ and ⑧ was observed. Significant increases in the diametral velocity of both pairs of points, particularly ⑦ and ⑧, are the most notable features of Figure 10b. The observed pattern of increase in the axial and diametral velocity of points in the front element indicate that impact velocity has a greater effect on the growth of this element than $t/D$ ratio.

31

**(a)**                           **(b)**
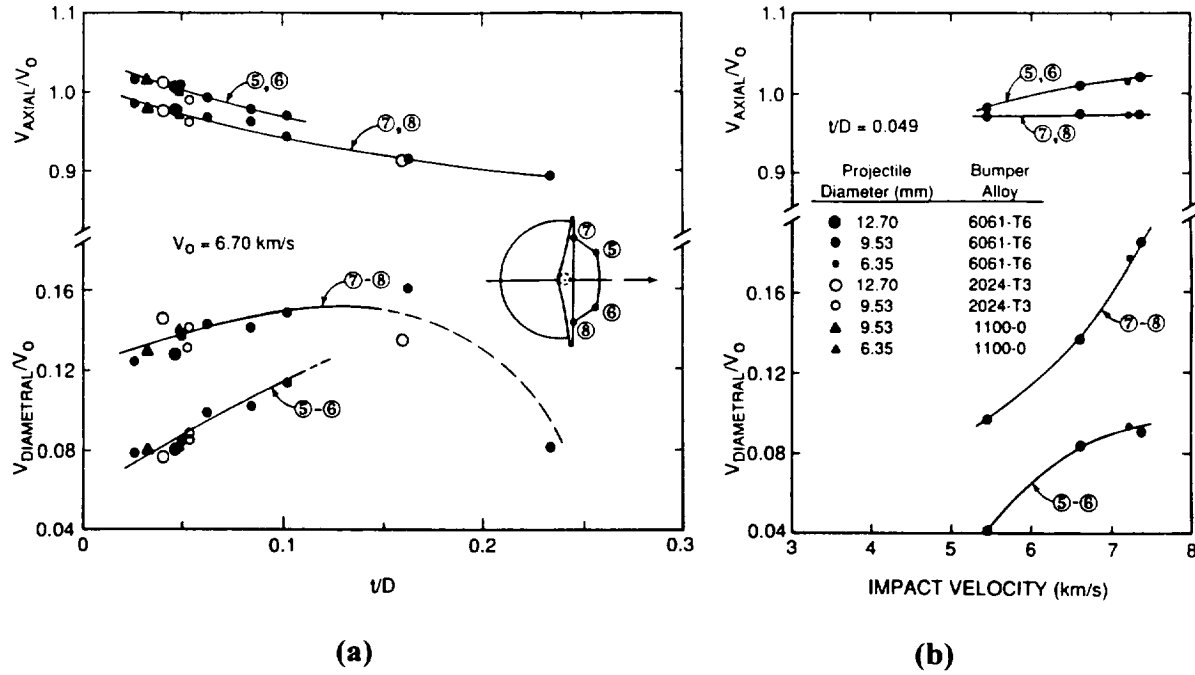
Figure 10. Normalized axial and diametral velocities of the front element of the debris cloud versus $t/D$ ratio and impact velocity.

Normalized axial and diametral velocities of points ⑨ and ⑩ are shown in Figure 11. A decrease in the axial velocity and an increase in the diametral velocity of these points occurred when the $t/D$ ratio was increased. These points ceased to be distinct in the cloud when the $t/D$ ratio was between 0.10 and 0.16, because of rearward flow at the periphery of the center element. As impact velocity was increased, little change in the axial velocity of the center element was observed; however, a moderate increase of the diametral velocity of these points occurred.

When the sphere impacted the bumper, a transient stress pulse was generated in the sphere and the bumper. The stress pulse in the sphere moved toward the rear surface of the sphere, was reflected, and a release wave was generated. When the transient stress exceeded the spall strength of the projectile, material spalled from the rear surface of the sphere. The velocity the spalled material acquired was approximated as $V_r$ (see Figure 8) and was indicative of the strength of the transient stress pulse in the projectile. A more

32
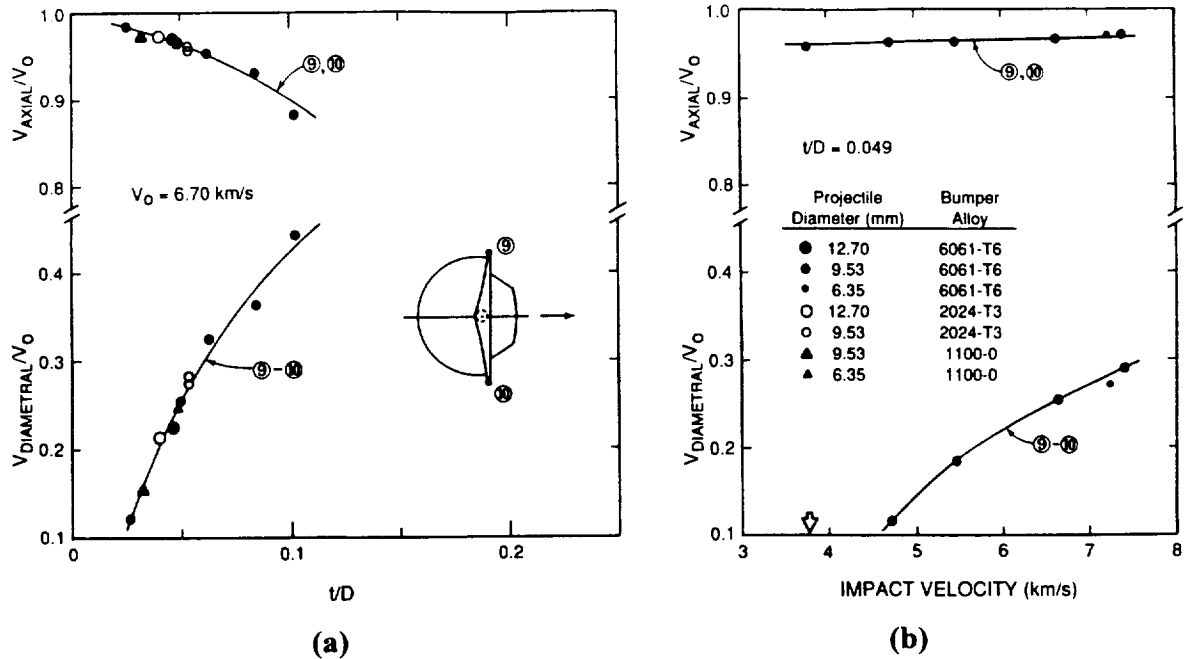
Figure 11. Normalized axial and diametral velocities of the center element of the debris cloud versus $t/D$ ratio and impact velocity.

detailed discussion of the nature of the shock wave interactions in the projectile and bumper is given in Section VI.

Normalized radial expansion velocity, $V_r / V_0$, is shown as a function of $t/D$ ratio in Figure 12 for a nominal impact velocity of 6.70 km/s. Since the projectile, bumper material, and impact velocity were nearly the same for all of the tests, the strength of the transient pulse at the front of the sphere should be the same for most of the tests shown in this figure. However, the duration of the stress pulse in the bumper was controlled by the transit time of the shock wave to the free or front surface of the bumper. Upon reaching the front surface of the bumper, a release wave was generated and traveled back through the compressed bumper material. The duration of the stress pulse in the projectile was the total transit time of the shock and release waves in the bumper. The velocity of the spalled material shown in Figure 12, then, would be more of a function of the duration of the stress pulse than of shock strength. The normalized velocity appears to approach a maximum value near a $t/D$ ratio of 0.16 to 0.17, suggesting that the duration of the stress

33
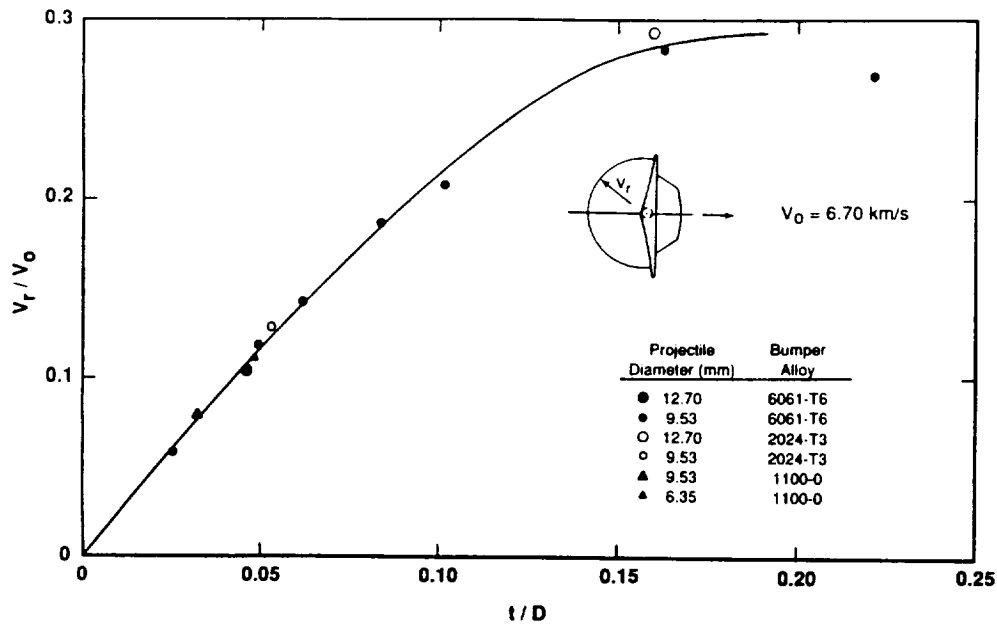
Figure 12. Normalized radial velocity of the hemispherical shell of spall fragments as a function of $t/D$ ratio for impacts at 6.7 km/s.

pulse was sufficient to "saturate" the projectile fragmentation process. Further increases in the $t/D$ ratio did not result in increased projectile fragmentation as long as impact velocity remained constant. Although the external bubble of debris for the test using a $t/D$ ratio of 0.424 was too thick to clearly identify a shell of spall fragments in all x-ray views, one did exist. Qualitatively, the shape of the shell and the apparent expansion velocity of fragments in the shell for the $t/D$ = 0.424 test (Shot 4-1353) were not significantly different from the shape and expansion velocity of the shells for the tests with $t/D$ ratios of 0.163 and 0.234 (Shots 4-1291 and 4-1352, respectively). See Figure 6 for radiographs of the debris clouds for the tests just mentioned.

The effect of impact velocity on the normalized expansion velocity, $V_r/V_0$, is shown in Figure 13 for a constant $t/D$ ratio of 0.049. Although a spall failure developed in the rear of the sphere when the impact velocity was 3.77 km/s, the shell of spall fragments had not formed (see Shot 4-1428, Figure 7). The spall shell developed quickly as impact velocity was increased from 3.77 km/s and, as shown in Figure 13, continued to expand (at a lower rate) as impact velocity increased.

34

Projectile | Bumper
Diameter (mm) | Alloy

● 9.53 — 6061-T6
■ 6.35 — 6061-T6

$t/D = 0.049$

$v_r / v_o$

0.2

0.1

0

IMPACT VELOCITY (km/s)
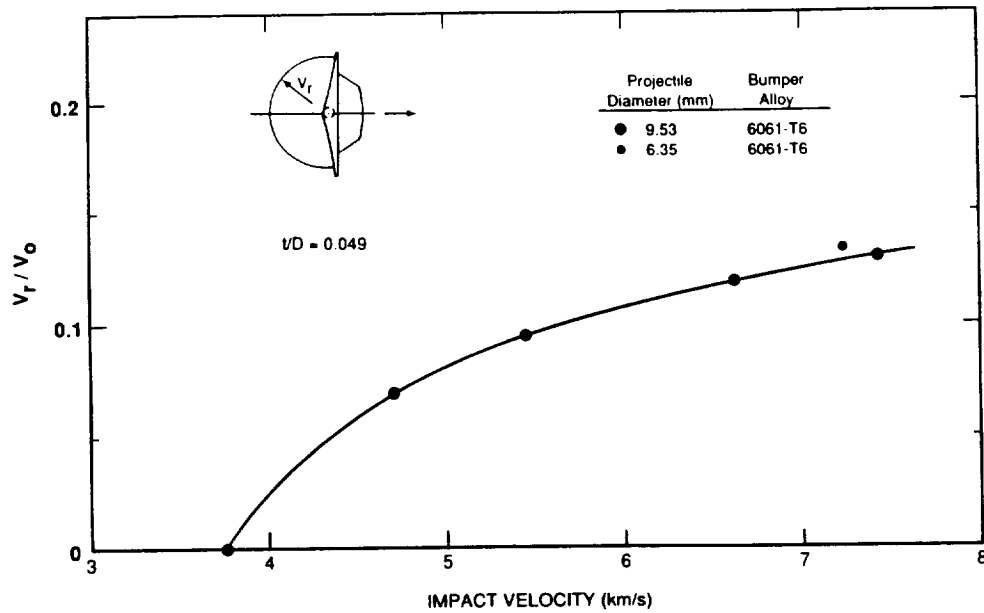
Figure 13. Normalized radial velocity of the hemispherical shell of spall fragments as a function of impact velocity for a $t/D$ ratio of 0.049.

Growth of the debris-cloud internal structure occurred as $t/D$ ratio and/or impact velocity were increased. A comparison of the normalized debris-cloud velocities used to evaluate this growth agreed (within measurement limits) despite a factor-of-two variation in projectile diameter and a factor of eight in projectile mass.

Bumper-material alloy did not appear to significantly affect the normalized axial and diametral velocities of most of the measurement points. However, a slight increase in the normalized radial velocity of the spall-shell fragments was observed for tests with the 2024-T3 aluminum bumpers. This was not surprising since the density of 2024-T3 aluminum (2.781 g/cm³) is higher than for 1100-O aluminum (2.712 g/cm³) and 6061-T6 aluminum (2.702 g/cm³). Because of the differences in bumper density, the intensity of the shock developed in the projectile and bumper would be slightly higher for the 2017-T4 / 2024-T3 aluminum combination.

While most of the data presented in this section were for tests with relatively thin bumpers, several trends in the data did emerge. These trends were helpful in predicting

the response of spheres striking thicker bumpers or impacting at velocities higher than those used for the tests. Data presented in Figures 10a and 12 would indicate that the $t/D$ ratio for a bumper of optimum thickness would be between 0.18 and 0.20 for an impact velocity of 6.7 km/s. Optimum bumper thickness is the minimum bumper thickness that results in maximum breakup of the projectile, and in minimum total weight of a Whipple-bumper system for the velocity of interest. Maiden *et al.* [11] indicate "that, as impact velocity increases, the optimum shield thickness decreases." As shown in Figures 9, 10b, 11b, and 13, greater axial and diametral expansion of the debris cloud occurred as impact velocity was increased. The greater dispersion of the debris clouds at the higher impact velocities will reduce the threat of penetration to the rear wall of a given Whipple-bumper shield system. It should be emphasized that the preceding statements apply to the normal impact of spherical projectiles. Debris clouds produced by the hypervelocity impact of nonspherical projectiles may not conform to the trends described for spherical projectiles.

# SECTION IV. FRACTURE AND FRAGMENTATION OF PROJECTILE

Characterization of the fragments and fragment-size distribution in a debris cloud produced by a hypervelocity impact is an area of significant interest. Coincident with this interest is work to incorporate dynamic fracture and fragmentation models in numerical simulations of impact events. As interest in fragmentation developed, a variety of static and dynamic techniques were employed to obtain experimental data used to further understanding of the impact process and to evaluate the models.

In some static techniques, "catcher" materials were placed in the path of the debris to decelerate and capture fragments in the debris clouds. Foams, foam boards, ceiling tiles, and particle boards are some of the materials used singly or in combination to "catch" debris particles. Fragment size and size-distribution data were obtained when the particles were separated from the "catcher" material and analyzed to determine their sizes and numbers, usually by sieving and weighing, respectively. In other instances, witness plates made of thin sheets or thick plates of a material (usually a metal), were placed in the path of the debris. Fragment number, size, and velocity data were inferred from the analyses of the holes left in the thin sheets or from the dimensions of craters produced in the thick plates. While these collection techniques have provided valuable data for fragmentation studies, they do not provide much information regarding the source of the fragments (i.e., projectile or target) unless different materials were used for the projectile and target.

The combination of one or more static techniques with a dynamic technique (e.g., high-speed photography, flash radiography, or, more recently, holography [20]) facilitates identification of some of the fragments. Use of a dynamic technique permits analysis of fragments during their movement from the impact site to the "catcher" or witness plate,

37

making identification of the source material a trivial matter. Front- and back-lit, high-speed photography are the most direct ways of viewing the impact of projectiles with target plates. Unless measures are taken to exclude the impact flash from the viewed area, however, severe overexposure of the film occurs during the most critical part of the event. Consequently, flash radiography is frequently used when impact flash, smoke, dust, motion blur, etc., will not permit the use of high-speed photography. While the use of flash radiography to observe small aluminum fragments presents certain technical difficulties, this dynamic technique was used successfully in the analysis of aluminum-fragment debris clouds. The remainder of this section will describe the results of analyses made to determine the size and size distribution of projectile fragments in the flash radiographs of the all-aluminum debris clouds presented in this report.

## A. Use of Flash Radiography

Flash radiographs are really shadowgraphs. When an x-ray source is pulsed, the radiation emitted by the source is absorbed by an object located between the source and a piece of film; consequently, a shadow of the object is cast on the film. In an ideal situation, the x-ray source is a point source, the object is near the film, and the film is fully responsive to the radiation. The combination of these conditions will produce a clean, sharp shadow of the object on the film.

An x-ray source is not a point source, however. Rather, it has finite dimensions and emits radiation from an area. The emitting area is a function of the source type and construction, and can be as small as 1 mm in diameter. Sources several millimeters in diameter are not uncommon. Since the source is finite, the shadow cast on the film is not sharp. A partially lit region or penumbra surrounds the shadow of the object as shown in Figure 14. The penumbra hampers accurate measurement of the dimensions of

38
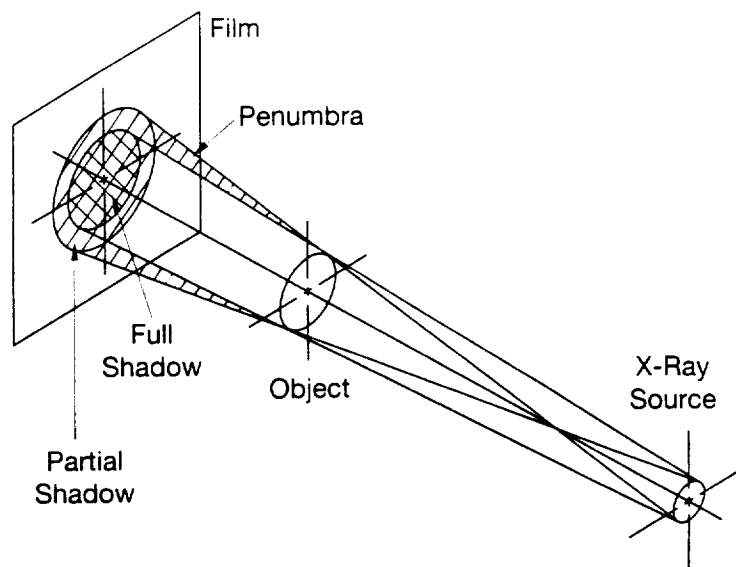
Figure 14. Penumbra and its relationship to x-ray source, object, and film.

objects in the path of the radiation, particularly small objects. Reasonably sharp flash radiographs can be made, however, if the ratio of the source-to-object and object-to-film distance is at least 5:1.

X-ray sources are usually designated as soft or hard sources. Soft sources have low-energy radiation present in their spectrum of emitted radiation; this low-energy radiation is not present in the spectrum of a hard source. Both soft and hard x-rays are simultaneously present in the x-ray beams produced by most sources. However, the material used in the construction of the window of an evacuated x-ray tube may or may not absorb the low-energy radiation as the beam leaves the tube. Materials with very low x-ray absorption characteristics (i.e., beryllium and some plastics) are commonly used as windows in the construction of soft x-ray tubes. Denser (and usually more rugged) materials are used in the construction of windows for hard x-ray tubes. The x-ray tubeheads used for the tests described in this report had a combination mylar/aluminum-foil window that permitted passage of the soft portion of the source's radiation spectrum.

Because of the extremely short exposure times, films used for flash radiography must be "fast." Fast films tend to be grainy and not suited to showing fine detail. When

hard x-rays are used, most radiation passes through the film, leaving little evidence of its passage. Image-intensifier screens are commonly placed on one or both sides of the film to enhance the response of the film to the x-rays. Increased graininess of the shadow, resulting from use of the image-intensifier screens, can be eliminated with use of direct-exposure film (i.e., film that responds directly to radiation and does not require screens); however, soft x-ray sources are usually required for proper exposure of this film. Finally, thin aluminum fragments are fairly transparent to hard x-rays but are somewhat opaque to soft x-rays. These characteristics of the direct-exposure film and the soft x-rays facilitated the production of flash radiographs that were suitable for use in fragmentation studies of debris clouds, particularly all-aluminum debris clouds.

A final comment regarding use of flash radiography (as well as high-speed photography) has to do with motion blur. The duration of a typical flash x-ray pulse is 25 to 35 nanoseconds. An object traveling at 6 km/s will move about 0.15 mm during this time interval. This motion of the object will produce a shadow that is blurred at the front and rear, with respect to the direction of travel of the fragment. Shadows of fragments traveling faster or slower than 6 km/s will exhibit more or less blur, respectively. Use of an x-ray source with a shorter pulse duration is the only way to reduce the effects of motion blur on the radiographic shadow.

## B. Radiographs of Fragments

An enlarged, late-time oblique view of the internal structure of a debris cloud is presented in Figure 15. The view shown in Figure 15 clearly exhibits the features of the internal structure and illustrates the constraints placed on the analysis of the radiographs. The front element of the structure consisted of very fine droplets of molten aluminum that appeared to be developing in streams. This portion of the internal structure was not
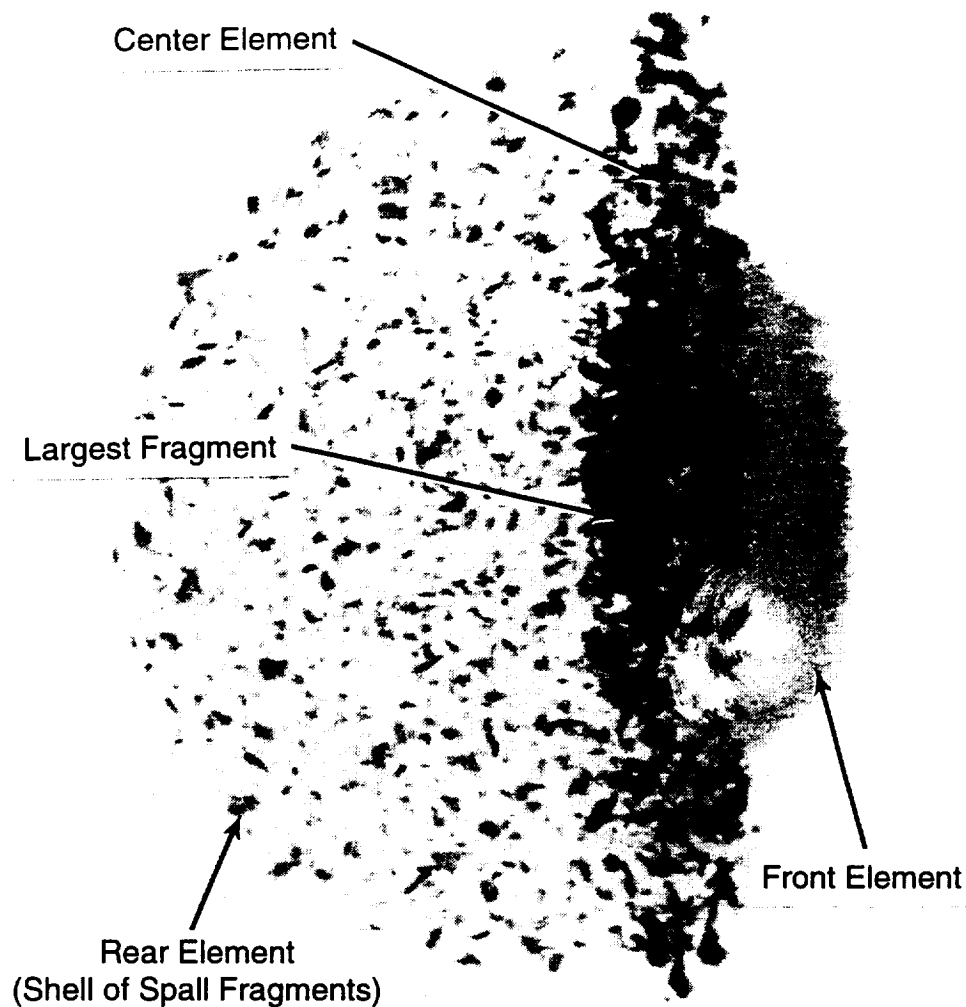
Figure 15. Late-time view of debris cloud (46 μs after impact). This view was used in the analysis of the spall-shell fragments and to determine the dimensions of the large central fragment. The white areas are film damage caused by the impact of ejecta from the witness plate used for this test. The projectile was a 12.70-mm-diameter, 2017-T4 aluminum sphere that impacted a 0.59-mm-thick, 6061-T6 aluminum sheet at 6.26 km/s (Shot 4-1358).

41

analyzed. The bulk of the post-impact projectile mass was concentrated in the center element. The center element consisted of a large central fragment of projectile that was surrounded by numerous solid slivers, comma-shaped, and/or chunky pieces of fragmented projectile. The dimensions of the large central fragment and limited fragment-size data were obtained for the fragments surrounding the central fragment. The expanding shell of spall fragments forming the rear element was the most noticeable portion of the debris-cloud internal structure in terms of area covered on film. Fragments in this shell tended to be flaky when the $t/D$ ratio and impact velocity were low, but were chunky when the impact velocity was increased. Most of the analyses, results, and discussion presented in the remainder of this section will focus on the fragments in the spall shell.

Radiographs of debris clouds showing the effect of $t/D$ ratio and impact velocity on the size, number, and distribution of fragments in the shell of spall fragments are shown in Figures 16 and 17. In these figures, the size of the spall-shell fragments and the large central fragment is shown to decrease with increasing $t/D$ ratio or impact velocity. Although not clearly visible in the photographic reproduction of the debris "cloud" from Shot 4-1428 (Figure 17, upper left), the radiograph from this test displayed the first sign of failure of the sphere — development of a spalled region at the rear of the projectile.

Radiographs from two tests employing 12.70-mm-diameter aluminum projectiles are shown in Figure 18. Different projectile materials were used for these tests. The debris cloud produced by the impact of the 1100-O aluminum sphere (Shot 4-1601) showed that the cloud contained many more fragments than were evident in the cloud from the test with a 2017-T4 aluminum sphere (Shot 4-1358). While the size of the front element was essentially the same for both debris clouds, the expansion and growth of the center and rear elements were significantly different. The concentrated mass of projectile fragments in the center element was expanding radially four percent faster for the 2017-T4

42

t/D = 0.026

$V_0$ = 6.70 km/s   43.4 μs   4-1395

**t/D = 0.084**   $V_0$ = 6.68 km/s    45.4 μs   4-1289

Increasing *t/D* ratio shown
clockwise from upper right

**t/D = 0.062**   $V_0$ = 6.78 km/s    44.8 μs   4-1359   **t/D = 0.049**  $V_0$ = 6.62 km/s  43.8 μs  4-1360
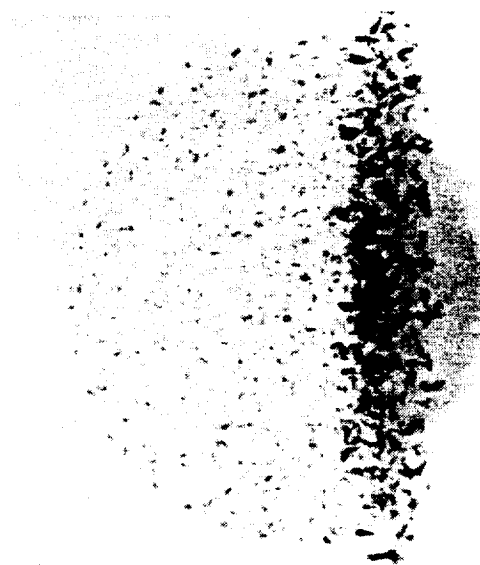
Figure 16.   Late-time views of debris clouds showing the effect of *t/D* ratio on the size, number, and distribution of fragments in the spall shell.  The projectiles were 9.53-mm-diameter, 2017-T4 aluminum spheres and the bumpers were 6061-T6 aluminum sheets.  All views are at the same magnification.  Time after impact is shown below the radiograph of each debris cloud.

t/D = 0.049

**3.77 km/s**

68.7 μs
4-1428

**4.71 km/s**

61.5 μs
4-1433

**5.45 km/s**

53.8 μs
4-1394
→

**6.62 km/s**

43.8 μs
4-1360
↓

t/D = 0.084

**3.84 km/s**

84.9 μs
4-1622

**4.62 km/s**

64.2 μs
4-1621
→

**6.68 km/s**

45.4 μs
4-1289
↓

89
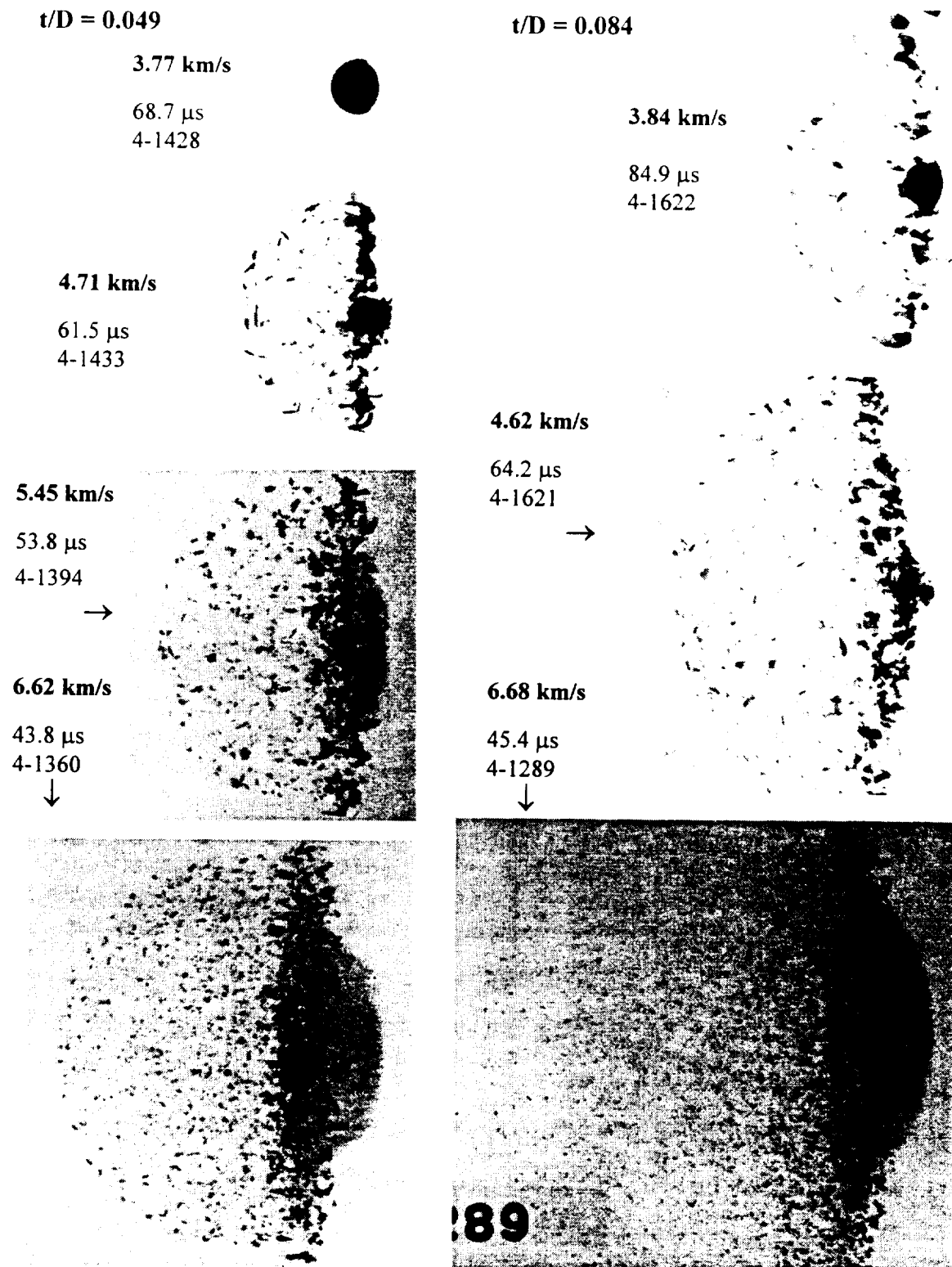
Figure 17. Late-time views of debris clouds showing the effect of impact velocity on the size, number, and distribution of fragments in the spall shell for two *t/D* ratios. The projectiles were 9.53-mm-diameter, 2017-T4 aluminum spheres and the bumpers were 6061-T6 aluminum sheets. All views are at the same magnification. Time after impact is shown near the radiograph of each debris cloud.

44

**1100-O Aluminum Sphere**

6.37 km/s    46.5 μs    4-1601
(Normal View)
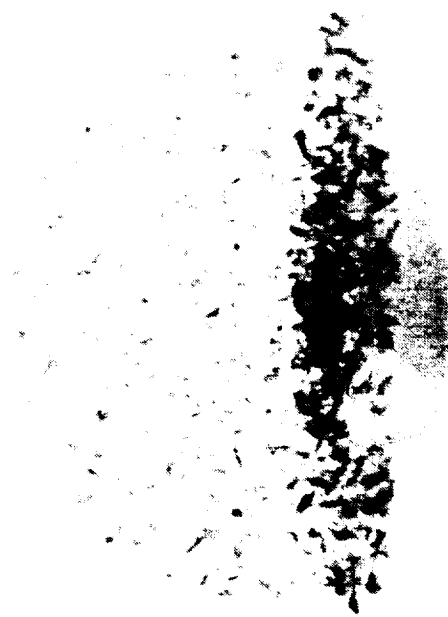
**2017-T4 Aluminum Sphere**

6.26 km/s    46.0 μs    4-1358
(Oblique View)

Figure 18. Late-time views of debris clouds showing the difference in the number and size of fragments in the spall shell for projectiles of different materials. Projectiles were 12.70-mm-diameter, 1100-O and 2017-T4 aluminum spheres. Bumpers were 0.59-mm-thick, 6061-T6 aluminum sheets. Views are at the same magnification; other parameters are as noted. Time after impact is shown below each radiograph.

aluminum cloud than for the 1100-O aluminum cloud. On the other hand, the normalized radial expansion velocity of the spall-shell fragments was 14 percent less for the 2017-T4 aluminum debris cloud than for the 1100-O aluminum debris cloud. These differences in the radial-expansion velocities of the spall shell and the center element were reflected in the damage patterns formed on the witness plates used for the tests. The impact of the spall-shell fragments for Shot 4-1601 produced craters in a circular region outside the ring of craters produced by the large fragments at the periphery of the center element. Center-element-fragment craters defined the edge of the pattern for Shot 4-1358.

45

# C. Analytical Procedures

Fairly complete analyses of the size and size distribution of fragments in the shell of spall fragments were made for the tests. Comparison of the results of these analyses permitted a determination of the trends in the data sets and reasonable speculation on their behavior in those regions where data were not available. Attempts to determine the size and number of fragments in the center element were severely restricted for most of the tests because the fragments were numerous and their shadows overlapped in the radiographs; however, limited center-element, fragment-size data were obtained. The large central fragment in the center element could usually be distinguished in all late-time views. The dimensions of the large fragment were obtained using this late-time-view radiograph.

Several comments regarding the analysis of the radiographs of the spall-shell fragments are in order before the analytical procedures are described. Since the shell is three-dimensional, some "overlapping" of fragment shadows is inevitable. During analysis, care was taken to distinguish those fragments that were clearly overlapped and to treat them accordingly. Measurements taken from the films were adjusted for film magnification. The film magnification factor is the ratio of the source-to-object distance and the source-to-film distance. The fragment was assumed to be in a plane that passed through the range center line normal to the center line of the x-ray beam. However, fragments in the debris cloud were clearly above and below this plane. Appropriate magnification corrections for fragments not in the plane through the range center line could not be determined. For tests where the debris cloud expanded significantly (i.e., touched the film), the error bounds on the adjusted fragment size could be as large as ± 13 percent (for fragments behind the center element and near the center line of the debris cloud). The error in the magnification adjustment would be less for fragments further

away from the central portion of the shell or for tests with less expansion of the shell. After magnification corrections were applied, fragments that were above the plane (nearer the source) would appear to be larger than their actual size. Correspondingly, fragments that were below the plane would appear to be smaller. This distortion of the fragment-size distribution could not be avoided unless some unique feature of each fragment allowed its position in the side and top views to be determined and the appropriate factors to be used during the magnification adjustment.

In principle, analysis of the spall fragments in the radiographs is straightforward — merely count and measure the appropriate dimensions of all fragments in the shell. This kind of analysis appears to be suited to an automated analysis procedure. Analysis of a radiograph from a test using a 12.70-mm-diameter sphere (Shot 4-1358, side view) was made using IMAGE ANALYSIS by OLYMPUS CUE-2. In addition to the problems with the general analysis of radiographs noted in the preceding paragraph, several problems unique to electronic-image analysis appeared. After the radiograph was scanned, the contrast of the image was adjusted before the variable-tone radiographic image was converted to a black-and-white image. Adjustment of the contrast level caused the apparent size of the fragments to change. Selection of a contrast level, prior to conversion of the variable-tone image, was arbitrary at best. Background noise and graininess of the film produced an extremely large number of single- and double-pixel phantom fragments that had to be eliminated before the actual analysis could be made. Finally, the electronic technique joined or combined fragments that clearly overlapped. Considerable effort was expended in the analysis of just one radiograph; therefore, an alternate method of analysis was developed.

The alternate method of analysis was manual and used enlarged prints (~ 2.5X) of the radiographs. A complete analysis of each print (i.e., examination of every fragment) would be tedious and was judged not necessary. It was assumed that spall-shell

fragments could be characterized using some statistical description of fragment sizes. Accordingly, the procedure illustrated in Figure 19 was developed and used to perform the analysis. The forward boundary of the shell area was determined by drawing a line as close as possible to the rear of the center element. The forward boundary of the sampled area was drawn parallel to the forward shell boundary and through the center of a circle that just enclosed the shell of spall fragments. The sampled area was divided into circular fields that enclosed approximately 20 percent of the sampled area. Further analysis was limited to those fragments in the circular fields. By the arbitrary convention shown in the upper left of Figure 19, fragments that intersected the lower-right boundary of the field (with respect to the diagonal dashed line) were not analyzed. Fragments that intersected the upper-left boundary of the field were analyzed. Characteristics of the distribution of fragment sizes in the fields were extended to all fragments in the shell area. The total number of fragments in the shell area, $N_T$, was estimated by multiplying the number of fragments counted in the fields, $N_F$, by the shell-area-to-total-field-area ratio.

In addition to counting all appropriate fragments in the fields, the Martin's statistical diameter of each fragment was measured using a 6X pocket optical comparator. Herdan [21] defines Martin's statistical diameter as follows: "Martin's 'statistical' diameter is defined as the mean length of a line intercept by the profile boundary which approximately bisects the area of the profile. The bisecting line is taken parallel to a fixed direction, irrespective of the orientation of each particle. This has the effect of avoiding bias as to the direction in which the profiles coming up for inspection are bisected." A second statistical diameter, Feret's diameter, is shown at the lower left of Figure 19. In discussing the relative accuracy of the various methods of determining the projected diameter of irregularly shaped particles, Herdan states: "Taking the determination of the profile area by planimeter and the corresponding mean projected
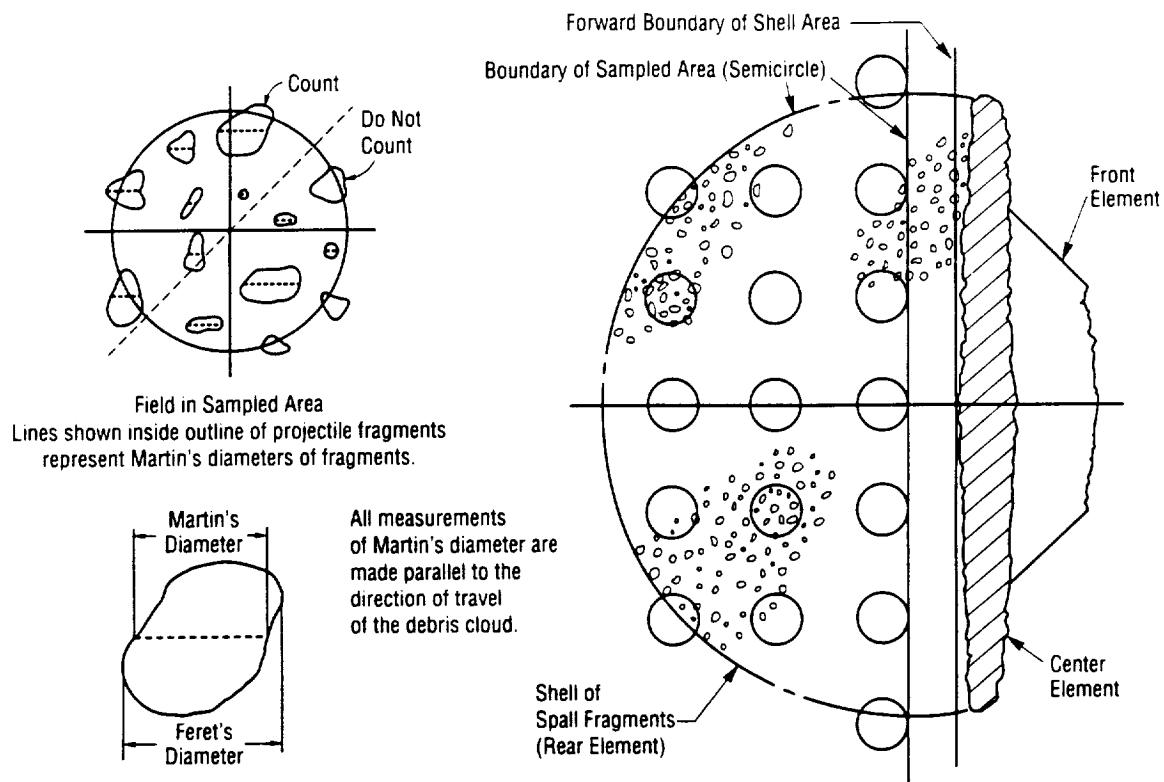
Figure 19. Illustration of the sampling procedure used to estimate the number and the size of particles in the shell of spall fragments. Refer to Figure 15 for a late-time view of a radiograph analyzed using this procedure.

diameter as a standard, the approximation by using transparent circle comparison had the smallest error, next came Martin's statistical diameter, and then the method using opaque circle comparison. Feret's statistical diameter is not recommended on account of its large errors." He further states that experimental investigations have confirmed that "Martin's diameter is, on the whole, less than the mean projected diameter, and Feret's is on the whole, greater."

Radiographs from tests with lower $t/D$ ratios (thinner bumpers) were more amenable to the analytical procedures just described because the external bubble of debris was much thinner and contributed relatively few fragments to those in the shell area. In addition, the spall fragments for the tests with lower $t/D$ ratios were usually larger and

easier to analyze. Numerous, small spall-shell fragments appear in the radiographs of the tests with larger $t/D$ ratios, but attempts to count and measure them were unsuccessful.

In order to evaluate the accuracy of the fragment measurements taken from the films, radiographs were made of 0.79-, 0.90-, 1.00-, 1.14-, and 1.25-mm-diameter 2017-T4 aluminum spheres positioned in the plane of the range center line. The diameters of the spheres in the radiographs were measured and adjusted using the same procedures followed with the debris-cloud radiographs. A comparison of the adjusted diameters of the aluminum sphere "standards" to their true diameters indicated the overall error of the measurement procedure was about $\pm$ 0.05 mm or the precision of the measurements themselves.

Problems with the penumbra and effects related to the transmissivity of the fragments also affected the usefulness of the analytical technique. Grain size of the direct exposure film limited the smallest fragments that could be resolved to about 0.2 mm in diameter under ideal viewing conditions. A more realistic resolution limit for fragments in the radiographs of the tests is about 0.4 mm.

The late-time-view radiographs of the debris clouds were projected on the screen of an optical comparator at a magnification of 10X in order to determine the dimensions of the large central fragment. Readings taken from graduated dials used to move cross hairs across the magnified image of the fragment provided the fragment's dimensions. Since these large fragments were irregularly shaped, the actual dimensions measured were those of a box that would just enclose the fragment.

Height and one value for the thickness of the large central fragment were obtained from the side x-ray view. Width and a second value for the thickness of this fragment were obtained from the top x-ray view. The measured values were then adjusted using the appropriate magnification factors. Every precaution was taken to insure the measurements were of the large fragment and not several overlapping fragments. To

further insure that the most reliable measurements were used to determine the volume of this fragment, the smaller thickness measurement was used in the computation.

When the impact velocity or $t/D$ ratio was low, the length-to-diameter ratio of the large fragment was near unity. When the impact velocity or $t/D$ ratio was increased, the length-to-diameter ratio of the large fragment decreased and tended toward values of 0.5 to 0.6. The large central-fragment height, $H$, width, $W$, thickness, $T$, and the relationship given in Figure 20 were used to compute the equivalent diameter, $d_f$, of a sphere having the same volume as an ellipsoid with these dimensions. Use of a single value to describe the irregular fragment shape facilitated comparison of central-fragment size as a function of impact velocity and $t/D$ ratio.
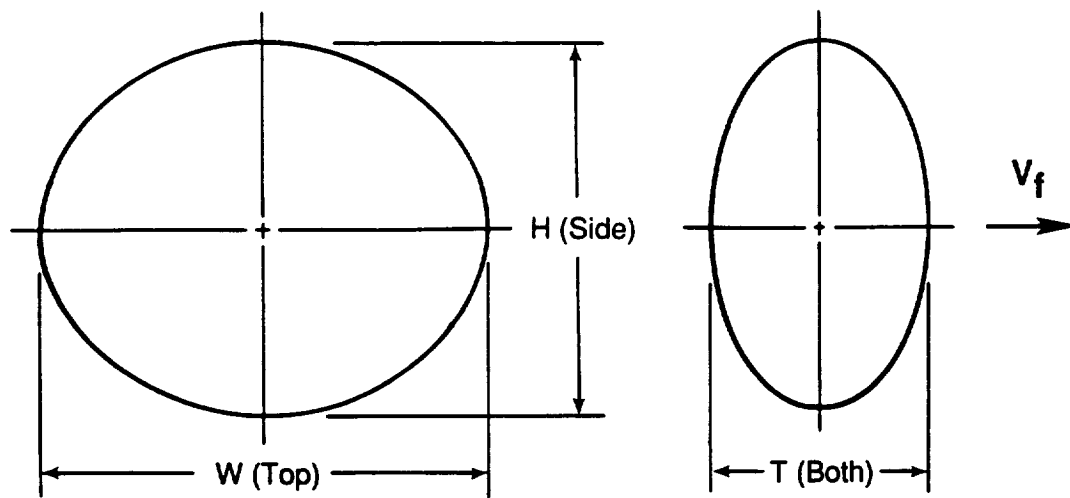


Volume of Ellipsoid $= \frac{\pi}{6}$ HWT   (Use Smaller Value of T)

Volume of Equivalent Sphere $= \frac{\pi}{6} d_f^3$

Equivalent Fragment Diameter, $d_f = (HWT)^{1/3}$

Figure 20. Dimensions of the ellipsoid and computational procedures used to determine the equivalent diameter of the large central fragment.

51

The many fragments surrounding the large fragment in the center element varied considerably in size and shape. Detailed analyses of the size and size distribution of these fragments were not possible because of the number of fragments and their tendency to form a "disk" of overlapping fragments. However, scattered center-element fragments were isolated in the late-time views for a number of the tests. Fragments near the "top" and "bottom" of the view (i.e., close to the plane through the range center line) were selected for measurement to minimize the film magnification problems described earlier. The length and width of ten fragments, five near the "top" and five near the "bottom" of the center element, were measured for a limited number of tests.

## D. Results and Discussion

Fairly complete analyses of the size and size distribution of fragments in the shell of spall fragments were made for 12 tests. Limited center-element fragment data were obtained for 11 of the tests. The large central fragment in the center element could be distinguished in most late-time view radiographs and the dimensions of this fragment were obtained for 34 tests using the late-time view-radiographs.

Results of the analysis of the spall fragments and other relevant spall-fragment data are presented in Table 5; the raw fragment-size data and other values obtained during the analysis of each test are presented in the appendix. The distribution of the fragment Martin's diameters, $d_m$, for each test was evaluated for log normality using the Shapiro-Wilk goodness-of-fit test at a 0.05 level of significance. The test for log normality of the distributions was prompted by these statements by Herdan [21]: "Materials showing a normal distribution of particle size are relatively rare, and are found chiefly among the particulate substances produced by chemical processes like condensation, precipitation." and "If the dispersion is attained by comminution (milling, grinding, crushing), the distribution appears to be governed very often by the log normal law." Because of the

## TABLE 5

## SPALL FRAGMENT DATA

All bumper sheets were 6061-T6 aluminum. All projectiles were 2017-T4 aluminum spheres except for Shot 4-1601. Shot 4-1601 used an 1100-O aluminum sphere.

| Shot Number | $\frac{t}{D}$ | Impact Velocity, (km/s) | Frequency Distribution of Fragments | | | Number of Fragments, $(N_F)$ [a] | Area Ratio [b] |
| --- | --- | --- | --- | --- | --- | --- | --- |
| | | | Mean $\ln d_m$ | Standard Deviation | Log Normality of Distribution | | |
| **$t/D$ Effects, $V_0$ = 4.70 km/s, $D$ = 9.53 mm** | | | | | | | |
| 4-1433 | 0.049 | 4.71 | -0.214 | 0.537 | Fail to Reject | 43 | 4.14 |
| 4-1621 | 0.084 | 4.62 | -0.436 | 0.409 | Reject | 82 | 5.05 |
| 4-1716 | 0.135 | 4.71 | -0.568 | 0.337 | Reject | 185 | 5.90 |
| **$t/D$ Effects, $V_0$ = 6.70 km/s, $D$ = 9.53 mm** | | | | | | | |
| 4-1395 | 0.026 | 6.70 | -0.206 | 0.463 | Fail to Reject | 84 | 2.86[c] |
| 4-1360 | 0.049 | 6.62 | -0.455 | 0.369 | Reject | 164 | 5.47 |
| 4-1359 | 0.062 | 6.78 | -0.511 | 0.331 | Reject | 238 | 6.00 |
| 4-1289 | 0.084 | 6.68 | -0.680[d] | 0.279 | Fail to Reject | 222 | 8.98[e] |
| 4-1283 | 0.102 | 6.72 | --- | --- | --- | 418[f] | 8.68[e] |
| **$V_0$ Effects, $t/D$ = 0.049, $D$ = 9.53 mm** | | | | | | | |
| 4-1433 | 0.049 | 4.71 | -0.214 | 0.537 | Fail to Reject | 43 | 4.14 |
| 4-1394 | 0.049 | 5.45 | -0.307 | 0.412 | Fail to Reject | 61 | 5.35 |
| 4-1360 | 0.049 | 6.62 | -0.455 | 0.369 | Reject | 164 | 5.47 |
| 4-1744 | 0.049 | 7.38 | -0.629 | 0.303 | Reject | 200 | 5.74 |
| **$V_0$ Effects, $t/D$ = 0.084, $D$ = 9.53 mm** | | | | | | | |
| 4-1622 | 0.084 | 3.84 | -0.160 | 0.525 | Fail to Reject | 53 | 2.58[c] |
| 4-1621 | 0.084 | 4.62 | -0.436 | 0.409 | Reject | 82 | 5.05 |
| 4-1289 | 0.084 | 6.68 | -0.680[d] | 0.279 | Fail to Reject | 222 | 8.98[e] |
| **Projectile Material Effects, $D$ = 12.70 mm** | | | | | | | |
| 4-1358 | 0.047 | 6.26 | -0.316 | 0.492 | Fail to Reject | 142 | 5.38 |
| 4-1601[g] | 0.047 | 6.37 | -0.567 | 0.468 | Reject | 232 | 5.93 |

[a] Number of fragments in fields used in the sampling procedures. (See Figure 19).
[b] Ratio of shell area to field area used in sampling procedure.
[c] Additional fields were used in the analysis of this test.
[d] Shadows of fragments were faint on film.
[e] Spall shell extended beyond the edges of film. Data are for fragments in the portion of the spall shell that was viewed.
[f] Fragments were not distinct enough for measurement or accurate count. Value shown is the best available count.
[g] Projectile was 1100-O aluminum.

limitations of the manual analytical procedures, the spall-fragment data were not evaluated to determine the suitability of other distributions frequently used to describe fragment sizes (e.g., Mott, exponential, Weibull, bimodal, etc.). The failure to reject a distribution of fragment sizes for log normality does not necessarily imply that the distribution is log normal. Rather, it merely indicates that the criteria for rejection of log normality do not apply to the test data. The median Martin's diameter, $\tilde{d}_m$, for each test was estimated assuming a log-normal distribution fit to the data (i.e., $\tilde{d}_m = \exp[\overline{\ln d_m}]$).

Several comments regarding the accuracy and/or appropriateness of the analytical procedures are in order. The comparison of the adjusted diameters of aluminum sphere "standards" to their true diameters indicated the error of the measurement procedure was about ± 0.05 mm, or the precision of the measurements themselves. It was assumed that all fragment measurements were made with about the same accuracy. The companion (side) view to the radiograph shown in Figure 15 (Shot 4-1358, top view) was evaluated using electronic image-analysis procedures. After "corrections" for overlapping fragments were made, the results of the electronic analysis indicated that the shell area contained 683 fragments with a mean Feret's diameter of 0.75 mm. The Feret's diameter for each fragment was the average of 18 Feret's diameters measured at ten-degree increments around the fragment. The manual procedure used to obtain the results presented in this section indicated there were 672 fragments with a median Martin's diameter of 0.73 mm. The "agreement" between the results of the two methods was considered remarkable.

The effect of motion blur on the median Martin's diameter was evaluated for Shot 4-1621 by comparing measurements made as shown in Figure 19 to measurements made perpendicular to the direction shown in Figure 19. The same fragments were measured in both cases. Median Martin's diameters of the fragments in the sampled area, measured parallel and perpendicular to the direction of travel of the debris cloud, were 0.646 mm and 0.619 mm, respectively. Because of a desire to maintain a sense of "length" of the

particle and its ability to penetrate a rear wall, all fragment measurements were made as shown in Figure 19. The reader is left to decide whether adjustments to the reported diameters, to compensate for motion blur, are in order.

The results of the measurements of the large central-fragment dimensions and velocities are presented in Table 6. In Table 6, the central-fragment velocity, $V_f$, was normalized by dividing it by the appropriate impact velocity. In three of the tests, the large fragment was partially blocked from view in one of the radiographs because of overlapping or superposition of other fragments in the center element. For these tests, the third dimension used in the computation of the volume of the ellipsoid was generated by averaging the two measured values. Where two thicknesses were measured, the smaller value was used in the computation since it was presumed the larger measurement was the "thickness" of overlapping fragments. Equivalent diameters of fragments for two cases (Shots 4-1352 and 4-1353) were obtained by randomly sampling and measuring the diameters of fragments clearly visible near the outer edges of the debris cloud. In both of these tests, witness plate damage indicated a single central fragment did not exist. (Selection of fragments in the outer regions of the clouds minimized errors due to use of an inappropriate magnification factor when adjusting the measured dimensions of the fragments.) The normalized central-fragment velocity was estimated for three of the tests (Shots 4-1352, 4-1353, and 4-1357) since direct measurement of the fragment velocity could not be made. Where the large central-fragment velocity was estimated, the center element of the internal structure had thinned considerably. In two of these cases (Shots 4-1352 and 4-1353), the velocity of point ② in Figure 8 was used as the velocity of the large fragment, since the large fragment was in that region for the lower $t/D$ ratio tests. The velocity of the front of the cloud, point ①, was used as the velocity of the large fragment for the $t/D$ = 0.424 test (Shot 4-1353).

55

## TABLE 6

## LARGE CENTRAL-FRAGMENT DATA

All bumpers were 6061-T6 aluminum sheet unless noted otherwise in table.

| Shot Number | $\frac{t}{D}$ | Impact Velocity, (km/s) | H, (in) | W, (in) | T (Side / Top), (in) | Equivalent Diameter, $d_f$ (mm) | $\frac{V_f}{V_0}$ |
|---|---|---|---|---|---|---|---|
| **Projectile - 6.35-mm-diameter, 2017-T4 aluminum sphere. Nominal mass = 0.373g** | | | | | | | |
| 4-1318 | 0.048[b] | 6.64 | 0.139 | 0.131 | 0.096 / 0.066 | 2.70 | 0.970 |
| 4-1449 | 0.050 | 7.23 | 0.101 | 0.101 | 0.056 / 0.056 | 2.11 | 0.971 |
| **Projectile - 9.53-mm-diameter, 2017-T4 aluminum sphere. Nominal mass = 1.275g** | | | | | | | |
| 4-1715 | 0.026 | 4.67 | 0.395 | 0.396 | 0.362 / 0.367 | 9.75[c] | 0.978 |
| 4-1392 | 0.026 | 6.54 | 0.208 | 0.287 | 0.191 / 0.180 | 5.60 | 0.988 |
| 4-1395 | 0.026 | 6.70 | 0.260 | 0.219 | 0.177 / 0.192 | 5.49 | 0.985 |
| 4-1290 | 0.032[b] | 6.67 | 0.196 | 0.206 | 0.163 / 0.173 | 4.75 | 0.973 |
| 4-1428 | 0.049 | 3.77 | 0.412 | 0.411 | 0.356 / 0.355 | 9.95[c] | 0.959 |
| 4-1433 | 0.049 | 4.71 | 0.267 | 0.278 | 0.245 / 0.212 | 6.36 | 0.970 |
| 4-1394 | 0.049 | 5.45 | 0.210 | 0.195 | 0.147 / 0.183 | 4.62 | 0.982 |
| 4-1360 | 0.049 | 6.62 | 0.128 | --- | 0.105 / --- | 2.95 | 0.977 |
| 4-1744 | 0.049 | 7.38 | 0.081 | 0.079 | 0.070 / 0.081 | 1.94 | 0.963 |
| 4-1284 | 0.053[d] | 6.58 | 0.158 | 0.182 | 0.088 / 0.090 | 3.45 | 0.968 |
| 4-1633 | 0.062 | 3.65 | Spall petals on rear of sphere | | | --- | 0.950 |
| 4-1359 | 0.062 | 6.78 | 0.139 | 0.144 | 0.080 / 0.090 | 2.97 | 0.968 |
| 4-1632 | 0.084 | 3.47 | 0.315 | 0.302 | 0.289 / 0.289 | 7.67 | 0.928 |
| 4-1631 | 0.084 | 3.64 | 0.299 | 0.297 | 0.292 / 0.290 | 7.52 | 0.934 |
| 4-1622 | 0.084 | 3.84 | 0.316 | 0.326 | 0.280 / 0.281 | 7.79 | 0.935 |
| 4-1621 | 0.084 | 4.62 | 0.210 | 0.224 | 0.144 / 0.176 | 4.80 | 0.950 |
| 4-1289 | 0.084 | 6.68 | 0.079 | 0.122 | 0.054 / 0.056 | 2.03 | 0.952 |
| 4-1283 | 0.102 | 6.72 | 0.076 | 0.062 | 0.046 / 0.040 | 1.45 | 0.949 |
| 4-1722 | 0.132 | 2.54 | 0.423 | 0.422 | 0.322 / 0.318 | 9.76[c] | 0.893 |
| 4-1716 | 0.135 | 4.71 | 0.123 | 0.158 | 0.106 / 0.133 | 3.23 | 0.930 |
| 4-1291 | 0.163 | 6.71 | --- | 0.050 | --- / 0.037 | 1.09 | 0.928 |
| 4-1717 | 0.168 | 4.96 | 0.127 | 0.128 | 0.124 / 0.112 | 3.10 | 0.921 |
| 4-1718 | 0.233 | 1.98 | 0.431 | 0.450 | 0.297 / 0.294 | 9.78[c] | ---[e] |
| 4-1720 | 0.233 | 2.44 | 0.339 | 0.335 | 0.265 / 0.277 | 7.90 | 0.811 |
| 4-1719 | 0.233 | 2.83 | 0.463 | 0.433 | 0.230 / 0.235 | 9.11[c] | ---[e] |
| 4-1352 | 0.234 | 6.64 | --- | --- | --- / --- | 0.64[f] | 0.893[g] |
| 4-1353 | 0.424 | 6.68 | --- | --- | --- / --- | 1.00[f] | 0.793[h] |
| 4-1721 | 0.504 | 2.23 | 0.444 | 0.492 | 0.259 / 0.283 | 9.02[c] | 0.623 |
| **Projectile - 12.70-mm-diameter, 2017-T4 aluminum sphere. Nominal mass = 3.000g** | | | | | | | |
| 4-1281 | 0.040[d] | 6.46 | 0.239 | 0.254 | 0.174 / 0.166 | 5.49 | 0.977 |
| 4-1358 | 0.047 | 6.26 | 0.234 | 0.232 | 0.244 / 0.186 | 5.49 | 0.976 |
| 4-1357 | 0.160[d] | 6.38 | 0.058 | --- | 0.031 / --- | 1.09 | 0.917[g] |
| **Projectile - 12.70-mm-diameter, 1100-O aluminum sphere. Nominal mass = 2.918g** | | | | | | | |
| 4-1601 | 0.047 | 6.37 | 0.148 | 0.139 | 0.082 / 0.087 | 3.02 | 0.981 |

[a] Adjustments to measured dimensions have been made for film magnification. Dimensions are presented in the units in which they were measured. H = height and W = width of the large central fragment, taken from the side- and top-view radiographs, respectively. The thickness, T, of the large central fragment was measured in both views.
[b] 1100-O aluminum bumper sheet.
[c] Projectile did not break up significantly after impact.
[d] 2024-T3 aluminum bumper sheet.
[e] Velocity measurement not possible since late-time-view was the only view available for this test.
[f] Average diameter of fragments that were selected at random in the radiographs.
[g] Used velocity of point ② in Figure 8.
[h] Used velocity of point ① in Figure 8.

56

The central-fragment equivalent diameter. $d_f$. was normalized by dividing it by the projectile diameter and plotted as a function of $t/D$ ratio for tests at 6.70 km/s in Figure 21. Normalized central-fragment velocity for these tests is presented as a function of $t/D$ ratio in Figure 22. Two features of the data shown in these figures are noteworthy. First, the scaled large-fragment diameter appears to approach a minimum value when the $t/D$ ratio is about 0.18 to 0.20, indicating that additional fragmentation of the spherical projectile did not occur when the $t/D$ ratio was greater than 0.18 to 0.20. Second, fracture and fragmentation of the projectile were processes that did not appear to be sensitive to the alloy of aluminum used in the bumper. Normalized central-fragment equivalent diameters scaled geometrically for projectiles ranging from 6.35 mm to 12.7 mm in diameter, and $t/D$ ratios ranging from 0.026 to 0.163. Data for comparisons at larger $t/D$ ratios were not available.

The total number, $N_T$, and median Martin's diameter, $\tilde{d}_m$, of the fragments in the spall shell are presented in Table 7. The large-fragment equivalent diameter and the median Martin's diameter of the spall fragments are shown in Figure 23 as a function of impact velocity. Data for two series of tests in which the $t/D$ ratio was kept constant are shown with lines in the figure. Fragment diameters for tests with other $t/D$ ratios at an impact velocity of 6.7 km/s are also presented.

As implied in Figure 23, a threshold impact velocity must be reached for each $t/D$ ratio before the sphere will fragment. A more detailed discussion of the sphere-failure process, and the threshold impact velocity required to initiate failure, is given in Section VI. Plastic deformation of the front surface of the sphere and the development of a spall failure beneath the rear surface of the sphere preceded fragmentation of the projectile. The decrease in the equivalent diameter, $d_f$, of the large fragment had a power-law dependence on the impact velocity. Changing the $t/D$ ratio did not alter the power-law dependence but did change the size of the large fragment. Equations of the lines shown in Figure 23
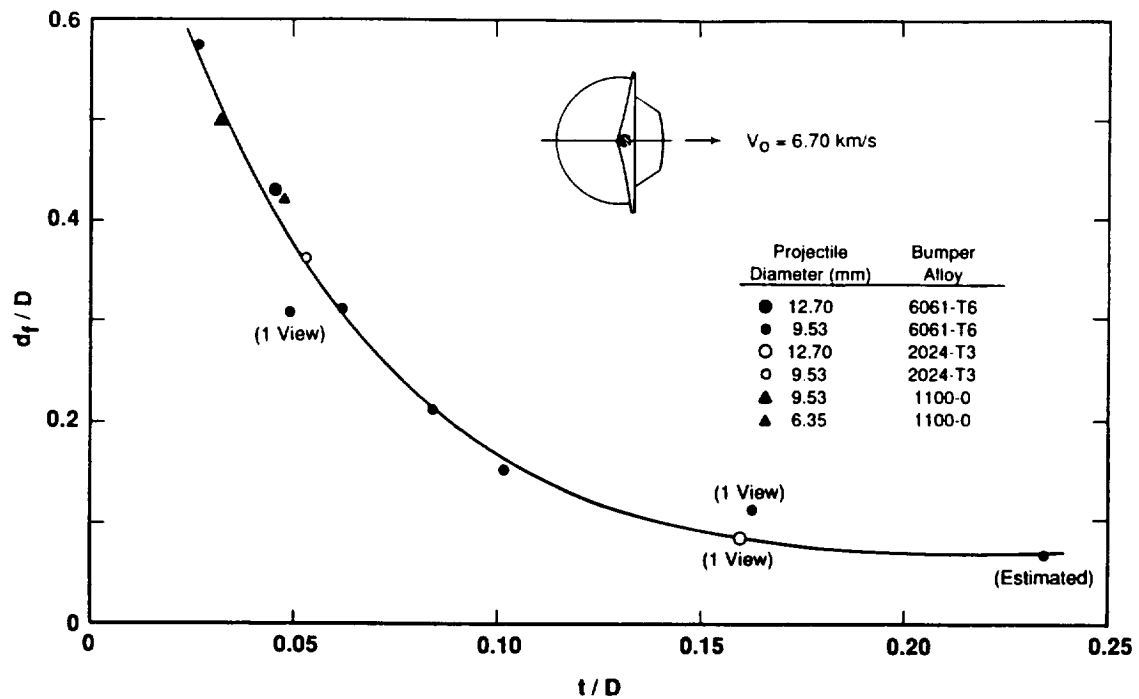
Figure 21.  Normalized equivalent diameter of large central fragment as a function of $t/D$ ratio for impacts at 6.7 km/s.
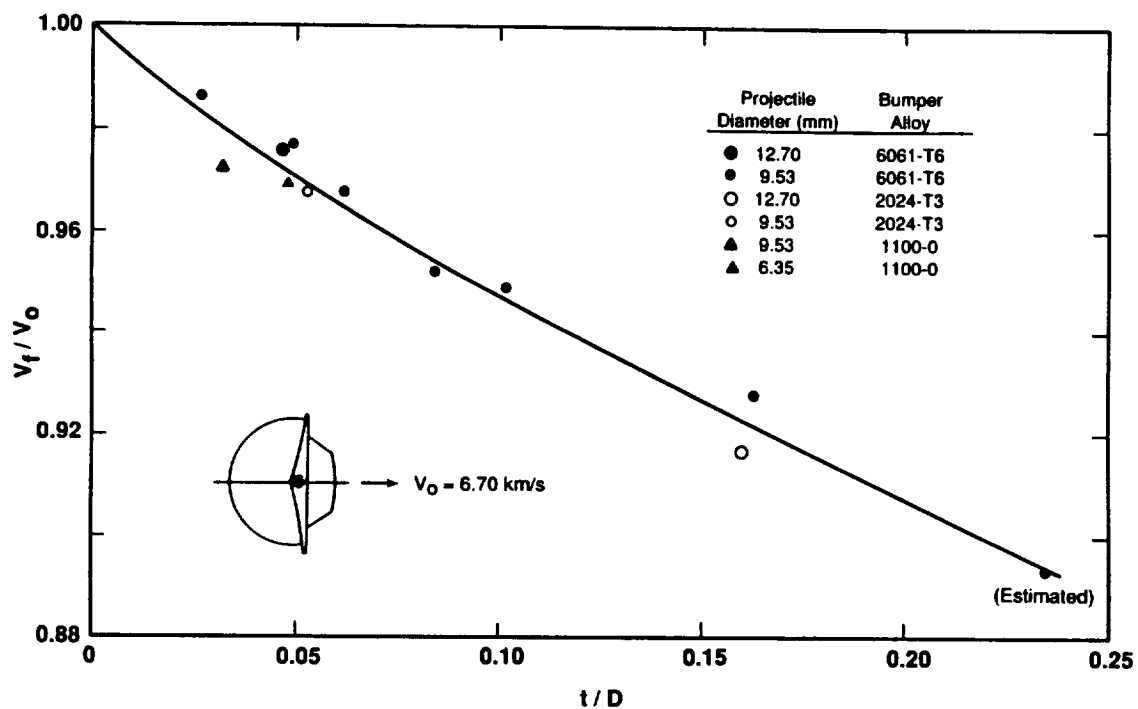


Figure 22.  Normalized velocity of large central fragment as a function of $t/D$ ratio for impacts at 6.7 km/s.

## TABLE 7

## FRAGMENT SIZE DATA

All bumper sheets were 6061-T6 aluminum. All projectiles were 2017-T4 aluminum except for Shot 4-1601. Shot 4-1601 used an 1100-O aluminum projectile.

| Shot Number | $\frac{t}{D}$ | Impact Velocity, (km/s) | Median Martin's Diameter, (mm) | Number of Fragments, $N_T$ | Diameter of Large Central Fragment, (mm) |
|---|---|---|---|---|---|
| **$t/D$ Effects, $V_0$ = 4.70 km/s, $D$ = 9.53 mm** | | | | | |
| 4-1715 | 0.026 | 4.67 | --- | --- | ~9.53[a] |
| 4-1433 | 0.049 | 4.71 | 0.807 | 178 | 6.36 |
| 4-1621 | 0.084 | 4.62 | 0.646 | 414 | 4.80 |
| 4-1716 | 0.135 | 4.71 | 0.567 | 1092 | 3.23 |
| **$t/D$ Effects, $V_0$ = 6.70 km/s, $D$ = 9.53 mm** | | | | | |
| 4-1395 | 0.026 | 6.70 | 0.814 | 240 | 5.49 |
| 4-1360 | 0.049 | 6.62 | 0.636 | 897 | 2.95[b] |
| 4-1359 | 0.062 | 6.78 | 0.600 | 1430 | 2.97 |
| 4-1289 | 0.084 | 6.68 | 0.506[c] | 1995 | 2.03 |
| 4-1283 | 0.102 | 6.72 | --- | ~3600[d] | 1.45 |
| **$V_0$ Effects, $t/D$ = 0.049, $D$ = 9.53 mm** | | | | | |
| 4-1428 | 0.049 | 3.77 | --- | 1 | ~9.53[a] |
| 4-1433 | 0.049 | 4.71 | 0.807 | 178 | 6.36 |
| 4-1394 | 0.049 | 5.45 | 0.736 | 326 | 4.62 |
| 4-1360 | 0.049 | 6.62 | 0.636 | 897 | 2.95[b] |
| 4-1744 | 0.049 | 7.38 | 0.533 | 1148 | 1.94 |
| **$V_0$ Effects, $t/D$ = 0.084, $D$ = 9.53 mm** | | | | | |
| 4-1632 | 0.084 | 3.47 | --- | 10-20[e] | 7.67 |
| 4-1631 | 0.084 | 3.64 | --- | 40-60[e] | 7.51 |
| 4-1622 | 0.084 | 3.84 | 0.852 | 136 | 7.79 |
| 4-1621 | 0.084 | 4.62 | 0.646 | 414 | 4.80 |
| 4-1289 | 0.084 | 6.68 | 0.506[c] | 1995 | 2.03 |
| **Projectile Material Effects, $D$ = 12.70 mm** | | | | | |
| 4-1358 | 0.047 | 6.26 | 0.729 | 764 | 5.49 |
| 4-1601[f] | 0.047 | 6.37 | 0.567 | 1376 | 3.02 |

[a] Projectile did not break up.
[b] Dimensions available from only one view.
[c] Shadows of fragments were faint on film.
[d] Fragments were not distinct enough for measurement or accurate count. Value shown is the best available count.
[e] Difficult to distinguish between the center and the rear elements of the debris cloud.
[f] Projectile was 1100-O aluminum.
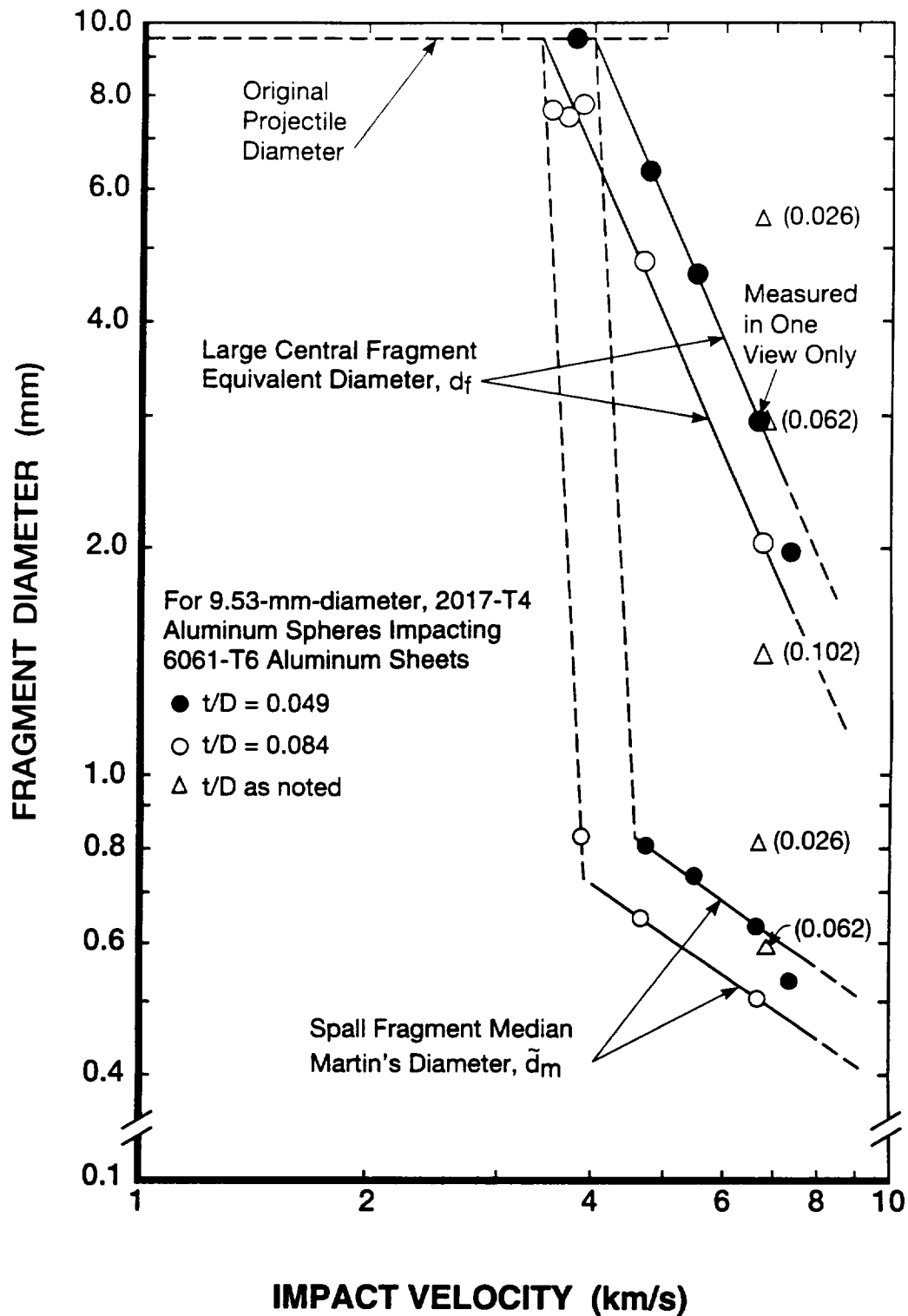
Figure 23. Large central-fragment diameter and median Martin's diameter of spall fragments as a function of impact velocity for two $t/D$ ratios.

60

for the equivalent diameter of the central fragment are:

$$d_f = 204.8 \ V_0^{-2.24} \text{ for } t/D = 0.049, \text{ and}$$

$$d_f = 147.1 \ V_0^{-2.24} \text{ for } t/D = 0.084.$$

In contrast to the large-central-fragment curves, which showed a well-behaved departure from the original projectile diameter, the median Martin's diameter of the spall fragments appeared to decrease suddenly and significantly after fragmentation began. The severe transition in the spall-fragment diameter occured over a rather narrow range of impact velocities. Sufficient data for accurate definition of the transition phase were not available, but the relationship shown by the pair of dashed lines in Figure 23 appeared reasonable.

The threshold velocity for the onset of fragmentation was defined, in Figure 23, by the intersection of the large-fragment line and the line labeled "Original Projectile Diameter." The transition phase occured within a narrow range of impact velocities for each $t/D$ ratio (see Section VI, Part A) and was complete when the fragmentation-threshold velocity was exceeded by 400 to 500 m/s. The decrease in spall-fragment, median Martin's diameter, after completion of the transition phase, also showed a power-law dependence on impact velocity. Changing the $t/D$ ratio did not alter the power-law dependence but did change the median Martin's diameter of the fragments. Equations of the lines shown in Figure 23 for the spall-fragment, median Martin's diameter are:

$$\tilde{d}_m = 2.30 \ V_0^{-0.68} \text{ for } t/D = 0.049, \text{ and}$$

$$\tilde{d}_m = 1.85 \ V_0^{-0.68} \text{ for } t/D = 0.084.$$

The median Martin's diameters of the spall fragments were compared with diameters computed using the following relationships suggested by Grady [22]:

$$d = (20^{1/2} \ K_{Ic}/\rho c \dot{\varepsilon})^{2/3} \text{ (from Grady [23], Eq. 12), and}$$

$$s = 2 \ (3^{1/2} \ K_c/\rho c_0 \dot{\varepsilon})^{2/3} \text{ (from Grady [24], Eq. 14).}$$

In these relationships. $d$ and $s$ are the nominal fragment diameters. $K_c$ and $K_{Ic}$ are the critical stress intensity factor or fracture toughness ($\sim 3 \times 10^7$ Nm$^{-3/2}$ for aluminum), $\rho$ is the density of the projectile (2.791 g/cm$^3$), and $c$ and $c_0$ are the bulk sound speed in the projectile (6420 m/s). The strain rate. $\dot{\varepsilon}$, was approximated by $V_r/R_0$, where $V_r$ was the radial expansion velocity of the spall fragments measured from the radiographs of the tests and $R_0$ was the radius of the sphere. Strain rates determined for the tests ranged from $0.9 \times 10^5$ s$^{-1}$ for a $t/D$ ratio of 0.026 to $2.6 \times 10^5$ s$^{-1}$ for a $t/D$ ratio of 0.084. The nominal fragment diameters computed using these relationships were approximately two times larger than the median Martin's diameters determined from the analysis of the radiographs.

A comparison, with an allowance for the difference in impact velocity, of the only data available for scaling of spall-fragment data, Shots 4-1360 and 4-1358, indicated that spall-fragment diameters did not scale geometrically. Formation of spall fragments was a shock-related process that was sensitive to rate effects and other material properties that did not scale. The large central fragment, on the other hand, appeared to originate from near the center of the sphere and was a part of the sphere that remained intact after all processes that worked to reduce the size of the sphere were complete; thus it did not appear to form as a direct result of shock-related processes.

The number of spall fragments, $N_T$, is shown as a function of impact velocity and spall-fragment, median Martin's diameter in Figures 24 and 25, respectively. The comments made regarding the data presented in Figure 23 apply to the data shown in these plots (i.e., the dependent variable exhibits a power-law dependence on the independent variable). Changes in the $t/D$ ratio merely changed the number of fragments when impact velocity and/or the median Martin's diameter were held constant.
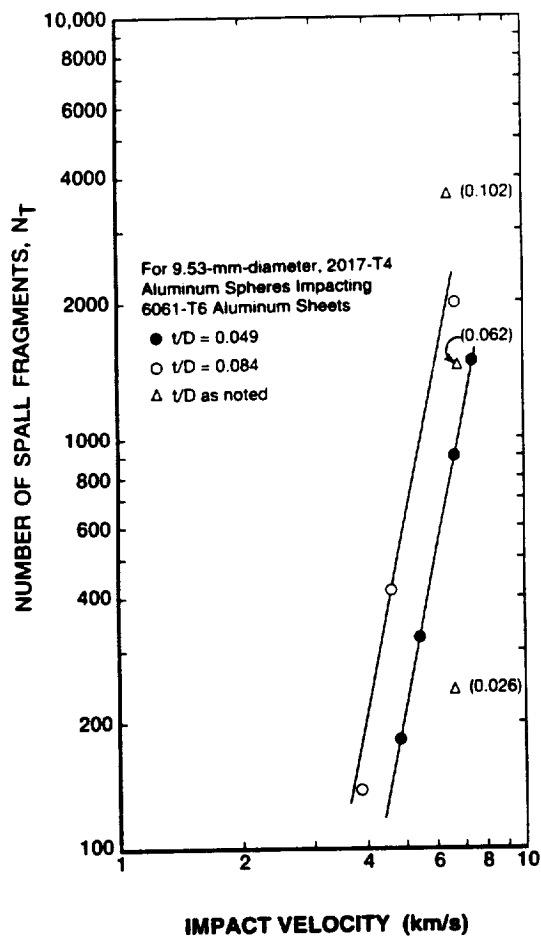
Figure 24. Number of spall fragments versus impact velocity for two t/D ratios.
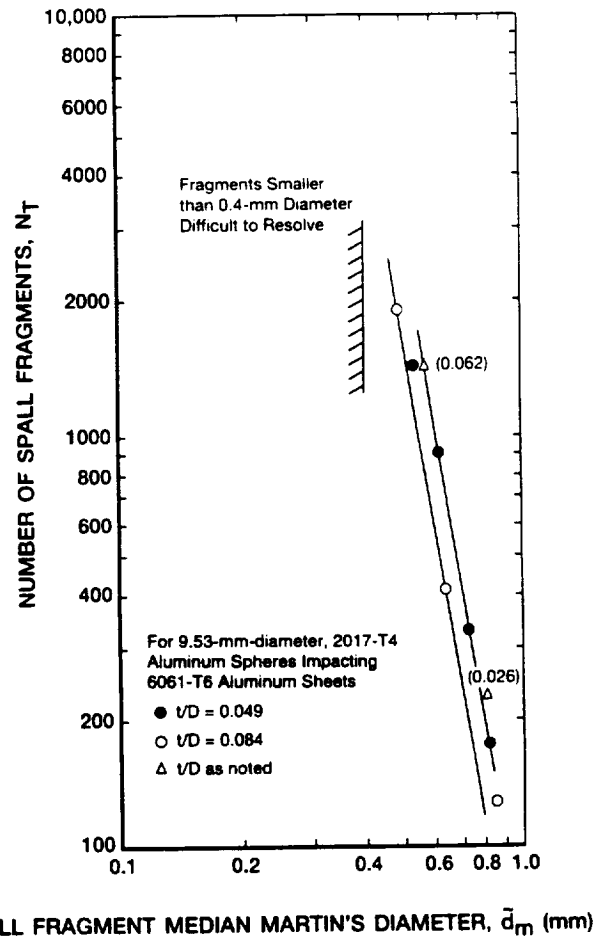


Figure 25. Number of spall fragments versus median Martin's diameter of spall fragments.

Equations for the lines shown in Figure 24 are:

$$N_T = 0.082 \ V_0^{4.9} \ \text{for } t/D = 0.049, \text{ and}$$

$$N_T = 0.225 \ V_0^{4.9} \ \text{for } t/D = 0.084.$$

Equations for the lines shown in Figure 25 are:

$$N_T = 44.6 \ (\tilde{d}_m)^{-6.6} \ \text{for } t/D = 0.049, \text{ and}$$

$$N_T = 23.2 \ (\tilde{d}_m)^{-6.6} \ \text{for } t/D = 0.084.$$

The fragments surrounding the large fragment in the center element varied considerably in size and shape. Because of the number and the tendency of the fragments to form a "disk" of overlapping fragments, detailed analyses of the size and size distribution of the fragments in this element were not possible. Scattered center-element fragments were isolated in the late-time views for a number of the tests, however. To minimize film magnification problems described earlier, fragments near the "top" and "bottom" of the view (i.e., close to the plane through the range center line) were selected for measurement. Ten fragments selected at random, five near the "top" and five near the "bottom" of the element, were measured. Their average length and width and a brief description of the general shape of the fragments are given in Table 8. The fragment dimensions shown in Table 8 are one and one-half to two times larger than the fragment dimensions estimated using the equations from Grady [23,24].

Material properties of the projectile significantly affected the fragmentation process, as evidenced in the radiographs presented in Figure 18. Notable differences in the internal structure of the debris cloud were observed when the projectile material was changed from 2017-T4 aluminum to 1100-O aluminum. The diameter of the large central fragment produced by the 1100-O aluminum test was only about half the diameter of the large central fragment produced by the 2017-T4 aluminum test. Differences in the radial velocities of the center and rear elements of the debris cloud were noted when the figure was presented. The spall-fragment, median Martin's diameters for the two tests were significantly different, with the 2017-T4 aluminum producing the larger fragments — 0.729 mm diameter versus 0.567 mm diameter. Not surprisingly, therefore, the number of spall-shell fragments was considerably smaller for the 2017-T4 aluminum test (764 versus 1376). Surmounting the difficulties with the resolution of smaller fragments in the 1100-O aluminum test would simultaneously increase the number of fragments reported for that test and reduce the median Martin's diameter of the spall fragments.

# TABLE 8

## CENTER-ELEMENT FRAGMENT SIZE DATA

All bumper sheets were 6061-T6 aluminum. All projectiles were 2017-T4 aluminum except for Shot 4-1601. Shot 4-1601 used an 1100-O aluminum projectile. Lengths and widths shown are the average of the lengths and widths, respectively, of 10 fragments randomly selected from the outer "edges" of the center element.

| Shot Number | $\dfrac{t}{D}$ | Impact Velocity, (km/s) | L, (mm) | W, (mm) | Fragment Shape |
|---|---|---|---|---|---|
| | | $t/D$ Effects, $V_0 = 4.70$ km/s, $D = 9.53$ mm | | | |
| 4-1433 | 0.049 | 4.71 | 3.74 | 1.17 | Banana-shape |
| 4-1621 | 0.084 | 4.62 | 2.26 | 1.08 | Very flaky |
| 4-1716 | 0.135 | 4.71 | 1.88 | 0.85 | Chunky, many sizes |
| | | $t/D$ Effects, $V_0 = 6.70$ km/s, $D = 9.53$ mm | | | |
| 4-1395 | 0.026 | 6.70 | 3.26 | 1.30 | Comma- to banana-shape |
| 4-1360 | 0.049 | 6.62 | 3.02 | 0.86 | Wedge |
| 4-1359 | 0.062 | 6.78 | 2.11 | 1.08 | Chunky to slivers |
| 4-1289 | 0.084 | 6.68 | 2.23 | 0.74 | Rods |
| | | $V_0$ Effects, $t/D = 0.049$, $D = 9.53$ mm | | | |
| 4-1433 | 0.049 | 4.71 | 3.74 | 1.17 | Banana-shape |
| 4-1394 | 0.049 | 5.45 | 2.94 | 1.02 | Comma-shaped flakes |
| 4-1360 | 0.049 | 6.62 | 3.02 | 0.86 | Wedge |
| 4-1744 | 0.049 | 7.38 | 2.02 | 0.74 | Potato-shape |
| | | $V_0$ Effects, $t/D = 0.084$, $D = 9.53$ mm | | | |
| 4-1621 | 0.084 | 4.62 | 2.26 | 1.08 | Very flaky |
| 4-1289 | 0.084 | 6.68 | 2.23 | 0.74 | Rods |
| | | Projectile Material Effects, $D = 12.70$ mm | | | |
| 4-1358 | 0.047 | 6.26 | 4.02 | 1.44 | Chunky to comma-shape |
| 4-1601[a] | 0.047 | 6.37 | 3.44 | 1.85 | Chunky |

[a] Projectile was 1100-O aluminum.

65

This page intentionally left blank

# SECTION V. PERFORATION OF BUMPER

Holes produced in thin sheets by the hypervelocity impact of spherical projectiles have been the subject of study for more than 40 years. Extensive sets of measurements were taken of holes produced by many of the impact experiments performed during the 1960's and 1970's (e.g., Maiden and McMillan [25] and Carson and Swift [26]). More recently, Hörz et al. [27, 28] have performed detailed studies of the holes produced in 1100 aluminum and Teflon sheets.

Study of the holes produced in thin sheets and their description as functions of sheet thickness, projectile diameter, and impact velocity is of interest for several reasons. A hole left in a shield or any other component of a spacecraft represents damage that may or may not affect the performance of the spacecraft. Examination and careful study of the holes left in spacecraft components returned to earth (e.g., the Long Duration Exposure Facility) provided data which were used to estimate the size and velocity of the particles that produced the holes and to refine the definition of the orbital-debris environment. Currently available orbital-debris-environment models, spacecraft component design information, and reliable hole-dimension data are used to evaluate the probability of a disabling collision with a debris fragment. Hypervelocity-impact-test hole data can also be used in the validation of models developed for computer simulation of impact events by comparing "holes" produced by the simulations with experimental data.

The bumper sheets used for the tests described in this report were cleanly perforated by the projectiles. Holes produced by the normal impact of 9.53-mm-diameter, aluminum spheres traveling at 6.70 km/s are shown in Figure 26 for seven $t/D$ ratios. An arrow in each hole identifies the location of a portion of the bumper sheet that was removed and used to provide the micrographic cross sections shown to the left of the hole photographs. The holes are shown from the front or impacted side of the sheet and the
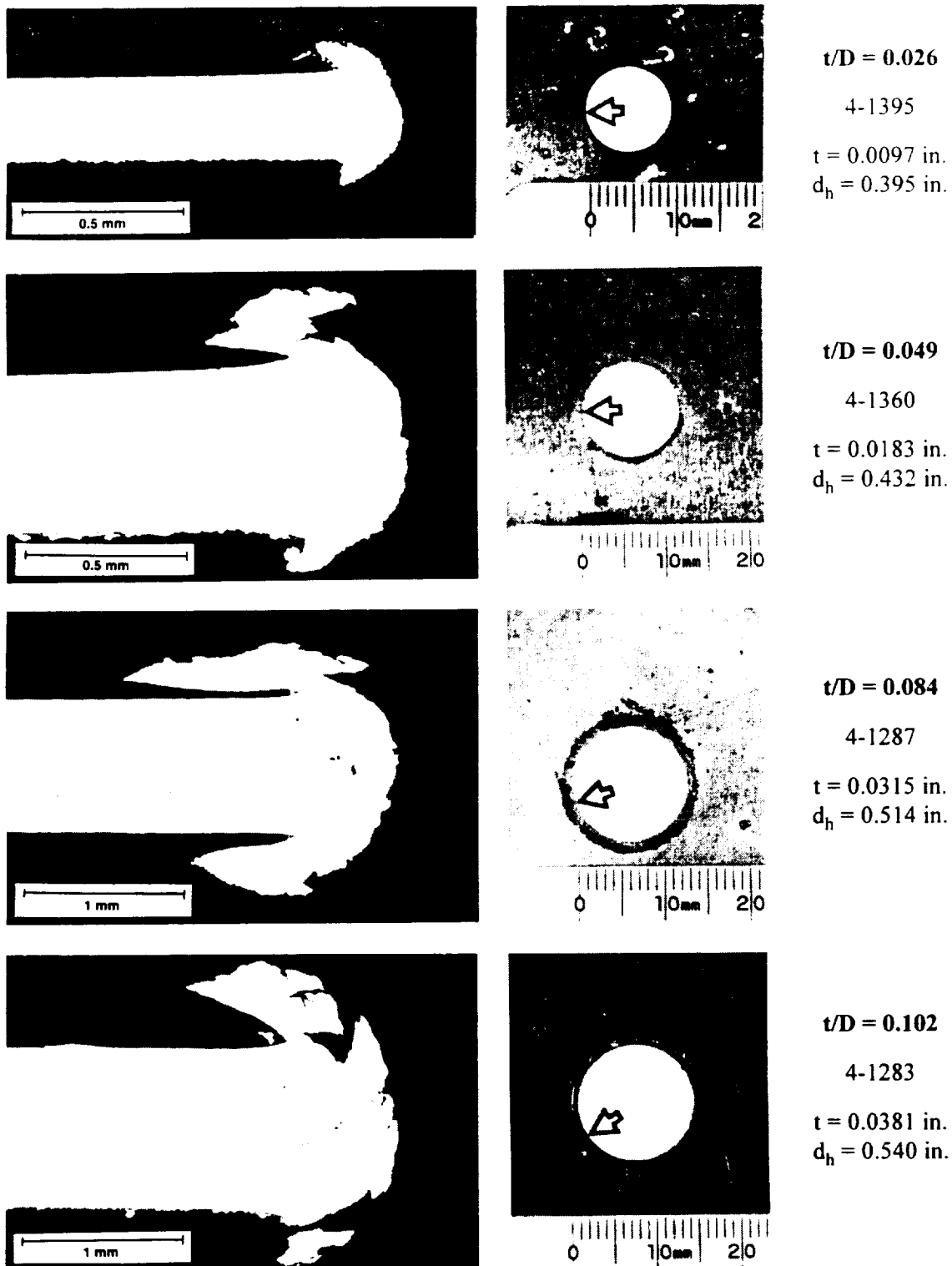
Figure 26. Photographs and cross sections of holes formed by impact of 9.53-mm-diameter, 2017-T4 aluminum spheres with various thicknesses of 6061-T6 aluminum sheets at 6.70 km/s. Holes are shown from the impacted side of the bumper. Cross sections are shown with the impacted side toward the top of the page.

t/D = 0.163

4-1291

t = 0.0610 in.
$d_h$ = 0.652 in.

t/D = 0.234

4-1352

t = 0.0876 in.
$d_h$ = 0.767 in.

t/D = 0.424

4-1353

t = 0.1590 in.
$d_h$ = 1.08 in.
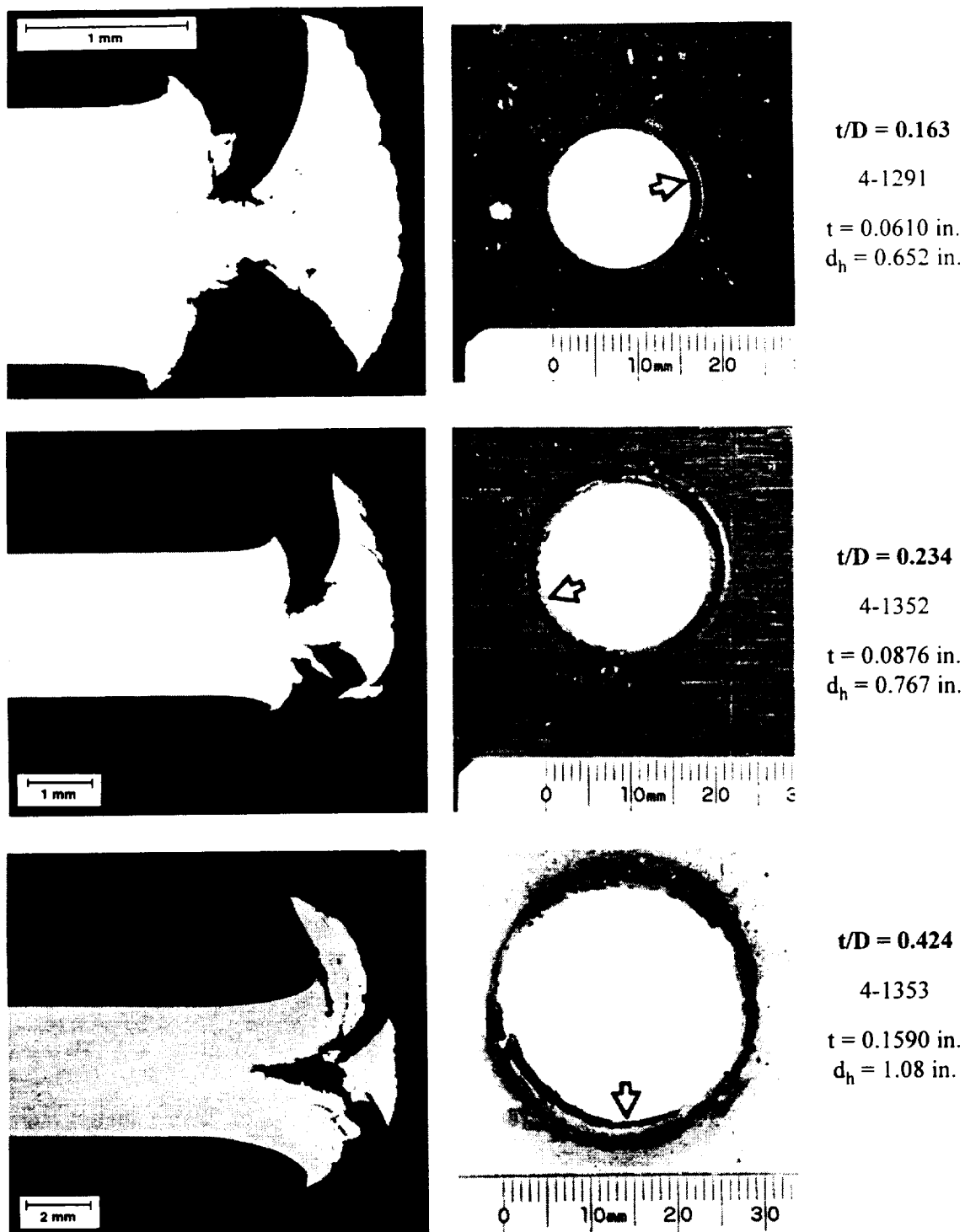
Figure 26. (Concluded). Photographs and cross sections of holes formed by impact of 9.53-mm-diameter, 2017-T4 aluminum spheres with various thicknesses of 6061-T6 aluminum sheets at 6.70 km/s. Holes are shown from the impacted side of the bumper. Cross sections are shown with the impacted side toward the top of the page.

69

cross sections are shown with their impacted side toward the top of the figure. The series of photographs and cross sections shown in Figure 26 clearly illustrate a relationship between $t/D$ ratio and hole size and morphology. As the $t/D$ ratio increased, the holes tended to be less circular, the hole diameter, $d_h$, increased, and the structure of the region surrounding the hole became more complex. A description of the holes, results of the measurement of their dimensions, and a discussion of the results of these measurements are presented in this section. These data and discussions are provided to complement the description of the formation of debris clouds. A description of the propagation of the impact shock into the bumper sheet is given in Section VI, Part D.

The bumper-sheet holes were surrounded by flaps or lips which developed on both sides of the bumper. The micrographs showed that the flap on the impacted side was larger than the flap on the rear side of the bumper for all seven of the holes shown in Figure 26. Grain structure visible in the micrographs indicated that the flaps were formed from portions of bumper which overturned during the hole-formation process. As bumper-sheet thickness increased, from $t/D = 0.026$ to $0.084$, the width of the overturned flaps increased. At a $t/D$ ratio of $0.102$, large cracks were evident in the flaps. As the cracks grew and joined together, pieces of the flap separated from the sheet and reduced the width of the flaps. The cross sections for the tests with $t/D$ ratios of $0.163$ or greater merely exhibited a small lip on the front and rear surfaces of the bumper sheet. These small lips appeared to be all that remained of the overturned flaps. As the material in the flap overturned, it was stressed excessively, cracked, and was separated from the bumper sheet. The newly-formed fragments became a part of the ejecta veil or the external bubble of debris.

The cross sections for Shots 4-1291 and 4-1352 also show a large ring of material which was attached to the bumper by a thin web of material at the center of the sheet. The surfaces of the ring that were toward the bumper were concave and appeared to be smooth or polished, in contrast to the more irregular surfaces evident on material closer to

70

the bumper sheet. The smooth appearance of the ring in these regions indicated that the ring had been in contact with material in the overturned flap. It is likely that material in the ring was originally closer to the impact site but moved outward during hole growth. As this material moved outward, it developed a sliding contact with the material in the overturned flap and probably contributed to the late-time formation of the flap. The cross section for the $t/D = 0.424$ test (Shot 4-1353) clearly showed a detached wedge, a split in the sheet, and a section of overturned flap that was smooth on the surface which had been in contact with the wedge. The split in the sheet extended all around the inside of the hole. The mating surface irregularities in the split section of the sheet and the position of the wedge strongly suggested that the outward motion of the wedge was responsible for the separation of the sheet. It is probable that the wedge-shaped ring was a continuous structure during the hole formation process. As shown in Figure 26, however, only a portion of the ring remained in the hole after the impact. The remaining pieces of the ring were recovered from the target-chamber floor after the test.

The hole shown in Figure 27 exhibits features that were observed for a number of tests in which 12.70-mm-diameter, 2017-T4 aluminum spheres were fired at 1.976-mm-thick, 6061-T6 aluminum sheets with an impact velocity of about 6.4 km/s. For most of the 6.4-km/s tests, the major opening in the sheet was defined by a fragile ring of aluminum surrounded by a series of small holes, as shown in Figure 27. The interior rings were weakly attached to the surrounding bumper sheet and, in some instances, pieces of the ring simply fell from the hole after hole growth ceased. The transition from an attached ring to a detached ring undoubtedly occured as a result of the loss of material from the thin web which joined the ring structure to the center of the sheet. Features of the bumper-sheet cross section presented in this figure appear to be identical to those presented in Figure 26 for tests with $t/D$ ratios of 0.163 and 0.234. Several small holes were occasionally observed around the holes in bumper sheets from other tests which used
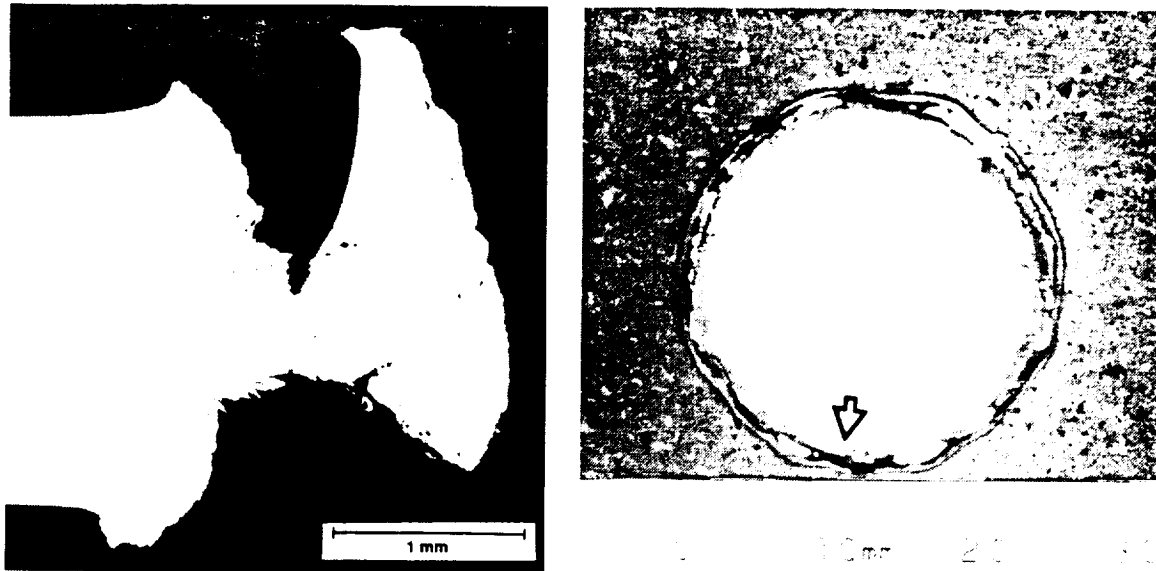
**4-0609**

t = 0.0778 inch                  t/D = 0.156                  $V_0$ = 6.42 km/s

$d_h$ = 0.848 inch (Inside), 0.954 inch (Outside)

Figure 27. Photograph and cross section of a hole displaying a ring structure surrounded
by small holes and openings. Hole was formed by the impact of a 12.70-mm-
diameter, 2017-T4 aluminum sphere with a 6061-T6 aluminum sheet.

9.53-mm-diameter, 2017-T4 aluminum spheres and 6061-T6 aluminum bumper sheets.
The average impact velocity and t/D ratio for these tests was about 6.4 km/s and 0.21,
respectively. While it is possible that the formation of this series of small holes around
the main opening will only occur when specific conditions of impact velocity and
bumper-sheet thickness, strength, and ductility are met, it is probable that the hole
features shown in Figure 27 could be produced by other combinations of sphere diameter,
t/D ratio, and impact velocity (e.g., the 6.7 km/s impact of a 9.53-mm-diameter sphere
with a sheet having a t/D ratio greater than 0.234 but less than 0.424).

The diameters of the holes left in the bumper sheets were carefully measured
using an optical comparator. Results of the hole-diameter measurements are presented in
Table 9. As shown in Table 9, measurements were taken parallel and perpendicular to the
rolling direction of the sheet stock. The average of the two measurements was taken to

# TABLE 9

## BUMPER HOLE DATA

Diameter of hole was measured perpendicular and parallel to the rolling direction of the bumper-sheet stock. Diameters are presented in the units in which they were measured. Typical measurement error was ±0.0005 inch.

| Shot Number | $t \over \overline{D}$ | Impact Velocity, (km/s) | Hole Diameter, ($\perp$, in) | Hole Diameter, ($\parallel$, in) | Average Hole Diameter, $d_h$ (in) | $d_h \over \overline{D}$ |
|---|---|---|---|---|---|---|
| **1100-O Aluminum Bumper, $D$ = 6.35 mm** | | | | | | |
| 4-1318 | 0.048 | 6.64 | 0.302 | 0.302 | 0.302 | 1.208 |
| **1100-O Aluminum Bumper, $D$ = 9.53 mm** | | | | | | |
| 4-1286 | 0.031 | 6.42 | 0.421 | 0.421 | 0.421 | 1.122 |
| 4-1288 | 0.031 | 6.71 | 0.421 | 0.422 | 0.422 | 1.125 |
| 4-1285 | 0.032 | 6.67 | 0.421 | 0.421 | 0.421 | 1.123 |
| 4-1290 | 0.032 | 6.67 | 0.424 | 0.423 | 0.424 | 1.131 |
| 4-1292 | 0.032 | 6.69 | 0.424 | ---[a] | 0.424 | 1.131 |
| **2024-T3 Aluminum Bumper, $D$ = 9.53 mm** | | | | | | |
| 4-1282 | 0.053 | 6.58 | 0.431 | 0.428 | 0.430 | 1.147 |
| 4-1284 | 0.053 | 6.58 | 0.433 | 0.430 | 0.432 | 1.152 |
| **2024-T3 Aluminum Bumper, $D$ = 12.70 mm** | | | | | | |
| 4-1281 | 0.040 | 6.46 | ---[a] | 0.549 | 0.549 | 1.098 |
| 4-1357 | 0.160 | 6.38 | 0.842 | 0.817 | 0.832 | 1.664 |
| **6061-T6 Aluminum Bumper, $D$ = 6.35 mm** | | | | | | |
| 4-1449 | 0.050 | 7.23 | 0.294 | 0.298 | 0.296 | 1.184 |
| **6061-T6 Aluminum Bumper, $D$ = 9.53 mm** | | | | | | |
| 4-1715 | 0.026 | 4.67 | 0.397 | 0.393 | 0.395 | 1.053 |
| 4-1392 | 0.026 | 6.54 | 0.396 | 0.394 | 0.395 | 1.053 |
| 4-1395 | 0.026 | 6.70 | 0.392 | 0.398 | 0.395 | 1.053 |
| 4-1428 | 0.049 | 3.77 | 0.413 | 0.413 | 0.413 | 1.101 |
| 4-1433 | 0.049 | 4.71 | 0.426 | 0.425 | 0.426 | 1.136 |
| 4-1394 | 0.049 | 5.45 | 0.426 | 0.428 | 0.427 | 1.139 |
| 4-1360 | 0.049 | 6.62 | 0.431 | 0.433 | 0.432 | 1.152 |
| 4-1744 | 0.049 | 7.38 | --- | --- | ---[b] | --- |
| 4-1633 | 0.062 | 3.65 | 0.434 | 0.432 | 0.433 | 1.155 |
| 4-1359 | 0.062 | 6.78 | 0.456 | 0.460 | 0.458 | 1.221 |
| 4-1632 | 0.084 | 3.47 | 0.461 | 0.462 | 0.462 | 1.232 |
| 4-1631 | 0.084 | 3.64 | 0.466 | 0.463 | 0.464 | 1.237 |
| 4-1622 | 0.084 | 3.84 | 0.467 | 0.473 | 0.470 | 1.253 |

[a] Bumper struck by a piece of piston. Hole was stretched in this direction.
[b] Bumper struck by a piece of piston. More than half of bumper torn away. Hole diameter could not be determined.

## TABLE 9 (Concluded)

### BUMPER HOLE DATA

Diameter of hole was measured perpendicular and parallel to the rolling direction of the bumper-sheet stock.  Diameters are presented in the units in which they were measured.  Typical measurement error was ±0.0005 inch.

| Shot Number | $\dfrac{t}{D}$ | Impact Velocity, (km/s) | Hole Diameter, ($\perp$, in) | Hole Diameter, ($\parallel$, in) | Average Hole Diameter, $d_h$ (in) | $\dfrac{d_h}{D}$ |
|---|---|---|---|---|---|---|
| **6061-T6 Aluminum Bumper, $D$ = 9.53 mm (Concluded)** | | | | | | |
| 4-1621 | 0.084 | 4.62 | 0.482 | 0.484 | 0.483 | 1.288 |
| 4-1289 | 0.084 | 6.68 | 0.509 | 0.515 | 0.512 | 1.365 |
| 4-1287 | 0.084 | 6.74 | 0.511 | 0.517 | 0.514 | 1.371 |
| 4-1283 | 0.102 | 6.72 | 0.540 | 0.540 | 0.540 | 1.440 |
| 4-1722 | 0.132 | 2.54 | 0.472 | 0.475 | 0.474 | 1.264 |
| 4-1716 | 0.135 | 4.71 | 0.559 | 0.561 | 0.560 | 1.493 |
| 4-1291 | 0.163 | 6.71 | 0.650 | 0.653 | 0.652 | 1.739 |
| 4-1717 | 0.168 | 4.96 | 0.618 | 0.606 | 0.612 | 1.632 |
| 4-1718 | 0.233 | 1.98 | 0.507 | 0.504 | 0.506 | 1.349 |
| 4-1720 | 0.233 | 2.44 | 0.549 | 0.550 | 0.550 | 1.467 |
| 4-1719 | 0.233 | 2.83 | 0.577 | 0.583 | 0.580 | 1.547 |
| 4-1351 | 0.233 | 6.66 | 0.776 | 0.776 | 0.776 | 2.069 |
| 4-1352 | 0.234 | 6.64 | 0.765 | 0.769 | 0.767 | 2.045 |
| 4-1353 | 0.424 | 6.68 | --- | --- | 1.08[c] | 2.88 |
| 4-1721 | 0.504 | 2.23 | 0.636 | 0.637 | 0.636 | 1.696 |
| **6061-T6 Aluminum Bumper, $D$ = 12.70 mm** | | | | | | |
| 4-1358 | 0.047 | 6.26 | 0.567 | 0.571 | 0.569 | 1.138 |
| 4-1601[d] | 0.047 | 6.37 | 0.569 | 0.563 | 0.566 | 1.132 |

[c] Nearly all of the interior "ring" was missing from the hole.  Diameter corresponds to the diameter of the hole without the interior "ring."

[d] Projectile was 1100-O aluminum.

be the hole diameter, $d_h$.  Use of the normalized hole diameter, $d_h/D$, permitted the comparison, on the basis of $t/D$ ratio and impact velocity, of hole diameters produced by the impact of spheres of various diameters.  Selected bumper-hole data from other tests performed at UDRI for Martin Marietta Manned Space Systems are presented in Table 10.  The tests chosen for presentation in this table were selected on the basis of sphere diameter and/or $t/D$ ratio in order to supplement the data presented in Table 9.

TABLE 10

## BUMPER HOLE DATA (OTHER UDRI TESTS)

Diameter of hole was measured perpendicular and parallel to the rolling direction of the bumper-sheet stock. Diameters are presented in the units in which they were measured. Typical measurement error was ±0.0005 inch.

| Shot Number | $t$ over $\overline{D}$ | Impact Velocity, (km/s) | Hole Diameter, ($\perp$, in) | Hole Diameter, ($\parallel$, in) | Average Hole Diameter, $d_h$ (in) | $d_h$ over $\overline{D}$ |
|---|---|---|---|---|---|---|
| 6061-T6 Aluminum Bumper, $D$ = 7.94 mm | | | | | | |
| 4-0646 | 0.194 | 6.74 | 0.587 | 0.582 | 0.584 | 1.869 |
| 6061-T6 Aluminum Bumper, $D$ = 8.84 mm | | | | | | |
| 4-0561 | 0.226 | 6.36 | 0.699 | 0.695 | 0.697 | 2.003 |
| 6061-T6 Aluminum Bumper, $D$ = 9.53 mm | | | | | | |
| 4-0511 | 0.216 | 6.42 | 0.727 | 0.738 | 0.732[a] | 1.952 |
| 4-0608 | 0.209 | 6.57 | 0.734 | 0.734 | 0.734 | 1.957 |
| 4-0660 | 0.160 | 6.67 | 0.643 | 0.641 | 0.642 | 1.712 |
| 6061-T6 Aluminum Bumper, $D$ = 12.70 mm | | | | | | |
| 4-0609[b] | 0.156 | 6.42 | 0.848 | 0.848 | 0.848 | 1.696 |
| | | | 0.950 | 0.958 | 0.954 | 1.908 |
| 4-0611 | 0.157 | 6.28 | 0.847 | 0.846 | 0.846 | 1.693 |
| 4-0661 | 0.125 | 6.24 | 0.761 | 0.762 | 0.762 | 1.523 |

[a] Some "lace" or small holes in bumper at various positions just beyond the periphery of the large hole.

[b] A photograph of the hole from this test is shown in Figure 27. Hole is completely surrounded by a series of small openings that give the appearance of lace edging. Set of smaller diameters in this table is for the central or main opening; the set of larger diameters describes the outer dimensions of the lace-edged opening.

Pieces of the piston used in the operation of the two-stage, light-gas gun struck three of the bumper sheets. Holes in two of the sheets were stretched in one direction after being struck by this material (Shots 4-1281 and 4-1292). The diameter reported for these holes, in Table 9, was the diameter measured in the direction that was not stretched. A third bumper sheet (Shot 4-1744) was torn into several pieces; consequently, a hole diameter could not be determined for that test. The hole for Shot 4-1353 was very irregular in outline (see Figure 26) and the hole diameter reported for this test was the approximate outer diameter of the hole (i.e., without the interior ring). Two diameters were reported for Shot 4-0609 (shown in Figure 27). The smaller diameter was the inside

diameter of the interior ring and the larger diameter was the outer diameter of the series of small holes that surrounded the interior ring. A number of the tests at the higher velocities and $t/D$ ratios produced holes that were out-of-round and irregular in outline. Of the 49 tests listed in Tables 9 and 10, 45 holes provided two measurements of the hole diameter. Twenty-three of the holes, or 51 percent, were larger in the dimension parallel to the rolling direction of the sheet. The hole diameter perpendicular to the rolling direction of the sheet was larger for 16 (36 percent) of the tests; hole diameter was the same in both directions for six (13 percent) of the tests.

Observations made during the measurement of bumper-sheet thicknesses and hole diameters emphasized the sensitivity of the hole diameter to very small variations in sheet thickness. The normalized bumper-hole diameter, $d_h/D$, is shown in Figure 28 as a function of $t/D$ ratio for all tests which used 2017-T4 aluminum spheres and an impact velocity in the range of 6.24 to 6.78 km/s. In a number of instances, multiple data points were available for certain $t/D$ ratios; nearly identical hole diameters were produced by these tests. The normalized inner and outer diameters of the hole for Shot 4-0609 are shown as two points in Figure 27. Finally, the simple equation

$$d_h/D = 4.5(t/D) + 1$$

describes the relationship that exists between $t/D$ ratio and normalized hole diameter for the normal impact of 2017-T4 aluminum spheres with thin aluminum sheets when the nominal impact velocity was about 6.7 km/s. As noted in the figure, this relationship does not apply for $t/D$ ratios of less than 0.08. For $t/D$ ratios of less than 0.08, the relationship was nonlinear and was not defined.

The lower-left-hand region of Figure 28 is shown, at a larger scale, in Figure 29. Further discussion of the normalized hole-diameter data for the nominal 6.7-km/s tests will be made with reference to Figure 29. Two features of the curve in this figure are
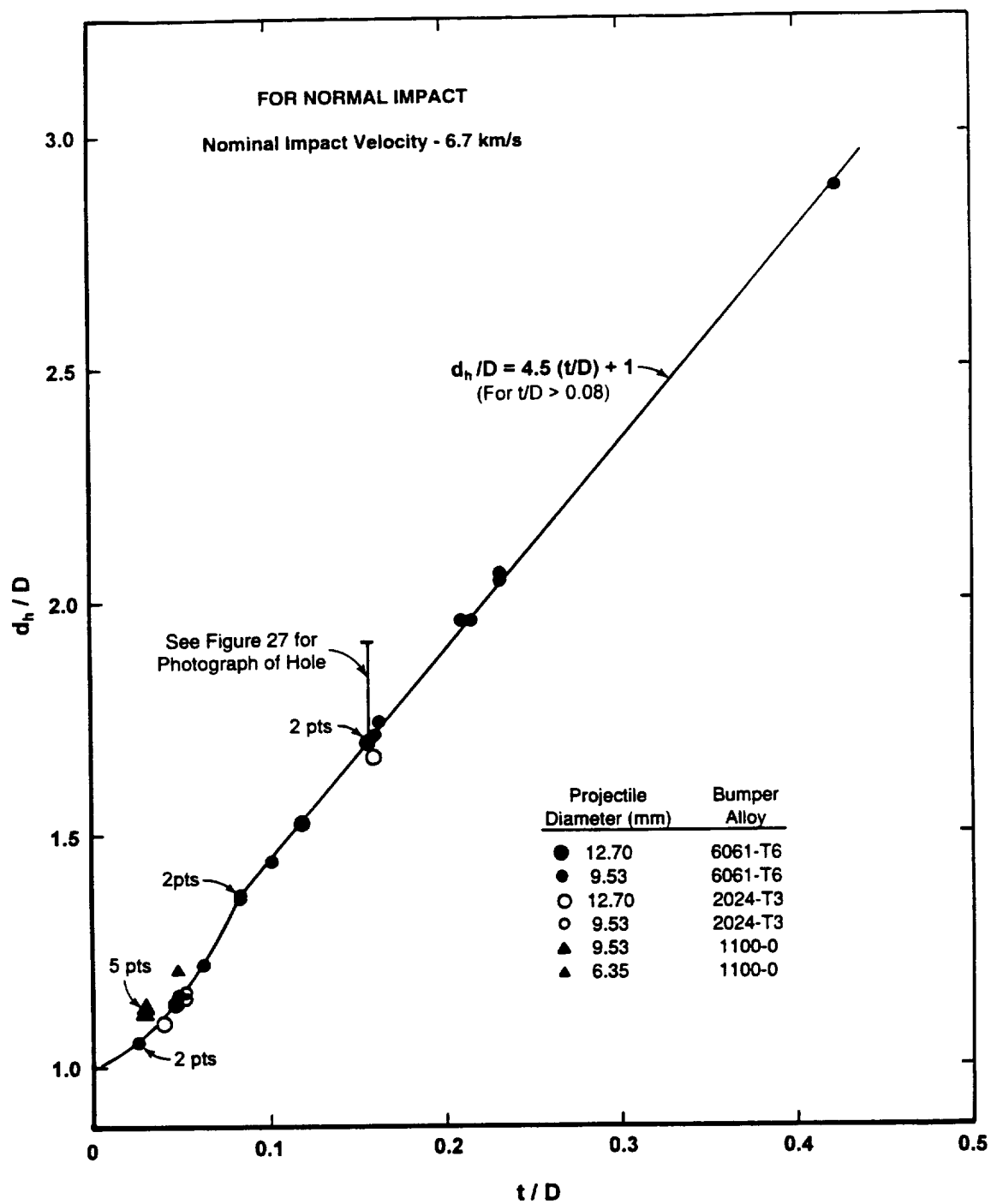
Figure 28. Normalized hole diameter as a function of $t/D$ ratio. Holes were produced by the normal impact of various diameters of 2017-T4 aluminum spheres that impacted several alloys of aluminum sheet at a nominal velocity of 6.7 km/s.
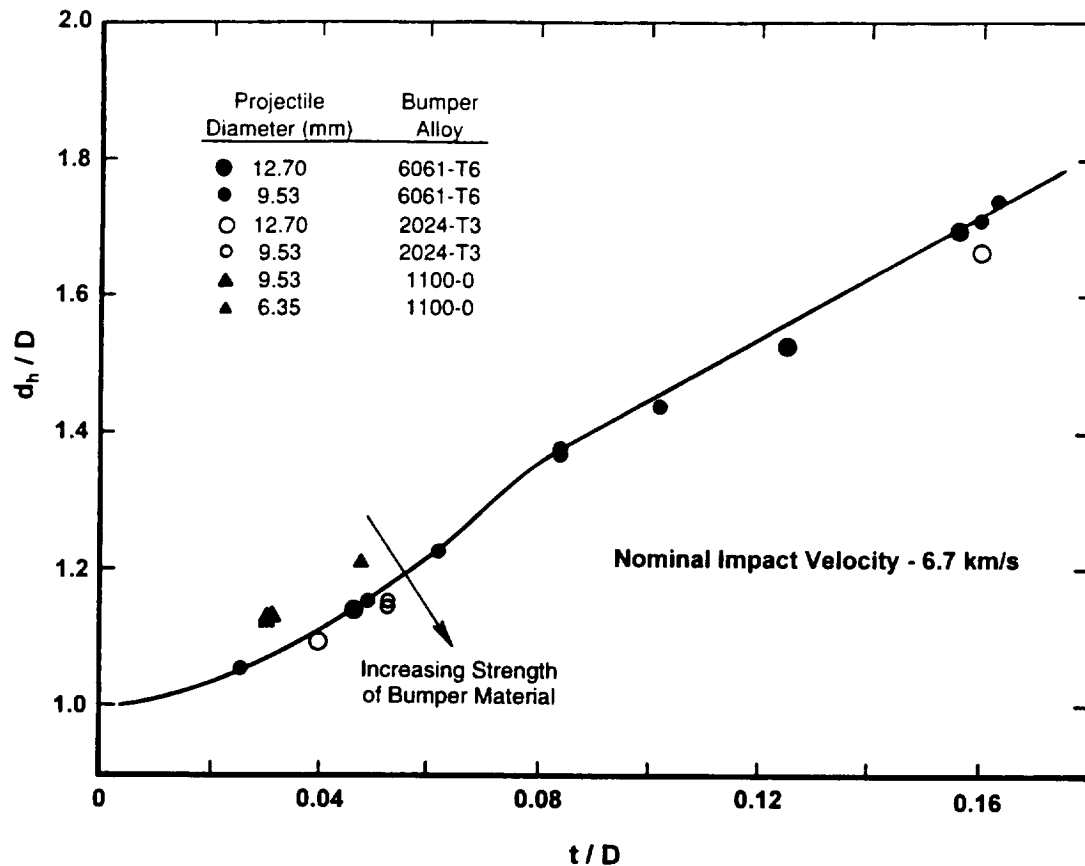
Figure 29. Normalized hole diameter as a function of $t/D$ ratio. This figure is an expansion of the lower-left portion of Figure 28.

noteworthy. First, normalization of the hole-diameter data using the projectile diameter, $D$, permitted the diameters of holes produced by spheres ranging from 6.35 to 12.70 mm in diameter to be compared on the basis of $t/D$ ratio. The comparisons indicated that the use of this simple geometric scaling technique was extremely effective for the range of data that was examined. The ability to compare hole data with use of this scaling technique was shown by Hörz et al. [27] for experiments that employed projectile diameters and $t/D$ ratios that ranged from 50 to 3200 μm and 0.006 to 5, respectively. Second, the data indicate that bumper strength played a significant role in determining the final diameter of the hole. The holes formed in the weaker 1100-O aluminum bumpers were considerably larger than those produced in the higher strength 6061-T6 or 2024-T3 aluminum bumpers. Holes produced in the 6061-T6 aluminum bumpers were slightly larger than those

produced in the stronger 2024-T3 aluminum sheets. Strength of the aluminum bumper-sheet material apparently affected the growth of the hole during the later stages of the hole-formation process, when material strength would become significant in comparison to shock-induced stresses.

Data presented in the two preceding figures examined the effect of $t/D$ ratio, at constant impact velocity, on the diameter of the hole. The effect of impact velocity on hole diameter is also of interest. Normalized hole diameter is shown as a function of $t/D$ ratio for four impact velocities in Figure 30. Although the data sets shown in this figure are limited in range and numbers of points, they do indicate that hole diameter increased as $t/D$ ratio and/or impact velocity increased. In addition, the four "curves" appeared to converge on the point $d_h/D = 1$ and $t/D = 0$. Hörz et al. [27] and others have shown that projectile and hole diameter are essentially identical when the $t/D$ ratio is very small. A linear relationship between hole diameter and $t/D$ ratio was shown previously for impacts
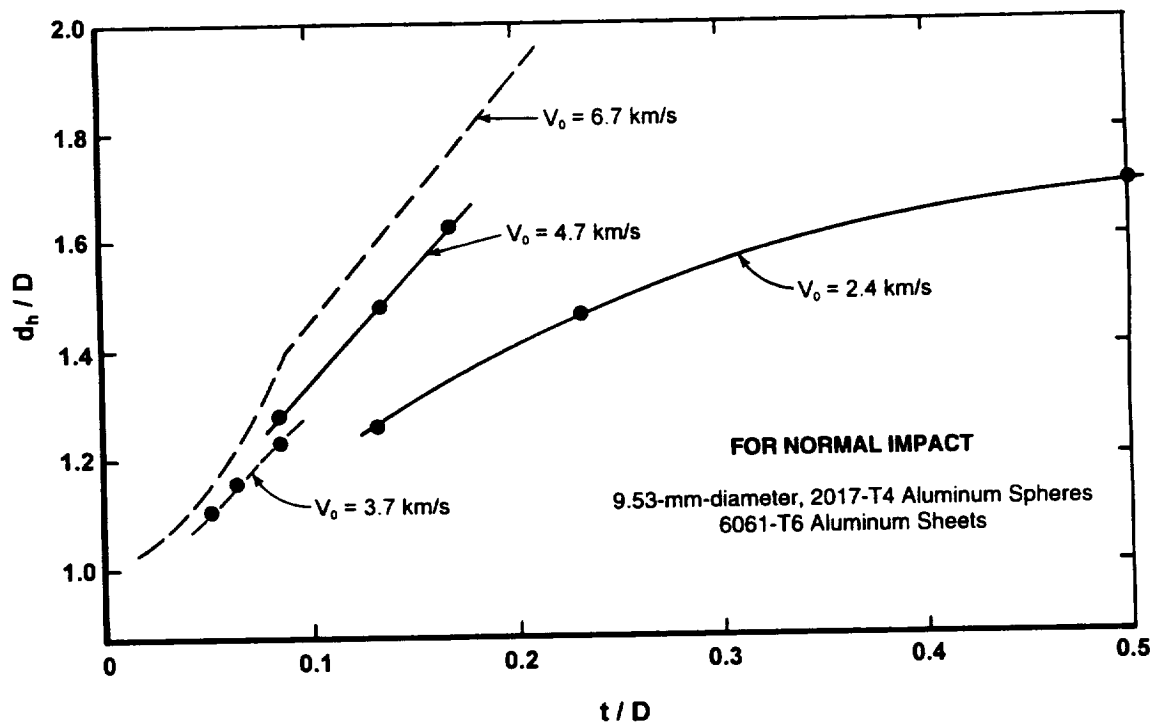


Figure 30. Normalized hole diameter as a function of $t/D$ ratio for four impact velocities.

at 6.7 km/s. A linear relationship may exist for impacts at 4.7 km/s: however, insufficient data were available to draw a conclusion for impacts at 3.7 km/s. The data for impacts at 2.4 km/s indicate that hole diameter is not a linear function of $t/D$ ratio, at least for the range of $t/D$ ratios shown in Figure 30. Carson and Swift [26] speculated that a linear dependence of hole diameter upon projectile velocity may be invalid at sufficiently low impact velocities, but did not have experimental data to confirm their suspicion.

Normalized hole diameter is shown as a function of impact velocity, in Figure 31, for seven $t/D$ ratios. Sufficient data were available to provide a reasonably good indication of the relationship that existed between hole diameter, $t/D$ ratio, and impact velocity, at least for the range of test conditions examined in this study. All curves indicate that the hole diameter will approach the diameter of the projectile at low impact velocities. Similar results were obtained from a set of impact experiments [29] in which hardened
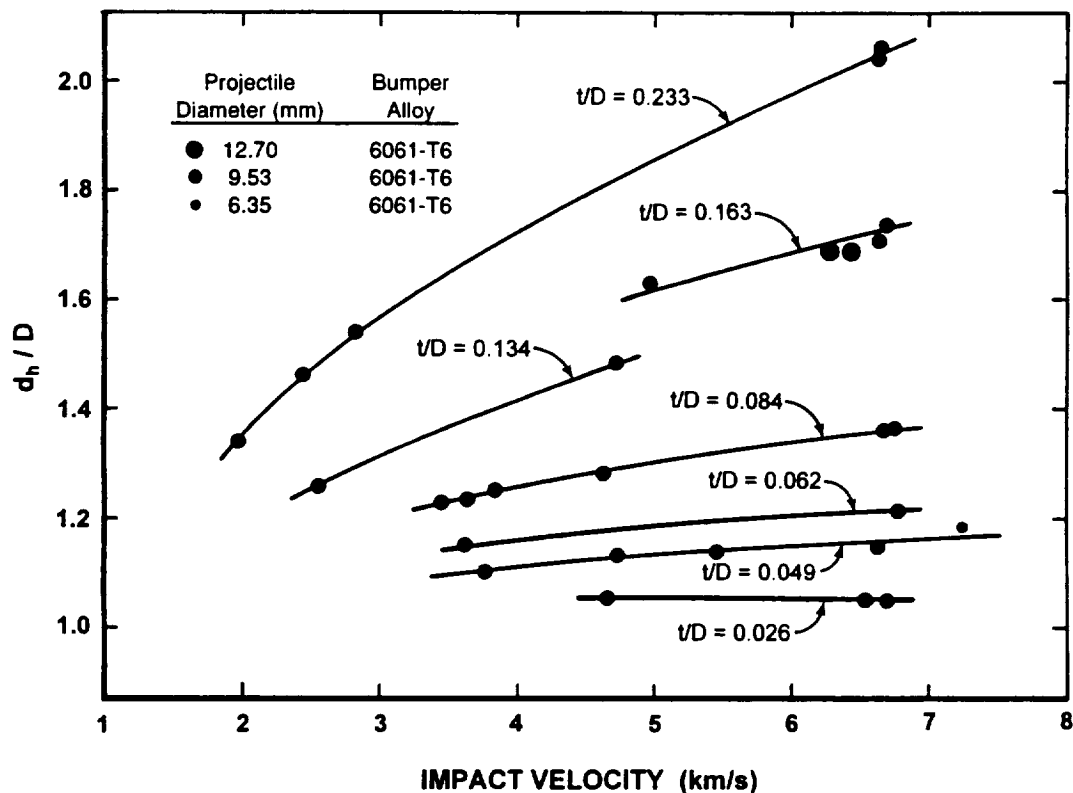


Figure 31. Normalized hole diameter as a function of impact velocity for seven $t/D$ ratios.

steel spheres were fired at semi-infinite, 6061-T6 aluminum plates. At the lower impact velocities, rigid-body penetration of the spheres produced tunnel-like craters whose diameters were slightly less than the diameter of the sphere. Crater diameters began to increase when the impact velocity was high enough to cause the spheres to crack and shatter. Two other features of Figure 31 are noteworthy. First, the holes produced in the thinnest bumpers ($t/D$ = 0.026) were about 5 percent larger than the projectile, regardless of the impact velocity. A similar observation has been made by many other investigators. Second, many of these same investigators have suggested that a linear relationship may exist between hole diameter and impact velocity (for $t/D$ = constant). As shown in Figure 31, this relationship may hold for a limited range of the higher impact velocities, but clearly does not hold for the lower velocity impacts with higher $t/D$ ratios.

The $t/D$ ratio was varied from ~ 0 to 3.5 in a series of impact tests using 3.18-mm-diameter, 2017 aluminum spheres and 6061-T6 aluminum bumper sheets [30]. Results of these tests indicated that hole diameter was greatest when the $t/D$ ratio was about 1.5. As $t/D$ ratio was increased above 1.5, hole diameter decreased and eventually reached the point where a hole was not formed ($t/D$ < 3.5). Similar results would have been expected if the test series described in this report had included tests with higher $t/D$ ratios.

Experimentalists have developed a number of equations used to relate hole diameter to various parameters of the target and projectile. In general form, many of the equations are similar to the following equation given by Maiden and McMillan [25]:

$$d_h/D = 0.45 V_0 (t/D)^{2/3} + 0.9$$

Later, this equation was modified by Maiden and McMillan as follows:

$$d_h/D = 2.4 (V_0/c)(t/D)^{2/3} + 0.9$$

where $c$ is the sound speed of aluminum. This equation was generated to describe data resulting from the impact of 3.18-mm-diameter aluminum spheres with 2024-T3 aluminum

81

sheets. Nysmith and Denardo [14] provided the following equation fit to data generated by the impact of 3.18-mm-diameter pyrex and aluminum spheres with 2024-T3 aluminum sheets:

$$d_h / D = 0.88(\rho)^{0.5}(V_0)^{0.5}(t/D)^{0.45}$$

where $\rho$ was the projectile density. More complicated equations, involving a wide variety of projectile and bumper parameters, were derived by other investigators.

Both of the equations provided by Maiden and McMillan and the equation from Nysmith and Denardo were evaluated to determine their adequacy for describing the data obtained in this study. In the words of Carson and Swift, when comparing their data for the impact of 2017 aluminum spheres with 6061-T6 aluminum sheets to other data, the equations "correctly predict the general trends of the presented data but do not accurately describe them." Maiden and McMillan's original equation underestimated (< 2 percent) the hole diameter for the higher velocity, higher $t/D$ ratio tests. It overestimated the hole diameters for the higher velocity, lower $t/D$ ratio tests by as much as 15 percent. Use of this equation for the lower velocity tests worked well for the lower $t/D$ ratio tests but underestimated the hole diameter for the higher $t/D$ ratio tests by about 10 percent. Use of their modified equation reduced the "error" at the lower $t/D$ ratios but increased the difference between the computed and actual hole diameters for the higher $t/D$ ratio tests. Nysmith and Denardo's equation consistently underestimated the hole diameters by 5 to 10 percent (as $t/D$ ratio decreased) for the higher velocity tests and 10 to 30 percent for the lower velocity tests. Examination of the data used by the investigators just cited showed that most of the data was from tests with a limited range of impact velocities. In addition, most of the tests used relatively thick bumper sheets (and high $t/D$ ratios). Although the hole data from the tests presented in this report exhibit clear trends, they are insufficient to develop a relationship suitable for use in describing hole diameter as a function of impact velocity and $t/D$ ratio.

# SECTION VI. MODEL FOR PROJECTILE-BUMPER INTERACTION

The model presented in this section is used to characterize the normal impact, at hypervelocity, of an aluminum sphere with a thin aluminum sheet. The model describes the events which occur immediately after the impact and lead to the formation of the debris-cloud structural features. Formation of the debris-cloud elements, the external bubble of debris, and the ejecta veil are described. The distribution of mass within the debris-cloud elements is discussed and a method of estimating the state of the material in the debris cloud is presented. Finally, the propagation of a shock in the bumper and its effects on the dimensions of the hole left in the bumper sheet are presented.

Bumper-sheet thickness, sphere diameter, and impact velocity are parameters which most influence the design and the response of an aluminum shield to the hypervelocity impact of an aluminum sphere. In the preceding sections, test results were presented in tables and figures as functions of bumper-thickness-to-projectile-diameter ratio and/or impact velocity. With the exception of fragment size and fragment-size distributions, properties of the debris clouds were shown to scale geometrically with sphere diameter. Consequently, the various figures presented in the preceding sections can be used to determine the position, velocity, and dispersion of elements in a debris cloud, the equivalent diameter of the large central fragment, and the diameter of the hole left in the bumper for impacts produced by spheres of any diameter.

Formulation of a single relationship or model to describe all aspects of the formation of a debris cloud was not realistic, since sufficient data for use in the development of a comprehensive model were not available. As a result, the model is presented as a collection of smaller models which are used to describe the formation or development of specific elements of the debris cloud. Development of the smaller

83

models was guided by conclusions drawn from the analysis of the quantitative data presented in Sections III, IV, and V, and from observations made during examination of the radiographs, bumper sheets, and witness plates from the tests.

A description of the impact of a sphere with a thin sheet cannot be given without some discussion of shocks and shock-propagation processes. When two objects collide, a disturbance is propagated away from the impact site in both the impacting and the impacted object. If the velocity of the disturbance exceeds the velocity of sound in the material, the disturbance almost instantly develops into a discontinuity of negligible thickness and is termed a shock. Material ahead of the shock remains at rest (in the case of the impacted object), or traveling at constant velocity in a stress-free state (in the case of the impacting object). Material behind the shock can be severely disturbed, experiencing extremely high stresses (pressures) and strains. The properties of the material on both sides of a shock have been studied extensively and can be defined within the regions of their study.

Before proceeding to a description of the rather complicated shock structure developed in the aluminum sphere and the thin aluminum sheet, it will be helpful to review shock behavior for an ideal, one-dimensional impact of two semi-infinite plates of the same thickness and material. Following impact, shocks form in both plates. When the shock in each plate encounters the free surface opposite the impacted surface, a relief or release wave is generated. Release waves are not shocks but are "disturbances" that spread out or lengthen as they propagate through the shocked material. The release waves travel through the shocked material (back to the impact site) and relieve all stresses in the material behind them. Eventually, the release waves meet. Since the semi-infinite plates are of the same thickness and material, and the shock and release waves travel at the same velocity, the meeting occurs at their impacting surfaces. If the impact velocity is low and the collision is elastic, the plates simply separate. If the impact velocity is

high, large plastic deformation and/or failure of the plates occurs. In either case, both plates will change velocity. For the elastic collision, the impacted plate will acquire the velocity of the impacting plate, and the impacting plate will come to rest. For the higher velocity, inelastic collision, both plates, or portions of the plates, will be in motion.

In the one-dimensional impacts just described, propagation of the shock was treated as an ideal process. Propagation of a "real" planar shock is not ideal. A planar shock traveling through a thick plate, for example, can be transformed into an elastic wave by the time it reaches the free surface of the plate because energy in the shock is dissipated during propagation of the shock. If the planar shock in the thick plate was generated by the impact of a relatively thin plate, a release wave will develop in the thin plate when the shock in the thin plate is reflected at its free surface. The release wave will travel back through the thin plate, across the interface between the plates, and into the thicker plate. After passage of the shock, particles in the shocked material (in both plates) acquire a velocity in the direction of the shock. When the particle velocity of material in the thicker plate is added to the velocity of the leading edge of the overtaking release wave in that plate, the resultant velocity is greater than the shock velocity and the release-wave front can overtake and decrease the intensity of the advancing shock [31].

As will be shown in the next subsection, a quasi-planar shock is developed in a portion of the sphere and the thin sheet after impact. The quasi-planar shock is degraded by the dissipation of shock energy, by the effects of spherical divergence of the shocks as they propagate in both materials, and by the overtaking release wave formed at the free surface of the thin sheet. The shock is further degraded and distorted, in the sphere and the thin sheet, by release waves generated when the "edges" of the shock front continuously encounter the free surfaces of the sphere and the thin sheet. However, the complex stress states that are produced in the sphere and thin sheet, by propagation of the shock and release waves, are symmetric about the shot-line axis of the sphere.

In the preceding paragraphs, the duration of the shock pulse and its effect on the development of the debris cloud was not discussed. Actual response of a material to a shock depends on the intensity and the duration of the shock [32]. The duration of the shock pulse, in the case of a sphere impacting a thin sheet, is determined by the combined transit time of the shock and release wave in the thin sheet. For the tests presented in this report, this combined transit time ranges from 30 ns for Shot 4-1395 to about 1.38 $\mu$s for Shot 4-1721. The stress level in the sphere begins to decrease when the release wave originating at the free surface of the bumper arrives at the sphere/bumper interface. Fracture, fragmentation, and all other processes observed during the formation of debris clouds are the direct result of the passage of stress pulses through the spheres.

The various shock degradation processes described in the preceding paragraphs also alter the stress-pulse characteristics. For identical impact conditions of velocity and materials, the stress pulse produced in the sphere by an impact with a thin sheet is of shorter duration and of lower average intensity than one produced by an impact with a thick sheet. Because most of the tests presented in this report employed low $t/D$ ratios, only a portion of the sphere used for each test was under a state of stress at any instant following the impact. Details of the shape and the extent of the stressed region, and its progress through a sphere, were shown in a series of computer simulations performed by Alme and Rhoades [33]. The calculations were performed, using CALE, in a center-of-mass frame of reference in which the projectile and bumper sheet are both moving. Figure 32 illustrates the impact of a 9.5-mm-diameter aluminum sphere with an aluminum sheet ($t/D = 0.20$) at 8 km/s. Stresses in the sphere and bumper are shown at times of 0.2, 0.4, 0.6, 0.8, and 1 $\mu$s after impact. During transit through the sphere, peak stress at the shock front decreased from 130 GPa to 47 GPa. The stressed region averaged 3 mm in thickness (measured along the shot line) and extended laterally to the edges of the sphere. At 0.2 $\mu$s, shocked sphere and bumper material is enclosed in a lens-shaped region. Stresses in the shocked material

86
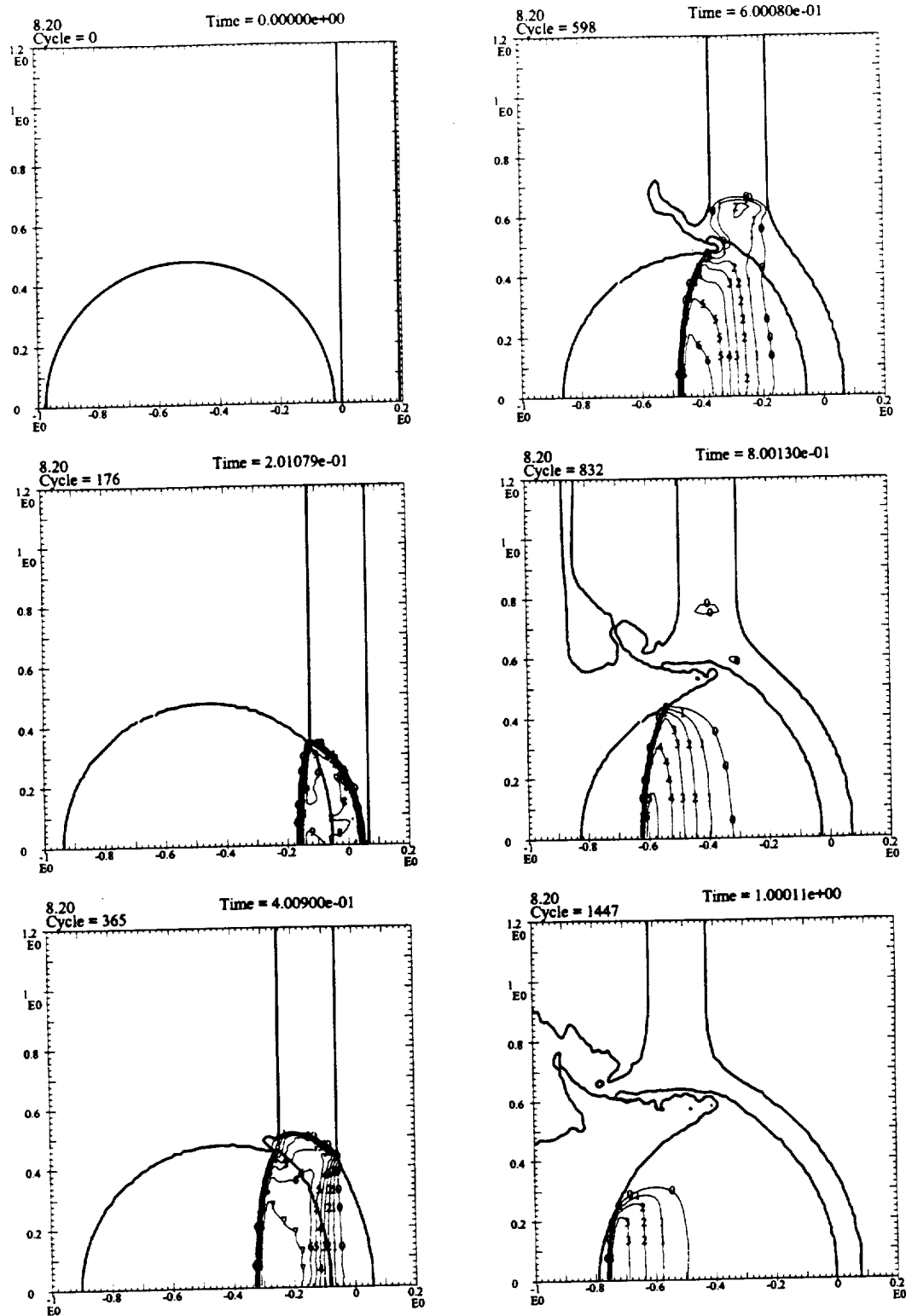
Figure 32. Computer simulation showing stressed region in a 9.5-mm-diameter, aluminum sphere after impact with a 1.9-mm-thick aluminum sheet at 8 km/s. Stressed region is shown at 0, 0.2, 0.4, 0.6, 0.8, and 1µs after impact. Isobar contours as follows: 0 = 10 GPa, 1 = 20 GPa, ..., 9 = 100 GPa. (Figure provided by Alme and Rhoades [33]).

are nearly uniform throughout the region. At 0.4 μs, the affected material lies in a curved band of uniform width (concave towards the front) and extends into the bumper. The stress-reducing effects of release waves originating in the bumper and at the free surfaces of the sphere are evident along the front (towards the bumper) and sides of the band. A uniformly stressed region, attached to the shock traveling through the sphere, makes up about two-thirds of the material in the band at this time. At 0.6, 0.8, and 1.0 μs, the stresses in the bumper continue to diminish and the shocked region in the sphere becomes lens shaped, with the most highly stressed material immediately behind the shock. The lateral extent of the shocked region decreases as the shock approaches the rear of the sphere and the stress-reducing effects of the release waves are more evident in the affected material at the later times.

## A. Development of Debris-Cloud Structure

Failure and fragmentation of a sphere initiated by hypervelocity impact is an orderly process. Several stages of failure of the sphere were observed as impact velocity was varied. When impact velocities were low, plastic deformation of the front (impacting) surface and the development of a spall failure inside the rear surface of the sphere were the first manifestations of failure of the sphere. At slightly higher impact velocities, a shell of spall fragments developed when the spall layer broke open and the spall petals separated from the back of the sphere. As impact velocity continued to increase, a cloud of projectile fragments formed and eventually developed into a structure with the three well-defined elements shown in the radiographs presented in the preceding sections. The formation of each of the three elements, the ejecta veil, and the external bubble of debris will be described in the remainder of this subsection.

As impact velocity was increased above that required to produce plastic deformation of the front of the sphere, a spall failure developed inside the rear surface of the sphere.

This spall failure was reasonably evident in the radiographs of several tests, but was difficult to reproduce in the photographic prints made from the radiographs. An enlarged print of a radiograph from Shot 4-1428 is presented in Figure 33. The drawing to the left of the photograph illustrates the various features observed in the radiographs. The deformed front surface and the increased radius of the rear of the sphere were evidence of failure of the front and rear surfaces of the sphere, respectively. When the $t/D$ ratio was greater than 0.13, the formation of cracks and swelling of the rear surface of the spheres were the first evidence of failure. For tests with the larger $t/D$ ratios, onset of cracking or swelling was used to define the failure-threshold velocity.

Definition of the spall-failure-threshold impact velocity, or more simply — threshold velocity, is important because it defines a unique stress state at the rear of the
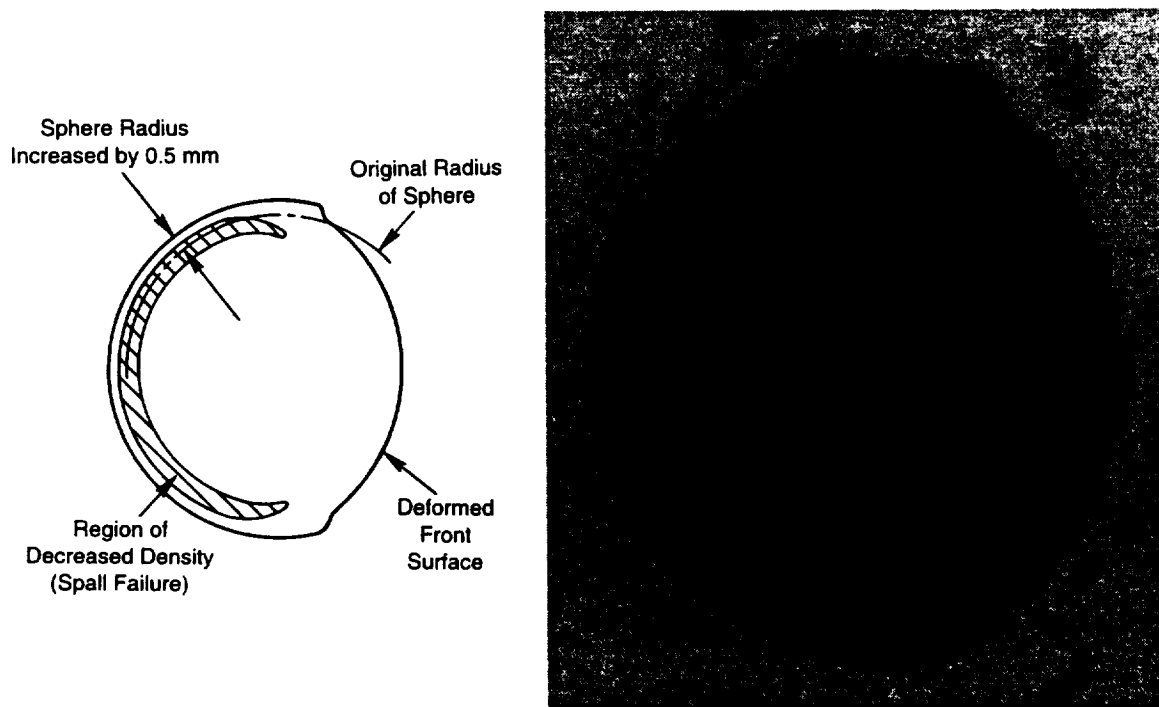


Figure 33. Illustration and radiograph showing deformation and spall failure at the rear of a sphere after an impact near the spall-failure-threshold impact velocity. Radiograph is of a 9.53-mm-diameter, 2017-T4 aluminum sphere that struck a 0.465-mm-thick, 6061-T6 aluminum sheet at 3.77 km/s (Shot 4-1428).

sphere. Because deformation of the front surface and formation of the spall failure were the first signs of failure of the sphere, and the first stage of development of a debris cloud, data used to define the threshold velocity are presented at the beginning of this subsection as a first step in the description of the evolution of the debris-cloud structural features. Further use of the threshold velocity will be made in the subsection describing a method for estimating the state of the material in the debris cloud.

The threshold velocity is unique for each combination of impact velocity and $t/D$ ratio. The transition from no failure to failure occurs within a narrow range of impact velocities for each $t/D$ ratio. Table 11 presents conditions for nine tests near the threshold velocity and a description of the post-impact condition of the sphere. Late-time-view

## TABLE 11

### TESTS NEAR SPALL-FAILURE-THRESHOLD IMPACT VELOCITY

All bumper sheets were 6061-T6 aluminum. All projectiles were
9.53-mm-diameter, 2017-T4 aluminum spheres fired at normal incidence.

| Shot Number | $\dfrac{t}{D}$ | Impact Velocity (km/s) | Projectile Weight, Before (g) | After (g) | Data Source | Post-Impact Condition of Rear of Sphere |
|---|---|---|---|---|---|---|
| 4-1715 | 0.026 | 4.67 | 1.2751 | --- | X rays | Attached spall shell |
| 4-1428 | 0.049 | 3.37 | 1.2750 | --- | X rays | Attached spall shell |
| 4-1633 | 0.062 | 3.65 | 1.2753 | --- | X rays | Spall shell petaled open, No material lost |
| 4-1632 | 0.084 | 3.47 | 1.2754 | --- | X rays | Spall shell petaled open, Petals detached |
| 4-1722 | 0.132 | 2.54 | 1.2751 | 1.2172 | X rays and recovered sphere | Attached spall shell |
| 4-1719 | 0.233 | 2.83 | 1.2750 | 0.6002 | X rays and recovered sphere | Rear surface spalled away |
| 4-1720 | 0.233 | 2.44 | 1.2745 | 0.7787 | X rays and recovered sphere | Several large cracks |
| 4-1718 | 0.233 | 1.98 | 1.2750 | 1.2138 | X rays and recovered sphere | Smooth, no spall or cracks |
| 4-1721 | 0.504 | 2.23 | 1.2755 | 0.6024 | X rays and recovered sphere | Flattened, several small cracks |

radiographs of the projectiles used for the tests listed in Table 11 are shown in Figure 34. The determination of the post-impact condition of the sphere was made with use of the radiographs from each test and, for the lower impact velocities, from an examination of the recovered projectiles. Foam blocks were used in place of witness plates for the lower velocity tests to facilitate soft recovery of the projectiles. Photographs of the rear surface of five projectiles recovered from the foam blocks are also shown in Figure 34. The radiographs for Shots 4-1715 and 4-1722 show a narrow region of reduced density just
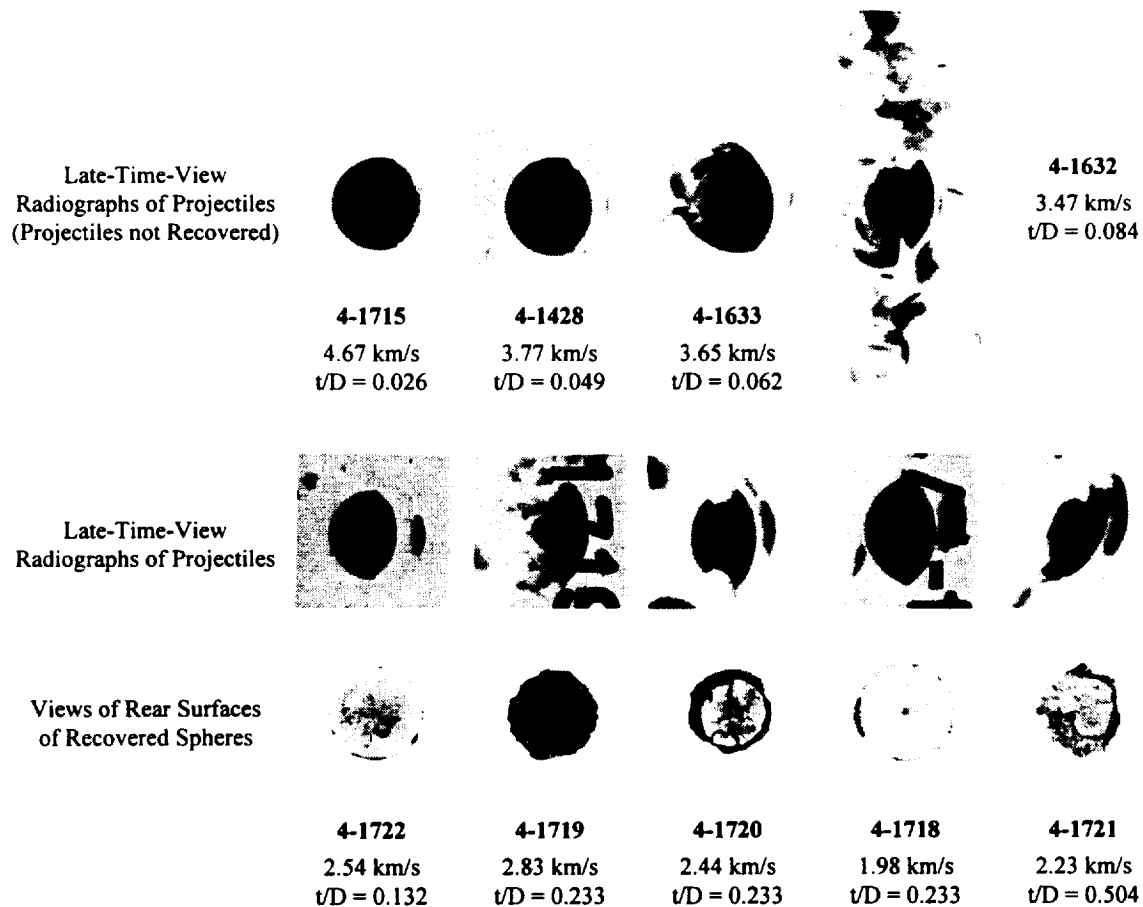


Figure 34. Late-time-view radiographs and photographs of 9.53-mm-diameter, 2017-T4 aluminum spheres after impact with various thicknesses of 6061-T6 aluminum sheets. Spheres are shown traveling from left to right in the radiographs. The rear surfaces of the spheres recovered from foam blocks are shown in the photographs below the appropriate radiographs. Impact conditions for each test are shown below the radiographs/photographs.

inside the rear surface of the sphere and an increase in the radius of curvature of the rear of the sphere, features similar to those shown for Shot 4-1428 in Figure 33.

The threshold velocity for failure of the sphere is shown as a function of $t/D$ ratio in Figure 35. In Figure 35, open circles denote test conditions that produced a separation or a loss of material from the rear surface of the sphere. Solid circles denote points where the rear surface of the sphere developed a spall failure but remained intact or was cracked. The equation of the line drawn through the points shown in Figure 35 is:

$$V_S = 1.436 \, (t/D)^{-0.333}$$

$V_S$ is the threshold velocity for failure of the spall shell attached to the rear of the sphere. Shot 4-1428 (attached spall shell) and Shot 4-1633 (detached spall shell) provide a
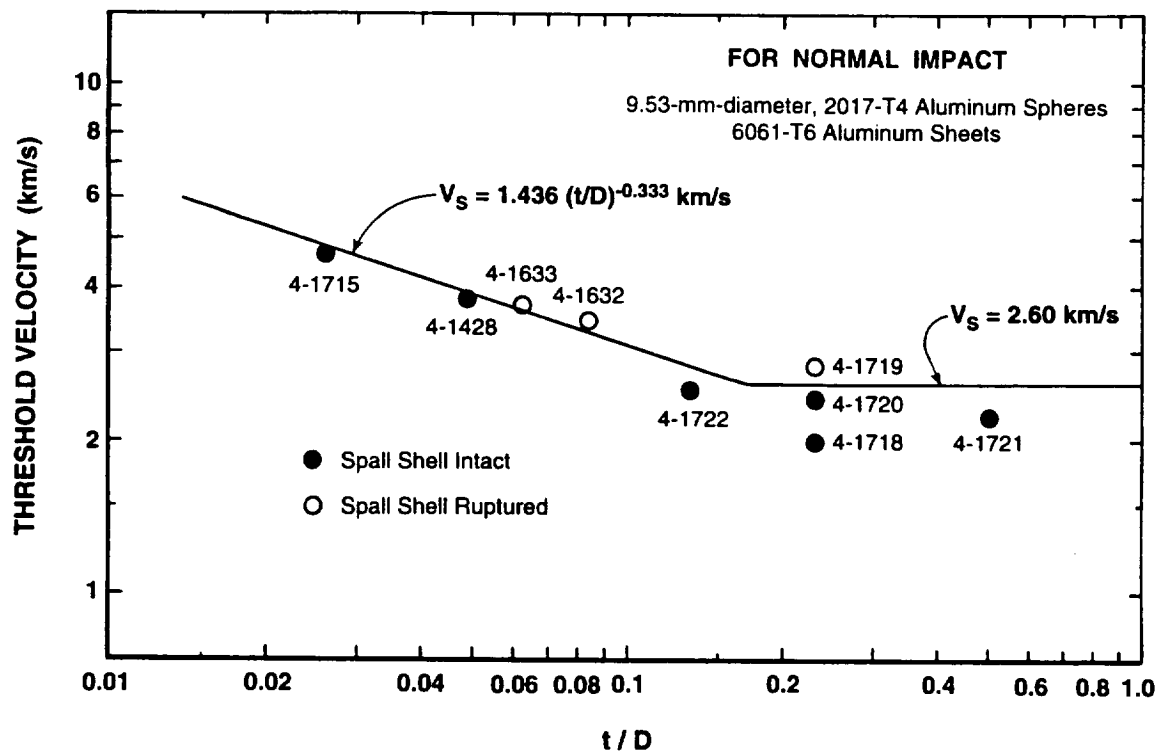


Figure 35. Spall-failure-threshold impact velocity as a function of $t/D$ ratio. Shot numbers are shown in this figure to facilitate identification with the radiographs and the photographs shown in Figure 34.

reasonably hard "point" through which the line should pass. Exponents ranging from -0.3 to -0.4 would fit a line describing most of the data presented in Figure 35. A value of 0.333 was arbitrarily selected, however, because Gilath *et al.* [34] had shown that the energy required to produce spall-threshold conditions in aluminum was a cubic function of sheet thickness for hemispherical shock waves, a situation similar to the propagation of shocks in the aluminum spheres.

The equation of the line shown in Figure 35 applies for $t/D$ ratios less than 0.16. A constant threshold velocity of 2.6 km/s was assumed for $t/D$ ratios greater than 0.16. This assumption was based on the observed behavior of the expansion velocity, $V_r$, of the shell of spall fragments. When impact velocity was held constant and the $t/D$ ratio was increased, the radial expansion velocity of the shell of spall fragments approached a maximum value when the $t/D$ ratio reached 0.16 to 0.17 (see Figure 12). The expansion velocity remained relatively constant when the $t/D$ ratio was greater than 0.17. When the $t/D$ ratio was greater than 0.17, an evaluation of the transit times of the shock and release waves in the projectile indicated that the shock would arrive at the rear surface of the sphere relatively unaffected by the release wave originating at the free surface of the bumper. Release waves originating in thinner bumpers, on the other hand, could easily overtake the shock moving toward the rear of the sphere, thereby decreasing the intensity of the shock and the velocity of spall fragments produced when stresses in that region were relieved.

Spall-failure-threshold velocity data were only available for tests which used 9.53-mm-diameter, 2017-T4 aluminum spheres. However, study of the results of tests using different sphere diameters indicated that the velocity and morphologic features of the debris clouds scaled geometrically when compared on the basis of $t/D$ ratio and impact velocity [35]. Consequently, it is likely that the threshold-velocity relationship given in Figure 35 would properly describe the onset of failure for spheres of other diameters.

1. Front Element and Early-Time Processes. Late-time views of five debris clouds are shown in Figure 36. These late-time views clearly show the development and growth of the front element of the debris-cloud internal structure as impact velocity is increased. In the views in Figure 36, the front element consisted of the following: a single fragment and several solid fragments, (a) and (b), respectively; a small cloud of solid fragments, (c); and a large cloud of fine droplets of molten aluminum, (d) and (e).

A model for the formation of the front element is presented in this subsection. The essential features of the model are shown in the upper right of Figure 37. The kinematics of the model draw heavily on a description of the impact process given by Ang [36] and used to determine the source of material dominating an impact flash signature. In Figure 37, $U$ is the shock velocity, $u_p$ is the particle velocity behind the shock, $V_0$ is the impact velocity, $V_{CP,P}$ is the velocity of the collision point between the surface of the sphere and the target in the reference frame of the projectile, and $V_{CP,T}$ is



| 3.77 km/s | 4.71 km/s | 5.45 km/s | 6.62 km/s | 7.38 km/s |
|-----------|-----------|-----------|-----------|-----------|
| 4-1428 | 4-1433 | 4-1394 | 4-1360 | 4-1744 |
| (a) | (b) | (c) | (d) | (e) |
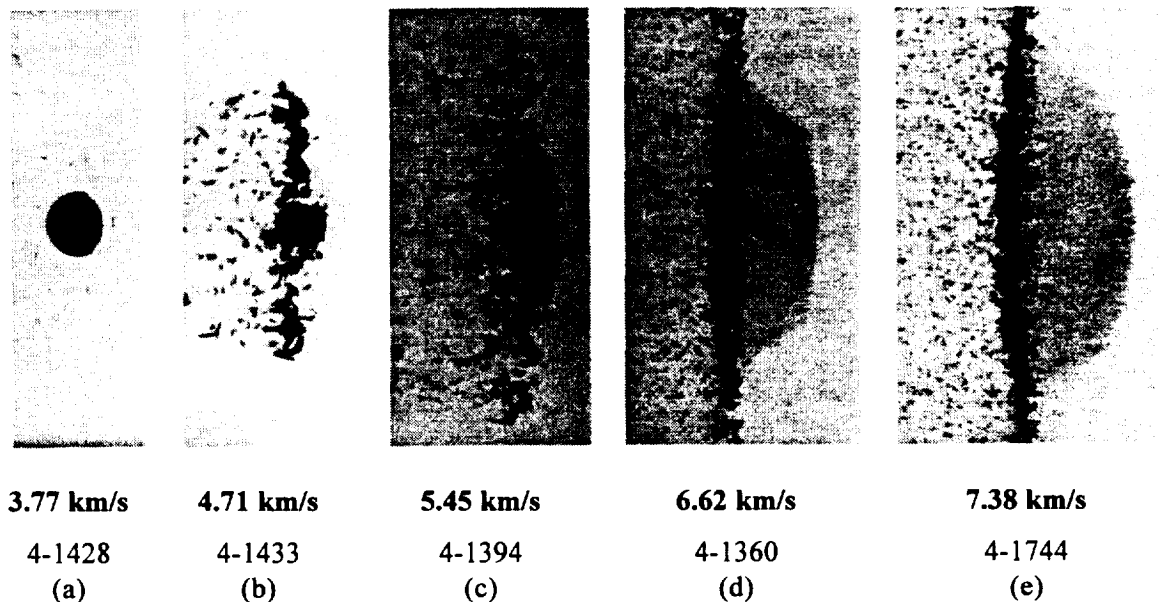
Figure 36. Late-time views of debris clouds showing the development of the front element of the internal structure as impact velocity is increased. All tests used 9.53-mm-diameter, 2017-T4 aluminum spheres and 6061-T6 aluminum bumper sheets ($t/D = 0.049$). See Figure 7 for earlier views of these clouds.

94

the velocity of the collision point in the reference frame of the target. $V_{CP,P}$ and $V_{CP,T}$ are given as functions of impact velocity, $V_0$, sphere radius, $R_0$, and elapsed time after impact, $\tau$, as follows:

$$V_{CP,P} = \frac{R_0 V_0}{\sqrt{2 R_0 V_0 \tau - V_0^2 \tau^2}}$$

and

$$V_{CP,T} = \frac{R_0 V_0 - V_0^2 \tau}{\sqrt{2 R_0 V_0 \tau - V_0^2 \tau^2}}$$
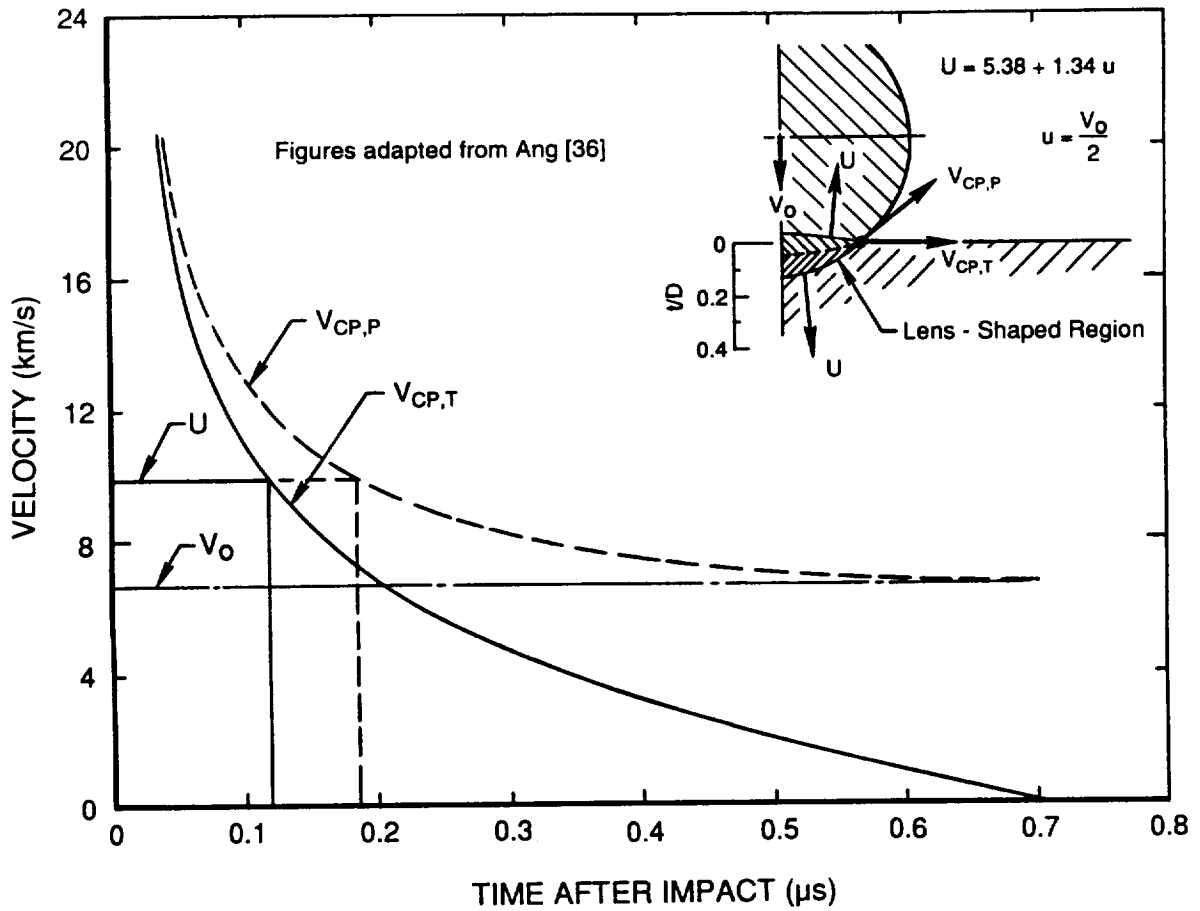


Figure 37. Illustration of interactions at impact site. Collision-point velocities are shown as a function of time after impact for a 9.53-mm-diameter sphere traveling at 6.70 km/s. In the inset, the impacting sphere and impacted sheet are shown with appropriate notation for the velocities referenced in this report.

The collision-point velocity, in both frames of reference, is presented in Figure 37 as a function of time after impact for a 9.53-mm-diameter sphere traveling at 6.70 km/s. Also shown in Figure 37, as horizontal lines, are $V_0$ and $U$. The shock velocity was determined using the relationship given in the upper right of Figure 37.

As shown in Figure 37, $V_{CP,T}$ is greater than $U$ for the first 0.12 μs after impact. Consequently, loading of the lens-shaped region shown in the inset was quasi one-dimensional during this time interval. Formation of release waves at the boundaries of the lens-shaped region was not possible as long as $V_{CP,T}$ was greater than $U$. When $V_{CP,T}$ was less than $U$, release waves were generated in the target prior to contact by the oncoming sphere. As the impact process continued, formation of release waves in the sphere began and the description of the shock-wave interactions was quickly complicated for the remainder of the impact event. In the inset in Figure 37, the lens-shaped region of compressed material is shown to scale at the time $V_{CP,T}$ equals $U$ (0.12 μs after impact). The diameter of the compressed region is approximately 56 percent of the diameter of the sphere. Also shown in the inset is a $t/D$ scale that allows the reader to determine the fraction of bumper-sheet thickness that experienced quasi one-dimensional loading during impact.

Figure 38a illustrates the growth of the lens-shaped region in Figure 37 into the dark substructure visible in the front element of the debris cloud shown in Figure 38b. Figure 38a is drawn to scale, although the horizontal axis is compressed. The diameter of the heavily shaded region in Figure 38b was determined from the radiograph. The diameter of this region at 19.8 μs after impact and the measured diametral velocity of this portion of the debris cloud were used to compute the diameter of the lens-shaped region at 0.12 μs after impact. The nominal diameter of this region (56 percent of the sphere diameter) and the computed diameter agreed exactly. The dark substructure in the front element was also observed in radiographs of the tests with $t/D$ ratios of 0.026 and 0.049
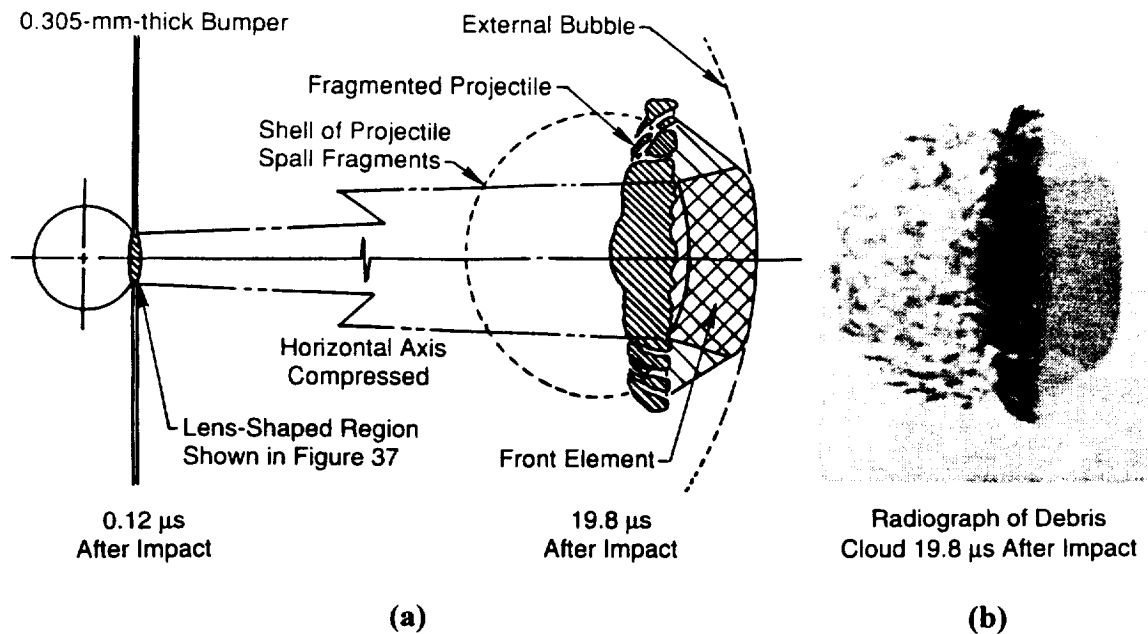
Figure 38. Development of features in front element of internal structure of debris cloud.
(a) Expansion of the region in which collision-point velocity in target exceeds
the shock velocity (see Figure 37). (b) View of the debris cloud produced by
the impact of a 9.53-mm-diameter, 2017-T4 aluminum sphere with an 1100-O
aluminum sheet ($t/D$ = 0.032) at 6.67 km/s (Shot 4-1290).

(see Figure 6). An explanation for the formation of the dark substructure in the front

element of the debris cloud was not developed.

For low impact velocities, the front element was a plug of bumper material whose

diameter was smaller than the diameter of the sphere. At low impact velocities, the plug

separated from the sphere as shown in the radiographs presented in Figure 34. For Shot

4-1715, however, the front element was a cluster of very small fragments close to the

front of the sphere. As impact velocity was increased, the collision became inelastic and

the plug attached to the front of the sphere.

When the impact velocity was higher, the plug experienced stress levels that were

intense enough to cause it to fragment. As impact velocity continued to increase, the

fragmented plug developed into a cloud of finely-divided solid or solid and liquid

material. In the later stages of development, it is probable that the front element is

97

composed of the bumper plug and a small portion of the front of the sphere. Prominence of the front element was a strong function of impact velocity. As shown in Figure 39, the relative size of this element (with regard to the rest of the debris-cloud structure) increased as impact velocity increased from 5.45 km/s to 7.38 km/s. In this figure, note that the leading edges of all three debris clouds are approximately the same distance, $x$, downrange of the bumper. Growth of the front element, as a function of impact velocity, was shown quantitatively in Figure 10.

The nearly constant radiographic density and shape of the front element, for the low $t/D$ ratio tests in Figure 6, would suggest that the materials involved in the formation



| 5.45 km/s | 6.62 km/s | 7.38 km/s |
|-----------|-----------|-----------|
| 4-1394 | 4-1360 | 4-1744 |
| x = 28.8 cm | x = 29.0 cm | x = 31.1 cm |
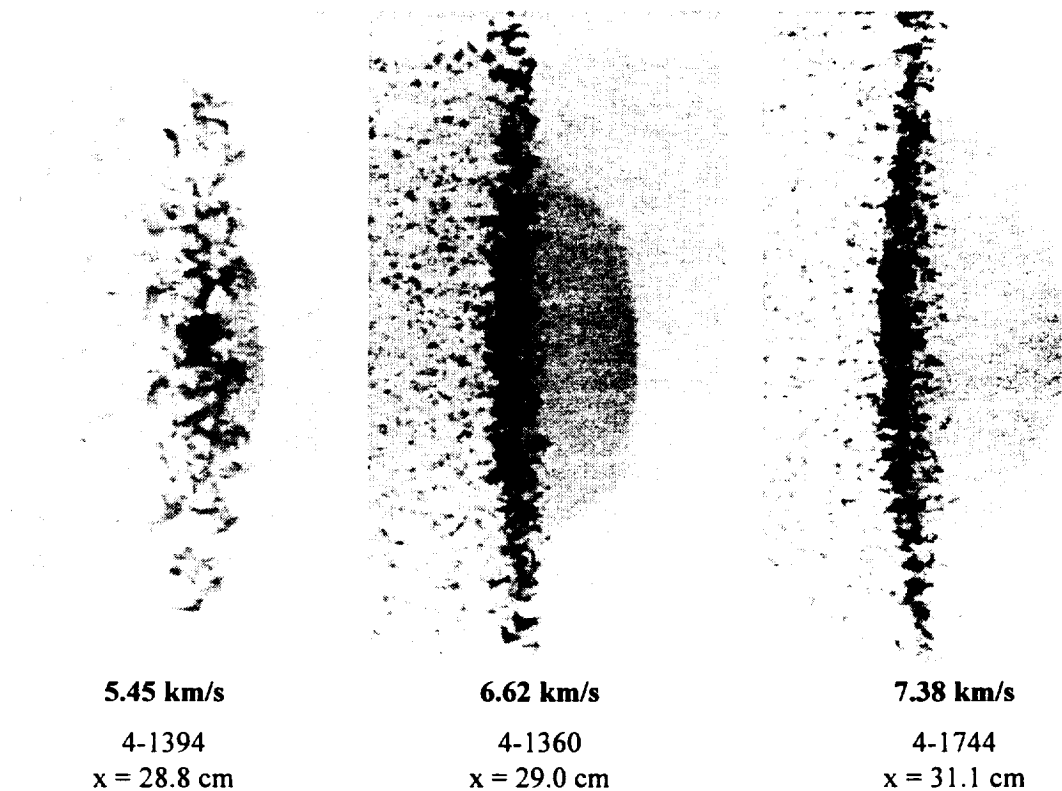
Figure 39. Late-time views of debris clouds produced by the impact of 9.53-mm-diameter, 2017-T4 aluminum spheres with 0.46-mm-thick, 6061-T6 aluminum sheets. These views show an increasingly larger front element as impact velocity was increased. Debris clouds are shown traveling from left to right. In the legend, $x$ is the distance from the front of the bumper to the leading edge of the debris cloud at the time the radiograph was made.

of the front elements of the debris clouds experienced similar shock loading. For the $t/D = 0.049$ tests shown in Figure 9b, the normalized velocity, $V_1/V_0$, of point ① began to increase when the impact velocity was greater than 5.5 km/s. As will be shown later in this section, melting of the material near the sphere/bumper interface should begin when the impact velocity reaches 5.7 km/s. Once melting occured, only surface tension forces needed to be overcome for the material in this region to divide into a cloud of very fine droplets. For tests with $t/D$ ratios of less than 0.1, the lens-shaped region that experienced quasi one-dimensional loading made up almost all of the bumper plug that subsequently developed into the front element. As a result, the intensity of the shock loading and the extent of melting in this region should be similar for tests with $t/D$ ratios of 0.1 or less and similar impact velocities. Consequently, dispersion of the melted material into elements with similar shapes and radiographic density was not surprising.

The normalized velocity of point ① for the test at 7.38 km/s (Shot 4-1744) was 1.031. Similar velocity ratios were obtained for the tests with $t/D$ ratios of 0.026 and impact velocities of 6.54 and 6.70 km/s (Shots 4-1392 and 4-1395). Calculations made using rigorous one-dimensional, shock-wave analysis programs indicated that the free-surface velocity of a semi-infinite, thin aluminum plate impacted by a semi-infinite thick aluminum plate would be about 2.5 percent greater than the impact velocity. In the calculations, strength of the impacted material was not a consideration. As the strength of the impacted bumper sheet was reduced by melting, it was not surprising that the free surface velocity of the bumper increased to the value computed with use of the shock-wave analysis program.

For the debris clouds with the higher $t/D$ ratios (see Figure 6), increasingly larger volumes of material were involved in the formation of the front element. In Figure 6, the shape of the front element changed from a truncated cone, for the tests with $t/D$ ratios of 0.102 or lower, to a spherical sector for tests with $t/D$ ratios of 0.163 and 0.234. It did not

exist for the test with a *t/D* ratio of 0.424. As *t/D* ratio was increased. the material in the front element was derived from regions where the shock interactions were complicated and where stresses were lower. The reduced intensity of the shock in the material nearer the free surface of the bumper and the relatively short duration of the shock pulse in this region combined to promote the production of larger fragments in the front element. It is probable, therefore, that impacts of spheres with thick plates will always produce solid fragments at the leading edge of the front element, even for tests in which the impact velocities were high enough to melt and/or vaporize material at the sphere/bumper interface.

The radiographs of the debris clouds from the tests in this study do not clearly illustrate the distribution of bumper and projectile material in the front element. Close examination of the radiographs, particularly those from the tests with lower *t/D* ratios, does reveal that the radiographic density of the leading edge of the front element was greater than the rest of this element. It is probable that the increased density in this region was due to an increase in the concentration of material near the leading edge. The late-time view radiographs from one of these tests, Shot 4-1282, is shown in Figure 40.

Experimental evidence to support or reject the assumption that the front-element mass was concentrated near the leading edge was not obtained during this study. However, tests were performed at UDRI in the late 1960's to examine the distribution of material in debris clouds [37]. In these tests, a curved dissector plate was used to capture all but a narrow "slice" of a debris cloud produced by the impact of a sphere with a bumper sheet placed a short distance uprange of the dissector plate. A 12.7-mm-wide slot in the dissector plate allowed a strip or "slice" of the debris cloud to pass through the plate and be viewed with flash x-rays. An illustration of the dissection technique and a radiograph from one of the 1960's tests (with a *t/D* ratio of 0.25) is shown in Figure 41. Before its dissection, the debris cloud was identical to the debris cloud in the multiple-view
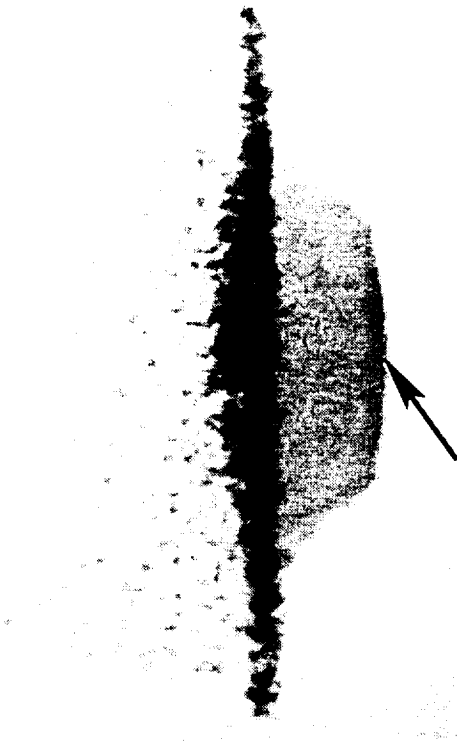
Figure 40. Late-time view of Shot 4-1282, showing the increased density of material at the leading edge of the front element, indicating a heavier concentration of bumper debris in this region (arrow). Debris cloud was produced by the impact of a 9.53-mm-diameter, 2017-T4 aluminum sphere with a 0.51-mm-thick, 2024-T3 aluminum sheet ($t/D = 0.053$).

radiograph also shown in Figure 41 (Shot 4-1352, $t/D = 0.234$). The radiograph of the "slice" clearly shows two layers of material at the front of the debris cloud. Material in the front element of the cloud is concentrated at the leading edge of the element. It is probable that the front elements of the debris clouds from tests with $t/D$ ratios of 0.25 or less would show that the material in the front element was concentrated at the leading edge of the element.

2. Center Element. The center element contained the heaviest concentration of projectile fragments. In general, it is a disk-like component of the debris-cloud internal structure and was oriented with its axis coincident with the shot-line axis. The center element was composed of a large central fragment surrounded by numerous smaller fragments.
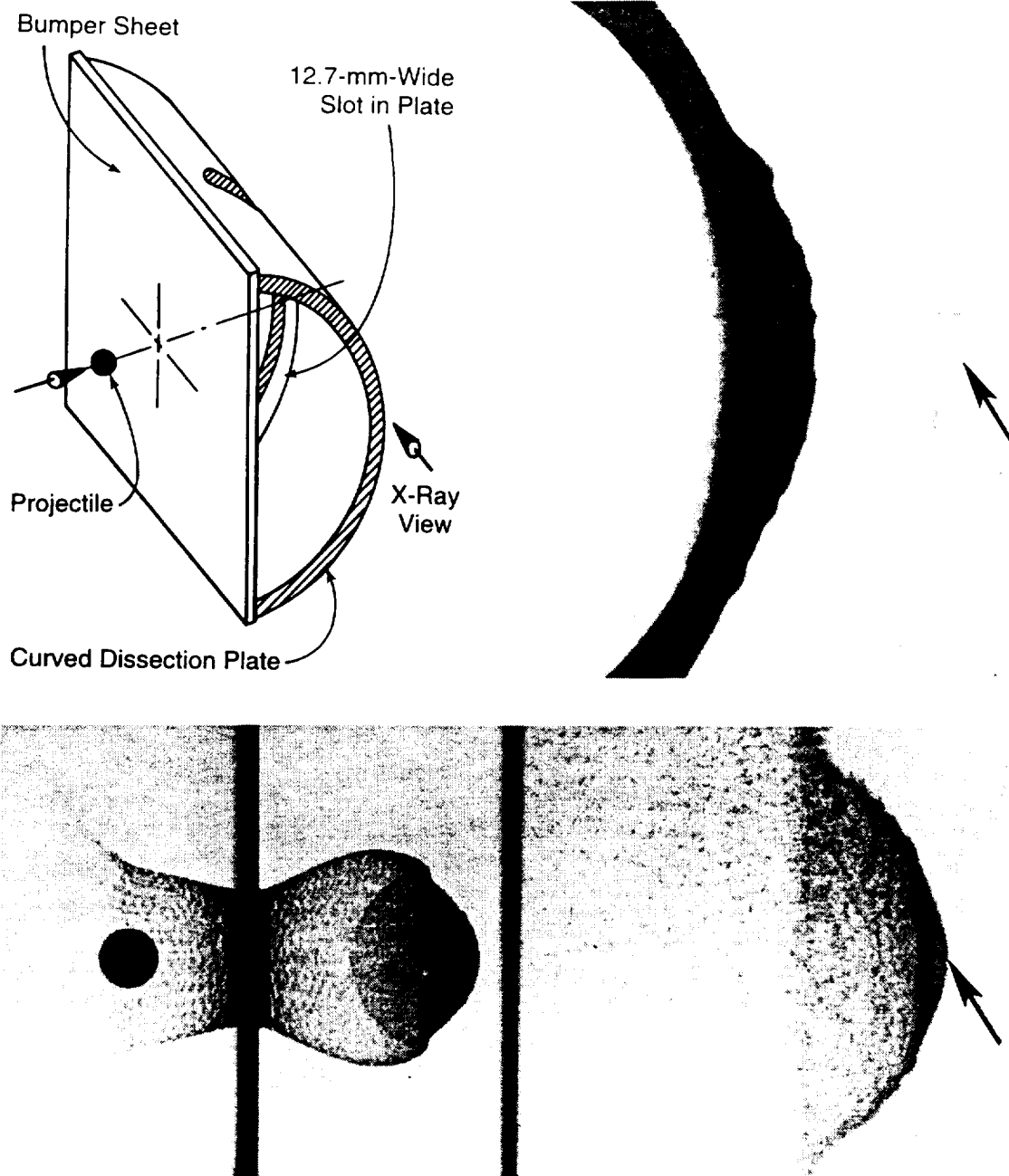
Figure 41. Illustration of the technique used to dissect a debris cloud, a radiograph of a "slice" produced using this technique, and a multiple-view radiograph of a debris cloud produced by a test with a $t/D$ ratio of 0.234 (Shot 4-1352). The radiograph at upper right clearly shows two layers of material at the front and center of the "slice." Material in the front element was concentrated at the leading edge of this element (arrow). The "slice" was taken from a debris-cloud produced by the impact of a 6.35-mm-diameter aluminum sphere with a 1.60-mm-thick aluminum sheet ($t/D$ = 0.25) at 7.13 km/s (Shot 2660, [37]).

Views of the center elements from four debris clouds are presented, in Figure 42, for tests in which the impact velocity was held constant and the $t/D$ ratio was varied. In these debris clouds, the center-element fragments and the large central fragments (arrow) decreased in size as $t/D$ ratio increased. Center-element fragment shapes ranged from flaky to comma-shaped slivers to chunky. In a second set of late-time-view radiographs of four debris clouds, presented in Figure 43, the shapes of the center-element fragments are shown to change from large flakes (Shots 4-1433 and 4-1621) to large slivers (Shot 4-1360) to a mixture of small slivers and chunky fragments (Shot 4-1289). These changes in the shape of the center-element fragments occurred as $t/D$ ratio and impact velocity were increased. In debris clouds with large central fragments, the large fragments tended to be chunky when the $t/D$ ratio and impact velocity were low and disk-like when the $t/D$ ratio and impact velocity were high.



| $t/D = 0.026$ | $t/D = 0.062$ | $t/D = 0.084$ | $t/D = 0.102$ |
| 6.70 km/s | 6.78 km/s | 6.68 km/s | 6.72 km/s |
| 4-1395 | 4-1359 | 4-1289 | 4-1283 |
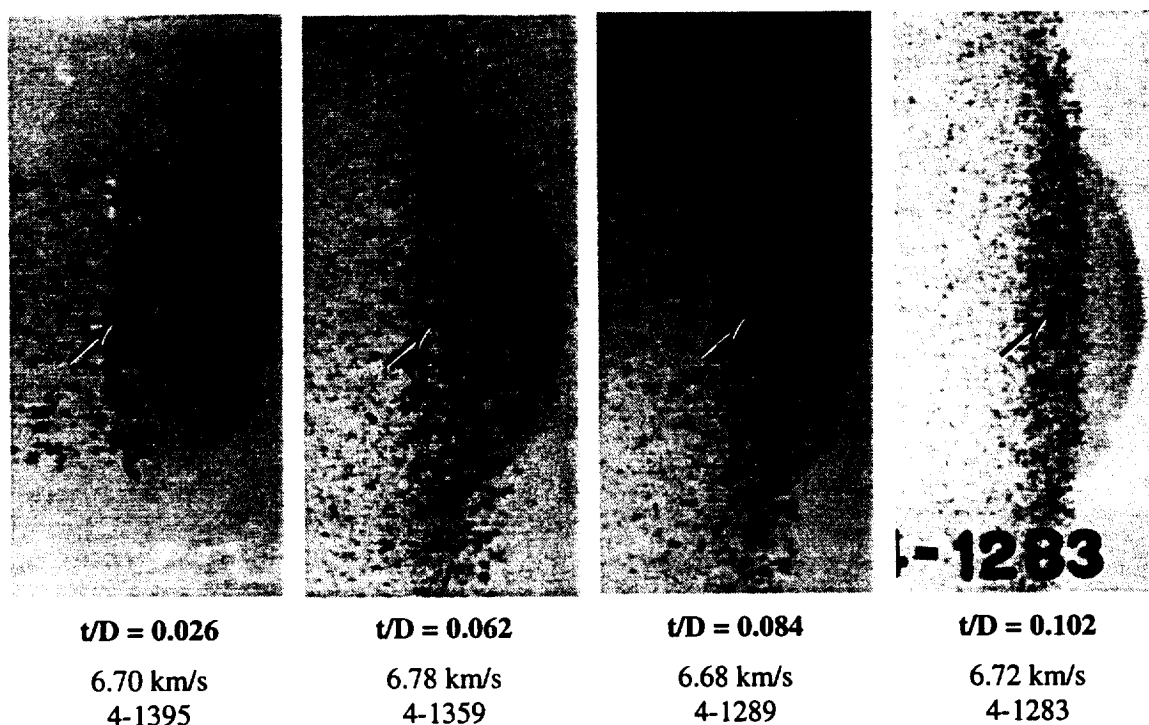
Figure 42. Views of the center element and large central fragment for tests in which impact velocity was held constant and the $t/D$ ratio was varied.

| 4-1289 | 4-1360 | 4-1621 | 4-1433 |
|--------|--------|--------|--------|
| 6.68 km/s | 6.62 km/s | 4.62 km/s | 4.71 km/s |
| t/D = 0.084 | t/D = 0.049 | t/D = 0.084 | t/D = 0.049 |
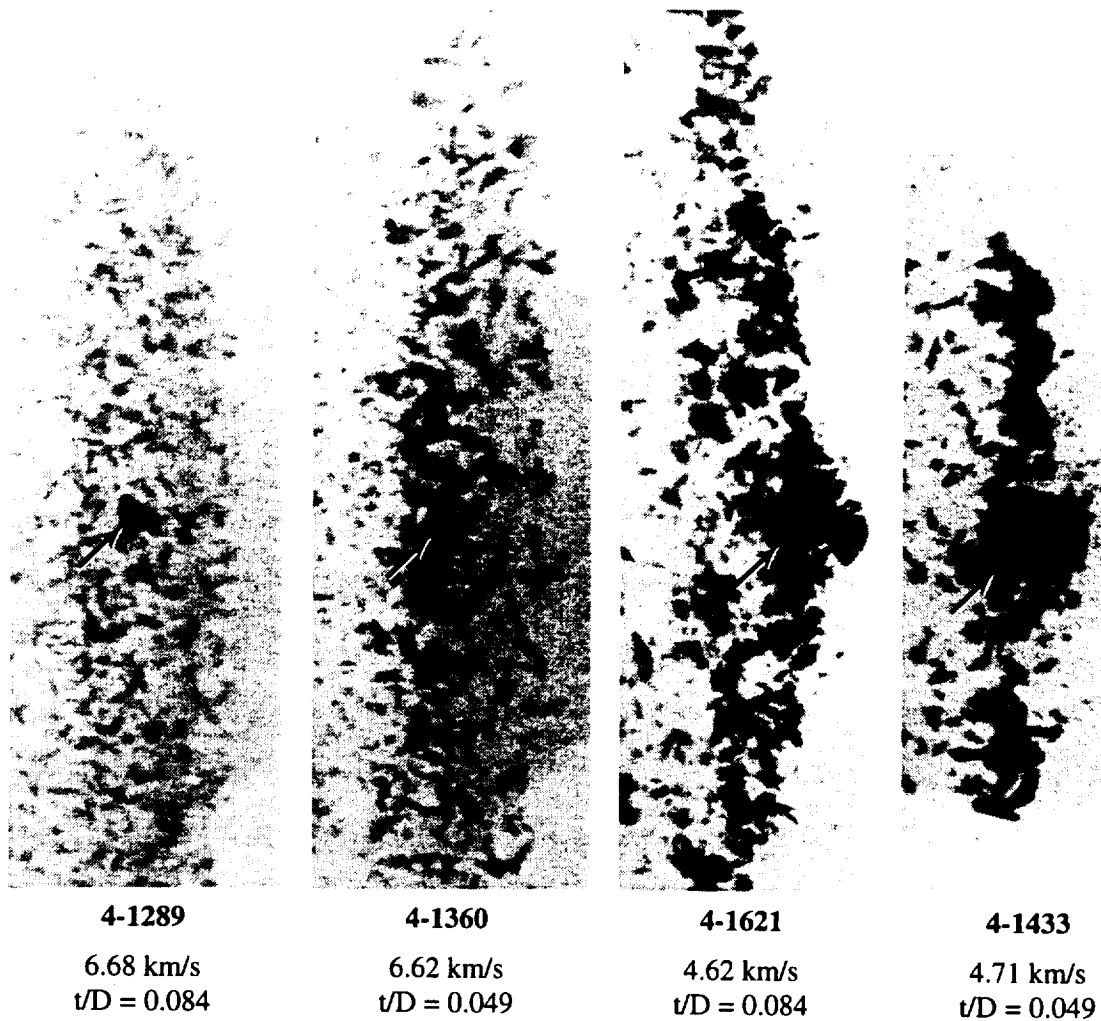
Figure 43. Radiographs of the center element of four debris clouds, showing the effect of impact velocity and $t/D$ ratio on center-element-fragment size and shape. All debris clouds were produced by the impact of 9.53-mm-diameter, 2017-T4 aluminum spheres with 6061-T6 aluminum sheets.

The center-element fragments appeared to be formed by the coalescence of shear failures that developed in the sphere as a result of the compressive loads applied to the sphere at impact. As the sphere disintegrated, the fragments that formed the center element dispersed, following trajectories that were at a wide range of angles to the original line of flight of the sphere. The axial-velocity component of the center-element fragments was less than the impact velocity of the sphere (see $V_2/V_0$ in Table 4, Section III). Their normal or radial-velocity component varied directly with distance from the shot-line axis,

104

with the largest radial-velocity component belonging to the fragments at the periphery of the center-element disk. For the tests with lower $t/D$ ratios, the profile of the center element (as seen in the normal-view radiographs) indicated that the center-element fragments were confined to a disk-like structure that was relatively flat at the front and slightly tapered at the rear, decreasing in thickness as it approached the periphery of the disk. An implication of the flat-faced-disk configuration is that all fragments at the front of the center element have the same axial velocity. Late-time views of the three higher velocity tests in the series of $t/D = 0.049$ tests (see Figure 7) were presented in Figure 39. In Figure 39, the normal-view radiographs for the 6.62- and 7.38-km/s tests showed that the center-element profile changed from nearly flat faced at 6.62 km/s to chevron shaped at 7.38 km/s. Analysis of the radiographs for the 7.38-km/s test (Shot 4-1744) indicated that the axial velocity of points ⑨ and ⑩ was about 0.08 km/s faster than that of point ②; the same analysis for the 6.62-km/s test (Shot 4-1360) showed that the axial velocity of points ⑨ and ⑩ was about 0.09 km/s slower than that of point ②. The observed velocity differences were within the estimated error for the determination of the absolute velocity of the points. While the magnitude of the dynamics of the motion of the center-element fragments was too subtle to be resolved in the radiographs, differences in the profile of the center element were observed as impact velocity changed.

Study of the radiographs from the tests with low $t/D$ ratios could suggest that the center-element fragments of all debris clouds would form disk-like structures were it not for the influence of external forces acting on them during their expansion. Primary sources for these external forces are: (1) the external bubble of debris and (2) the edge of the hole evolving in the bumper sheet. An enlarged radiograph of a sphere, taken 0.9 μs after impact, is shown in Figure 44. A view of the debris cloud formed by this sphere, taken 19.5 μs after impact, is also shown in Figure 44. (A late-time-view radiograph of the same debris cloud, made 44.9 μs after impact, was shown in Figure 8.) The enlarged

**0.9 μs**                                    **19.5 μs**

Figure 44. Radiographs of a deformed sphere and the debris cloud produced by the expansion of the fragments of the sphere. The time shown below each radiograph is the time, after impact, of the exposure. The $t/D$ ratio for this test was 0.053.

radiograph shows: (1) the sphere has experienced significant deformation of its front surface; (2) a very small external "bubble" of debris attached to small "horns" on the sphere and to the downrange side of the bumper sheet; and (3) a small ejecta veil on the impact side of the sheet. The second view of the debris cloud shows a fully-developed debris cloud in which the center-element fragments have formed a flat-faced-disk structure. The development of this debris cloud occurred with minimal interference of the external bubble and, as shown in the early-time view, with little involvement of the edge of the hole in the bumper sheet.

The internal structure and the external bubble of debris are shown for six tests in Figure 45. In these tests, the impact velocity was held constant at 6.7 km/s and the $t/D$ ratio varied from 0.026 to 0.163. The radial velocity of the center-element fragments increased with increasing $t/D$ ratio and impact velocity. The rate of increase in the diameter

106

t/D = 0.026
6.78 km/s
4-1395

t/D = 0.049
6.62 km/s
4-1360

t/D = 0.062
6.78 km/s
4-1359

t/D = 0.084
6.68 km/s
4-1289

t/D = 0.102
6.72 km/s
4-1283

t/D = 0.163
6.71 km/s
4-1291
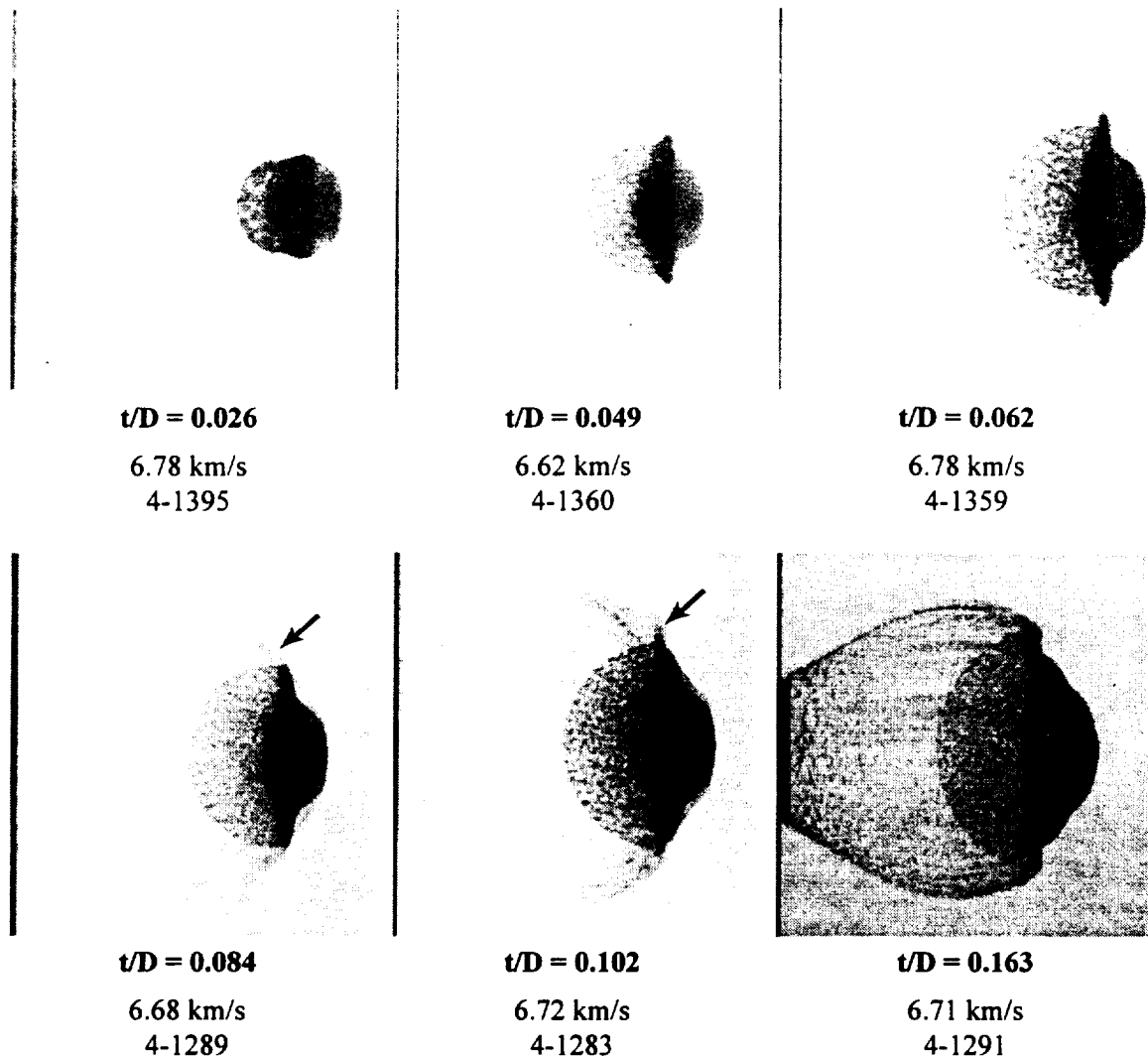
Figure 45. Views of the internal structure and the external bubble of debris formed by the impact of 9.53-mm-diameter, 2017-T4 aluminum spheres with various thicknesses of 6061-T6 aluminum sheet, showing the effects of interference of the center element with the external bubble of debris.

of the center element, $V_{9-10}$, was shown previously in Figure 11 (Section III) as a function of $t/D$ ratio and impact velocity. In Figures 11 and 45, significant increases in the diameter of the center element were observed for small changes in the $t/D$ ratio. Uninhibited growth of the center element appeared to stop when the $t/D$ ratio was between 0.062 and 0.084. Evidence of a collision of the periphery of the center element with the external bubble was first observed when the $t/D$ ratio was 0.084. A significant distortion of the outer portion of the center element and a disruption of the external bubble of debris

107

occurred for the test with a $t/D$ ratio of 0.102. In the debris clouds for both tests, however, a small part of the external bubble was still evident on either side of the front element.

The alteration of the shape of the periphery of the center element, for the tests with $t/D$ ratios of 0.084 and 0.102, was the result of a collision of the rapidly expanding disk of projectile fragments with the external bubble of debris. When the $t/D$ ratio was 0.163, most of the outer portion of the center element was distorted, folded back, and coincident with the leading edge of the external bubble of debris. As shown in Figure 41, the center element of Shot 4-1352 ($t/D = 0.234$) was also distorted and folded back. The "slice" of the dissected debris cloud, also shown in Figure 41, exhibited a fairly abrupt change in the density of the leading edge in the region where the center element, spall shell, and external bubble of debris met. Since the sectioned debris cloud's $t/D$ ratio was 0.250, it is reasonable to assume that a similar meeting of these features occurred for Shot 4-1352. The first-view radiographs of the debris clouds for the $t/D = 0.163$ and 0.234 tests also showed that the spall shell extended beyond the center element but was confined by the external bubble of debris.

An implication of the observations made in the previous paragraphs is that the radial velocity of the fragments in the center element will continue to increase as $t/D$ ratio is increased. However, growth of the center element will be impeded by its interaction with the external bubble of debris and the edge of the hole in the bumper sheet. A test was performed to examine growth of the center element for that case where the external bubble of debris and the edge of the bumper-sheet hole did not affect the debris-cloud formation process. In the test, an 11.12-mm-diameter, 1.55-mm-thick disk ($t/D = 0.163$) of 6061-T6 aluminum sheet was held at the center of a large hole in an aluminum sheet by small strips of Mylar film, as shown in Figure 46. The aluminum sheet was used to position the disk in the target chamber. Four brass fiducial pins were pressed into the front of the aluminum sheet and used, during analysis of the radiographs from the test, to
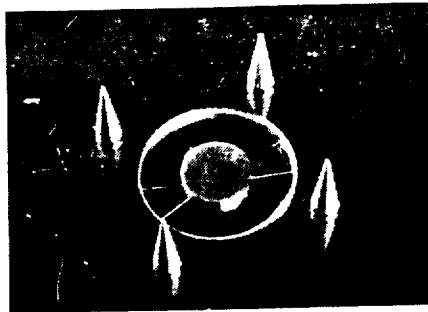
Front of Target

Rear of Target

**Test Setup Showing Location of X-Ray Film and Impact Site on Disk Target**

X-Rays (Top View)

Side-View Film

3.56 mm

0.67 mm

Center of Target

Shot Line

Projectile

11.12-mm-Diameter Target Disk

Top-View Film

X-Rays (Side View)
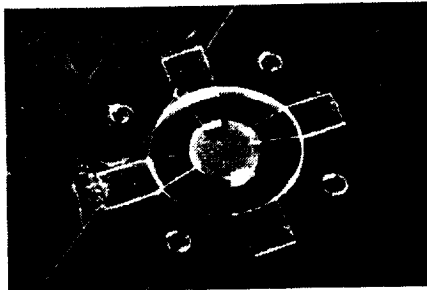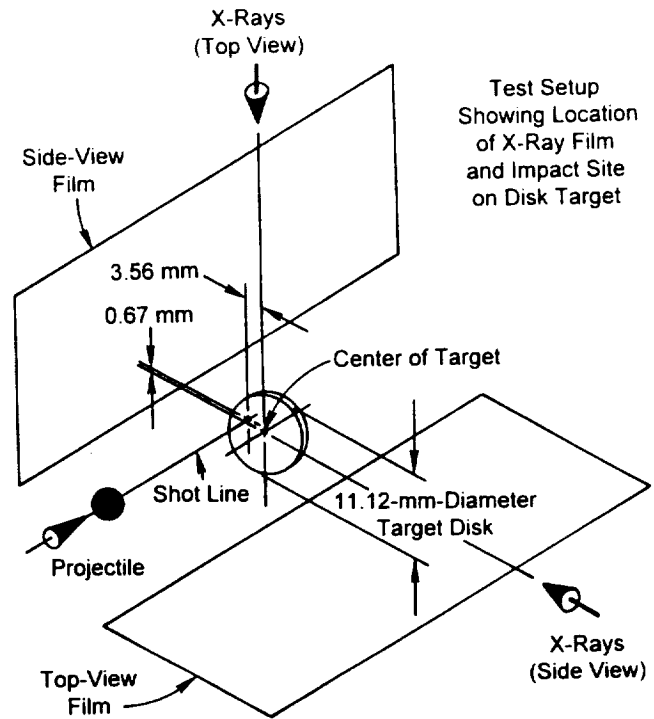
**Side View**

**Projectile:**
9.53-mm-diameter, 2017-T4 aluminum sphere

**Target:**
11.12-mm diameter, 1.55-mm-thick, 6061-T6 aluminum disk

**Impact Velocity:**
6.57 km/s

**Top View**
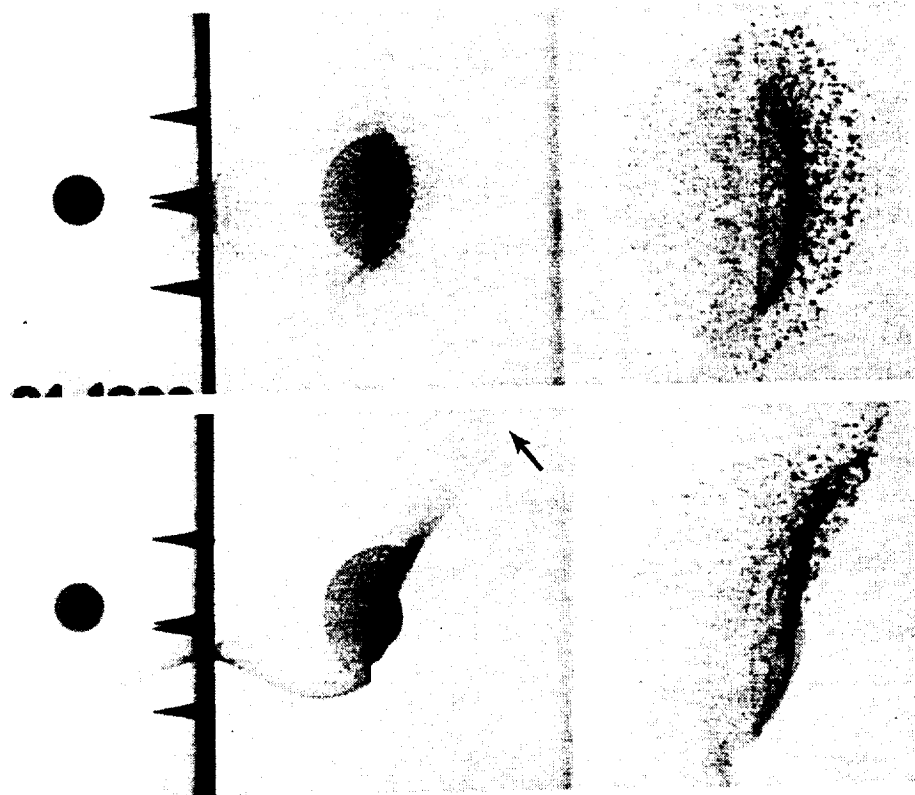
Figure 46. Test setup, target, and flash radiographs from a test using a disk target (Shot 4-1300). The diameter of the disk and the location of the impact site are exaggerated in the illustration of the test setup.

109

determine the precise location of the impact site of the sphere with respect to the center of the target disk. The radiographs of the debris cloud produced by the impact of a 9.53-mm-diameter, 2017-T4 aluminum sphere and an illustration showing the location of the impact site of the sphere with the disk target are also presented in Figure 46.

The impact site of most of the spheres used in the tests was within 3 mm of the range center line. Selection of a target disk whose diameter was slightly larger than the sphere used for the test provided an opportunity for an impact that would occur near the edge of the disk. If the radial velocity of the center-element fragments was altered by interference with the external bubble of debris or the edge of the hole, use of an off-center impact and the disk target provided a means of evaluating center-element growth in an environment free of these two influences. The portion of the debris cloud formed in the region where the impact was closest to the edge of the disk should not exhibit an external bubble of debris. Additionally, the design of the target assembly prohibited contact of the evolving center element with the edge of the hole in the bumper sheet. As shown in the radiographs, the impact occurred within 2 mm of the edge of the disk. Fortuitously, the shot-line axis and the target center line were nearly coincident in the side-view radiograph.

Although the debris cloud produced by the test was different than one formed under normal circumstances, it does provide considerable insight into the debris-cloud formation process. The diameter of the lens-shaped region of the sphere that experienced quasi one-dimensional loading was about 5.33 mm (see Figure 37). A small portion of this region extended beyond the edge of the target since the impact occurred 2 mm from the edge of the target. This difference in the superposition of the lens-shaped region and the corresponding disk of target material probably had some effect on the impact-induced stresses in the sphere. However, the normal development of the spall shell would indicate that the stress pulse developed in the sphere was relatively unaffected by the configuration of the target. Since the "surface" defined by the leading edge of the debris-cloud fragments

was distorted or warped, some care was required during the interpretation of the radiographs from this test. In the top-view radiograph, the upper portion of the debris cloud showed a center element composed of fragments whose radial velocity was considerably larger than the radial velocity of the center-element fragments in the lower or "normal" portion of the debris cloud. In addition, the axial velocity of the fragments in the upper portion of the debris cloud (the larger fragments at the leading edge of the debris cloud in the side view) was about 4 percent greater than the impact velocity of the sphere. The axial velocity of small fragments at the tip of the "rooster tail" (arrow in top view) was at least 12 km/s. The production of fragments with velocities in excess of the impact velocity may result from an interaction of a portion of the impacting sphere with material spalled from the edge of the target disk. Under normal impact conditions, these materials would be part of the lens-shaped region subjected to quasi one-dimensional loading. Finally, the formation of an ejecta veil and an external bubble of debris at the opposite edge of the target disk are features worth noting, particularly when evaluating the effect of boundaries on the debris-cloud formation process.

Comparison of several of the velocity-measurement points from a test using a sheet-target (Shot 4-1291, $t/D$ = 0.163) with their counterparts from Shot 4-1300 indicated that the axial velocities of point ② were essentially the same. The axial velocities of points ① and ④ were lower and higher, respectively, for the disk-target test. The radial expansion velocity of the spall-shell fragments was slightly lower for the disk-target test. In general, the properties of the debris cloud produced using the disk target appeared to be more like those for a debris cloud formed using a sheet that was slightly thinner than the disk.

The results of the disk-target test indicated that the radial velocity of the fragments in the outer regions of the center element continued to increase as the $t/D$ ratio of the test increased. Interaction of these fragments with the external bubble of debris and/or the edge of the hole in the bumper sheet affected their axial- and radial-velocity

111

components and changed the shape of the center element. Interaction of the center element with the bumper sheet, during evolution of the hole in the sheet, played a role in the development of the structure observed in the micrographs of the bumper-sheet sections presented in Section V. Further discussion and an illustration of the effects of this interaction on the bumper sheet are presented in Part D of this section.

As the impact-induced shock propagated through the sphere (prior to formation of the spall layer), shocked material at the front of the sphere traveled at a lower velocity than the material at the rear of the sphere. The tendency for the rear of the sphere to overtake the front of the sphere produced a consistent pattern of rotation of the newly-formed, center-element fragments as the debris cloud developed. Rotation of the fragments at the periphery of the center element is shown in Figure 47 for a test which produced comma-shaped fragments (Shot 4-1358). As shown in this figure, the ends of the fragments that were originally near the front of the sphere rotated toward the outside of the element. The angular velocity of the fragments was on the order of $6.3 \times 10^4$ radians per second. The energy required to produce this rotation of the fragments represented a sink for some of the energy released by the impact.

In Shot 4-1433 (Figure 43) and Shots 4-1632 and 4-1719 (Figure 34), the center element and the spall shell were shown in the early stages of development. For these tests, a significant portion of the central part of the sphere remained intact after the impact and formed the large central fragment. Examination of the radiographs of other debris clouds indicated that the large central fragment originated near the center of the sphere. It was probable that the large central fragment observed in the debris clouds was a piece of the sphere (derived from the near the center of the sphere) that remained intact after the fracture and fragmentation phases of debris-cloud formation were complete.

The expansion velocity, $V_r$, of the spall-shell fragments was an indicator of the intensity and duration of the shock-induced stress pulse in the projectile. When the

**7.5 μs**     **21.6 μs**     **31.4 μs**
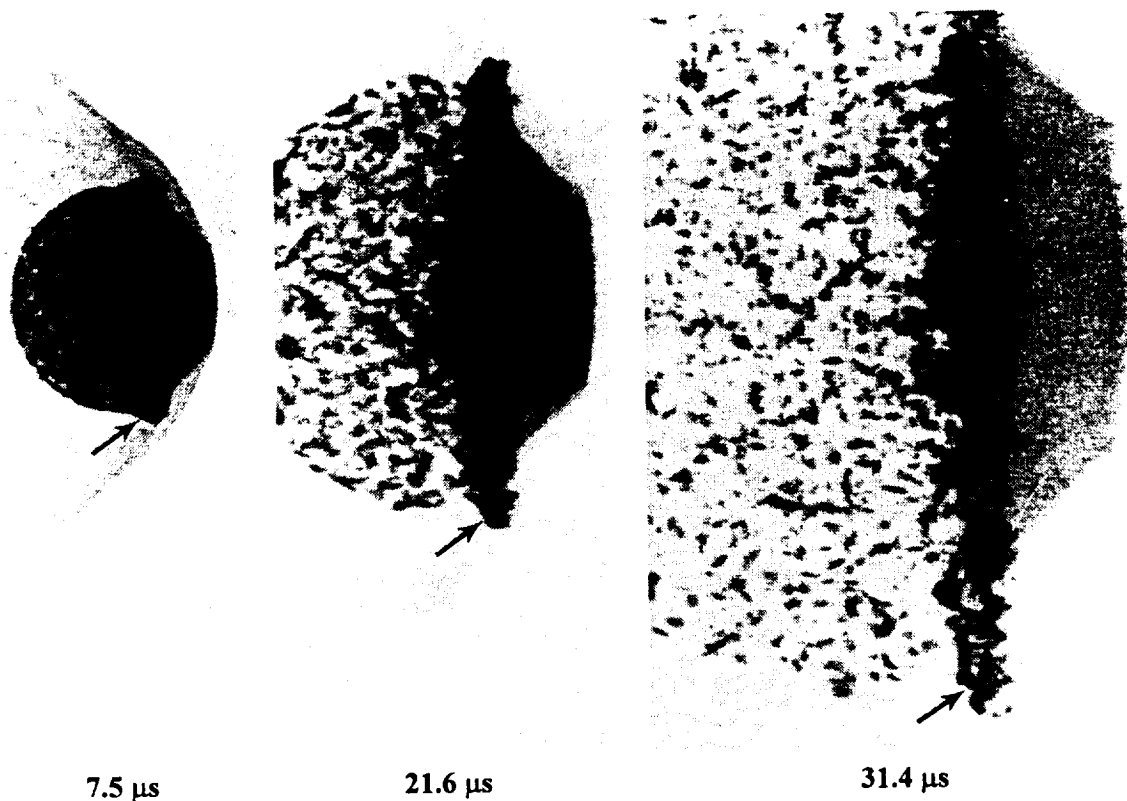
Figure 47. Sequence of radiographs showing the rotation of center-element fragments at various times after impact. Debris cloud was formed by the 6.26 km/s impact of a 12.70-mm-diameter, 2017-T4 aluminum sphere with a 0.59-mm-thick, 6061-T6 aluminum sheet (Shot 4-1358, $t/D = 0.047$).

normalized large-central-fragment diameter, $d_f/D$, and the normalized spall-shell-radial-expansion velocity, $V_r/V_0$, were divided by appropriate, normalized reference diameter and velocity ratios, the new diameter and velocity ratios can be used to indirectly relate the large-central-fragment equivalent diameter to the strength of the shock pulse. The normalized large-fragment diameter and spall-shell radial velocity were used to form the new ratio, instead of the actual fragment diameter and spall-shell velocity, to provide a larger set of data for use in the comparisons by accommodating the differences in sphere diameter and the slight variations in impact velocity in the data set. Table 12 presents a set of these ratios for tests with a nominal impact velocity of 6.7 km/s and a range of $t/D$ ratios. The normalized large central-fragment diameter and spall-shell-radial-expansion

113

# TABLE 12

## NORMALIZED LARGE-CENTRAL-FRAGMENT-DIAMETER AND SPALL-SHELL-EXPANSION-VELOCITY RATIO DATA FOR SELECTED TESTS

All projectiles were 2017-T4 aluminum spheres. Bumper sheet materials and sphere diameters were as noted. The nominal impact velocity for these tests was 6.7 km/s.

| Shot Number | $\dfrac{t}{D}$ | Impact Velocity, (km/s) | $\dfrac{d_f}{D}$ | $\dfrac{d_f/D}{(d_f/D)_{Ref}}$ | $\dfrac{V_r}{V_0}$ | $\dfrac{V_r/V_0}{(V_r/V_0)_{Ref}}$ |
|---|---|---|---|---|---|---|
| 1100-O Aluminum Bumper, $D$ = 6.35 mm |
| 4-1318 | 0.048 | 6.64 | 0.425 | 6.343 | 0.111 | 0.414 |
| 1100-O Aluminum Bumper, $D$ = 9.53 mm |
| 4-1290 | 0.032 | 6.67 | 0.499 | 7.448 | 0.079 | 0.294 |
| 2024-T3 Aluminum Bumper, $D$ = 9.53 mm |
| 4-1284 | 0.053 | 6.58 | 0.363 | 5.418 | 0.128 | 0.478 |
| 2024-T3 Aluminum Bumper, $D$ = 12.70 mm |
| 4-1281 | 0.040 | 6.46 | 0.432 | 6.448 | 0.091 | 0.339 |
| 4-1357 | 0.160 | 6.38 | 0.086[a] | 1.284 | 0.293 | 1.093 |
| 6061-T6 Aluminum Bumper, $D$ = 9.53 mm |
| 4-1392 | 0.026 | 6.54 | 0.588 | 8.776 | 0.064 | 0.239 |
| 4-1395 | 0.026 | 6.70 | 0.576 | 8.597 | 0.063 | 0.235 |
| 4-1360 | 0.049 | 6.62 | 0.309[a] | 4.612 | 0.118 | 0.440 |
| 4-1359 | 0.062 | 6.78 | 0.312 | 4.657 | 0.142 | 0.530 |
| 4-1289 | 0.084 | 6.68 | 0.213 | 3.179 | 0.187 | 0.698 |
| 4-1283 | 0.102 | 6.72 | 0.152 | 2.269 | 0.208 | 0.776 |
| 4-1291 | 0.163 | 6.71 | 0.115[a] | 1.716 | 0.283 | 1.056 |
| 4-1352 | 0.234 | 6.64 | 0.067[b] | 1.000 | 0.268 | 1.000 |
| 6061-T6 Aluminum Bumper, $D$ = 12.70 mm |
| 4-1358 | 0.047 | 6.26 | 0.432 | 6.448 | 0.104 | 0.388 |

[a] Dimensions of large central fragment were only available from one view.

[b] Average diameter of fragments that were selected at random in radiographs. See Figures 6 and 41 for views of the debris cloud for this test. Fragments selected for measurement were at the outside-front portion of the cloud.

velocity for each of these tests was divided by the normalized large-central-fragment diameter, $(d_f/D)_{Ref}$, and spall-shell-radial-expansion velocity, $(V_r/V_0)_{Ref}$, respectively, for Shot 4-1352. Ratios for Shot 4-1352 were chosen as the reference normalizing values because the $t/D$ ratio for this test was large enough that the characteristics of the stress pulse in the sphere were no longer influenced by the thickness of the bumper sheet. The

114

use, as the reference normalizing value, of normalized values from tests with other $t/D$ ratios would slightly change the values of the ratios shown in Table 12. However, their use would not affect the linearity of the relationship between the normalized large-fragment-diameter ratio and the normalized spall-shell-velocity ratio shown in Figure 48. The effects of differences in the diameter of the spherical projectiles, the alloy of the bumper sheet, and the differences between the actual test velocities and the nominal impact velocity of 6.7 km/s were not reflected in the data presented in the figure. When the $t/D$ ratio was very low ($< 0.026$), an impact velocity of 6.7 km/s could approach or be in the transition region above the spall-failure-threshold velocity. The diameter ratios for these very low $t/D$-ratio tests would lie above the line shown in Figure 48. When the impact velocity is at or below the spall-failure-threshold velocity, the velocity ratio will be zero and the diameter ratio will have a value of 14.9, (or the inverse of the normalized
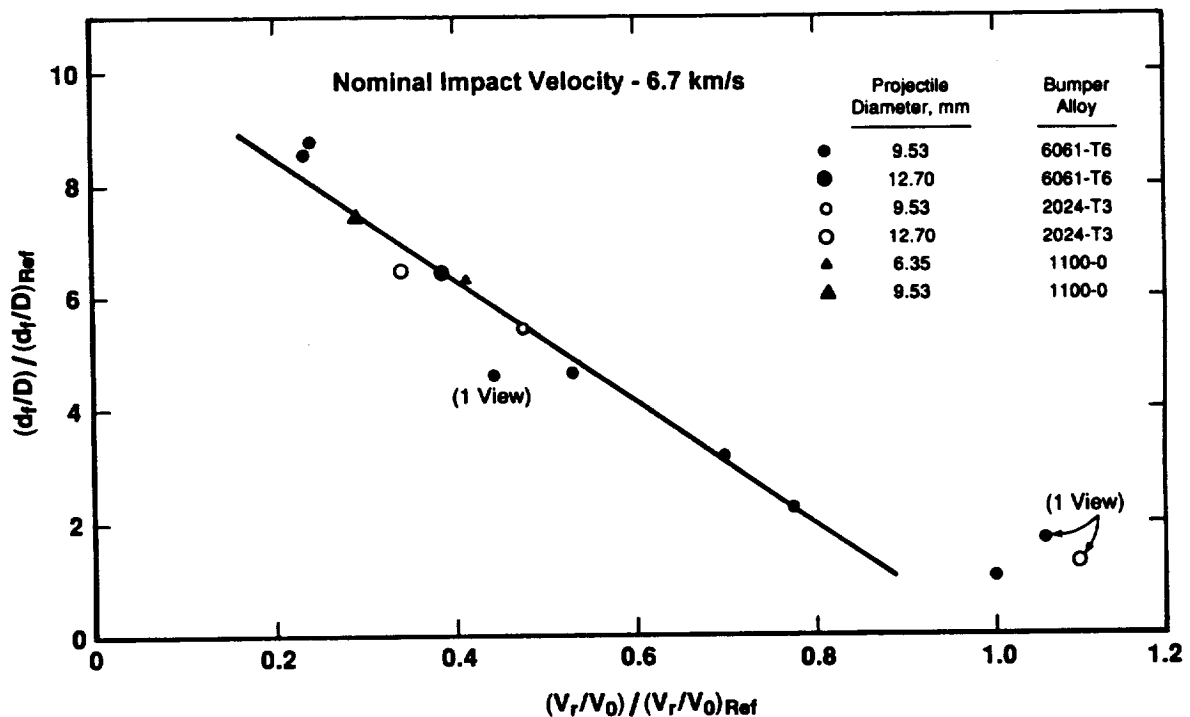


Figure 48. Normalized large-fragment-diameter ratio as a function of normalized spall-shell-velocity ratio for impacts at 6.7 km/s.

-fr___nt diameter used as the reference normalizing value). When the $t/D$ ratios

large (or near the $t/D$ ratio of the test used to provide the reference normalizing

:s), the diameter ratio was near unity. For the range of test conditions examined in

re 48, the diameter of the large central fragment appeared to be indirectly related to

mpact-induced stress pulse in the sphere, at least as manifested by the effects of its

sity and duration on the spall-shell expansion velocity. Major test-to-test variations

: large central fragment diameter were probably the result of errors and experimental

rtainties (overlapping, etc.) in the determination of the dimensions of this fragment.

3. Rear Element (Spall Shell). The spall shell is formed when microfractures at

ear of the sphere coalesce and facilitate the disintegration of a layer of material

:d from the rear surface of the sphere. The microfractures develop below the rear

ce of the sphere following the intersection of the impact-induced stress pulse and the

se wave formed when the shock was reflected at the free surface of the sphere. The

tati___ each microfracture is perpendicular to the principal stress that produced it.

iown in Figure 32, the incident shock-front intersects the periphery of the rear of the

e at continuously varying angles of obliquity. Although the individual micro-

ires form at a variety of angles to the surface of the sphere, they coalesce and form a

layer with an extremely flaky surface but a nearly uniform thickness [38].

ientum trapped in the spall layer pulled the spalled material away from the sphere.

1 excessive momentum was trapped in the spall layer, the layer disintegrated and

:d an expanding shell of fragments. The spall fragments followed trajectories that

normal to the surface of the sphere at the point of origin of the fragment.

The transition from the formation of a simple spall failure to a well-developed

of spall fragments occurred over a narrow range of impact velocities, usually less

500 m/s above the spall-failure-threshold impact velocity. The development of a

of spll fragments, during the transition phase, is shown in the late-time radiographs

presented in Figure 49. Note that both *t/D* ratio and impact velocity were varied for the tests shown in this figure. The radiograph for Shot 4-1428 was presented and discussed earlier in this section (Figure 33). It was included in this series of radiographs to illustrate the first stage in the development of the spall shell — a spall failure inside the rear surface of the sphere. In Shot 4-1633, the spall shell has ruptured and formed petals that remained attached to the deformed sphere. Fragmentation of the spall shell occurred for Shot 4-1632, but the shell of spall fragments was not well developed. Although a rudimentary center element formed for Shot 4-1632, it appeared to consist primarily of spall fragments. Further development of the spall shell is evident in Shot 4-1631, although it is not as fully developed as the shell of fragments shown for Shot 4-1622.

The results of the analysis of the size and size distribution of spall-shell fragments was presented in Section IV. The normalized expansion velocity of the shell of spall



| 3.77 km/s | 3.65 km/s | 3.47 km/s | 3.64 km/s | 3.84 km/s |
|---|---|---|---|---|
| $t/D = 0.049$ | $t/D = 0.062$ | $t/D = 0.084$ | $t/D = 0.084$ | $t/D = 0.084$ |
| 4-1428 | 4-1633 | 4-1632 | 4-1631 | 4-1622 |
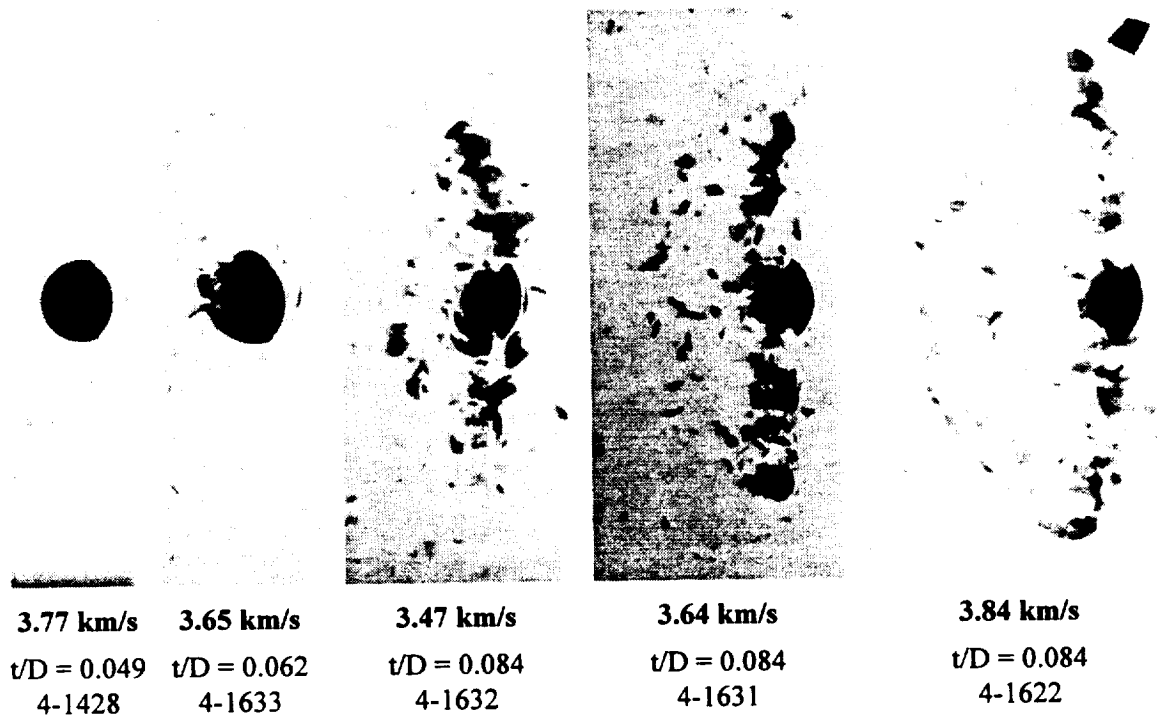
Figure 49. Radiographs showing the development of the shell of spall fragments, during the transition phase, as a function of impact velocity and *t/D* ratio.

117

fragments, $V_r/V_0$, was presented as a function of $t/D$ ratio and impact velocity in Figures 12 and 13, respectively, in Section III.

The expansion velocity of the spall shell was determined by: (1) measuring the radius of a circular arc that defined the perimeter of the shell of fragments in each x-ray view of the debris cloud and (2) dividing the change in the radius of the arc by the time interval between the views. During their construction, the centers of the arcs were placed on the debris-cloud center line. The normalized velocity of the center of the arc, $V_{CTR}/V_0$, was also determined and was presented earlier in Table 4 (Section III). During analysis of the radiographs, it was noted that the location of the center of the arc changed with respect to point ②, the leading edge of the center element. The normalized velocity of the center of the arc is shown in Figure 50 as a function of $t/D$ ratio, for tests with nominal impact velocities of 4.7 km/s and 6.7 km/s. Also shown in the figure, as a dashed line, is the
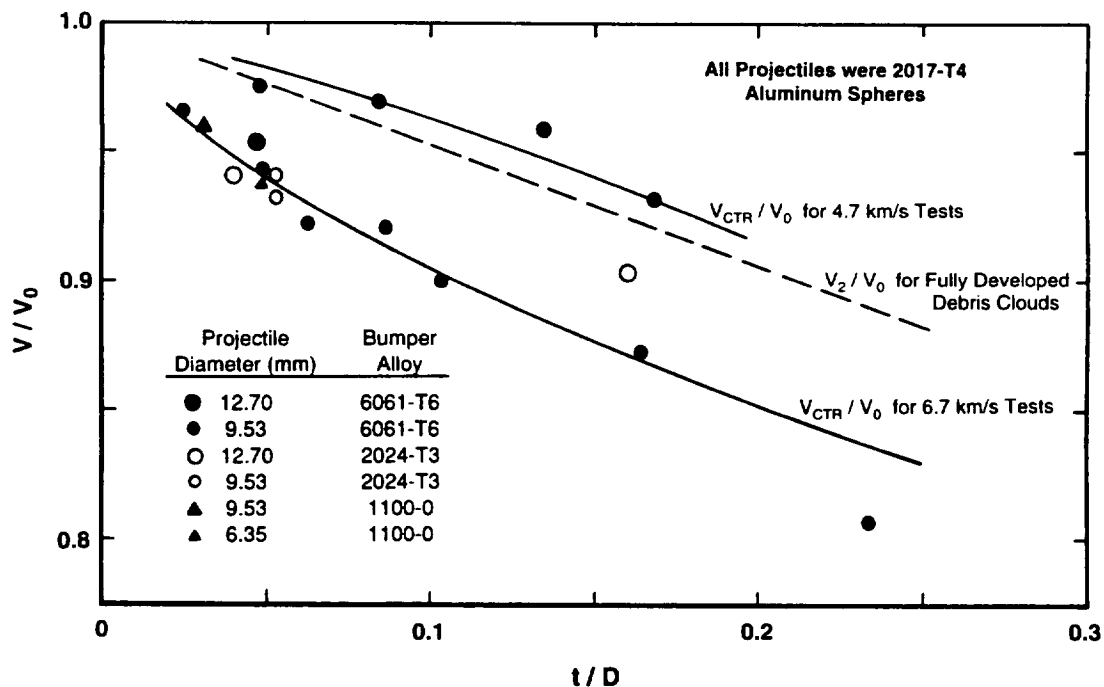


Figure 50. Normalized velocities of the leading edge of the center element and the center of the spall shell for two impact velocities. The velocities are shown for several sphere diameters and bumper-sheet alloys as a function of $t/D$ ratio.

normalized velocity, $V_2/V_0$, of the leading edge of the center element for fully-developed debris clouds. The slight variations in $V_2/V_0$ for each $t/D$ ratio, were averaged during preparation of the figure to facilitate the illustration of the general behavior of this measurement point. Debris clouds were considered to be fully developed when the impact velocity of the test was at least 500 m/s greater than the appropriate spall-failure-threshold impact velocity. As shown in Figure 50, the relationship between $V_2$ and $V_{CTR}$ indicated that the center of the arc was in front of the leading edge of the center element for tests at 4.7 km/s and behind the leading edge of the center element for tests at 6.7 km/s.

The velocity of the individual spall fragments was proportional to the intensity of the shock arriving at the rear surface of the sphere and the momentum trapped in the material spalled from this surface. While a circular arc always described the perimeter of the shell of spall fragments, systematic differences in the velocity of individual spall fragments, due to the effects of $t/D$ ratio and impact velocity, produced shells that were more or less circular with respect to the center of mass of the internal structure of the debris cloud. For purposes of further discussion, the intersection of the leading edge of the center element and the debris-cloud center line (i.e., point ②) will be assumed to be the center of mass of the internal structure of the debris cloud.

The circularity of the spall shell, with respect to the center of mass of the internal structure, was evaluated by comparing the velocity of fragments traveling along the debris-cloud center line with the velocity of fragments traveling normal to the shot-line axis. The spall-shell expansion velocity, $V_r$, was used as the velocity of fragments traveling normal to the shot-line axis. The difference in the velocity of points ② and ④ was used as the velocity of fragments traveling along the debris-cloud center line. The normalized velocity of points ② and ④, the normalized difference between the velocities of points ② and ④, and the normalized spall-shell-expansion velocity are listed in Table 13 for tests employing 9.53-mm-diameter, 2017-T4 aluminum spheres and various thicknesses

# TABLE 13

## SPALL-SHELL-EXPANSION VELOCITY DATA

All projectiles were 9.53-mm-diameter, 2017-T4 aluminum spheres.
All bumpers were 6061-T6 aluminum sheets.

| Shot Number | $\dfrac{t}{D}$ | Impact Velocity, (km/s) | $\dfrac{V_2}{V_0}$ | $\dfrac{V_4}{V_0}$ | $\dfrac{V_2-V_4}{V_0}$ | $\dfrac{V_r}{V_0}$ | $\dfrac{(V_2-V_4)/V_0}{V_r/V_0}$ |
|---|---|---|---|---|---|---|---|
| 4-1392 | 0.026 | 6.54 | 0.997 | 0.907 | 0.090 | 0.064 | 1.406 |
| 4-1395 | 0.026 | 6.70 | 0.991 | 0.901 | 0.090 | 0.063 | 1.428 |
| 4-1433 | 0.049 | 4.71 | 0.970 | 0.904 | 0.066 | 0.070 | 0.943 |
| 4-1394 | 0.049 | 5.45 | 0.971 | 0.866 | 0.105 | 0.095 | 1.105 |
| 4-1360 | 0.049 | 6.62 | 0.980 | 0.826 | 0.154 | 0.118 | 1.305 |
| 4-1744 | 0.049 | 7.38 | 0.966 | 0.804 | 0.162 | 0.127 | 1.276 |
| 4-1359 | 0.062 | 6.78 | 0.968 | 0.785 | 0.183 | 0.142 | 1.289 |
| 4-1631 | 0.084 | 3.64 | 0.937[a] | 0.887 | 0.050 | 0.082 | 0.610 |
| 4-1622 | 0.084 | 3.84 | 0.935[a] | 0.864 | 0.071 | 0.109 | 0.651 |
| 4-1621 | 0.084 | 4.62 | 0.950[a] | 0.814 | 0.136 | 0.152 | 0.895 |
| 4-1289 | 0.084 | 6.68 | 0.960 | 0.734 | 0.226 | 0.187 | 1.208 |
| 4-1283 | 0.102 | 6.72 | 0.955 | 0.696 | 0.259 | 0.208 | 1.245 |
| 4-1716 | 0.135 | 4.71 | 0.934[a] | 0.732 | 0.202 | 0.225 | 0.898 |
| 4-1291 | 0.163 | 6.71 | 0.915 | 0.596 | 0.319 | 0.283 | 1.127 |
| 4-1717 | 0.168 | 4.96 | 0.915[a] | 0.673 | 0.242 | 0.254 | 0.953 |
| 4-1352 | 0.234 | 6.64 | 0.894 | 0.536 | 0.358 | 0.268 | 1.336 |

[a] Point ② shown in Figure 8 did not exist because the front element did not form. Bumper plug remained attached to the front of the sphere. Used value for $V_1/V_0$ from Table 4.

of 6061-T6 aluminum sheets. Also presented in Table 13 is the circularity index of the spall shells for the tests listed in the table. The circularity index was the ratio formed by dividing the normalized velocity of the spall-shell fragments traveling along the debris-cloud center line, $(V_2-V_4)/V_0$, by the normalized velocity, $V_r/V_0$, of the fragments traveling normal to the shot-line axis. When the value of the circularity index was unity, the spall-shell-expansion velocity was uniform with respect to the center of mass of the internal structure. When the circularity index was less than unity, the radial growth of the spall shell was greater than the growth along the axis of the shell. Conversely, values greater than unity indicated that radial growth of the spall shell was less than the axial growth of the shell.

The spall-shell circularity index is shown as a function of impact velocity, in Figure 51, for the debris clouds listed in Table 13. This figure clearly shows that the axial rate of growth of spall shells was greater than their radial rate of growth as impact velocity was increased. At the lower impact velocities, the effect of $t/D$ ratio on the circularity index was minimal. At the higher impact velocities, however, the data indicate that the spall shells tended to be more circular as the $t/D$ ratio increased, at least to a $t/D$ ratio of 0.163. The spall-shell circularity index is shown as a function of $t/D$ ratio, in Figure 52, for tests with a nominal impact velocity of 6.7 km/s. The spall shell for Shot 4-1352 ($t/D = 0.234$) was very faint and poorly defined in the second view of the debris cloud (see Figure 41), making a determination of the radius of the shell difficult. Examination of the data presented in Figure 12 (a plot of $V_r/V_0$ vs. $t/D$) would indicate
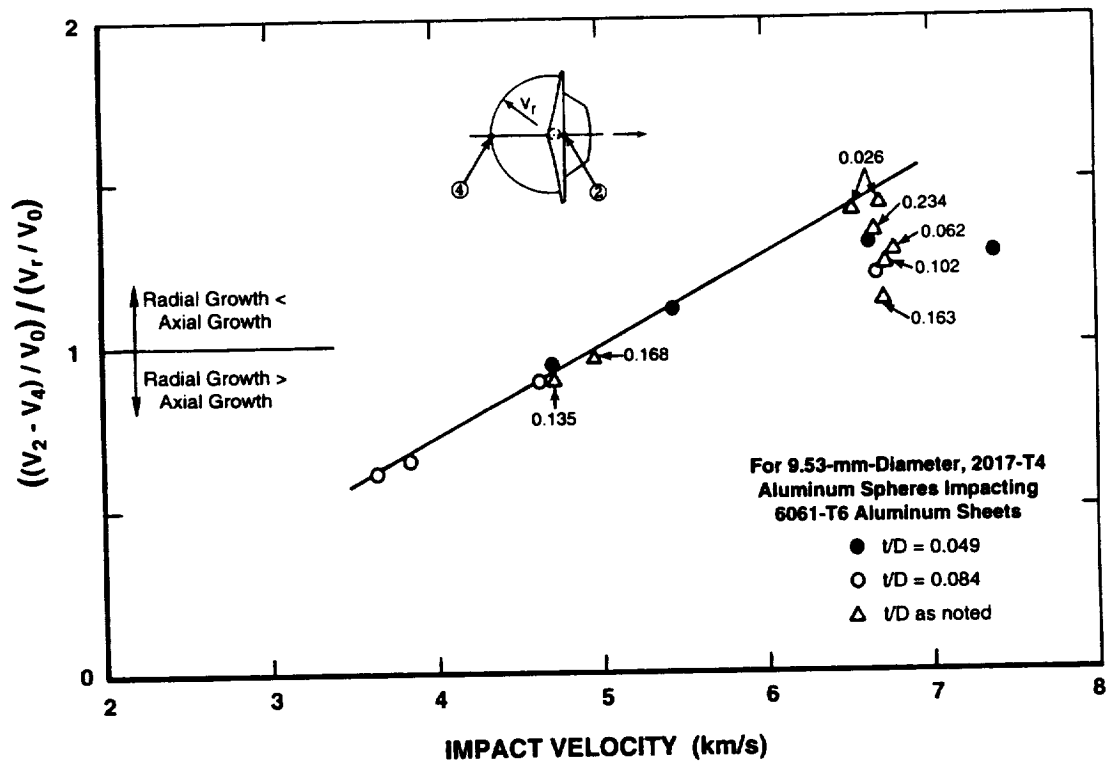


Figure 51. Spall-shell circularity index as a function of impact velocity for selected tests employing 9.53-mm-diameter, 2017-T4 aluminum spheres and various thicknesses of 6061-T6 aluminum sheet.

121
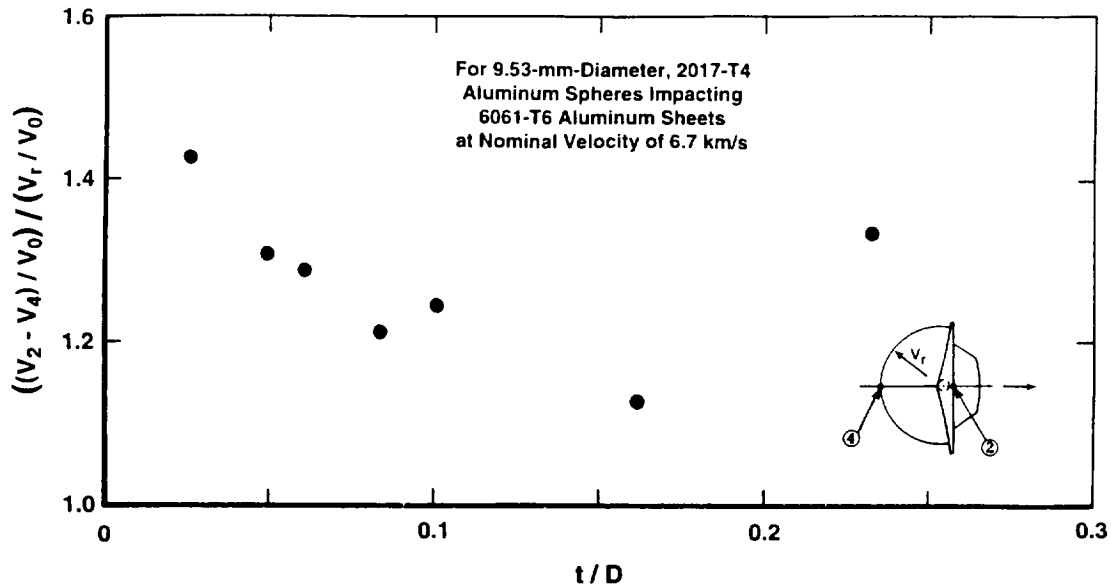
Figure 52. Spall-shell circularity index as a function of $t/D$ ratio for tests with a nominal impact velocity of 6.7 km/s.

that the reported value of $V_r/V_0$ may be at least ten percent low. While an increase in the value of $V_r/V_0$ for Shot 4-1352 would result in a reduced value for the circularity index of the spall shell for this test, the adjusted index would still be greater than the value for the $t/D = 0.163$ test. Further study of the effects of $t/D$ ratio on the circularity of the spall shells produced by the higher velocity impacts will require additional test data. Since the formation of the spall shell is an external expression of the characteristics of the stress pulse that is propagated in the sphere, further work with numerical simulations of hypervelocity impacts should focus on carefully matching the results of the simulations to the data presented in this subsection.

4. Ejecta Veil and External Bubble. All of the debris clouds produced by the tests described in this report exhibited, to a lesser or greater degree, the following features: (1) an ejecta veil on the side of the bumper impacted by the sphere, (2) an external bubble of fragments on the side of the bumper downstream of the impact, and (3) a significant internal structure at the front of the external bubble. The description of the internal structure of the debris clouds has been the subject of the test results and discussions presented thus

122

far. A brief presentation and discussion of the features of the ejecta veil and the external bubble of debris are given in this subsection to complete the description of debris clouds produced by the hypervelocity impact of aluminum spheres with thin aluminum sheets. In the remainder of this subsection, the expressions "external bubble of debris" and "debris bubble" will be used interchangeably when referring to the bubble of fragments on the downstream side of the bumper sheet.

Views of the ejecta veils and external bubbles of debris produced by the impact of 9.53-mm-diameter, 2017-T4 aluminum spheres with three different thicknesses of 6061-T6 aluminum sheet are presented in Figure 53. Nominal impact velocity for these tests was 6.7 km/s. Note that the impact velocities were nearly identical for these tests and that the radiographs were made at about the same time after impact, facilitating comparison of the features of the ejecta veils and the external bubbles of debris produced by the impacts. A very faint, but full, ejecta veil and debris bubble were formed for the $t/D = 0.026$ test, but were difficult to reproduce for presentation in the figure. However, the front portion of the external bubble of debris is evident in the print of the radiograph from this test. A full ejecta veil and debris bubble are displayed in the radiographs for the $t/D = 0.084$ and 0.163 tests. In both of these tests, the fragments in the rear portion of the debris bubble were aligned in narrow streams or chains. The impact of the fragments in these streams produced the chains of craters that form the ray patterns evident on the damaged surfaces of rear walls and/or witness plates placed behind the bumper sheets. The radiographs of the three debris clouds presented in Figure 53 clearly indicate that the amount of material in the ejecta veil and external bubble increased as the $t/D$ ratio increased. It is evident, therefore, that the bulk of the material in the ejecta veil and the external bubble of debris was derived from the bumper sheet.

The external dimensions of the debris bubble were, for all purposes, the same for the tests shown in Figure 53. The maximum diameter of the external bubble of debris
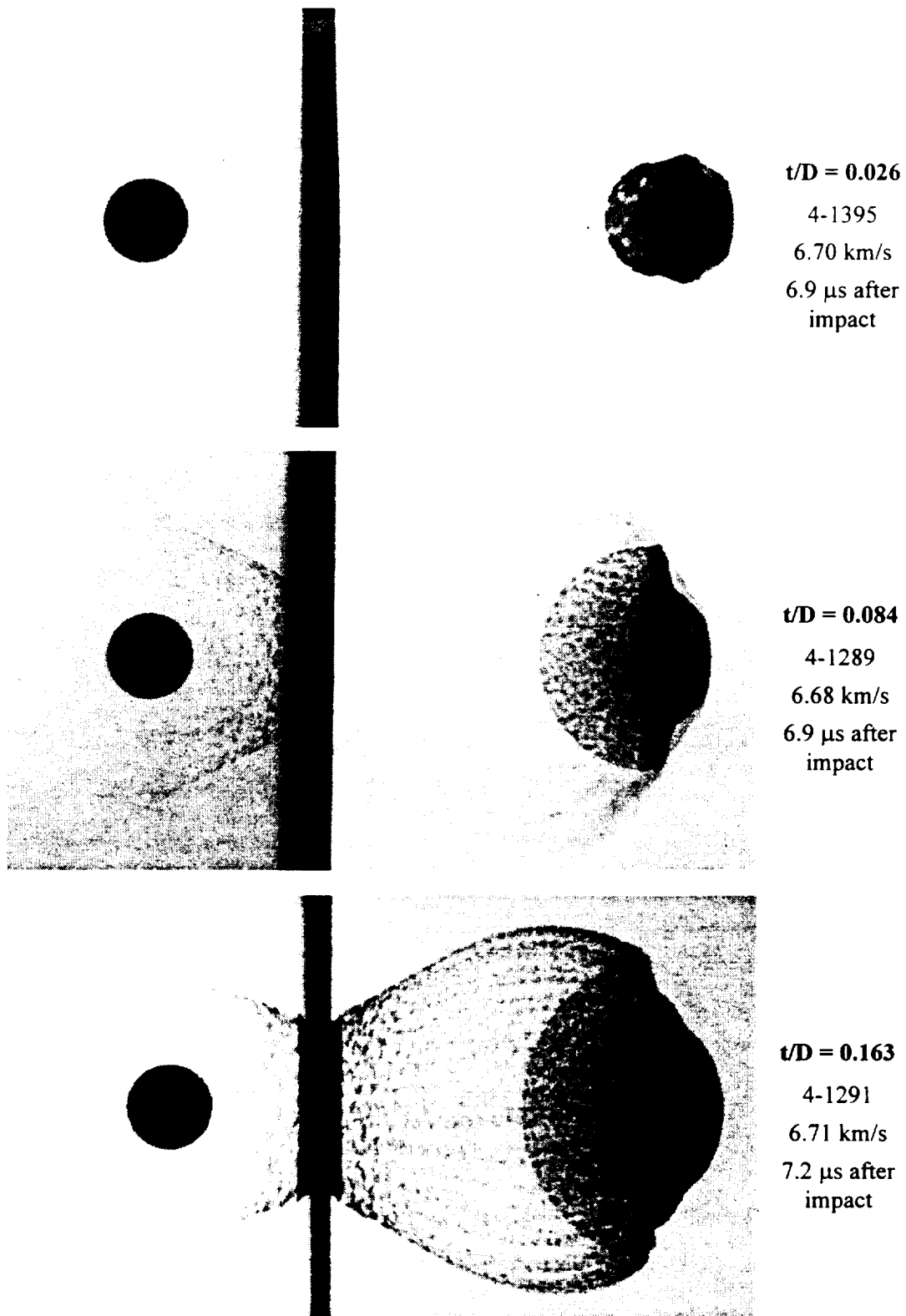
Figure 53. Views of the ejecta veils and the external bubbles of debris produced by the 6.7 km/s impact of spheres with bumper sheets of three different thicknesses.

t/D = 0.026
4-1395
6.70 km/s
6.9 μs after impact

t/D = 0.084
4-1289
6.68 km/s
6.9 μs after impact

t/D = 0.163
4-1291
6.71 km/s
7.2 μs after impact

occured at a point that was about 60 percent of the distance from the bumper to the leading edge of the debris cloud. The location of this point did not appear to be sensitive to $t/D$ ratio. When compared on the basis of time after impact, the diameter of the external bubble of debris was about the same for tests with $t/D$ ratios of 0.1 or less, but decreased somewhat as the t/D ratio was increased from 0.1. The shape of the ejecta veil changed from a gracefully-curved to a cone-shaped to a nearly tubular structure as the $t/D$ ratio was increased. (See Figure 6 for additional views of the ejecta veil and the external bubble of debris for tests with other $t/D$ ratios.)

The view of Shot 4-1291 that is presented in Figure 53, clearly shows a fairly large and continuous overturned flap on both sides of the bumper sheet. The large flaps were not evident in the cross section of the bumper, shown in Figure 26, for this test. The boundary between the flap and the fragments in the ejecta veil and the debris bubble was straight and distinct. The radiograph from Shot 4-1291 suggested that the fragments were being ejected from the region of the bumper sheet between the flap and the center of the sheet. Ejection of material from this region could eventually result in the formation of the deep, V-shaped grooves seen behind the attached ring that defined the edge of the hole in the bumper. It would seem reasonable, therefore, given the somewhat irregular spacing of the fragments in the ejecta veil and debris bubble, that the edge of the overturned flap should be more irregular if the fragments were simply torn from the end of the flap as it turned over.

In general, the size of the fragments in the ejecta veil and the external bubble of debris decreased as impact velocity was increased. The size of the fragments ejected late in the time of formation of the ejecta veil and debris bubble was also a function of their time of departure from the bumper and the $t/D$ ratio of the test. Fragments ejected late in the debris-cloud formation process were larger than those ejected early in the process. Radiographs from two, low-velocity, high-$t/D$-ratio tests are shown in Figure 54. The

t/D = 0.233

4-1720

2.44 km/s

18.4 μs after impact

t/D = 0.504

4-1721

2.23 km/s

30.1 μs after impact
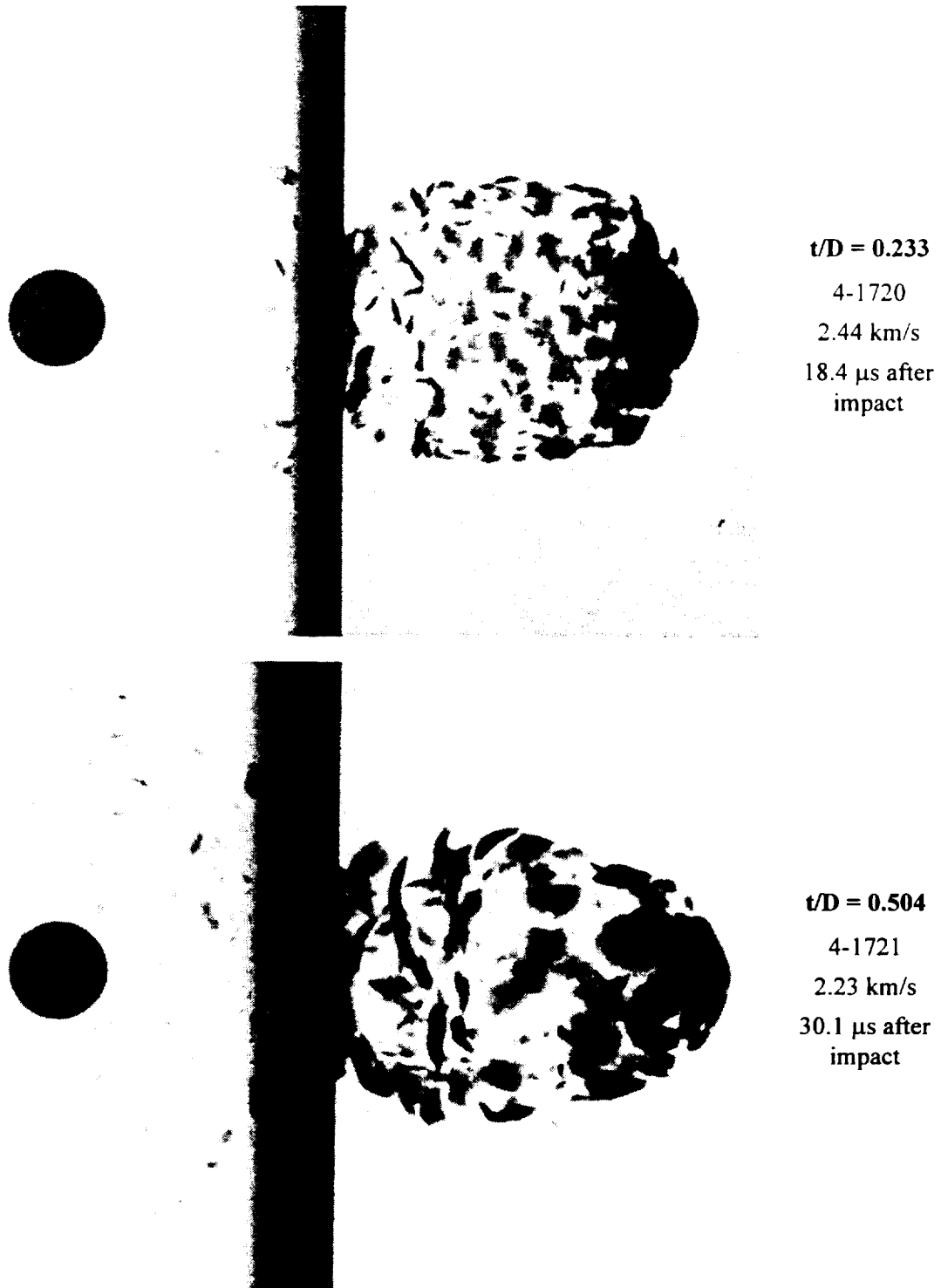
Figure 54. Views of the ejecta veils and the external bubbles of debris produced by the low-velocity impact of spheres with thick bumper sheets. Debris clouds were produced by the impact of 9.53-mm-diameter, 2017-T4 aluminum spheres with 6061-T6 aluminum sheets.

126

fragments in the external bubble of debris, for both of these debris clouds, were flaky and much larger than the fragments in the ejecta veil. In addition, most of the debris-bubble fragments were oriented with their flat side parallel to the "surface" of the debris bubble. The late-time fragments, however, were oriented with their flat side normal to the "surface" of the debris bubble. Similar abrupt changes in the orientation of debris-bubble fragments were observed in the radiographs from a number of the tests described in this report, albeit not as distinctly. The meaning of this change in orientation was not clear, but may be indicative of the two-stage process of hole growth that was proposed by Turpin and Carson [30]. They suggested that the first stage of hole growth was one of rapid growth during which the hole grew to a large fraction of its final size in a small fraction of the total growth time. During the second stage, growth was much slower as the hole expanded to its final size. Changes in the mechanisms and forces driving hole growth could be responsible for changes in the production and the orientation of the fragments that were ejected as part of the hole-formation process.

## B. Distribution of Mass in Debris Cloud

The model for the distribution of mass in the debris cloud was developed using observations made during examination of the radiographs of the debris clouds, the fragment-size data presented in this report, and the results of a limited effort to quantitatively determine the distribution of material in a debris cloud. The determination of the distribution of mass in the various debris-cloud features relied on an interpretation of the dimensions of fragments taken from the radiographs of the debris clouds, since the recovery and identification of thousands of individual fragments using other techniques was not practical. Use of two-dimensional objects (i.e., shadows of fragments on film) to estimate the volume and mass of a three dimensional object (i.e., the fragment) is a subjective process at best. An interpretation of the numerous observations made regarding

127

the distribution of projectile and bumper material in the debris cloud is portrayed in the illustration presented in Figure 55. This illustration identified the source of the material that eventually formed the ejecta veil, the external bubble of debris, and the three elements of the internal structure of a fully-developed debris cloud, and was drawn to scale for a test that employed a $t/D$ ratio of 0.1. Debris clouds formed by impacts with other $t/D$ ratios would have the same general distribution of material although the partitioning, on an element-by-element basis, would vary.

As shown in Figure 55, the front element was composed of the lens-shaped region of the sphere and bumper sheet that were subjected to quasi one-dimensional shock loading during the impact. The spall shell was formed from a thin layer of material at the rear of the sphere. The center element and the large central fragment were derived from the remainder of the sphere material. The ejecta veil consisted almost exclusively of bumper material from a thin, tapered flat ring on the impact side of the sheet. The ring was very thin when the ejecta veil formed, but increased in thickness as the veil became
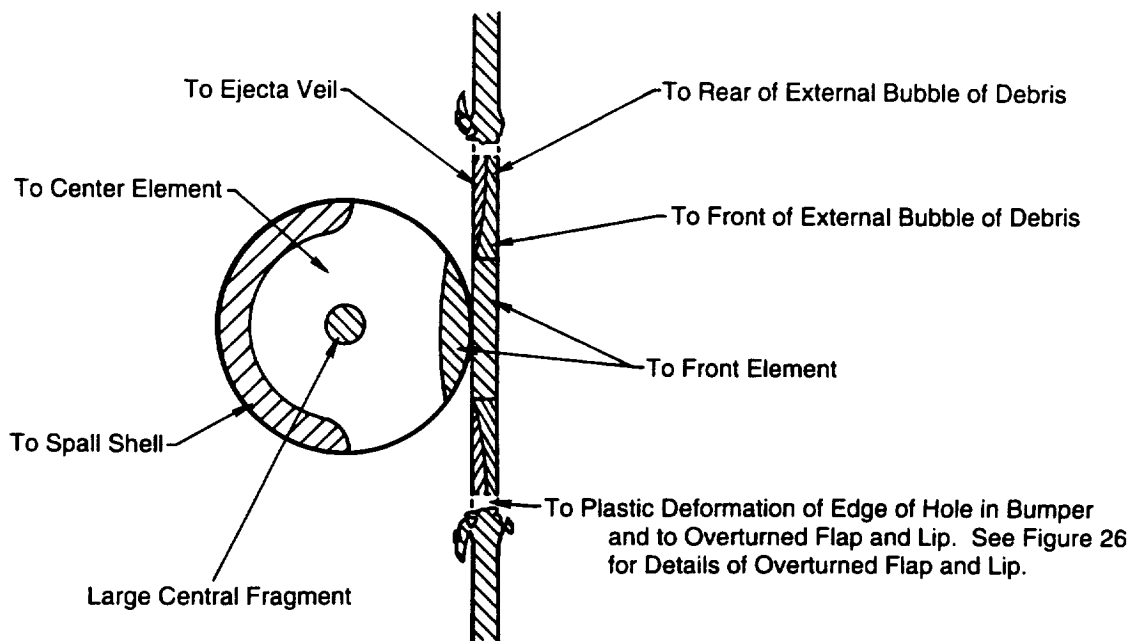


Figure 55. Illustration showing the estimated distribution of mass in a fully-developed debris cloud produced by an impact with a $t/D$ ratio of 0.1.

128

more developed. A very small portion of the sphere and bumper sheet were involved in the formation of an impact-flash jet that preceded development of the ejecta veil [36]. In addition, a very small amount of sphere material was probably mixed with the bumper-sheet fragments that formed the ejecta veil. The external bubble of debris was formed from a flat ring of bumper material from the downstream side of the sheet. Material from the inner part of the ring formed the front of the debris bubble and material from the outer part of the ring formed the thin shell of fragments that "connected" the front of the debris bubble to the bumper sheet. In Figure 55, a small gap is shown between the outer edges of flat rings and the inside of the hole that was produced in the bumper sheet. The small gap represented the material that was not actually separated from the sheet, but was plastically deformed and displaced during the later stages of hole growth.

The results of the fragment-size analyses presented in Section IV provided data that were used to estimate the distribution of mass in the internal structure of the debris cloud. Difficulties with the resolution of small particles and the overlapping of fragments in the radiographs limited or prevented the acquisition of fragment-size and size distribution data for the tests with the larger $t/D$ ratios. Consequently, the estimated mass distributions were made for the tests with the lower $t/D$ ratios. Trends observed in the various low-$t/D$-ratio test series can be extended to the fully-developed debris clouds produced by impacts with higher $t/D$ ratios.

With the exception of the material that formed the spall shell and the material that combined with bumper material to form the front element, the bulk of the projectile mass was contained in the center element. As shown in Figures 42 and 43, the fragments in the center element were closely spaced and overlapped, making an accurate measurement of the size and number of these fragments nearly impossible. The large central fragment was reasonably clear in most of the radiographs, however. The large-central-fragment equivalent diameter and the spall-shell-fragment data were used to compute the mass of

129

material in these components of the debris cloud. The mass of material in the center element was determined to be the difference between the pre-impact mass of the sphere and the combined mass of the front element, the spall shell, and the large central fragment. The results of the various computations are presented in Table 14 for a number of low-$t/D$-ratio tests.

The mass of the sphere involved in the formation of the front element, $m_p$, was assumed to be the same as the mass of the plug of bumper material that experienced quasi one-dimensional loading during the impact. Computation of the mass of the bumper plug was accomplished with use of the following assumptions and by applying the principle of conservation of momentum to the impact process. Work by Nysmith and Denardo [14] had shown that a negligible amount of projectile momentum was transmitted to the bumper sheet during impact. Consequently, the post-impact momentum of the disintegrated sphere and the bumper plug was assumed to be equal to the pre-impact momentum of the sphere. The velocity of point ② was assumed to be the velocity of the center of mass of the debris cloud. Accordingly, the mass of the bumper plug, $m_b$, was determined with use of the following relationship:

$$m_b = m(V_0 - V_2) / V_2$$

where $m$ is the mass of the sphere, $V_0$ is the impact velocity, and $V_2$ is the velocity of point ②. In Table 14, the results of the computations of $m_b$ are presented as $m_p$, the mass of the sphere that was part of the front element, since these masses were assumed to be equal. The diameter of a disk-shaped bumper plug with thickness, $t$, and mass, $m_b$, was found to be slightly larger (2 to 3 percent) than the diameter of the lens-shaped region at the time the velocity of the collision point, $V_{CP,T}$, was the same as the velocity of the shock in the projectile and target (see Figure 37). In addition, the edge of the bumper plug should be shown tapered and slightly curved, to more accurately reflect the shape of the shock front in this part of the bumper. For simplicity of illustration, however, the

130

## TABLE 14

### DISTRIBUTION OF PROJECTILE MASS BY DEBRIS-CLOUD ELEMENT

All projectiles were 9.53-mm-diameter, 2017-T4 aluminum spheres with a nominal mass of 1.275 g. All bumpers were 6061-T6 aluminum sheets.

| Shot Number | $\dfrac{t}{D}$ | Impact Velocity, (km/s) | Front Element, $m_p$ (mg) | Large Fragment, $m_f$ (mg) | Spall Shell, $M_S$ (mg) | Center Element $M_C$ (mg) | Center Element Percent of Original Wt. |
|---|---|---|---|---|---|---|---|
| | | | $t/D$ Effects, $V_0 = 4.70$ km/s | | | | |
| 4-1715 | 0.026 | 4.67 | 28.9[a] | ~1275 | --- | ~1275 | 100 |
| 4-1433 | 0.049 | 4.71 | 39.4 | 378.1 | 137 | 720 | 56 |
| 4-1621 | 0.084 | 4.62 | 67.1 | 162.8 | 163 | 882 | 69 |
| 4-1716 | 0.135 | 4.71 | 96.0 | 49.5 | 291 | 838 | 66 |
| | | | $t/D$ Effects, $V_0 = 6.70$ km/s | | | | |
| 4-1395 | 0.026 | 6.70 | 11.6 | 242.2 | 189 | 832 | 65 |
| 4-1360 | 0.049 | 6.62 | 26.0 | 37.5 | 334 | 878 | 69 |
| 4-1359 | 0.062 | 6.78 | 42.1 | 38.5 | 451 | 743 | 58 |
| 4-1289 | 0.084 | 6.68 | 53.1 | 12.5 | 378 | 831 | 65 |
| 4-1283 | 0.102 | 6.72 | 60.0 | 4.5 | --- | --- | --- |
| | | | $V_0$ Effects, $t/D = 0.049$ | | | | |
| 4-1428 | 0.049 | 3.77 | 55.9[a] | ~1275 | --- | ~1275 | 100 |
| 4-1433 | 0.049 | 4.71 | 39.4 | 378.1 | 137 | 720 | 56 |
| 4-1394 | 0.049 | 5.45 | 38.1 | 144.6 | 190 | 902 | 71 |
| 4-1360 | 0.049 | 6.62 | 26.0 | 37.5 | 337 | 874 | 68 |
| 4-1744 | 0.049 | 7.38 | 44.9 | 10.8 | 254 | 965 | 76 |
| | | | $V_0$ Effects, $t/D = 0.084$ | | | | |
| 4-1632 | 0.084 | 3.47 | 98.9 | 659.4 | ---[b] | <517 | 40 |
| 4-1631 | 0.084 | 3.64 | ~86[c] | 619.0 | ---[b] | <570 | 45 |
| 4-1622 | 0.084 | 3.84 | ~89[c] | 690.8 | 123 | 372 | 29 |
| 4-1621 | 0.084 | 4.62 | 67.1 | 162.8 | 163 | 882 | 69 |
| 4-1289 | 0.084 | 6.68 | 53.1 | 12.5 | 378 | 831 | 65 |

[a] Projectile did not break up. Value shown is the computed mass of the bumper plug.

[b] Difficult to distinguish between the center and rear elements of the debris cloud.

[c] Bumper plug remained attached to the front of the sphere (see Figure 49). Used the velocity of point ① in the computation of the bumper plug mass since the velocities of points ① and ② were coincident for these tests.

edge of the bumper plug was shown, in Figure 55, as a straight line normal to the surface of the bumper sheet.

The measured dimensions of the large central fragment were used to compute the equivalent diameter, $d_f$, of a sphere having the same volume as an ellipsoid with the dimensions of the large central fragment (see Section IV). In Table 14, the mass of the

large central fragment, $m_f$, was computed by assuming the density of the equivalent-diameter sphere was the same as that of the original projectile.

The mass of material removed from the sphere to form the spall shell changed as the $t/D$ ratio and impact velocity were varied. The mass of material in the shell, $M_S$, was estimated for each test, by determining the mass of the median fragment in the spall shell and multiplying that mass by the number of fragments, $N_T$, in the shell. The mass of the median fragment was computed by assuming the median Martin's diameter, $\tilde{d}_m$, was the diameter of a spherical fragment and the density of the fragment was the density of the unshocked projectile.

Except for two of the tests shown in Table 14, the mass of the center element, $M_C$, was computed by simply subtracting the mass of the front element, the spall shell, and the large central fragment from the original mass of the sphere. In Shots 4-1428 and 4-1715, the projectile did not break up and the mass of the sphere was used as the mass of the center element. The mass of the center element is shown as a percentage of the mass of the sphere in the extreme right-hand column of Table 14. Given the nature of the procedures used to estimate the masses of the various debris-cloud elements, this percentage was surprisingly consistent for tests in which the debris clouds were fully developed, (i.e., the impact velocity was more than 500 m/s above the spall-failure threshold impact velocity). In general, the mass of the center element (exclusive of the large central fragment) was shown to be 65 to 70 percent of the mass of the sphere. As the impact velocity or the $t/D$ ratio increased, the mass of the large central fragment decreased. However, the decrease in the large-central-fragment mass was usually offset by an increase in the mass of the front element and the spall shell. Although the procedure used to compute the masses of the elements was subjective, it is informative to compare the shapes and masses of the large central fragments for Shots 4-1622, 4-1631, and 4-1632 (Figure 49 and Table 14) with the shapes and the masses of the recovered projectiles for

Shots 4-1719, 4-1720, and 4-1721 (Figure 34 and Table 11). The shapes of the large central fragments were similar for all six tests and the computed large-central-fragment masses were well within the range of the masses of the recovered projectiles.

During analysis of the spall-shell fragments, it was noted that the fragments were evenly distributed over the shell area. Oblique, late-time views of the center elements and the damage patterns produced on the witness plates indicated that the center-element fragments were uniformly distributed within the boundaries of this disk-like element. Similar observations were made for the front element, the ejecta veil, and the external bubble of debris. Therefore, it appears reasonable to compute the areal density of the mass in any element of a debris cloud by dividing the mass of the element by the instantaneous area or footprint of the element. Estimates of element mass can be made using the data presented in this subsection. Information presented earlier in Tables 3 and 4 can be used to determine the dimensions of the element of interest at any time after impact.

## C. State of Material in Debris Cloud

Passage of a shock is an irreversible process resulting in an increase of the internal energy of the shocked material to the thermodynamic state $(P_H, V_H)$ on the Hugoniot. The material is shocked to this state along a Rayleigh line. Release from the shocked state follows a release isentrope. Since the recovered energy (area under the isentrope in $P$-$V$ space) is less than the energy required to drive the material to the shocked state, some energy remains in the material after release. This residual energy is ultimately dissipated by heating the material. Consequently, the postshock state of the material is a function of the energy remaining in the material after release from the shocked state.

A number of computations have been made to estimate the impact conditions required to produce phase changes in aluminum. Hopkins et al. [39] used an analysis based on planar shock wave theory to associate critical points on ballistic-limit curves

with phase changes of projectile and target materials. Anderson *et al.* [40] performed similar calculations to determine the impact velocity required to melt and/or vaporize the projectile and bumper. Bjork [41] reviewed options for a wide variety of equations of state and presented the results of an experimental/theoretical program that was performed to establish the effect of shock-induced phase changes in projectile and target response characteristics. A summary of the results of appropriate portions of the computational works and data from Shockey *et al.* [42] is presented in Table 15. In this subsection, use is made of the results of these computations and the results of several hypervelocity impact tests to develop a method of describing the state of the material in a debris cloud produced by the normal impact of an aluminum sphere with a thin aluminum sheet.

The procedures for determining the intensity of the pressure or stress generated at the impact site, using the Hugoniot, are well documented. This pressure, $P_H$, is a function

**TABLE 15**

**CONDITIONS FOR IMPACT-INDUCED PHASE CHANGES IN ALUMINUM**

| Condition | Hopkins et al. (Reference 39) | Anderson et al. (Reference 40) | Bjork (Reference 41) | Shockey et al. (Reference 42) |
|---|---|---|---|---|
| **Incipient Melt** | | | | |
| Particle Velocity (km/s) | 2.72 | 2.85 | --- | 2.6 - 3.6 |
| Pressure (GPa) | 65 | 71 | --- | --- |
| **Complete Melt** | | | | |
| Particle Velocity (km/s) | 3.38 | 3.45 | --- | 3.3 - 4.6 |
| Pressure (GPa) | 89 | 94 | --- | --- |
| **Incipient Vaporization** | | | | |
| Particle Velocity (km/s) | --- | 5.20 | 6.20 | 5.5 - 7.5 |
| Pressure (GPa) | --- | 174 | 225 | --- |
| **30 Percent Vaporization** | | | | |
| Particle Velocity (km/s) | --- | --- | 10.1 | --- |
| Pressure (GPa) | --- | --- | 500 | --- |
| **Complete Vaporization** | | | | |
| Particle Velocity (km/s) | --- | --- | --- | 12.5 - 16.5 |
| Pressure (GPa) | --- | --- | 2680 | --- |

of the properties of the colliding materials and the impact velocity. The stress state at the rear surface of the sphere is considerably more difficult to ascertain, however. The nine tests near the sphere-failure threshold velocity (described earlier in this section) will be used to help define the stress state in this region for various impact conditions. In the remainder of this subsection, reference to $P_H$ will be made in the context of a stress rather than a pressure.

When a shock (compressive stress) encounters a free surface, it is reflected as a release wave (tensile stress). For the tests near the threshold velocity (see Figures 34 and 35), the strength of the tensile release wave was near the spall strength of the aluminum sphere. Published values for the ultimate tensile strength and spall strength of several aluminum alloys are presented in Table 16. Although there is considerable variation in

## TABLE 16
## SPALL STRENGTH OF ALUMINUM

| Source | Material | Spall Strength (GPa) |
|--------|----------|---------------------|
| Handbook Value [43] | 2017-T4 | 0.43* |
| Rinehart [38] | 24S-T4 | 0.95 |
| Chhabildas et al. [44] | 6061-T6 | 1.72 |
| Gilath et al. [34] | Aluminum | 2.50 |

* Ultimate tensile strength

the magnitude of the published strengths, the variation was insignificant when compared to the stress level produced at the impact site. Because knowledge of the strain rate at the spall-failure location was uncertain, a spall strength of 2.5 GPa was assumed for the 2017-T4 aluminum spheres, since the tests of Gilath et al. [34], were performed at very high strain rates. The difference, $\Delta P$, between $P_H$ and 2.5 GPa will be called the stress differential in the sphere. The stress differential in the sphere is presented in Table 17 for several $t/D$ ratios. In Table 17, $V_S$ was determined with use of the relationship given in Figure 35 and $P_H$ was determined with use of the equation appearing as a footnote to the

135

table. In this equation, the particle velocity behind the shock wave, $u_p$, was assumed to be 1/2 $V_S$. The values of $\Delta P$ are shown as a function of $t/D$ ratio in Figure 56.

## TABLE 17
### STRESS DIFFERENTIAL IN SPHERE

| $t/D$ | $V_S$ (km/s) | $P_H$ (GPa)* | $\Delta P$ (GPa) |
|-------|--------------|--------------|------------------|
| 0.02 | 5.29 | 63.2 | 60.7 |
| 0.04 | 4.20 | 46.1 | 43.6 |
| 0.08 | 3.33 | 33.9 | 31.4 |
| 0.12 | 2.91 | 28.6 | 26.1 |
| 0.16 | 2.64 | 25.3 | 22.8 |
| >0.16 | 2.60 | 24.8 | 22.3 |

* $P_H = 14.41\, u_p + 3.59\, u_p^2$ (From Reference 45)
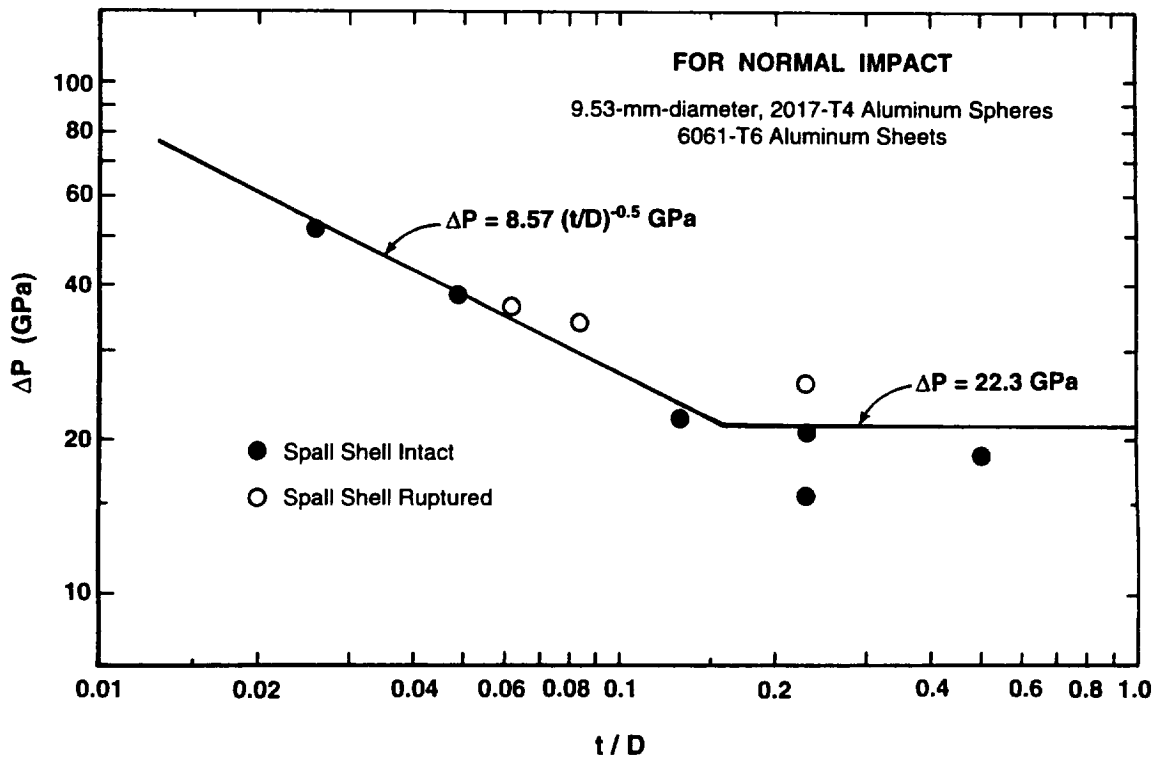


Figure 56. Stress differential, $\Delta P$, as a function of $t/D$ ratio.

136

Although the value of $\Delta P$ was determined for conditions existing at the threshold velocity, the stress differential is a function of the sphere-sheet geometry and the complex shock wave interactions occurring after impact. Consequently, $\Delta P$ is assumed to be a constant for each $t/D$ ratio and not affected by changes in impact velocity. Determination of the peak stress at any point along the shot-line axis of the sphere (a region relatively free of release waves formed at the free surface of the sphere) can be easily accomplished using the following procedure. First, the stress, $P_H$, at the front of the sphere is determined using the "folded" Hugoniot method or the equation given in Table 17. Next, the appropriate value of $\Delta P$ is determined using the equation given in Figure 56. The stress at the rear of the sphere is determined to be $P_H - \Delta P$. The peak stress level in the sphere is assumed to decrease linearly with distance from the front of the sphere and is bounded by $P_H$ at the front and $P_H - \Delta P$ at the rear.

The assumption of a linear decrease in peak stress with distance from the front of the sphere was, strictly speaking, made for convenience. However, work by Kipp *et al.* [32], Alme and Rhoades [33], and Alme *et al.* [46] would indicate that use of the assumption of a linear decrease in peak stress was not an unreasonable approximation. Kipp *et al.* presented the results of computations made to determine the minimum principal stress at five points along the axis of a 6.35-mm-diameter steel sphere after it struck a 3.38-mm-thick sheet of polymethyl-methacrylate (PMMA). Figure 57 is taken from their work. In this figure, a straight line can be drawn through the peak stresses at the contact point, the center of the sphere, and the trailing point (rear) of the sphere. Peak pressures at the 1/4 point and the 3/4 point are slightly below and above the line, respectively. The computations of Alme and Rhoades produced similar results. In Figure 58, computed pressure profiles are shown at 0.1 µs intervals along the shot-line axis of a 9.5-mm-diameter aluminum sphere after its impact with an aluminum sheet ($t/D = 0.20$) at 8 km/s. (Figure 32, presented earlier, showed the extent of the stressed region in the sphere, at 0.2 µs
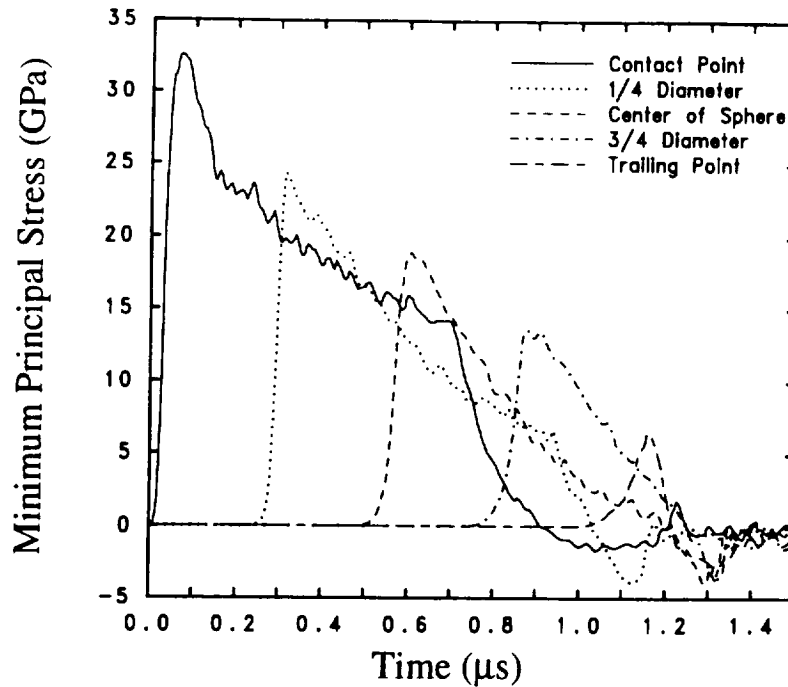
Figure 57. Histories of minimum principal stress at points along the axis of a 6.35-mm-diameter steel sphere that struck a 3.38-mm-thick polymethyl-methacrylate (PMMA) plate at 4.57 km/s. Figure taken from Kipp *et al*. [32].
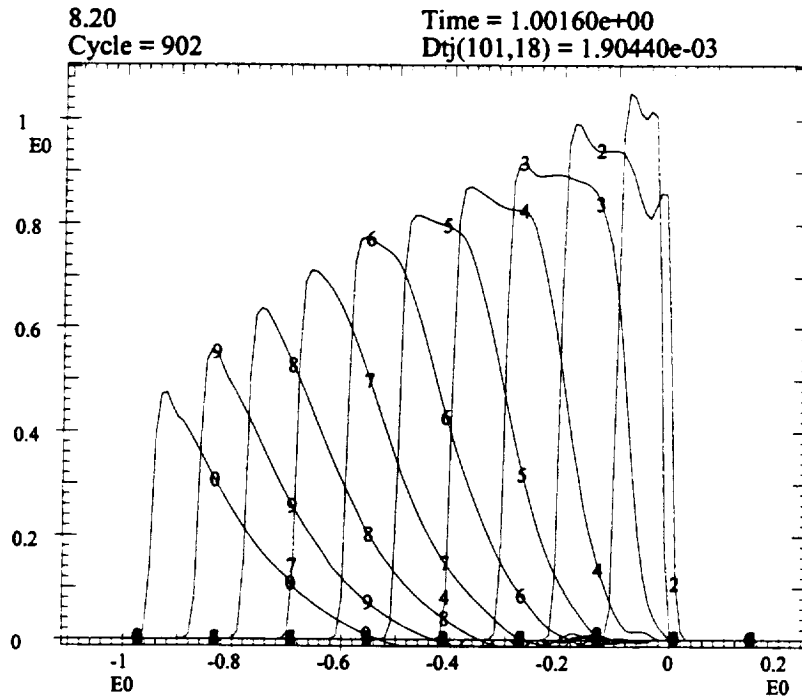


Figure 58. Pressure profiles along the shot-line axis of a 9.5-mm-diameter aluminum sphere after an impact with an aluminum sheet ($t/D$ = 0.20) at 8 km/s. Profiles are shown at 0.1 μs intervals (i.e., 2 = 0.2 μs, 3 = 0.3 μs, etc.). Figure courtesy Alme and Rhoades [33].

intervals, for these computations.) Peak stress at each time after impact decreased as the stress pulse moved through the sphere. However, peak stresses for all intermediate times lie slightly *above* a line drawn through the peak stress for the 0.1 μs and 1 μs curves, particularly at the later times. In a computation performed by Alme *et al.* [46], the impact of a 9.5-mm-diameter aluminum sphere with a 0.38-mm-thick ($t/D$ = 0.04), 1100-O aluminum sheet at 6.7 km/s was simulated. For this computation, the envelope of peak stresses along the shot-line-axis was concave upward with all intermediate peak stresses lying *below* a line drawn through the peak stress for the 0.1 μs and 1 μs curves. The rate of decrease in peak-stress level was significantly greater between the 0.1 to 0.4 μs curves than was observed between the 0.4 to 1 μs curves. The sudden decrease in early-time peak stresses was largely responsible for the "concavity" of the peak-stress envelope noted for this simulation. Given the bounds provided by the last two simulations, it appears reasonable that a nearly linear decrease in the peak-stress level in a sphere would occur for most impacts in which the $t/D$ ratio was between 0.04 and 0.20. Extension of the assumptions of a linear decrease in peak-stress profiles to spheres of all diameters can be made on the basis of the similarity of the results of the first two computations just described (involving spheres of different diameters and materials) and the previously cited observation that the morphological features and velocities of discrete points in the debris clouds scaled geometrically.

Calculations made by Anderson *et al.* [40], using a Tillotson equation of state, provide the particle velocity and stress at which phase changes occur (see Table 15). These points are shown (with a point for 30 percent vaporization from Bjork [41] and the lower pressure Hugoniot data from Marsh [47]) in Figure 59. The curve shown in Figure 59 provides a means of relating peak-stress levels behind the shock to the postrelease thermodynamic state of the material experiencing the stress. Determination of the peak stress at a point along the shot-line axis of a sphere and the use of Figure 59 permits a
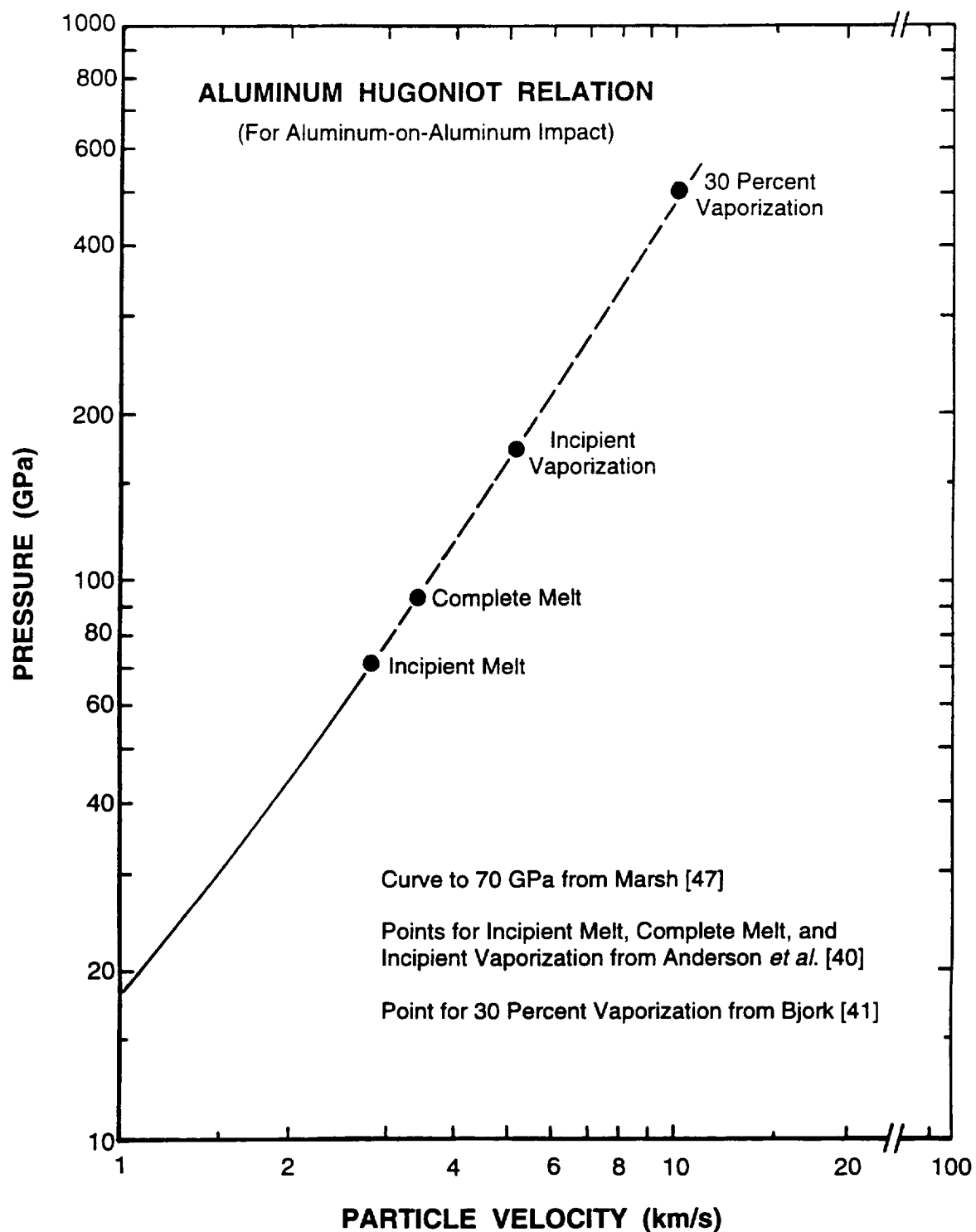
Figure 59. Hugoniot relation for an aluminum-on-aluminum impact. Data used to develop the curve were obtained from sources cited in the figure.

reasonable estimate of the state of the material at that point, after its release from the shocked state. The state of the material thus determined was assumed to extend to all material in a plane normal to the shot-line axis and through the point.

An illustration of the use of the procedures described in the preceding paragraphs is presented in Figure 60. For an aluminum-on-aluminum impact, the pressure (stress) $P_H$, was determined using the equation in Table 17. The stress differential, $\Delta P$, was determined using Figure 56. As shown in Figure 60b, material at the sphere-sheet interface is molten and material at the rear of the sphere is solid. The location of the incipient-melt and the complete-melt points along the shot-line axis of the sphere is determined by assuming a linear decrease in the peak-stress level from the front to the rear of the sphere and simply placing the appropriate points at the proper stress levels along the sphere axis. Composition of the material in the mixed-phase region was assumed



(a)                                              (b)
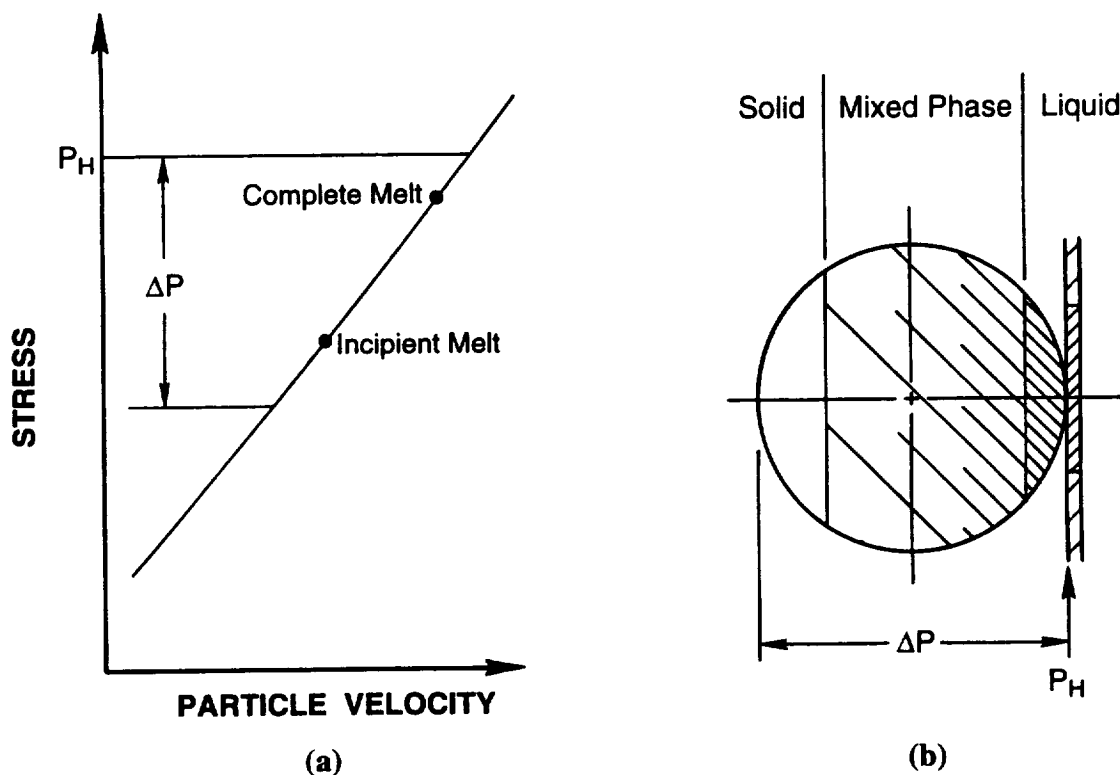
Figure 60. Illustration of procedures used to determine the composition and state of the material in a sphere after release from the shocked state.

141

to vary linearly with distance between the incipient- and complete-melt points. For example, material in the plane normal to a point one-third of the way from the complete-melt point would consist of two-thirds molten material and one-third solid material. The estimation procedure just described will be used to evaluate the state of the material making up the three debris clouds shown earlier in Figure 39. The $t/D$ ratio for the three tests was 0.049; accordingly, $\Delta P$ was determined to be 39 GPa.

The impact velocity for Shot 4-1394 was 5.45 km/s. Figure 59 indicates that $P_H$ is about 67 GPa for this test and that all material in the debris cloud is solid. The small front element of the cloud from Shot 4-1394 is shown, in Figure 39, to consist of small solid fragments. For Shot 4-1360 ($V_0$ = 6.62 km/s), $P_H$ is about 89 GPa. Aluminum released from this stress will be mixed-phase liquid and solid. The point where incipient melt will occur (71 GPa) is about 4.4 mm behind the front of the sphere. In accordance with assumptions made during development of the estimation procedure, (i.e., extending the condition at the shot-line axis of the sphere to all material in a plane through the point and normal to the axis) a spherical sector comprising 46 percent of the volume of the sphere would be mixed-phase material, with material at the front of the sphere having a higher liquid content. The front element of the debris cloud from Shot 4-1360 was made up entirely of molten material. There was some indication in the late-time, oblique view of this test (shown earlier in Figures 16 and 17) that melted material was present in a portion of the center element. Impact velocity for Shot 4-1744 was high enough to place $P_H$ in the melt portion of the curve. Determination of the incipient melt and complete melt points along the shot-line axis of the sphere for this test indicated that approximately 28 percent of the sphere (at the front) was completely melted. Fifty-nine percent of the sphere was a mixture of liquid and solid aluminum, with an increasing percentage of the solid material near the rear of the sphere. Thirteen percent of the sphere (at the rear) remained solid. Comparison of the radiographs from Shots 4-1360 and 4-1744 tended to

support the suggestion that the front elements of higher velocity tests should be larger and contain a larger percentage of molten aluminum.

As shown in Table 15, impact-induced vaporization of aluminum projectiles and targets would not occur until the impact velocity exceeded 10.4 km/s. Current launch capabilities limit the impact velocity of reasonably-sized aluminum spheres to less than 8 km/s. An examination and description of the debris clouds produced by the impact of aluminum spheres with thin aluminum sheets at velocities high enough to vaporize projectile and target material was, therefore, not possible. However, impact-induced vaporization of other projectile and target materials, notably cadmium, lead, and zinc, could be achieved using impact velocities of less than 7 km/s. The characteristics of vaporous, all-aluminum debris clouds will be inferred from the results of an analyses of the debris clouds produced by the impacts of cadmium and zinc spheres with cadmium and zinc targets, respectively.

A series of tests performed at UDRI for Boeing Defense & Space Group (Schmidt *et al.* [48]) provided radiographs of debris clouds produced by the impact of cadmium spheres with cadmium sheets ($t/D$ ratios ~ 0.16). Impact velocities for some of the tests were high enough to cause vaporization of projectile and bumper material. Radiographs of the debris clouds produced by four of the tests in the series are shown in Figure 61. Late-time-view radiographs of these tests are presented in Figure 62. Impact velocities for the four cadmium tests were 2.27, 3.36, 5.00, and 5.98 km/s.

Because the $t/D$ ratio for the cadmium tests shown in Figures 61 and 62 was 0.160, a significant portion of the bumper was not as highly shocked as the material in the lens-shaped region. The debris cloud for Shot 4-1443 contained a large number of solid, irregularly-shaped, bumper and projectile fragments and, as shown in Figure 62, a smudge or cloud of very fine droplets of molten material was evident behind the leading

2.27 km/s

4-1443

D = 7.94 mm

3.36 km/s

4-1427

D = 7.94 mm

5.00 km/s

4-1432

D = 7.94 mm

5.98 km/s

4-1442

D = 5.95 mm
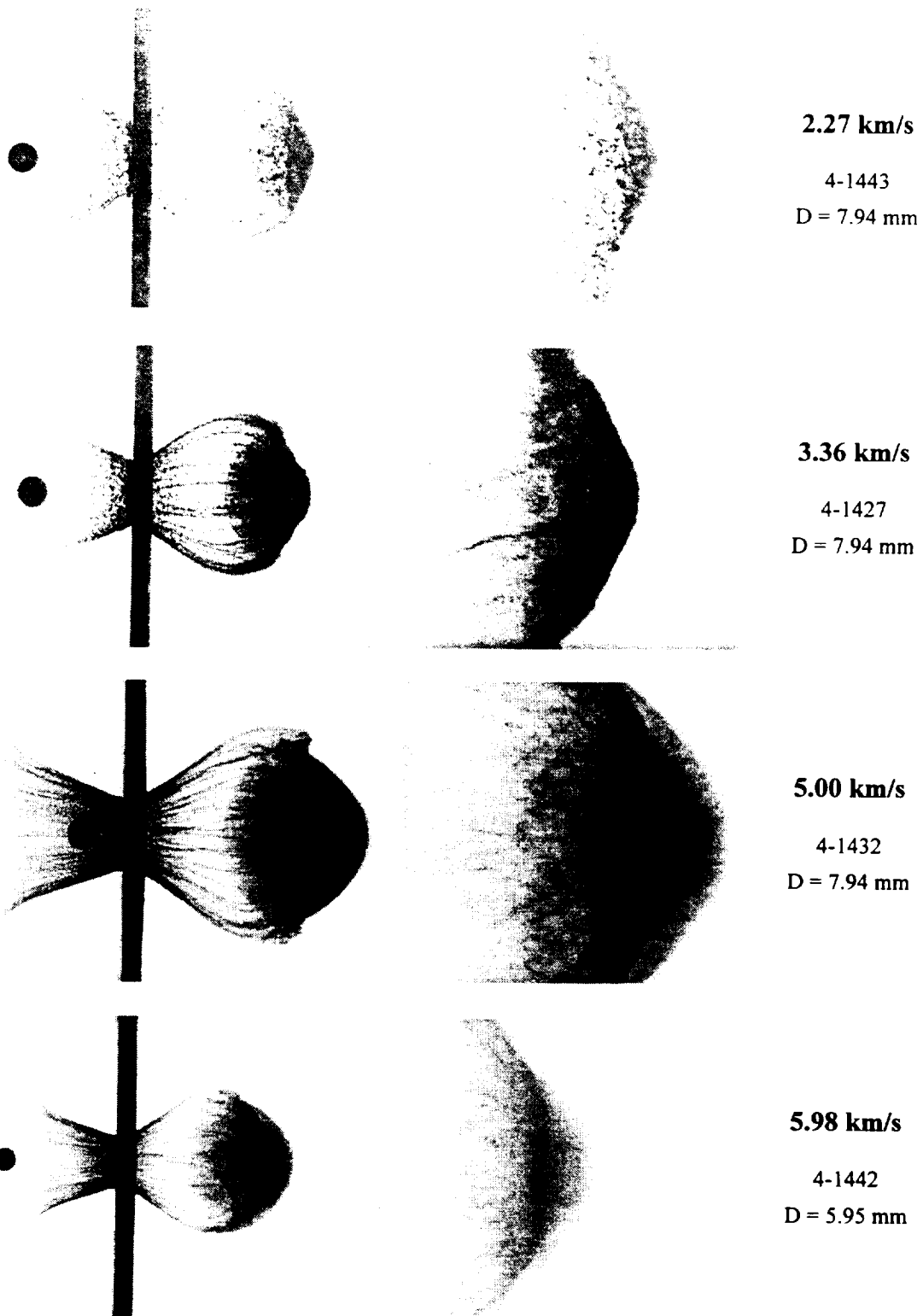
Figure 61. Views of debris clouds produced by the impact of cadmium spheres with cadmium sheets. Impact velocity varied and $t/D$ ratio held constant at 0.160. Note that Shot 4-1442 used a smaller sphere than was used for the other tests.

144

2.27 km/s      3.36 km/s      5.00 km/s      5.98 km/s
4-1443         4-1427         4-1432         4-1442
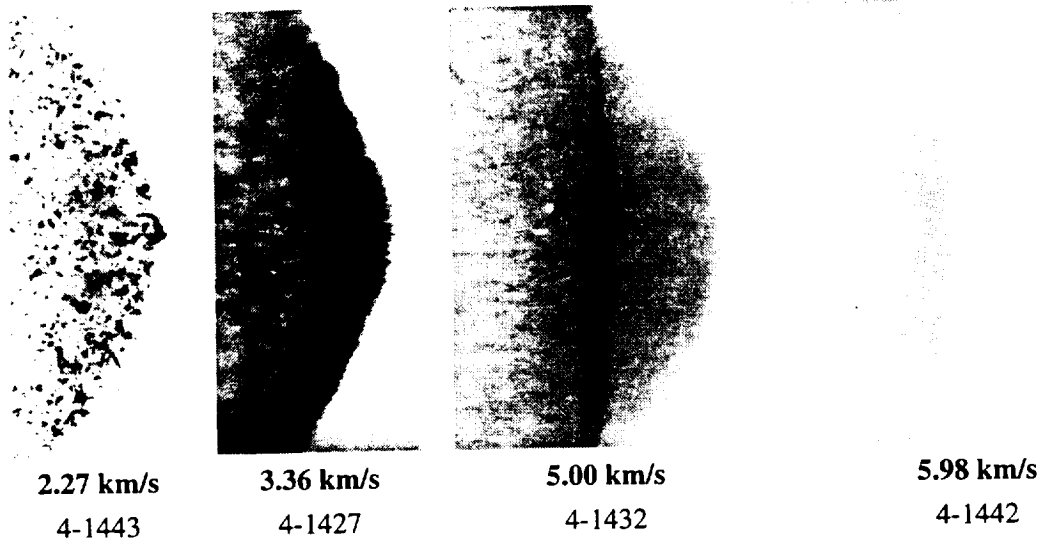
Figure 62. Late-time views of debris clouds showing the development of the front element of the internal structure as a function of an increase in impact velocity. Views (a) through (c) used 7.94-mm-diameter cadmium spheres. View (d) used a 5.95-mm-diameter cadmium sphere. All tests used cadmium bumpers ($t/D = 0.160$). (See Figure 61 for earlier views of these debris clouds.)

edge of solid fragments. It is likely that material in this smudge was originally in the lens-shaped region experiencing the highest peak stresses.

The debris cloud from Shot 4-1427 bore a striking resemblance to the all-aluminum debris cloud from Shot 4-1291 shown in Figure 6. The front of the cloud for Shot 4-1427 appears to be made up of droplets of liquid cadmium, with slight surface irregularities and jetting evident along its leading edge. The spall shell was well defined in this debris cloud and consisted of numerous small, solid fragments.

The first views of the debris clouds for Shots 4-1432 and 4-1442 were, in general, similar to the first view of the debris cloud for Shot 4-1427. Note that the center element of Shot 4-1432 was well defined and of uniform radiographic density, with little or no evidence of discrete fragments or drops. Initially, the center element of Shot 4-1442 has the same general appearance as the center element of Shot 4-1432, but became diffuse and not well defined by the time the third view was taken. Several new features were evident in the front element of the debris clouds for Shots 4-1432 and 4-1442. Four

145

points were distinct in these new features and were labeled ①a, ①b, ⑦a, and ⑧a as shown in Figure 63a. As shown in Figure 63b, the new features of the front elements of the debris clouds for Shots 4-1432 and 4-1442 appear to define regions of: (1) low-density vapor, points ① to ①a; (2) expanding vapor, points ①a to ①b; and (3) high-density vapor and liquid, points ①b to ②.

Normalized axial and diametral velocities of a number of points in the cadmium debris clouds were determined using the analytical procedures described in Sections II and III. The results of the analyses are presented in Table 18. Identification of the measurement points was more difficult for the cadmium debris clouds than for the aluminum debris clouds. Because of the heavy concentration of material at the front of the debris clouds and the opacity of the cadmium fragments to soft x-rays, very little internal detail was evident in the first view of the clouds. In addition, the large diametral expansion velocity associated with higher $t/D$-ratio debris clouds caused some of the off-



(a)                                   (b)
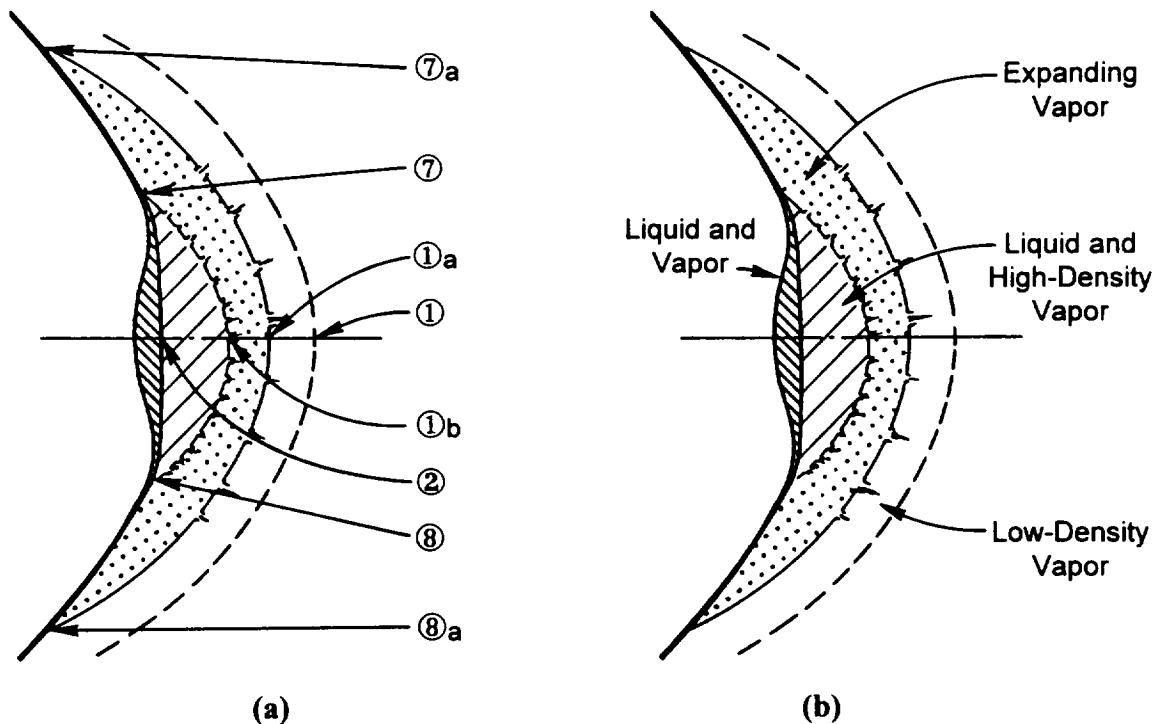
Figure 63. Illustration of the new debris-cloud features observed for the higher velocity cadmium-on-cadmium tests shown in Figures 61 and 62.

146

# TABLE 18

## NORMALIZED CADMIUM DEBRIS-CLOUD VELOCITY DATA

Velocity data have been normalized by dividing the various measured velocities by the impact velocity of the test. All bumpers were pure cadmium sheet. For Shots 4-1432 and 4-1442, normalized velocities of several additional points, shown in Figure 63, are preceded by the letter designation (in parentheses) of the points. Values shown without superscripts were determined using three views of the debris cloud. Values shown with superscripts were determined using the two views noted as superscripts

| Shot Number | $\frac{L}{D}$ | Impact Velocity, (km/s) | Normalized Debris-Cloud Velocities |
|---|---|---|---|

### Axial Debris-Cloud Velocities

| Shot Number | $\frac{L}{D}$ | Impact Velocity (km/s) | $V_1 / V_0$ | $V_2 / V_0$ | $V_3 / V_0$ | $V_4 / V_0$ | $V_{7,8} / V_0$ | $V_{9,10} / V_0$ |
|---|---|---|---|---|---|---|---|---|
| **Projectile - 5.95-mm-diameter, pure cadmium sphere. Nominal mass - 0.956 g.** | | | | | | | | |
| 4-1442 | 0.160 | 5.98 | $\sim 1.12^{1\text{-}2}$ | $0.933^{2\text{-}3}$ | $0.918^{2\text{-}3}$ | --- | $0.930^{2\text{-}3}$ | --- |
|  |  |  | (a) $1.09^{1\text{-}2}$ |  |  |  | (a) $\sim 0.79^{1\text{-}2}$ |  |
|  |  |  | (b) $1.01^{2\text{-}3}$ |  |  |  |  |  |
| **Projectile - 7.94-mm-diameter, pure cadmium sphere. Nominal mass - 2.265 g.** | | | | | | | | |
| 4-1443 | 0.160 | 2.27 | 0.920 | --- | --- | 0.687 | --- | $0.846^{1\text{-}2}$ |
| 4-4427 | 0.160 | 3.36 | 0.934 | $0.917^{2\text{-}3}$ | $0.911^{2\text{-}3}$ | $0.577^{1\text{-}2}$ | 0.917 | --- |
| 4-1432 | 0.160 | 5.00 | $\sim 1.05^{1\text{-}2}$ | $0.916^{2\text{-}3}$ | $0.922^{2\text{-}3}$ | --- | $0.926^{1\text{-}2}$ | --- |
|  |  |  | (a) $1.04^{1\text{-}2}$ |  |  |  | $0.912^{2\text{-}3}$ |  |
|  |  |  | (b) $0.98^{2\text{-}3}$ |  |  |  | (a) $0.856^{1\text{-}2}$ |  |

### Diametral Debris-Cloud and Spall-Shell Velocities

| Shot Number | $\frac{L}{D}$ | Impact Velocity (km/s) | $V_{7\text{-}8} / V_0$ | $V_{9\text{-}10} / V_0$ | $V_r / V_0$ | $V_{CTR} / V_0$ |
|---|---|---|---|---|---|---|
| **Projectile - 5.95-mm-diameter, pure cadmium sphere. Nominal mass - 0.956 g.** | | | | | | |
| 4-1442 | 0.160 | 5.98 | $\sim 0.19^{2\text{-}3}$ | --- | --- | --- |
|  |  |  | (a) $0.63^{1\text{-}2}$ |  |  |  |
| **Projectile - 7.94-mm-diameter, pure cadmium sphere. Nominal mass - 2.265 g.** | | | | | | |
| 4-1443 | 0.160 | 2.27 | --- | $0.410^{1\text{-}2}$ | 0.216 | 0.912 |
| 4-4427 | 0.160 | 3.36 | $0.089^{1\text{-}2}$ | --- | $0.286^{1\text{-}2}$ | $0.863^{1\text{-}2}$ |
| 4-1432 | 0.160 | 5.00 | $0.210^{1\text{-}2}$ | --- | --- | --- |
|  |  |  | $0.250^{2\text{-}3}$ |  |  |  |
|  |  |  | (a) $0.470^{1\text{-}2}$ |  |  |  |

axis points to move beyond the edge of the film in some of the views. Debris-cloud features for Shots 4-1432 and 4-1442 were transient and tended to diffuse and disappear before velocity determinations could be made using all three views. Consequently, most of the normalized velocities presented in Table 18 were determined using two instead of

the three x-ray views used for most of the aluminum tests. In Table 18, superscripts denote the views used to obtain the reported velocities. Values without superscripts were obtained using three views. In several instances, approximate values were given because features in one or both views could not be distinguished clearly.

Variation of the normalized velocities of the measurement points with impact velocity is shown in Figure 64. The general behavior of the points ①, ②, and ④ was similar to that observed for the aluminum tests in Figures 9b and 10b. Point ④ was not visible in the second or the third view of the debris clouds at the two higher velocities. Consequently, the velocity of this point could not be determined for these tests. Points ⑤ and ⑥ did not develop for the aluminum tests with a $t/D$ ratio of 0.16 or greater and did not develop for the cadmium tests with the same $t/D$ ratio. The behavior of points ⑦ and ⑧ was different for the cadmium and aluminum tests. In Figure 10b, the axial velocity of points ⑦ and ⑧ remained constant for the aluminum tests. In Shot 4-1432, points ⑦ and ⑧ were fairly distinct and their velocity could be determined using all three views. As
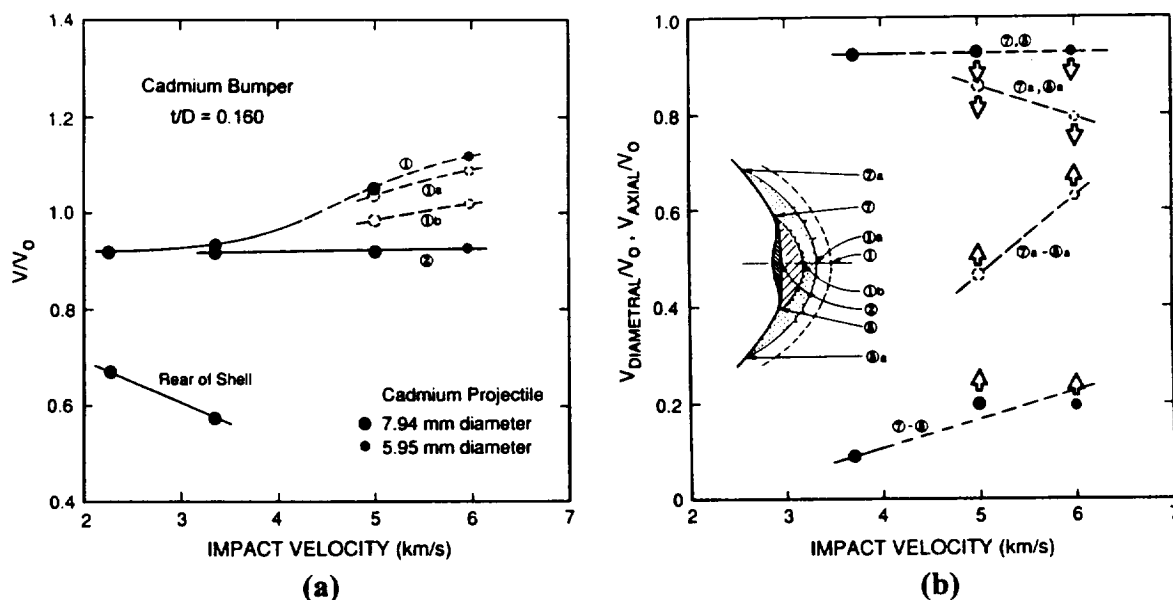


Figure 64. Normalized velocities of selected axial and diametral measurement points versus impact velocity for the cadmium tests shown in Figure 61.

148

shown in Table 18, two values were reported for these points. The normalized axial velocity of points ⑦ and ⑧, $V_{7,8}/V_0$, decreased, while the normalized diametral velocity of these points, $V_{7-8}/V_0$, increased as the cloud moved downrange for this test. The observed velocity differences of these points was the result of an expansion of the surface ⑦-①b-⑧ and the corresponding change in the intersection of this surface with the center element at points ⑦ and ⑧. Although the data in Figure 64b appear to indicate that the normalized velocities of points ⑦ and ⑧ were constant for the high-velocity cadmium tests, the values shown were merely the instantaneous values obtained using two views of the debris cloud. Arrows in the figure indicate that the instantaneous velocities of these points increased or decreased as the debris cloud developed.

Projectile and bumper-sheet material forming the front element are the most intensely shocked material in the debris cloud. Computations made by Anderson *et al.* [40] indicate that the residual temperature of the material in a cadmium-on-cadmium impact of 3 km/s or more, should be high enough to melt and vaporize a portion of the projectile and target. An adaptation of a figure taken from their work is presented in Figure 65. Shown on this figure are the results of their computations for cadmium and aluminum and the shot numbers for the cadmium and aluminum tests presented in this subsection and in Section III (Figure 7), respectively. The position, on the cadmium curve, of the particle velocities for the four cadmium tests indicated the shocked material will be in the liquid phase (Shot 4-1443) and the liquid-vapor mixed phase (Shots 4-1427, 4-1432, and 4-1442) following release from the shocked state.

Vaporous material at the front of the cloud is driven forward due to the expansion of the more highly compressed vapor in the interior regions of the front element. The forward motion of the surface ⑦-①b-⑧ produced as a result of the expansion, accounts for the previously described behavior of points ⑦ and ⑧. Expansion of the regions of high-density vapor produced a fuller and more rounded debris-cloud profile, and as the

149
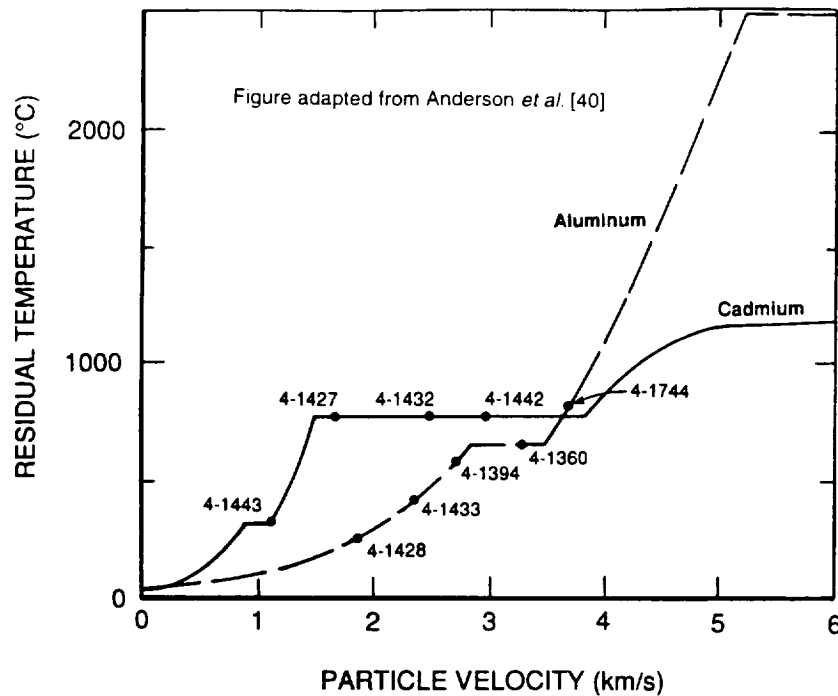
Figure 65. Estimated residual temperature versus particle velocity. Values were obtained using a Tillotson equation of state. Shot numbers are for tests discussed in text.

expansion process continued, these regions were exhausted and eventually disappeared. Diffusion of debris-cloud material and the inability to identify measurement points in the late-time-views of the high-velocity tests were noted earlier as the primary difficulties encountered during analysis of the radiographs of these tests.

A series of tests performed at UDRI (Konrad *et al.* [49]) for Sandia National Laboratories provided a radiograph of a debris cloud produced by the impact of a zinc sphere with a zinc sheet ($t/D$ = 0.167). The radiograph from this test is presented in Figure 66. The impact velocity of 6.73 km/s was high enough to cause vaporization of some bumper and projectile material. The additional front-element features shown in Figure 63 were evident in the front portion of the zinc debris cloud and were identical to those shown in Figures 61 and 62 for the cadmium test at 5.00 km/s (Shot 4-1432, $t/D$ = 0.160). Although the impact velocities of the cadmium and zinc tests were significantly different, the similarity of the morphological features of the debris clouds was striking. Similarity of debris-cloud structure has been observed in other UDRI tests involving

150
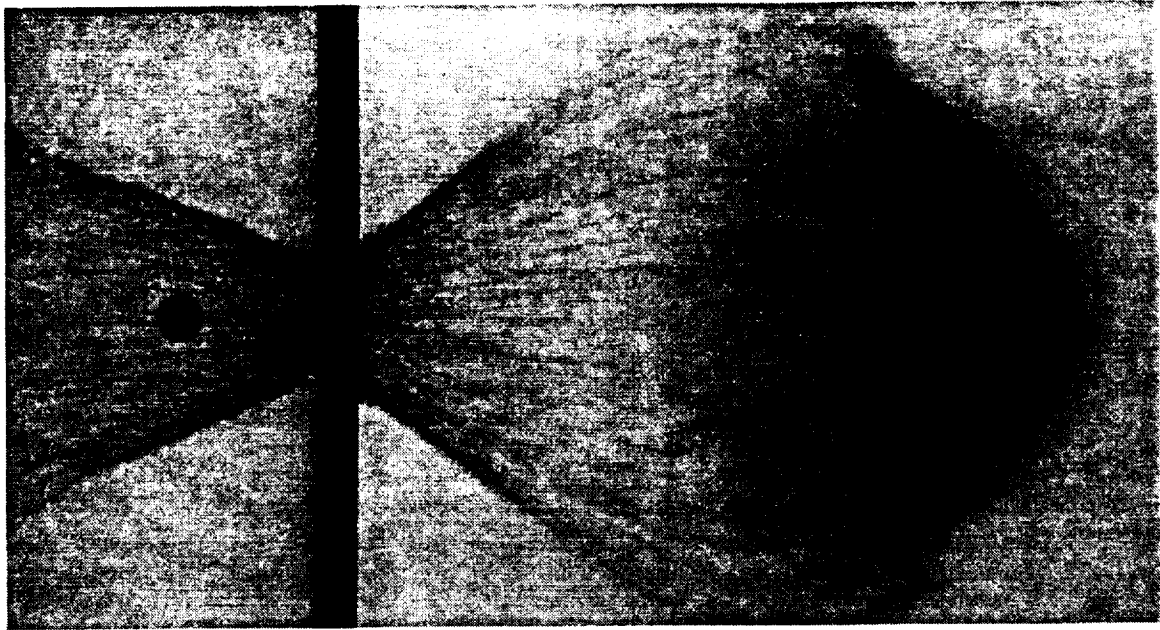
Figure 66. Radiograph of a debris cloud produced by the 6.73 km/s impact of a 5.76-mm-diameter zinc sphere with a 0.96-mm-thick zinc sheet ($t/D$ = 0.167, Shot 4-1522).

impacts of like materials (e.g., copper on copper, tantalum on tantalum, and steel on steel), particularly when the comparisons were made on the basis of $t/D$ ratio.

Early investigators used cadmium to examine the effects of melt and vaporization on debris-cloud behavior (see, for example, References 25 and 40). Later works examined the use of cadmium, zinc, or lead projectiles and targets as substitutes for aluminum projectiles and targets in scaled experiments to evaluate the response of an aluminum shield to the impact of an aluminum projectile at velocities well in excess of 7.5 km/s. A number of investigators have suggested various scaling techniques and low melting point materials for use in evaluating the response of candidate spacecraft shield systems to impacts of aluminum projectiles at velocities ranging from 7 to 18 km/s.

Mullin et al. [50] developed a set of dissimilar-material scaling relationships and evaluated them for use with tests in which cadmium and zinc would be used to model aluminum at higher impact velocities. They recommended preserving the geometry of the tests (i.e., same thickness, diameters, and spacing in the model and the prototype) and the

151

the use of the square root of the ratio of the heat of fusion of the model to the heat of fusion of aluminum as a velocity scaling factor. Mullin *et al.*'s recommended velocity scaling factor was 2.65 for cadmium and 1.95 for zinc. Holsapple [51] proposed a surrogate-material scaling relationship in which the scaling factor was based on the square root of the ratio of the static and dynamic values of energies required for: (1) heat to melt; (2) melt; (3) heat from melt to vaporization; and (4) vaporization for cadmium and aluminum. The square root of this ratio was typically $3.1 \pm 0.1$.

Schmidt *et al.* [48] used geometric size scaling and adopted a velocity scaling factor of 3.1 for a series of tests employing cadmium spheres and targets that were intended to simulate the high-velocity impacts of aluminum spheres with aluminum shields. Later, when the debris clouds produced by the scaled, lower velocity cadmium tests described by Schmidt *et al.* were compared with their aluminum counterparts by Poormon and Piekutowski [52], differences in the normalized expansion velocities of cloud features and the size of fragments in the debris cloud were observed. Normalized expansion velocities and fragment sizes for the cadmium and aluminum debris clouds were nearly the same when the velocity scaling factor was adjusted from a value of 3.1 to a value of $2.0 \pm 0.1$. This scaling factor of 2 was very close to the ratio of the shock velocity of aluminum to the shock velocity of cadmium. The apparent relationship to shock velocity, for these lower velocity cadmium and aluminum impact tests, was not surprising since propagation of the impact-induced shock in the projectile and target were directly responsible for the disintegration of these materials.

Although the comparisons of the structural features of aluminum and cadmium debris clouds by Poormon and Piekutowski were limited to two $t/D$ ratios and two impact velocities, many features of the debris clouds were similar (e.g., fragment size and normalized velocities of the measurement points in the clouds). Extension of the structure and properties of the higher velocity cadmium and zinc debris clouds to higher

velocity aluminum debris clouds (i.e., high enough to induce vaporization) appeared to be reasonable. All evidence presented in this report would indicate that the 11 or 12 km/s impact of an aluminum sphere with a thin aluminum sheet would produce a debris cloud with the features exhibited by the two higher velocity cadmium debris clouds shown in Figure 61 and the zinc debris cloud shown in Figure 66. A definitive comparison of a vaporous aluminum debris cloud with a scaled, vaporous cadmium or zinc debris cloud will continue to remain a much desired but elusive object of attention.

A final comment regarding the formation of vaporous debris clouds has to do with damage that may be inflicted on a shield structure by the high-pressure vapor produced by the impact. In most of the higher velocity cadmium tests performed for Boeing Defense & Space Group, failure of the main wall was the result of bulging and rupture due to the impulsive and pressure loads applied by the debris cloud. Bulging and deformation of the bumper sheet was also observed. In those cases where a rupture of the main wall did not occur, bulging and deformation of the bumper sheet appeared to be more severe, probably because debris-cloud vapor pressure between the bumper and the main wall was not relieved by failure of the main wall. It is conceivable that a section of spacecraft wall subjected to a high-velocity impact would resist penetration and rupture but would "fail" because of a loss of the bumper sheet and/or intermediate wall components as a result of excessive pressure buildup inside the wall following the impact.

## D. Shock Propagation in Bumper Sheet

When a sphere impacts a thin sheet at hypervelocity, a shock forms and propagates into the sheet. After a short period of quasi one-dimensional loading, during which the material in front of the sphere is driven forward, the shock in the sheet expands and, as shown in Figure 32 at $\tau = 0.4$ and $0.6$ $\mu$s, the perimeter of the shock turns and begins to

travel through the sheet. The intensity of the shock and the extent of its influence on the sheet material is a function of the *t/D* ratio and the impact velocity of the sphere.

From Figure 37, it was clear that the shock front in a sheet experiencing a 6.7-km/s impact will outrun the surface of the advancing sphere for all but the initial, brief period of quasi one-dimensional loading. An implication of this circumstance is that, during most of its encounter with the bumper sheet, the sphere will contact material that has been shocked and disturbed. The extent of the shock-induced disturbance in the sheet during impact is shown in the radiograph presented in Figure 67. The rear of the sphere shown in this figure was struck by a chip of steel from the sabot-stripper plate. Debris from the sabot-stripper plate or from the impact of the chip with the sphere pretriggered the x-ray sources by several microseconds and "caught" the sphere when it was half way through the sheet, or about 0.7 μs after impact. In the radiograph, the center of the 9.53-mm-diameter sphere was shown coincident with the front or impacted surface of the sheet. At
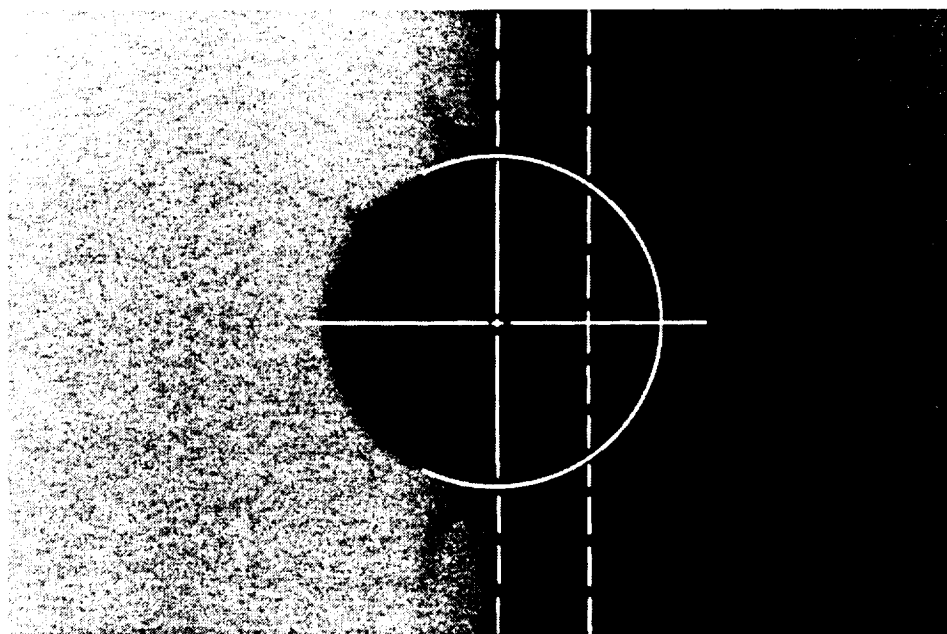


Figure 67. Radiograph of a 9.53-mm-diameter, 2017-T4 aluminum sphere taken 0.7 μs after impact with a 2.22-mm-thick, 6061-T6 aluminum sheet at 6.66 km/s. Solid and dashed white lines show the pre-impact configuration of the sphere and bumper sheet, respectively.

154

the time the radiograph was made, the thickness of the bumper sheet had increased considerably in the region surrounding the embedded sphere. The location, on both sides of the sheet, of the points where an increase in the thickness of the bumper was first evident indicated that the shock in the bumper was nearly normal to the surface of the sheet at the time the radiograph was made. In addition, the front of the sphere and the bumper sheet were highly compressed and a well-developed ejecta veil had formed on the front side of the sheet. Clearly, a strong shock had propagated in the bumper sheet and the hole-formation process was well underway. The sequence of bumper-sheet cross sections presented in Figure 26 demonstrated that the hole-formation process could produce a variety of morphological features in the region adjacent to the holes. The prominence of one feature over another was a function of $t/D$ ratio. Processes that were latent for tests with low $t/D$ ratios appeared to dominate the formation of lip-region features for tests with high $t/D$ ratios. When the $t/D$ ratio was low, a small lip formed on both sides of the sheet and surrounded the hole. At intermediate $t/D$ ratios, the lip grew and formed an overturned flap which developed localized voids and cracks that led to the separation of flap material from the bumper sheet. As material separated from the sheet, a thin web of material at the center of the sheet served to retain a wedge-shaped ring of material that was originally closer the impact site. At large $t/D$ ratios, the wedge-shaped ring detached from the bumper sheet and appeared to force the sheet to split apart.

An enlarged view of the cross section of the bumper sheet for the $t/D = 0.424$ test (Shot 4-1353) is shown in Figure 68 to illustrate the detached, wedge-shaped ring and overturned flap that were formed in the bumper used for this test. Although certain details of this cross section were discussed when a reduced-size view was presented in Section V, details of several of the features will be reviewed for the purpose of further discussion in this subsection. The smooth appearance of the surfaces of the wedge facing the split in the bumper (arrows) indicated that these surfaces were probably smoothed by

155

Figure 68. Cross section of a portion of the bumper sheet taken from the edge of the hole formed by the 6.68 km/s impact of a 9.53-mm-diameter, 2017-T4 aluminum sphere with a 4.04-mm-thick, 6061-T6 aluminum sheet (Shot 4-1353).

a sliding contact with the undersides of the overturned flaps of material on either side of the split in the bumper sheet. The inner surface of the flap shown in Figure 68 is smooth, indicating that some form of sliding contact occurred along this surface.

The large split in the bumper sheet was formed when the release waves generated at both free surfaces of the sheet met and produced the significant tensile stresses that led to a tensile failure along the center of the sheet. Additional growth of the crack could

have occurred when the momentum of particles in the wedge-shaped ring drove the wedge into the crack and applied additional tensile loads to the region at the tip of the crack. However, the hole-growth processes deteriorated quickly when the outwardly moving shock was transformed into a weaker elastic wave as a result of geometric dispersion of the shock and the interaction of the release waves with the stressed region of the bumper.

The cracks in the overturned flap shown in Figure 68 were probably formed when tensile stresses associated with the passage of release waves exceeded the spall strength of the sheet and formed cracks at several levels below the surface of the sheet. A similar system of cracks was formed in the flap that developed in the lower half of the sheet. Several of the cracks are visible at the damaged end of the lower section of the sheet. Pieces of material from the lower flap were the last fragments to be ejected as part of the external bubble of debris produced by the test. They were separated from the sheet when the bending stresses at the hinge point of the flap became excessive and the hinge failed. A significant reduction in the cross section of the hinge point of the flap was evident in the micrograph, indicating that the material in the flap was close to being ejected when shock-induced activity in the sheet terminated. The overturned flap was noticeably thinner than the material forming the upper part of the sheet in the split section, particularly in the region around the hinge point. It is likely that the missing material was spalled from the surface of the sheet during the later stages of growth of the ejecta veil.

In the sequence of bumper cross sections presented in Figure 26, it was clear that the formation of the wedge-shaped ring was fairly complete when the $t/D$ ratio was 0.163 or greater for impacts at 6.7 km/s. However, the wedge-shaped ring remained attached to the bumper until the $t/D$ ratio was greater than 0.234 but less than 0.424. The cross section of the $t/D = 0.102$ test shown in Figure 26 (Shot 4-1283) appeared to suggest that a rudimentary wedge may have developed for this test. The bumper section for Shot 4-1283 was etched and photographed using a differential-interference-contrast micrographic

technique to produce the micrograph shown in Figure 69. The micrograph of the bumper section exhibited numerous voids in the folded and distorted stratigraphy of the sheet. In the region where the grain structure was still somewhat parallel to the edges of the sheet (i.e., the left side of the figure) the voids tended to be circular while the voids in the disrupted portion of the sheet tended to be elliptical. In those regions where the
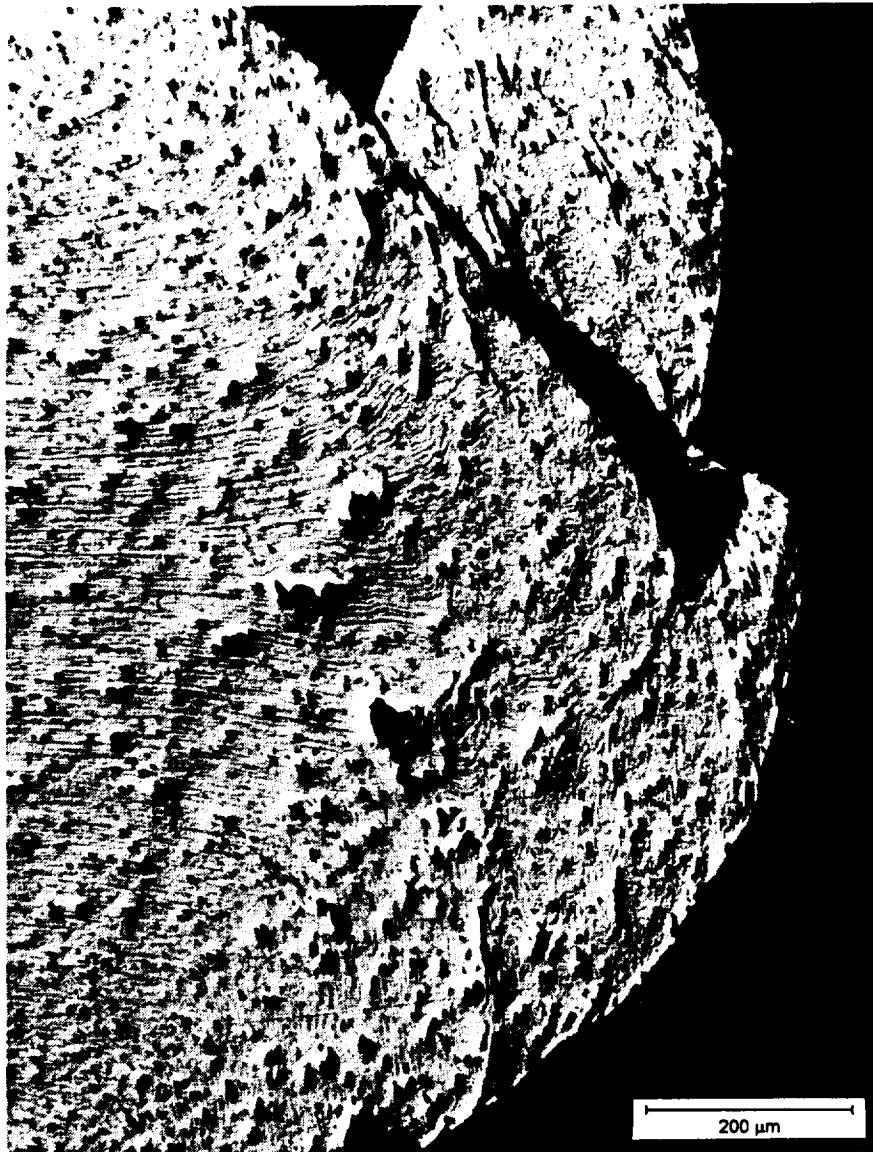


Figure 69. Micrograph of a portion of the bumper sheet taken from the edge of the hole formed by the 6.72 km/s impact of a 9.53-mm-diameter, 2017-T4 aluminum sphere with a 0.97-mm-thick, 6061-T6 aluminum sheet (Shot 4-1283). The section is shown with the impacted side at the top of the figure.

158

stratigraphy was severely distorted, the voids were flattened and gave the *appearance* of microcracks or shear failures. In their examination of the micrographs of the impacted ends of 6061-T6 aluminum rods, Shockey *et al.* [42] indicated that similar voids were initiated preferentially at inclusions of magnesium silicate. They also indicated that aluminum has a low propensity for a shear localization mode of failure and that these types of failure were not prevalent in the sectioned rods they examined. Localized shear failures do not appear to be prevalent in the bumper section presented in Figure 69.

Study of the grain structure exposed in Figure 69 provides insight into the processes that led to the development of the distorted stratigraphy exhibited in the micrograph and the effects of shock propagation in the bumper. The general flow of the severely distorted material closest to the hole opening (i.e., the right side of the figure) indicated that significant, outwardly-directed, radial forces were applied to this material from the inside of the hole. Essentially all of the voids in this material were closed, indicating that the voids were formed before the radial loads were applied. The voids in the material away from the edge of the hole remained circular. The flow of the grain structure in the left half of the figure indicated the tendency of the material in this region to separate, or at least establish a flow field that promoted additional separation of this material. Of interest were several large voids near the center of the sheet. These large voids appeared to form when several small voids coalesced, apparently as a result of excessive tensile loads in this region of the sheet. The "flow" pattern of material in the central part of the micrograph, as well as the location of the larger voids, tended to indicate the impending formation of the ring and thin web of material seen in the bumper-sheet cross sections shown in Figure 26 for tests with $t/D$ ratios of 0.163 or greater. It is worth noting that several large voids were also evident near the tip of the wedge shown in Figure 68.

Except for a relatively small central plug of material directly below the sphere, the bulk of the bumper material that is in the path of the impacting sphere is shocked and

159

disturbed before being contacted by the sphere. As the sphere advanced through the disturbed material, a secondary "shock" was driven into the void-filled bumper material. Momentum acquired by particles behind the shock in the virgin material and the secondary "shock" in the "porous" material caused the portion of the bumper nearest the sphere to apply a radial load to the bumper, and promoted severe compression, fracture, fragmentation, and ejection of bumper material as fragments in the ejecta veil and external bubble of debris. The grain structure, voids, and cracks displayed in the micrographs of the bumpers were the last features formed as the shock-related activities ceased.

Several investigators have described hole formation as a two-stage process. Bjork [41] and Backman and Finnegan [53] described the first stage as a plugging type process in which the impacting projectile simply drives target material forward. They go on to describe a second stage in which further growth of the hole is driven by momentum in the target sheet. Turpin and Carson [30] also noted that hole growth appeared to be a two-stage process, but did not describe the processes. The various processes described in this subsection required a minimum impact velocity and $t/D$ ratio to be fully "activated." While the $t/D$ = 0.424 test at 6.68 km/s (Shot 4-1353) exhibited significant disruption of the bumper sheet, a test with a $t/D$ ratio of 0.504 (Shot 4-1721) and an impact velocity of 2.23 km/s did not. If the energy that controlled hole growth was the energy that was deposited during the quasi one-dimensional phase of loading of the sphere and bumper sheet, the bumper-hole diameter should be a strong function of impact velocity. Data presented in Section V showed that hole diameter was a strong function of $t/D$ ratio and a weak function of impact velocity. Detailed microscopic examinations of bumper-sheet sections from tests with other combinations of impact velocity and $t/D$ ratio will provide additional information that can be used to more fully describe the details of mechanisms associated with the propagation of the impact shock in the bumper sheet.

160

# SECTION VII. WITNESS-PLATE DAMAGE PATTERNS

The damage patterns produced by the debris clouds were recorded, for 34 of the tests, on aluminum witness plates placed about 38 cm downrange of the bumper plate. Two-inch-thick hardwood planks were used for four tests to minimize damage to the x-ray film which occurred when heated fragments that were ejected from the aluminum witness plates came to rest on the film cassettes. Foam blocks were used for five tests in which the projectiles were recovered. Damage patterns produced on the wooden planks and the foam blocks were not documented.

Three alloys and several thicknesses of aluminum plates were used as the witness plates. Use of a particular alloy was dictated by the availability of the material in the laboratory at the time of the test and no other reason. Plate thickness was selected on the basis of the anticipated level of damage. Generally, the plate was thick enough to prevent a blowout type of failure but was thin enough to permit the formation of surface features on the rear of the plate. Following is a listing, by thickness and alloy, of the aluminum witness plates used for the tests: (1) 2.03-mm-thick, 6061-T6 (1 test); (2) 6.35-mm-thick, 6061-T651 (17 tests), 12.7-mm-thick, 6061-T651 (4 tests), 25.4-mm-thick, 6061-T651 (2 tests); (3) 3.18-mm-thick, 2219-T81 (1 test); (4) 3.18-mm-thick, 2219-T87 (1 test); and (5) 3.18-mm-thick, 5456-H116 (7 tests). Although most of the witness plates were perforated, the posttest condition of the plate (perforation/no perforation) was of secondary interest. The purpose of the plate was to provide a good record of the damage pattern produced by the impact of the projectile and bumper fragments.

Damage patterns produced by seven tests with a nominal impact velocity of 6.7 km/s are shown in Figure 70 for various $t/D$ ratios. In this figure, all plates are shown at the same scale to illustrate the spread of the internal structure of the debris cloud, the damage pattern produced by the external bubble of debris, and the diameter of the hole produced
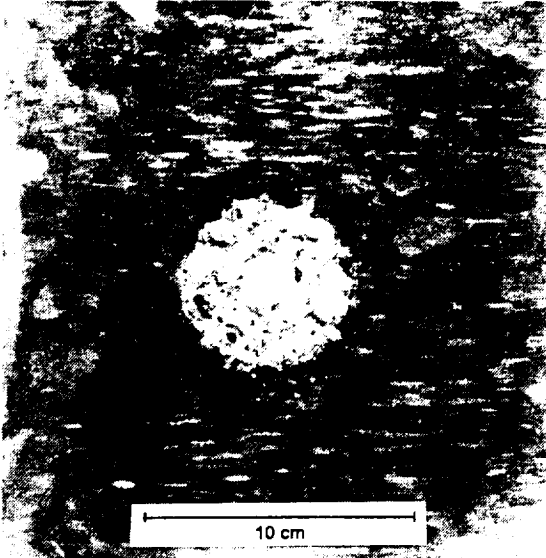
4-1395    **t/D = 0.026**    6.70 km/s
12.7-mm-thick, 6061-T651 plate
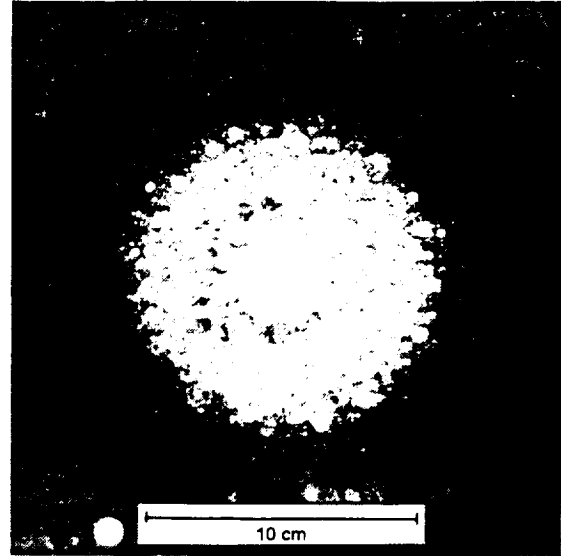
4-1360    **t/D = 0.049**    6.62 km/s
6.35-mm-thick, 6061-T651 plate
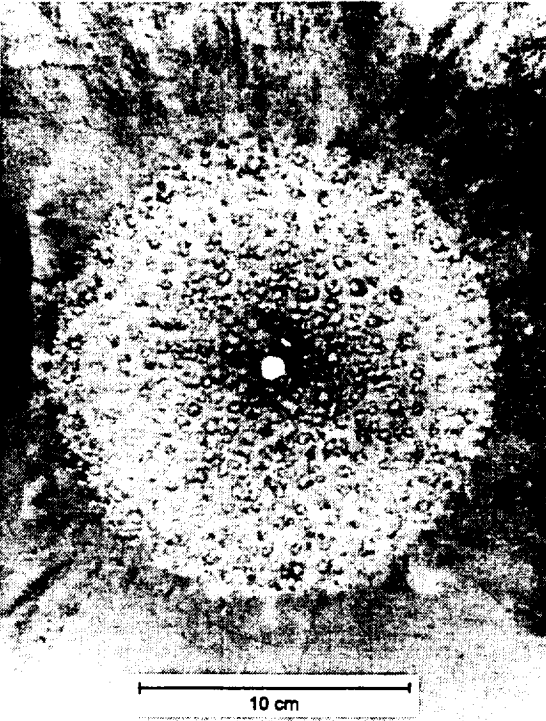
4-1287    **t/D = 0.084**    6.74 km/s
6.35-mm-thick, 6061-T651 plate
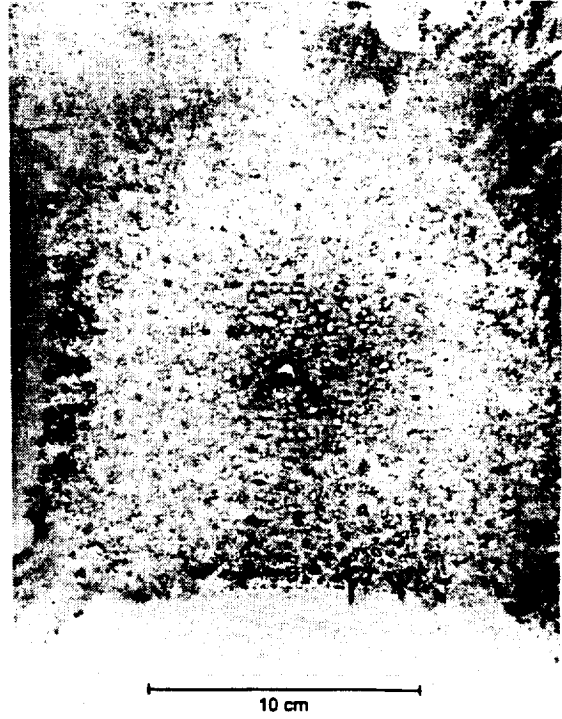
4-1283    **t/D = 0.102**    6.72 km/s
6.35-mm-thick, 6061-T651 plate

Figure 70. Damage patterns produced by debris clouds formed by the impact of 9.53-mm-diameter, 2017-T4 aluminum spheres with various thicknesses of 6061-T6 aluminum sheets at a nominal impact velocity of 6.7 km/s.

162
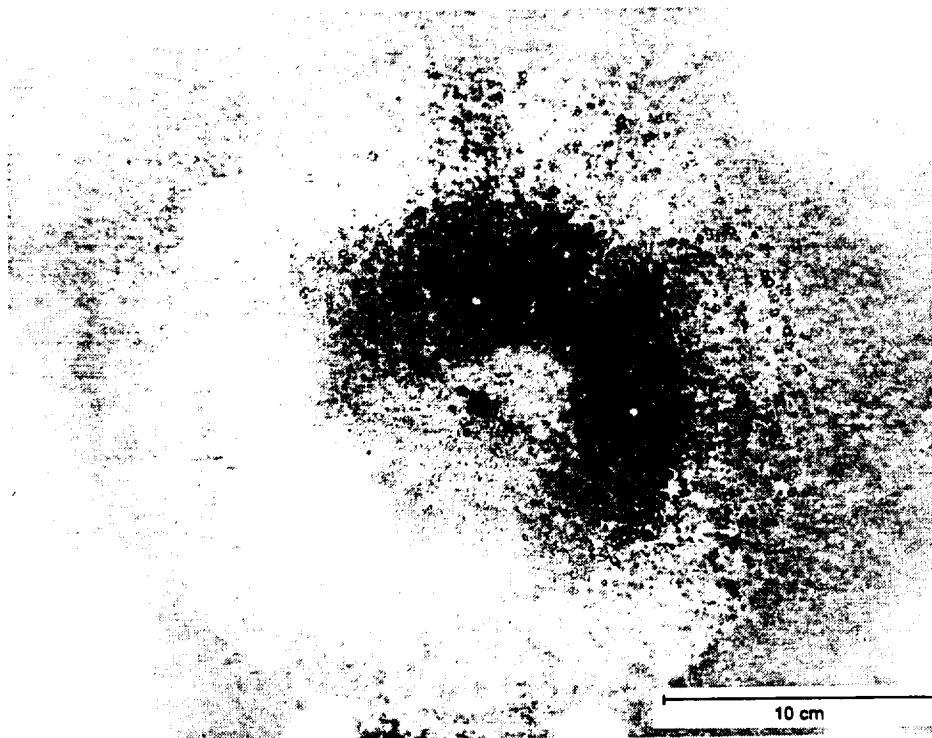
**t/D = 0.163**

4-1291
6.71 km/s
3.18-mm-thick,
2219-T87
plate
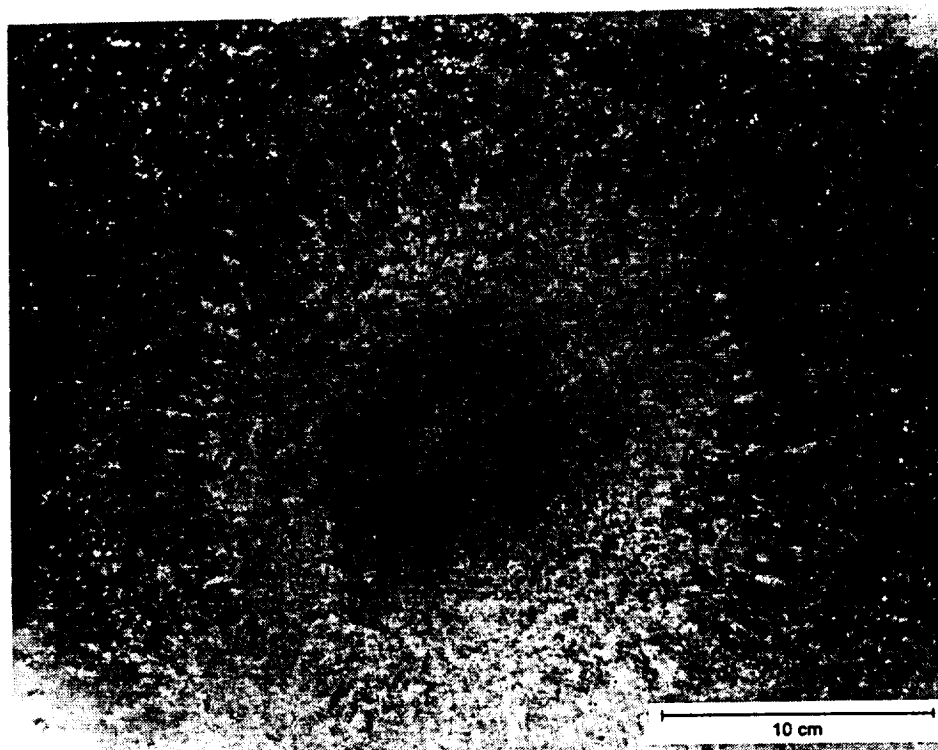
**t/D = 0.234**

4-1352
6.64 km/s
3.18-mm-thick,
5456-H116
plate

Figure 70. (Continued). Damage patterns produced by debris clouds formed by the impact of 9.53-mm-diameter, 2017-T4 aluminum spheres with various thicknesses of 6061-T6 aluminum sheets at a nominal impact velocity of 6.7 km/s.

t/D = 0.424

4-1353
6.68 km/s
3.18-mm-thick,
5456-H116
plate

10 cm

Figure 70. (Concluded). Damage patterns produced by debris clouds formed by the impact of 9.53-mm-diameter, 2017-T4 aluminum spheres with various thicknesses of 6061-T6 aluminum sheets at a nominal impact velocity of 6.7 km/s.

by the impact of the large central fragment with the witness plate. As shown in Figure 70, the witness plate damage patterns consisted of heavily cratered, circular areas that were surrounded by numerous small, randomly-spaced, craters and pits. As the $t/D$ ratio of the test increased, the following changes in the damage-pattern features were noted: (1) the diameter of the damaged area increased; (2) a second circular pattern of craters formed inside the main damage area; (3) the depth and diameter of the craters in the damage area decreased; and (4) the size of the craters in the region surrounding the circular area increased. A simple comparison of the features of the damage patterns with the radiographs of the debris clouds indicated that the craters in the circular region were produced by the bumper and projectile fragments that made up the internal structure of the debris cloud and the random pattern of craters outside the circular region was formed

164

by the impact of fragments in the external bubble of debris. A more detailed description of the origin of fragments in the circular region is presented later in this section.

The witness plates for the low-$t/D$-ratio tests exhibited a single large hole or set of interconnected holes at the center of the damage pattern. The size and the velocity of the large central fragment for the test with a $t/D$ ratio of 0.026 was sufficient to perforate a 12.7-mm-thick plate. The large central fragment for the tests with a $t/D$ ratio of 0.049, 0.084, and 0.102 were capable of perforating the 6.35-mm-thick witness plates. The large central fragment for the $t/D = 0.163$ test failed to perforate the 3.18-mm-thick witness plate. A cluster of craters, slightly larger and deeper than the surrounding craters, was produced at the center of the damage pattern for this test (Shot 4-1291). Large central fragments were not observed in the debris clouds of tests with $t/D$ ratios of 0.234 or greater. A very uniform pattern of small, evenly distributed craters was produced when the $t/D$ ratio was 0.234. The damage pattern produced by the test with a $t/D$ ratio of 0.424 (Shot 4-1353) exhibited a large number of fairly deep craters over the entire surface of the 38-cm-square witness plate. Although the fragments that produced the deep craters did not perforate the witness plate, spall failures were observed on the rear surface of the plate below many of the larger craters. It is reasonable to speculate that the perforation of a 3.18-mm-thick witness plate could occur for tests in which the $t/D$ ratio was greater than 0.424. Although the velocity of the fragments produced by the higher $t/D$-ratio tests would decrease, the size of the bumper fragments in the external bubble of debris would increase. The resulting combination of external-bubble fragment size and velocity could be capable of perforating a 3.18-mm-thick plate. As the $t/D$ ratio increased beyond the range where perforation occurred, the lethality of the bumper fragments would be reduced and rear wall integrity would be maintained.

Damage patterns produced by five tests in which the $t/D$ ratio was held constant at 0.049 and the impact velocity was varied from 3.77 km/s to 7.38 km/s are shown in Figure 71.

**3.77 km/s**

4-1428

t/D = 0.049

6.35-mm-thick,
6061-T651
plate
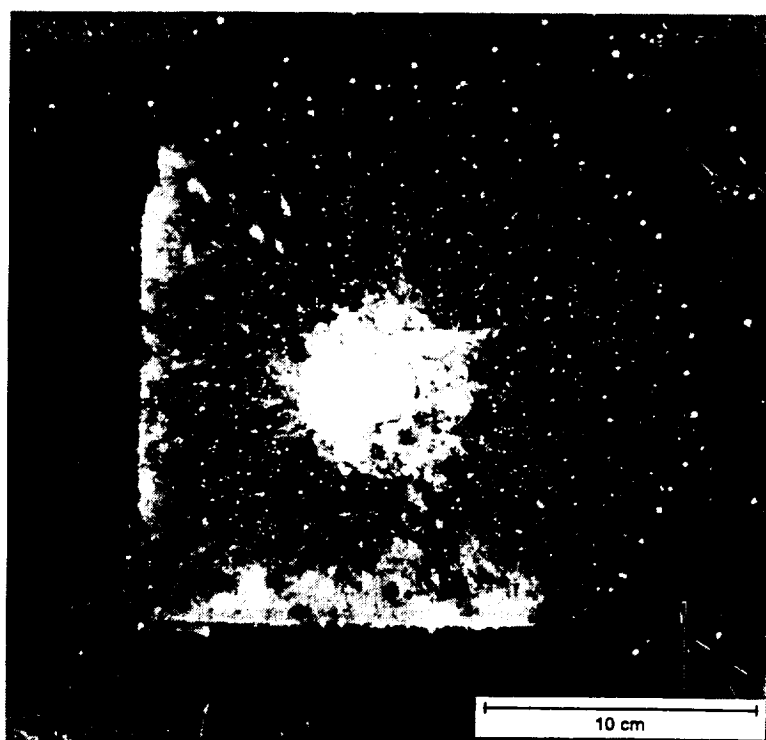


**4.71 km/s**

4-1433

t/D = 0.049

6.35-mm-thick,
6061-T651
plate

Figure 71. Damage patterns produced by debris clouds formed by the impact of 9.53-mm-diameter, 2017-T4 aluminum spheres with 0.047-mm-thick, 6061-T6 aluminum sheets. Impact velocity was varied as noted.

166
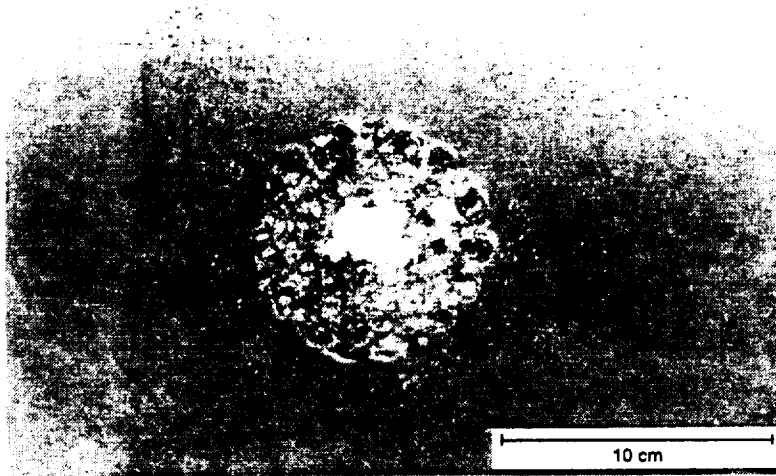
**5.45 km/s**

4-1394
t/D = 0.049
6.35-mm-thick,
6061-T651
plate
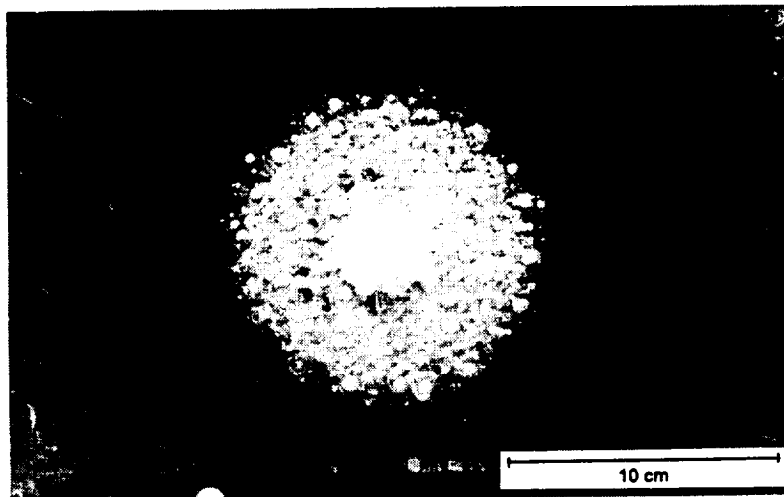
**6.62 km/s**

4-1360
t/D = 0.049
6.35-mm-thick,
6061-T651
plate
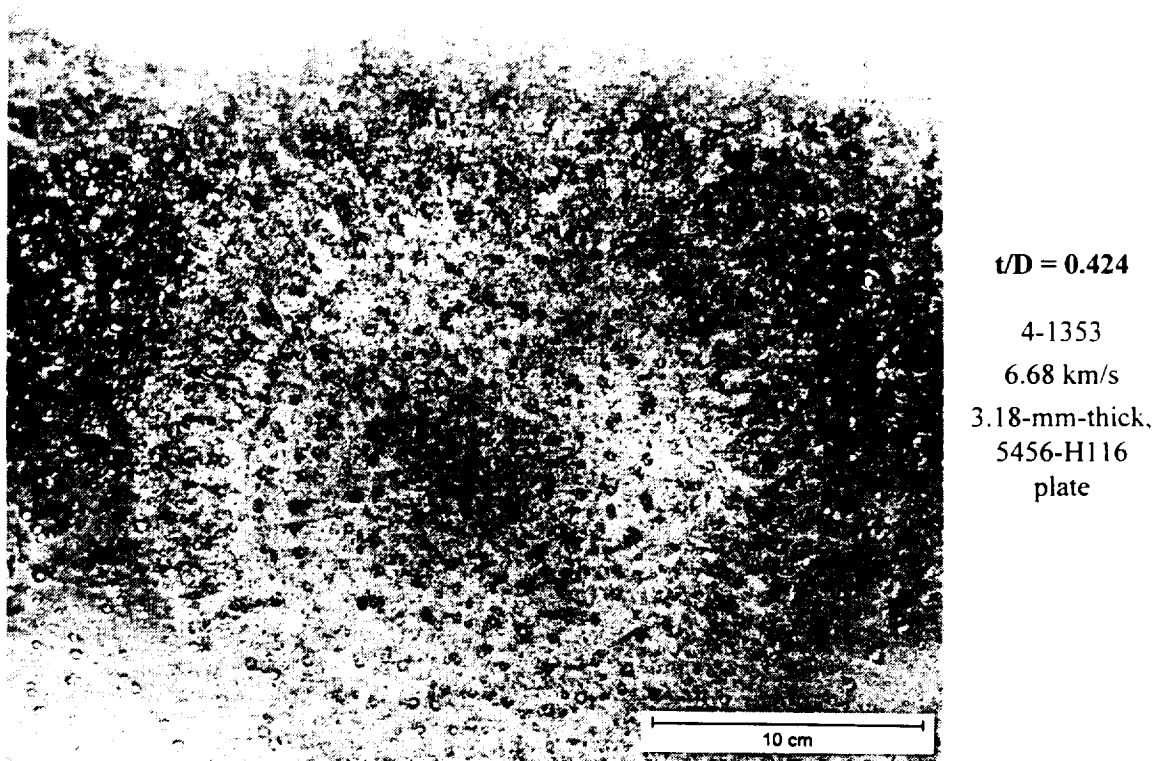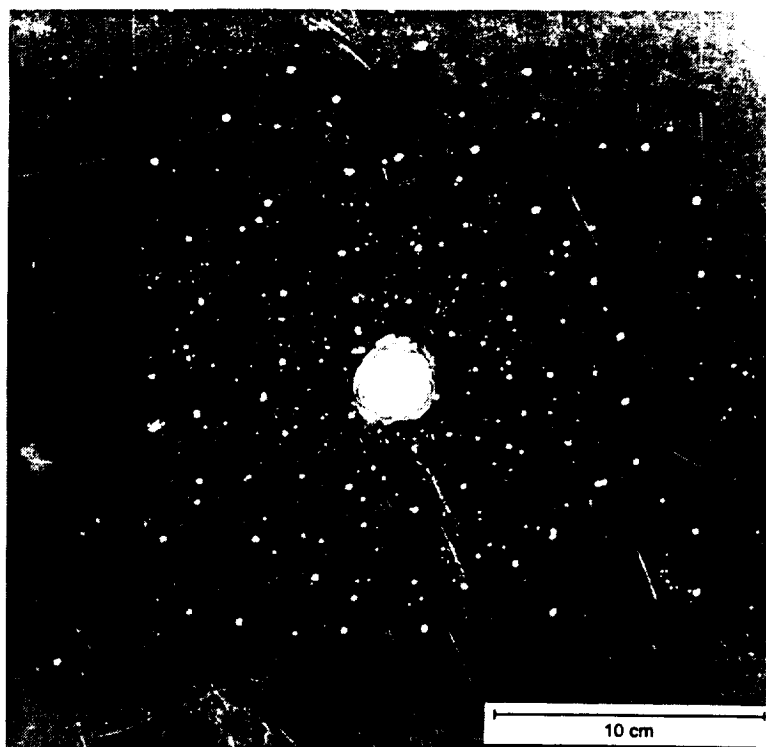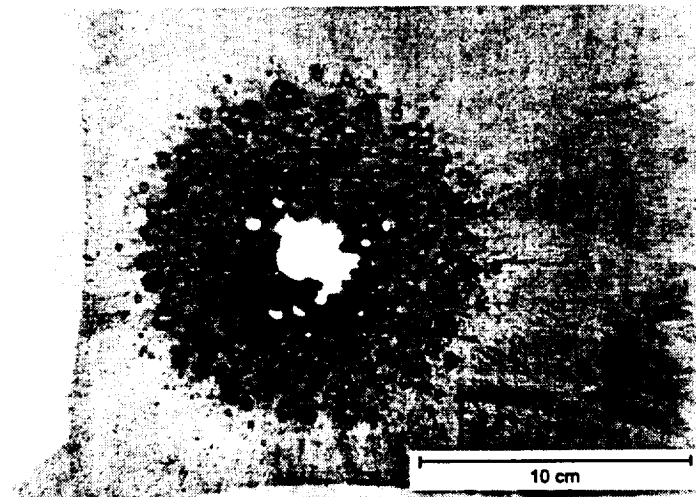
**7.38 km/s**

4-1744
t/D = 0.049
6.35-mm-thick,
6061-T651
plate

Figure 71. (Concluded). Damage patterns produced by debris clouds formed by the impact of 9.53-mm-diameter, 2017-T4 aluminum spheres with 0.047-mm-thick, 6061-T6 aluminum sheets. Impact velocity was varied as noted.

Radiographs of the debris clouds that produced the damage patterns on the witness plates shown in Figure 71 were presented in Figures 7 and 36. Since the sphere did not break up for the test at 3.77 km/s (Shot 4-1428), a single large hole was produced in the witness plate for this test. The hole is surrounded by a pattern of evenly-distributed but widely-scattered craters produced by the impact of bumper fragments. A number of the large fragments at the periphery of the center element (see Figure 36) for the test at 4.71 km/s (Shot 4-1433) perforated the 6.35-mm-thick witness plate at the edge of the central damage pattern. The impact of these fragments and the large central fragment resulted in a portion of the plate being "blown" from the plate. The ring of small craters, evident at a radius of about 11 cm from the center of the damage pattern, was produced by the impact of bumper fragments in the external bubble of debris. Aluminum spray deflected from the plastic sheets that were used to protect the x-ray film cassettes, produced the pattern of light markings seen on the plate for Shot 4-1433. The witness plate for this test (and for a number of other tests shown in this section) was partially shielded by the film cassettes that were placed along the left side and at the bottom of the plate and extended to within 10 mm of the front surface of the witness plate.

As impact velocity increased, the outer diameter of the damage pattern increased. However, the rate at which the diameter grew appeared to decrease as the velocity increased. The "diameter" of the opening at the center of the pattern did not appear to change as impact velocity was increased. The diameters and depths of the craters and pits formed by the impact of the fragments in the external bubble of debris decreased as impact velocity was increased. Damage produced by the fragments or molten droplets of debris for the 7.38 km/s test (Shot 4-1744) consisted of an even distribution of very small pits, most with diameters of much less than 0.5 mm.

The rear surfaces of a number of the witness plates exhibited spall failures that were more or less circular. An example of the type of spall failure that formed on the rear

surface of the witness plates is presented in Figure 72. The spall pattern was very pronounced for tests with lower $t/D$ ratios, even for the tests which used 12.7 and 25.4-mm-thick witness plates. The rear surfaces of the witness plates from Shots 4-1291 and 4-1352 ($t/D$ = 0.163 and 0.234, respectively) also exhibited a spall failure in the center of the damaged area; however, the spall was not a well-defined feature of these plates. The concentric rings shown in the damage pattern for Shots 4-1291 and 4-1252 and the spall failures observed for most of the tests were formed during the impact of the various elements that make up the debris-cloud internal structure. Views of the front and rear surface of an overmatched, 3.18-mm-thick witness plate are shown in Figure 73. Also shown at the top of the figure is a radiograph of the debris cloud that produced the damage pattern. In the figure, various features of the debris cloud were related to features in the



Front of Plate                    Rear of Plate
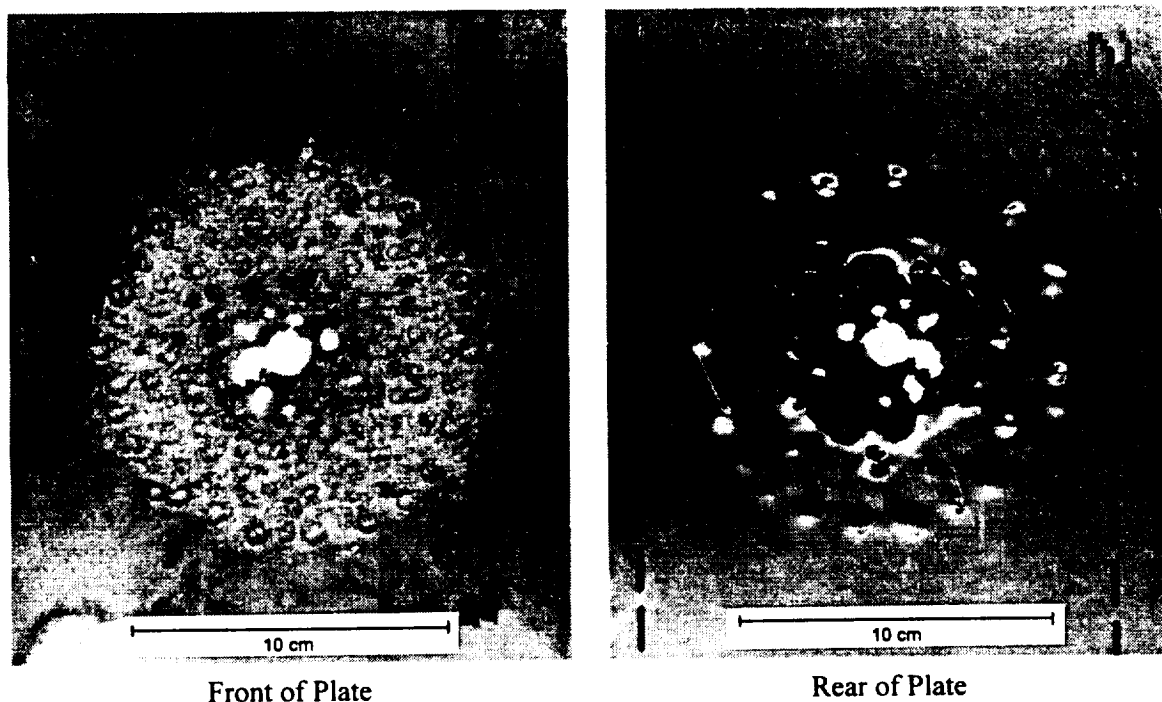
Figure 72. Views of the front and rear of a 6.35-mm-thick, 6061-T651 aluminum witness plate showing the damage pattern and spall failure produced on the front and rear of the plate, respectively. The plate was struck by the debris cloud formed by the 6.58 km/s impact of a 9.53-mm-diameter, 2017-T4 aluminum sphere with a 0.51-mm-thick, 2024-T3 aluminum sheet (Shot 4-1284).

169
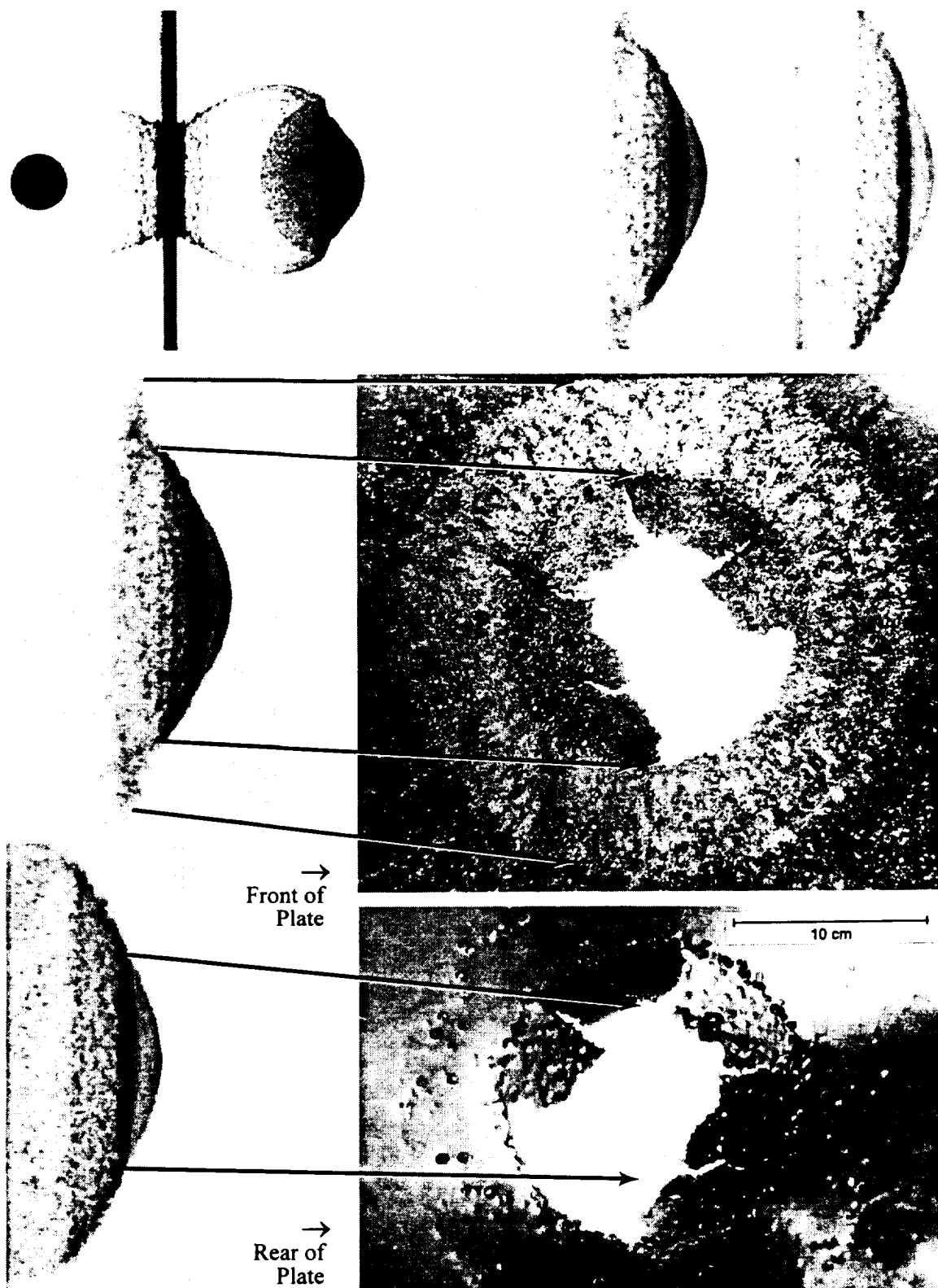
Figure 73. Views of the front and rear of a 3.18-mm-thick, 5456-H116 aluminum witness plate and radiograph of the debris cloud that produced the damage. Connecting lines relate structures in the debris cloud to features in the damage patterns on the front and the rear of the plate. (See text for test details, Shot 4-1357.)

170

damage pattern on the plate. The debris cloud was formed by the 6.38-km/s impact of a 12.70-mm-diameter, 2017-T4 aluminum sphere with a 2.03-mm-thick, 2024-T3 aluminum sheet (Shot 4-1357, $t/D = 0.160$). The debris-cloud features responsible for the witness-plate damage pattern can be matched to features on the plate by simply computing the diameters of the debris-cloud elements at the times they struck the witness plate and comparing these diameters to the features on the witness plate. (The diameters of the debris-cloud elements can be computed using the information provided in Tables 3 and 4.) The comparison was made easier for this test because the witness plate had been over-matched by the debris cloud and several damage features not clearly evident in the damage patterns for similar tests using thicker witness plates were evident on this plate.

Three witness-plate damage features are shown in Figure 73. They are: (1) an outer ring, (2) an inner ring, and (3) a spall ring. In the higher velocity, low-$t/D$-ratio tests, the diameter of the center element was larger than the diameter of the front element and the spall shell. In the higher velocity, high-$t/D$-ratio tests, the radial growth of the center element was suppressed because the periphery of the element interfered with the edge of the hole in the bumper. As shown in Figure 73, the inner ring was produced by the impact of fragments at the periphery of the altered center element. The spall shell was just beginning to form when the rear of the sphere passed through the hole in the bumper and was not affected by interference with the bumper. The impact of fragments at the periphery of the spall shell produced the outer ring shown in the figure.

The front surface of the front element of the debris clouds produced by the higher velocity, low-$t/D$-ratio tests was fairly continuous and flat faced (see Figure 40). The impact of the front element was capable of forming and propagating a shock in the witness plate. When the shock was reflected at the free, rear surface of the plate, a spall failure of the rear surface of the sheet could occur and form a spall ring similar to the one shown on the rear of the plate in Figure 72. Damage resulting from the impact of the front element,

the spall failure, and the impact of the center-element debris combined to remove the central part of the witness plate shown in Figure 73. Although not evident in the photograph of the rear surface of this plate, the remnants of a spall ring remained at the end of the petal shown along the right side of the central opening. The heads of the arrows projected from the front element in the radiograph at the lower right of the figure indicate the approximate diameter of the spall ring that was formed for this test.

The circularity of the inner and outer rings in the damage patterns was remarkable. The damage pattern produced by the debris cloud formed by the disintegration of the 12.70-mm-diameter sphere that was struck in the rear by a steel chip from the sabot stripper (Shot 4-1351, see Figure 67) was not circular. The altered timing sequence for the firing of the x-ray sources resulted in the view shown in Figure 76 and a view of the leading edge of the debris cloud taken about 22 μs later. Features of the leading edge of this cloud appeared to be identical to the features of the leading edge of the debris cloud for an identical test (Shot 4-1352, see radiograph in Figure 41). Damage patterns for Shots 4-1351 and 4-1352 are compared in Figure 74. The inner rings were similar in shape and size for both tests. The outer ring for Shot 4-1351 was distorted. The damage to the rear of the sphere resulted in the formation of an asymmetric spall shell and a distorted outer ring in the damage pattern. It was not clear whether the three small holes in the witness plate in the area of the disturbance in the outer ring were caused by the impact of fragments from the rear of the sphere or by the impact of steel chips from the stripper.

The vertical and horizontal diameters of the outer, the inner, and the spall rings were measured using a scale; the average diameter of each feature is presented in Table 19. Also presented in the table are the thicknesses and alloys of the witness plates and the spacing or distance between the rear of the bumper sheet and the front of the witness plate that was used for each test. As noted in the table, the standoff distance used for some of the tests was more or less than the nominal 38-cm (15-inch) spacing. The measured and

172
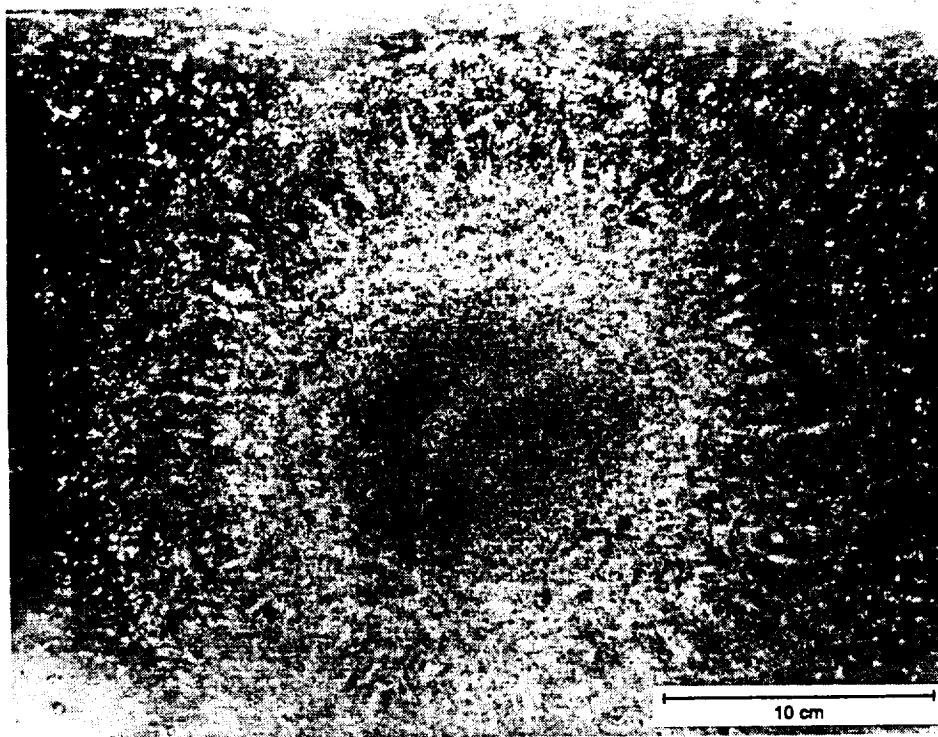
t/D = 0.234

4-1352
6.64 km/s
3.18-mm-thick,
5456-H116
plate
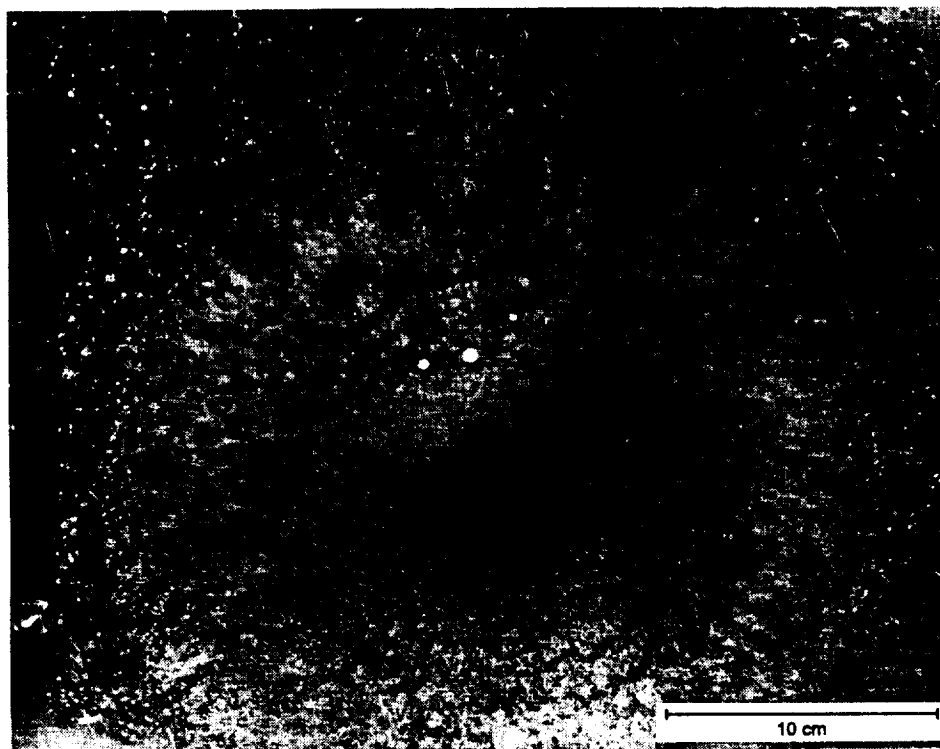
t/D = 0.233

4-1351
6.66 km/s
3.18-mm-thick,
5456-H116
plate

Figure 74. Damage patterns produced by debris clouds formed by the impact of 9.53-mm-diameter, 2017-T4 aluminum spheres with 2.22-mm-thick, 6061-T6 aluminum sheets. Rear of sphere for Shot 4-1351 was struck by a steel chip from sabot-stripper plate. An earlier-time radiograph of the sphere was shown in Figure 67.

173

# TABLE 19

## DIMENSIONS OF WITNESS-PLATE DAMAGE PATTERNS

All projectiles were 2017-T4 aluminum spheres except for Shot 4-1601. Shot 4-1601 used an 1100-O aluminum projectile. Diameters of damage features shown in parentheses are dimensions after adjustment of measured values to a 15-inch spacing.

| Shot Number | $\dfrac{t}{D}$ | Impact Velocity, (km/s) | Witness Plate Details Thickness (mm) | Material Alloy | Spacing (in) | Diameter of Damage Feature Inner Ring (in) | Outer Ring (in) | Spall Ring (in) |
|---|---|---|---|---|---|---|---|---|
| **1100-O Aluminum Bumper, $D$ = 6.35 mm** | | | | | | | | |
| 4-1318 | 0.048 | 6.64 | 3.18 | 5456-H116 | 15.0 | --- | 3.80 | 1.50 |
| **1100-O Aluminum Bumper, $D$ = 9.53 mm** | | | | | | | | |
| 4-1286 | 0.031[a] | 6.42 | 6.35 | 6061-T651 | 12.0[b] | --- | ~3.8 | None |
| 4-1288 | 0.031[a] | 6.71 | 6.35 | 6061-T651 | 12.0[b] | --- | ~3.8 | None |
| 4-1285 | 0.032[a] | 6.67 | 6.35 | 6061-T651 | 12.0[b] | --- | ~4.0 | None |
| 4-1290 | 0.032 | 6.67 | 6.35 | 6061-T651 | 15.0 | --- | 2.70 | 2.80 |
| 4-1292 | 0.032[c] | 6.69 | 2.03 | 6061-T6 | 3.0[d] | 0.42-in-deep bulge in plate. | | No craters |
| **2024-T3 Aluminum Bumper, $D$ = 9.53 mm** | | | | | | | | |
| 4-1282 | 0.053 | 6.58 | 25.4 | 6061-T651 | 12.62 | --- | 4.05 | 1.80 |
| | | | | | (15.0) | --- | (4.75) | (2.10) |
| 4-1284 | 0.053 | 6.58 | 6.35 | 6061-T651 | 15.0 | --- | 4.55 | 2.95 |
| **2024-T3 Aluminum Bumper, $D$ = 12.70 mm** | | | | | | | | |
| 4-1281 | 0.040 | 6.46 | 25.4 | 6061-T651 | 12.62 | --- | 3.10 | 2.95 |
| | | | | | (15.0) | --- | (3.60) | (3.45) |
| 4-1357 | 0.160 | 6.38 | 3.18 | 5456-H116 | 15.0 | 6.20 | 10.40 | 3.40 |
| **6061-T6 Aluminum Bumper, $D$ = 6.35 mm** | | | | | | | | |
| 4-1449 | 0.050 | 7.23 | 3.18 | 2219-T87 | 15.0 | --- | 4.40 | 2.40 |
| **6061-T6 Aluminum Bumper, $D$ = 9.53 mm** | | | | | | | | |
| 4-1392 | 0.026 | 6.54 | 12.7 | 6061-T651 | 14.88 | --- | 2.00 | 2.35 |
| 4-1395 | 0.026 | 6.70 | 12.7 | 6061-T651 | 14.88 | --- | 2.00 | 2.20 |
| 4-1428 | 0.049 | 3.77 | 6.35 | 6061-T651 | 15.0 | 0.9-in-diameter hole, scattered craters | | |
| 4-1433 | 0.049 | 4.71 | 6.35 | 6061-T651 | 15.0 | --- | 2.20 | 2.20 |
| 4-1394 | 0.049 | 5.45 | 6.35 | 6061-T651 | 14.88 | --- | 3.20 | 1.45 |
| 4-1360 | 0.049 | 6.62 | 6.35 | 6061-T651 | 14.88 | --- | 4.10 | 2.50 |
| 4-1744 | 0.049 | 7.38 | 6.35 | 6061-T651 | 15.0 | --- | 4.65 | 2.60 |
| 4-1359 | 0.062 | 6.78 | 6.35 | 6061-T651 | 14.88 | --- | 5.20 | 2.40 |
| 4-1622 | 0.084 | 3.84 | 6.35 | 6061-T651 | 15.0 | --- | 2.85 | None |
| 4-1621 | 0.084 | 4.62 | 6.35 | 6061-T651 | 15.0 | ~2.5 | 4.45 | ~1.0 |
| 4-1289 | 0.084 | 6.68 | 3.18 | 2219-T81 | 15.0 | 5.95 | 6.55 | 3.20 |
| 4-1287 | 0.084 | 6.74 | 6.35 | 6061-T651 | 15.0 | 5.95 | 6.45 | 2.90 |
| 4-1283 | 0.102 | 6.72 | 6.35 | 6061-T651 | 15.0 | 6.00 | 7.55 | 2.55 |

[a] Multiple-sheet bumper (two sheets, each with $t/D$ ratio shown, spaced 3 inches apart).
[b] Behind second sheet.
[c] Multiple-sheet bumper (five sheets, each with $t/D$ ratio shown, spaced 3 inches apart).
[d] Behind fifth sheet.

TABLE 19 (Concluded)

## DIMENSIONS OF WITNESS-PLATE DAMAGE PATTERNS

All projectiles were 2017-T4 aluminum spheres except for Shot 4-1601. Shot 4-1601 used an 1100-O aluminum projectile. Diameters of damage features shown in parentheses are dimensions after adjustment of measured values to a 15-inch spacing.

| Shot Number | $\dfrac{t}{D}$ | Impact Velocity, (km/s) | Witness Plate Details | | | Diameter of Damage Feature | | |
| --- | --- | --- | --- | --- | --- | --- | --- | --- |
| | | | Thickness (mm) | Material Alloy | Spacing (in) | Inner Ring (in) | Outer Ring (in) | Spall Ring (in) |
| **6061-T6 Aluminum Bumper, $D$ = 9.53 mm (Concluded)** | | | | | | | | |
| 4-1716 | 0.135 | 4.71 | 6.35 | 6061-T651 | 15.0 | 3.70 | ~7.0[e] | None |
| 4-1291 | 0.163 | 6.71 | 3.18 | 2219-T87 | 14.0 | 6.05 | 9.75 | 2.95 |
| | | | | | (15.0) | (6.45) | (10.45) | (3.15) |
| 4-1717 | 0.168 | 4.96 | 6.35 | 6061-T651 | 15.0 | 4.40 | 8.20 | None |
| 4-1351 | 0.233 | 6.66 | 3.18 | 5456-H116 | 15.0 | Projectile struck from rear by chip from sabot-stripper plate | | |
| 4-1352 | 0.234 | 6.64 | 3.18 | 5456-H116 | 15.0 | 7.70 | 11.35 | ~2.0 |
| 4-1353 | 0.424 | 6.68 | 3.18 | 5456-H116 | 15.0 | 6.60 | 9.85 | None |
| **6061-T6 Aluminum Bumper, $D$ = 12.70 mm** | | | | | | | | |
| 4-1358 | 0.047 | 6.26 | 12.7 | 6061-T651 | 14.5 | --- | 3.80 | 3.80 |
| | | | | | (15.0) | --- | (3.92) | (3.92) |
| 4-1601[f] | 0.047 | 6.37 | 12.7 | 6061-T651 | 16.0 | 1.65 | 4.10 | 3.20 |
| | | | | | (15.0) | (1.60) | (3.88) | (3.00) |

[e] Pattern has an irregular, noncircular outline.
[f] Projectile was 1100-O aluminum.

adjusted diameters (to a 15-inch spacing) are presented for these tests. The damage patterns for 31 tests were reported; the two oblique-test witness plates were not measured.

The radius of the inner and outer ring in the damage pattern produced by the debris clouds formed by the impacts of 9.53-mm-diameter, 2017-T4 aluminum spheres with various thicknesses of 6061-T6 aluminum sheets are shown as a function of $t/D$ ratio, in Figure 75, for tests with impact velocities of 4.7 and 6.7 km/s. The radius of the outer ring is shown as a function of impact velocity, in Figure 76, for these tests and three tests with other impact velocities and $t/D$ ratios. A second ordinate axis, the half angle of the spray pattern, was included on both figures to facilitate the comparison of the dispersion angle of the largest debris-cloud element described in this report with the dispersion angles reported by other investigators.
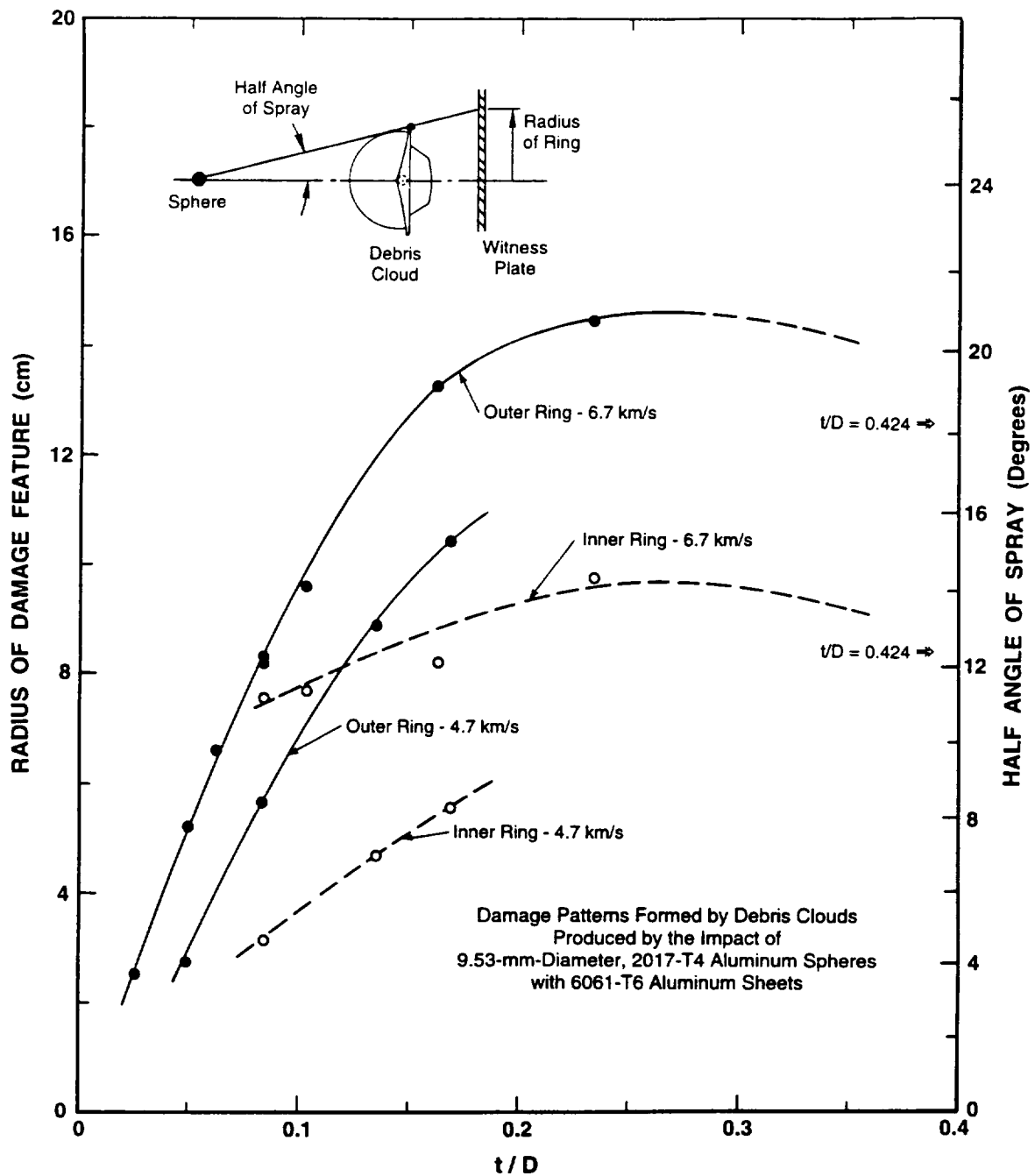
Figure 75. Radius of the inner and outer ring in the witness-plate damage pattern as a function of $t/D$ ratio for selected tests at impact velocities of 4.7 and 6.7 km/s.

In Figure 75, the radius of the outer ring of the damage pattern is shown to experience rapid growth for impact velocities of 4.7 and 6.7 km/s, when the $t/D$ ratio is less than 0.17. The inner ring was not evident for the 6.7-km/s tests until the $t/D$ ratio was
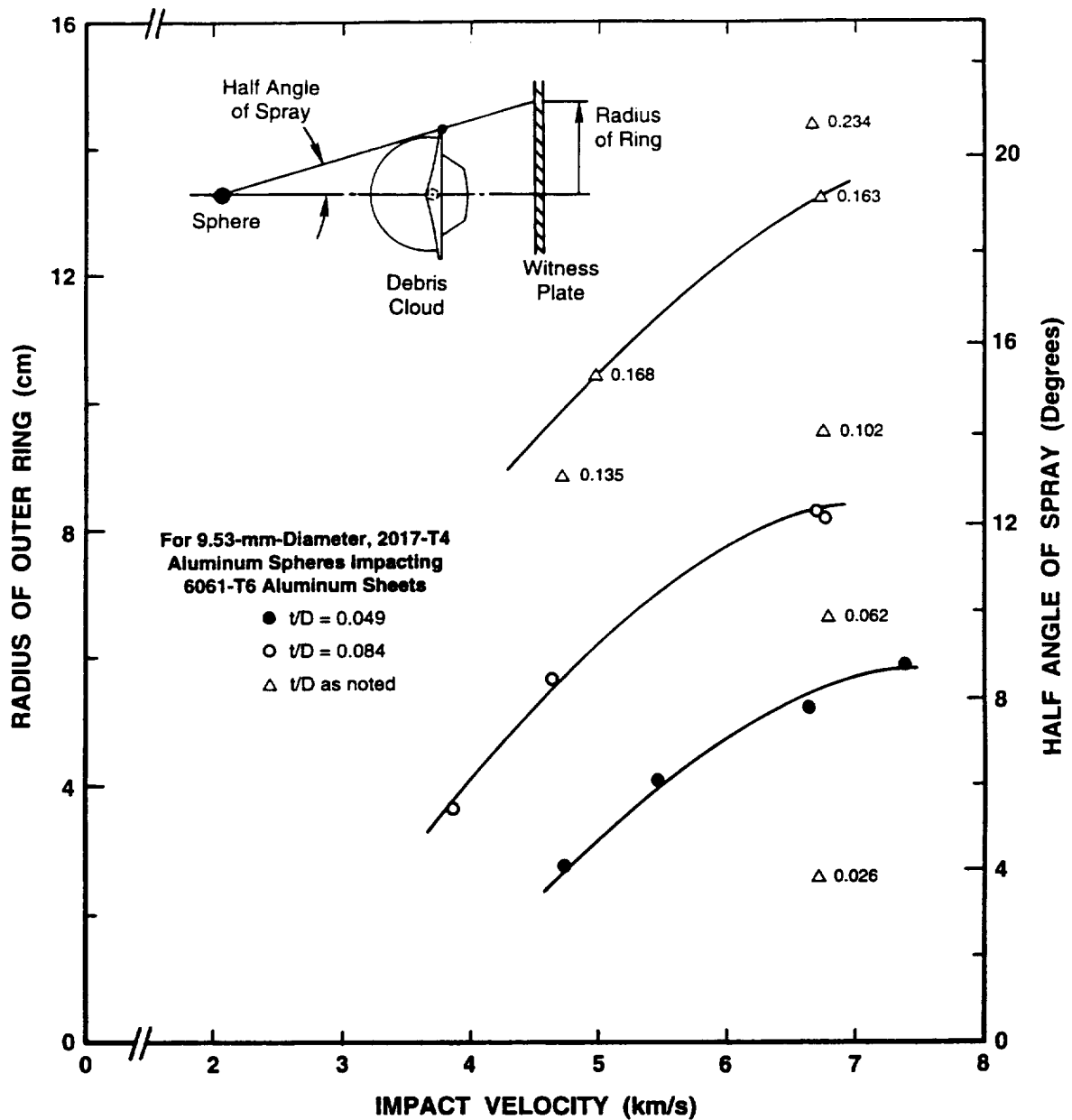
Figure 76. Radius of the outer ring in the witness-plate damage pattern as a function of impact velocity for selected tests at various $t/D$ ratios.

about 0.07, and its radius did not experience appreciable growth as the $t/D$ ratio increased. The radii of the inner rings for the 4.7-km/s tests were considerably smaller than the radii of the inner rings for the 6.7-km/s tests. The differences in the radii of the inner rings for the tests at these two impact velocities were not surprising when the growth patterns of the front element, particularly the diametral growth of points ⑦ and ⑧

(see Figures 10a and 10b), were examined. Perhaps the most significant feature of Figure 75 is that the apparent maximum radius (and dispersion angle ) of the outer ring of the damage pattern was achieved when the $t/D$ ratio was about 0.25. A long standing "rule of thumb" for Whipple-shield design has been that optimum shield performance was obtained when the $t/D$ ratio of the bumper was about 0.25. The results of the analyses of the fracture and fragmentation of the projectile indicated that the stresses and processes that controlled the disintegration of the sphere had saturated (i.e., reached their maximum effectiveness) when the $t/D$ ratio was about 0.18. In is reasonable, therefore, that the optimum shield was shown to be one in which the disintegration of the sphere and the dispersion of the fragments were maximized.

In Figure 76, the radius of the outer ring was shown to increase as impact velocity increased, at least for $t/D$ ratios of 0.049, 0.084, and 0.165. The data tend to indicate that the radius of the outer ring may approach a maximum value at some impact velocity in excess of 8 km/s. The existence of a maximum value will be difficult to establish experimentally because of restrictions on launcher capabilities and because the elements in these higher velocity debris clouds are likely to be vaporous and not leave a damage pattern that can be used to measure their dispersion.

In closing, several comments will be offered concerning the examination of witness-plate damage patterns. Not all features identified in the debris clouds leave a record of their existence on the witness plates. The damage to the front surface of the witness plate produced by the impact of the front element is obliterated by the impact of the center-element fragments. In addition, some, and perhaps many of the spall-shell fragments were consumed or reduced in size while passing through the ejecta thrown up by the impact of the center-element fragments. Nonetheless, examination and careful study of the damage patterns produced on witness plates does provide useful information related to debris-cloud structure.

178

# SECTION VIII. MULTICOMPONENT SHIELDS

In a classic Whipple-bumper system, the thin outer bumper or shield is placed a short distance away from the thick inner or main wall of the spacecraft. Over the years, investigators [54, 55, 56] have examined alternate forms of spacecraft-wall construction. In their investigations, the total mass of the shield and wall was redistributed into more than these two elements in an attempt to develop a more effective and lighter weight shield/wall system. Perhaps the simplest form of a multicomponent shield was one in which the thickness of the bumper and the main wall were reduced slightly and the "extra" material was consolidated in a third sheet that was placed between the thinned bumper and main wall. In operation, the intermediate layer interacted with the debris cloud that formed when the projectile struck the bumper and altered the characteristics of the impulse delivered to the rear wall by changing the velocity, size, and dispersion of the debris in the cloud. Multi-layer insulation (MLI) has been routinely installed between the bumper and inner wall of spacecraft. In some instances, inclusion of the MLI enhanced the performance of the spacecraft wall. Enhanced performance of a multicomponent shield system results when the multicomponent shield is more resistant to an impact than a Whipple shield of the same weight and total wall thickness (i.e., from the front of the bumper to the rear surface of the main wall).

A wide variety of materials have been used as bumpers or intermediate-sheet structures in multicomponent shield systems. In addition to thin metal sheets, loose blankets and fiber-reinforced composites of a number of nonmetallic materials (e.g., Kevlar, Nextel, Astroquartz, Spectra, etc.) have been evaluated for use as intermediate layers. The possible combinations of material, material thickness and configuration, and element spacing that can be considered for use in the construction of a multicomponent wall is extensive to say the least.

179

A considerable number of tests of multicomponent wall systems have been performed at the UDRI Impact Physics Laboratory for a wide variety of sponsors. Most of the test articles were scaled shields, however, and were impacted at various angles of obliquity and, in a large number of instances, employed a variety of materials in their construction. Consequently, the radiographs and test results for most of the shields were not suitable for use in a systematic examination of the operation of a multicomponent shield system. Fortunately, several series of tests were performed for McDonnell Douglas Space Systems Company to evaluate a multicomponent shield called the multi-shock shield. In this section, use will be made of a small body of detailed, quantitative data from several of these tests to illustrate operation of a multicomponent shield. Examples of multi-shock shields that employed metallic and nonmetallic elements will be presented. Insights into the operation of multi-shock shields will be qualitatively extended to a discussion of the operation of other multicomponent shield systems.

The multi-shock shield concept was described by Cour-Palais and Crews [57]. This shielding concept was developed in the advanced spacecraft shielding program conducted at the NASA Johnson Space Center Hypervelocity Research Laboratory. Use of multiple, spaced, thin sheets of aluminum was shown to be more effective, on the basis of equal areal density, in the protection of the spacecraft wall than a simple Whipple-type shield [58]. The multi-shock concept utilized ultra-thin shield elements to repeatedly shock aluminum projectile fragments to a high enough energy state to completely melt and partially vaporize them. The use of a number of very thin bumpers, each with a $t/D$ ratio of 0.032 and a critical spacing between them (7.62 cm), would result in the shocked state of the particulates produced by the initial impact being raised progressively as they encountered successive bumpers. As a result, their final state would be higher than would be produced by the impact of the projectile with a single bumper whose thickness was equal to the sum of the thicknesses of the individual bumpers.

Radiographs of debris clouds produced by the impact of a sphere with a single- and double-sheet bumper are presented in Figure 77. In this figure, the debris cloud formed by the impact of a 9.53-mm-diameter, 2017-T4 aluminum sphere with a single sheet of 1100-O aluminum sheet (Shot 4-1290, $t/D$ = 0.032) is shown at 6.7 and 19.8 μs after impact. The second radiograph in Figure 77, Shot 4-1286, illustrates the operation of a double-sheet bumper and its effect on the debris-cloud structure. Test conditions for Shot 4-1286 were similar to those for Shot 4-1290, except that an identical 1100-O aluminum sheet was placed 7.62 cm downrange of the first bumper. The first view, taken 5.4 μs after impact, shows a normal debris cloud. After this debris cloud interacted with the second sheet (view taken about 6.4 μs after impact with second sheet), several



**Single Sheet**
4-1290
6.67 km/s
t = 0.0119 in.

**Double Sheet**
4-1286
6.42 km/s
t = 0.0118 in.
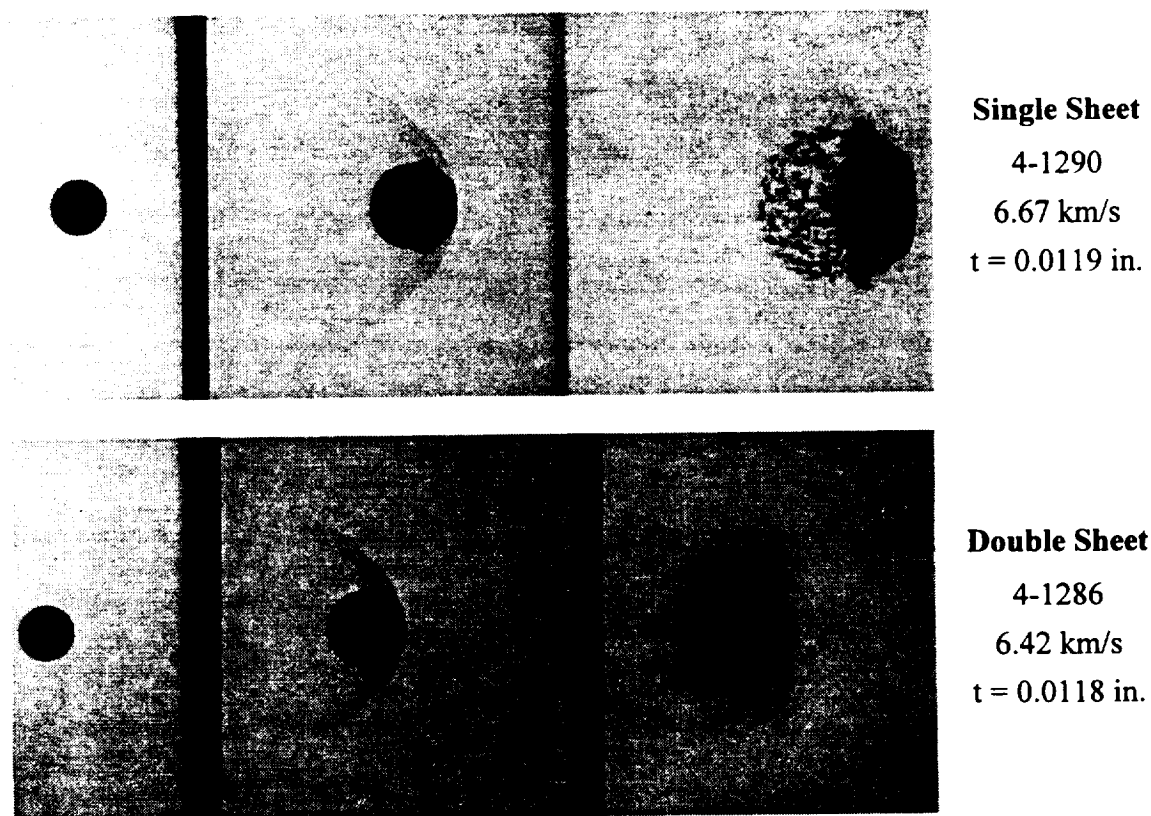
Figure 77. Radiographs of debris clouds produced by the impact of 9.53-mm-diameter, 2017-T4 aluminum spheres with single and double sheets of 0.303-mm thick, 1100-O aluminum. Spacing between the double-sheet structure was 7.62 cm.

181

significant changes occurred in the debris-cloud structure. First, the prominent front element was eliminated. Second, the separation and order within the center element and the spall shell was disrupted. Finally, an irregular smudge of very fine material mingled with and extended beyond the boundaries of the distorted center element and spall shell. Undoubtedly, the smudge was finely-divided, molten bumper and projectile debris that was produced by the impact of the front element with the second bumper sheet. Because the diameter of the front element had expanded to about two and one-half times the diameter of the sphere, the collision of the front element and the second sheet produced a considerable amount of debris. Conservation of momentum of the materials involved in the collision of the front element with the second sheet would dictate that the debris from this collision be traveling downrange at a greatly reduced velocity (~ 0.4 km/s). The second bumper had little effect on the remainder of the debris-cloud internal structure. The velocity of the leading edge of the debris cloud was reduced about 4 percent after the impact with the second sheet. Consequently, the center element and the spall shell were required to pass through the slow-moving, molten debris. As the fragments in both elements passed through this debris, numerous collisions with the droplets disrupted the fragment formations and dispersed the slow-moving material.

The impact of the debris clouds produced by the two tests shown in Figure 77 produced significantly different damage patterns on witness plates placed 38.1 cm downrange of the first bumper sheet. Photographs of the witness plates for these tests are presented in Figure 78. Also shown in the figure is the witness plate from Shot 4-1359, a test in which the thickness of the 6061-T6 aluminum bumper (0.0233 inches) was equivalent to the combined thickness of the two sheets of 1100-O aluminum used for Shot 4-1286. In Figure 78, all three, 6.35-mm-thick, 6061-T651 aluminum witness plates are shown at the same scale to facilitate the comparison of the damage patterns. The large hole formed in the center of the witness plate for Shot 4-1290 was produced by the impact
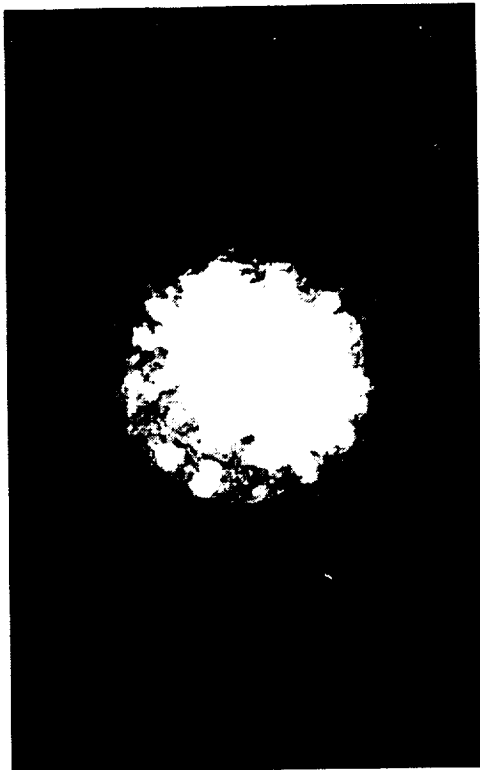
**Single-Sheet Bumper**
4-1290     6.67 km/s   t/D = 0.032

**Double-Sheet Bumper**
4-1286          6.42 km/s     t/D = 0.031 (2X)

**Single-Sheet Bumper**
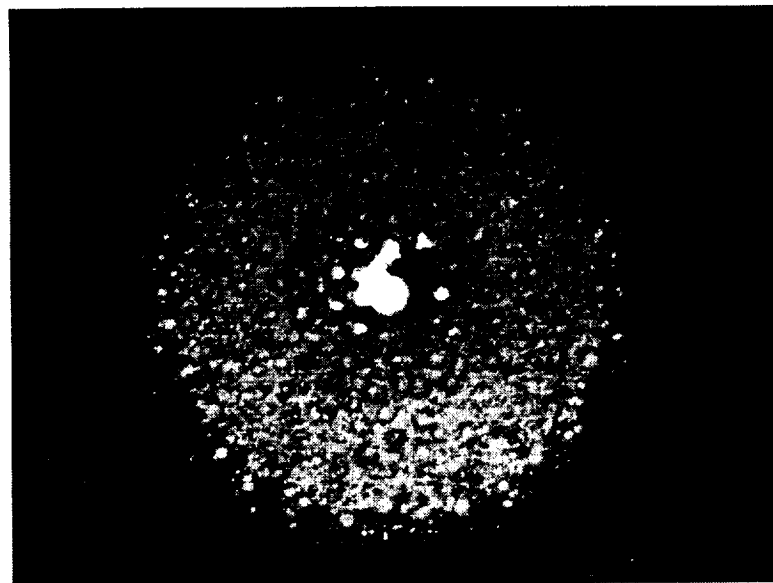4-1359          6.78 km/s          t/D = 0.062

Figure 78. Damage patterns produced by debris clouds formed by the impact of 9.53-mm-diameter, 2017-T4 aluminum spheres with single- and double-sheet aluminum bumpers. All witness plates are shown at the same scale.

of the center element of the debris cloud. The witness plate used for the test with a double-sheet bumper, Shot 4-1286, exhibited a much smaller central hole. The central hole was surrounded by irregularly spaced craters of varying sizes and a spray pattern of molten aluminum that radiated from the hole. The outer diameter of the damage pattern produced by Shot 4-1359 was considerably larger than the outer diameter of the damage pattern for Shot 4-1290 because of the increased dispersion of the center element of the debris cloud. The difference in the dispersion of the center-element fragments was not surprising since the $t/D$ ratios for these tests differed by a factor of two.

The effectiveness of the double-sheet bumper can be seen by comparing the damage done to the witness plates for Shots 4-1286 and 4-1359. Although the projectile encountered the same mass of bumper material for Shots 4-1286 and 4-1359, the extent and character of the damage patterns produced by the impact of the debris clouds was very different. Both plates had central holes of about the same diameter; however, the level of damage sustained by the plate in the region around the hole was significantly lower for the double-sheet-bumper test The rear surfaces of the witness plates for these two tests were also different. A significant spall failure, about 6 cm in diameter, occurred on the rear of the plate for Shot 4-1359. The rear of the plate for Shot 4-1286 exhibited several small raised areas below the larger craters shown on the front of the plate. Otherwise, the rear surface of the plate was smooth. The double-sheet bumper was considerably more effective in reducing the damage potential of the debris cloud than was a single-sheet bumper of the same mass and/or areal density.

The multi-shock shield developed and described by Cour-Palais and Crews [57], used five, equally-spaced, thin bumper sheets. Radiographs of debris clouds produced by the impact of a sphere with a five-sheet bumper and a single-sheet bumper of the same areal density, Shots 4-1292 and 4-1291, respectively, are compared in Figure 79. The radiograph of Shot 4-1292 illustrated the operation of the first three sheets of the five-sheet
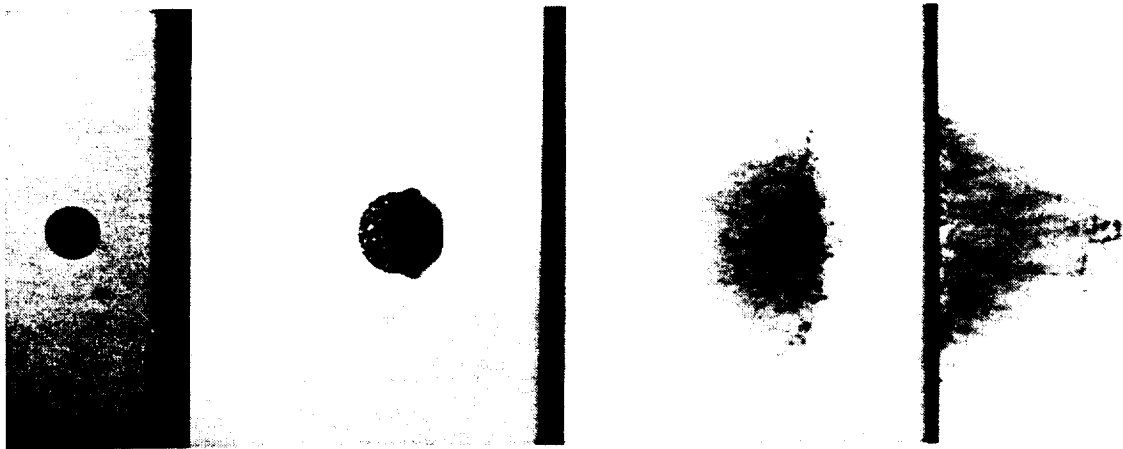
**Five-Sheet Bumper - 0.303-mm-thick, 1100-O Aluminum Sheets, Spaced 7.62 cm Apart**

4-1292                      6.69 km/s                  t/D = 0.031 (5X)



**Single-Sheet Bumper, - 1.549-mm-thick, 6061-T6 Aluminum Sheet**

4-1291                      6.71 km/s                  t/D = 0.163

Figure 79. Radiographs of debris clouds produced by the impact of 9.53-mm-diameter, 2017-T4 aluminum spheres with the first three sheets of a five-sheet, multishock shield and a single-sheet bumper with a similar areal density.

bumper and their effect on the center element of the debris cloud. Due to physical limitations imposed by the size of the fourth and fifth bumper sheet, radiographs of the modified debris-cloud structures produced by the impacts with the fourth and fifth sheets were not obtained. The debris cloud formed by the impact with the second sheet for Shot 4-1292 was identical to the debris cloud formed by the impact with the second sheet for Shot 4-1286 (see Figure 77). However, the structure of the debris cloud was severely

modified by the impact with the third sheet of the bumper system. The large central fragment observed in the second and third views of the double-sheet-bumper debris clouds was broken into several large fragments. (Details of the size and velocity of the large central fragments from the single- and double-sheet bumper tests are presented later in this section.) Several other changes in the debris-cloud morphology were noted. The front of the debris cloud changed from a flat-faced structure to a conical-shaped structure, with the larger fragments scattered at the front of its leading edge. The diameter of the trailing portion of the debris cloud increased and the axial velocity of most of the finely-divided and molten material in the debris cloud was reduced significantly. The changes in the distribution of material in the debris-cloud structure placed the larger fragments in positions that ensured their disintegration during impact with the fourth and fifth sheets of the structure.

Complete disintegration and, perhaps, melting of the projectile fragments occurred by the time the debris reached the 2.03-mm-thick, 6061-T6 witness plate that was placed 7.62 cm behind the fifth sheet for Shot 4-1292. The witness plate for this test is shown in Figure 80 with the witness plate from Shot 4-1291, a test with a single-sheet bumper of the same areal density as the five-sheet bumper. The 3.18-mm-thick, 2219-T87 aluminum witness plate used for Shot 4-1291 was not perforated, but was heavily cratered and exhibited a 7.5-cm-diameter spall on the rear surface of the plate. The thinner witness plate used for Shot 4-1292 did not have any craters or evidence of being struck by fragments of the projectile or the bumper sheets and was smooth on the rear. A thick layer of molten debris was deposited on the front surface of the witness plate and a 1.1-cm-deep bulge was formed in the plate. The spaced, five-sheet bumper was much more effective in reducing the damage to the witness plate than a single sheet of the same areal density.

Recent work with Nextel ceramic fiber cloth [59] has shown that multi-shock shields assembled using this fabric can be more effective than their equal-areal-density,
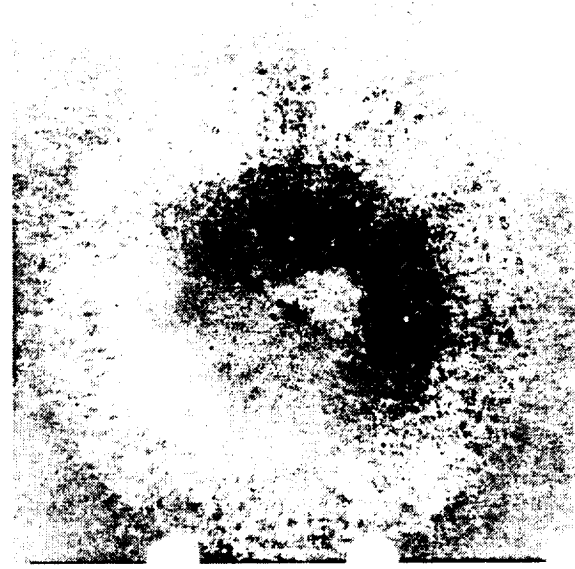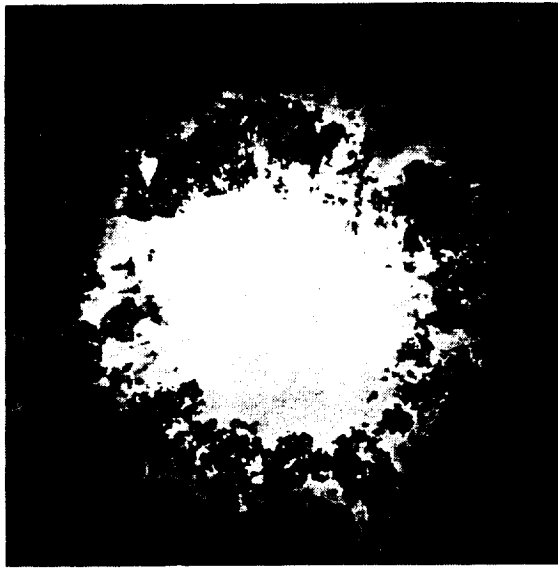
**Five-Sheet, Multi-Shock Bumper**     **Single-Sheet Bumper, Equal Areal Density**

4-1292     6.69 km/s     t/D = 0.031 (5X)     4-1291     6.71 km/s     t/D = 0.163

Figure 80. Damage patterns produced by debris clouds formed by the impact of 9.53-mm-
diameter, 2017-T4 aluminum spheres with a five-sheet, aluminum, multi-shock
bumper system and a single-sheet aluminum bumper with an equivalent areal
density. Witness plates are shown at the same scale.

all-aluminum counterparts. Nextel is a continuous, polycrystalline, metal-oxide fiber,
developed by the 3M Company, that is suitable for use in the production of high-
temperature, ceramic-fiber textiles [60]. The results of tests using a single-sheet and a
double-sheet Nextel bumper are presented in this section to illustrate the morphological
features of debris clouds produced by the impact of 9.53-mm-diameter, 2017-T4
aluminum spheres with nonmetallic bumper sheets. Two types of Nextel fabric were
used in the tests selected for presentation in this section. The areal density of each type of
fabric was used to determine the thickness, "$t$", of a sheet of 6061-T6 aluminum with an
equivalent weight per unit area. Determination of the equivalent thickness of an aluminum
sheet facilitated the comparison of the aluminum and Nextel test results. Equivalent
thicknesses of the two types of Nextel fabric were: (1) AF40 (0.085g/cm$^2$), "$t$" = 0.315 mm
and (2) AF62 (0.100g/cm$^2$), "$t$" = 0.371 mm. A single sheet of Nextel AF40 was used as

187

the bumper for Shot 4-1523. Two sheets of Nextel AF62, spaced 7.62 cm apart, were used as the bumpers for Shot 4-1525. Radiographs of the debris clouds produced by the Nextel tests are presented in Figure 81. The debris clouds produced by these two tests were different from the debris clouds produced by the aluminum tests (Shots 4-1290 and 4-1286 ) in two respects. First, the ejecta veil and the external bubble of debris did not visualize on the radiographs for the Nextel tests. Undoubtedly, an ejecta veil and debris bubble formed for these tests but consisted of short lengths of Nextel fibers. However, the penumbra surrounding the shadow of each fiber significantly exceeded the size of the fiber and "washed out" the shadow of the fiber in the radiographs. Second, the front element of the internal structure shown in the first view of the debris clouds for Shots 4-1290 and 4-1286



**Single Sheet
AF40 Nextel**

4-1523
6.67 km/s
"t" = 0.315 mm

**Double Sheet
AF62 Nextel**

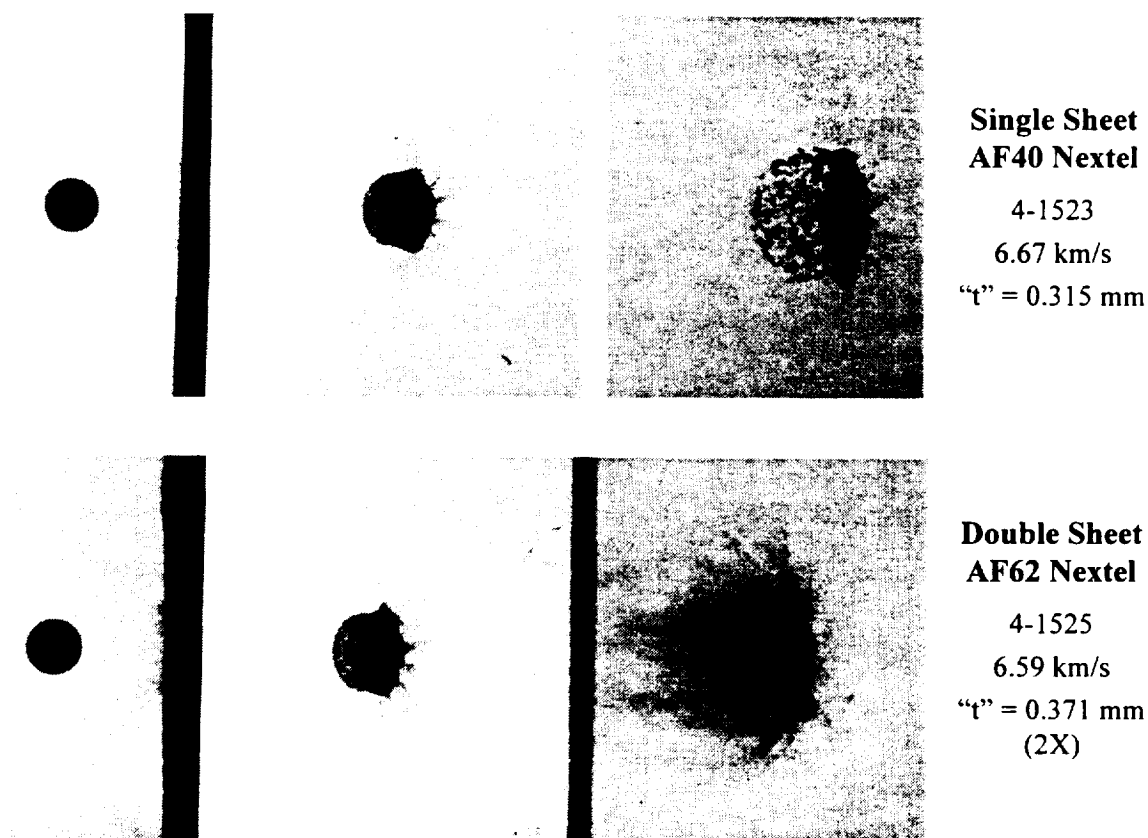4-1525
6.59 km/s
"t" = 0.371 mm
(2X)

Figure 81. Radiographs of debris clouds produced by the impact of 9.53-mm-diameter, 2017-T4 aluminum spheres with single and double sheets of Nextel fabric. Spacing between the double-sheet structure was 7.62 cm.

was not evident for the Nextel shots. The front element of the internal structure in the all-aluminum tests was composed of bumper and projectile material. In the Nextel tests, the "front element" consisted of jets of projectile fragments and Nextel fibers. The jets were formed when projectile fragments were deflected by the strands of fibers used to produce the woven fabric. Fracture and fragmentation of the projectile did not appear to be a significantly different process for impacts with aluminum or Nextel sheets. The apparent absence of a significant front element, ejecta veil, and external bubble of debris, however, were noteworthy features of the debris clouds produced by the Nextel tests.

The axial and radial velocities of several of the points shown in Figure 8 were determined for the debris clouds produced by Shots 4-1286, 4-1290, 4-1359, 4-1523, and 4-1525. The expansion velocity of the spall-shell fragments was also determined. Velocities that were compared for the single-sheet aluminum and Nextel bumpers were as follows: (1) axial velocities, $V_2$, $V_3$, and $V_4$; (2) diametral velocity, $V_{9-10}$; and (3) the axial velocity, $V_f$, of the large central fragment. In addition to the debris-cloud velocity measurements, the dimensions of the large central fragment in each debris cloud was obtained from the late-time-view radiographs using the procedures described in Section IV. Late-time views of the debris clouds for Shots 4-1286, 4-1290, 4-1523, and 4-1525 are presented in Figure 82. Results of the analyses of the radiographs for these four tests (and Shot 4-1359) are presented in Table 20. In Table 20, all measured velocities were normalized by dividing them by the impact velocity, $V_0$, to facilitate the comparison of values for tests with different impact velocities.

The normalized axial velocities, $V_2/V_0$ and $V_3/V_0$, were slightly lower for the Nextel tests. In Section VI, the velocity of the center of mass of the debris cloud was assumed to be the velocity of the front of the center element, $V_2$; the velocity of point ③, the trailing edge of the center element, was essentially the same as the velocity of point ②. The lower velocities of points ② and ③ for the Nextel tests indicated, from conservation

189

**Single-Sheet Aluminum Bumper**

45.3 µs After Impact

4-1290     6.67 km/s     t/D = 0.032

**Double-Sheet Aluminum Bumper**

44.1 µs After Impact

4-1286     6.42 km/s     t/D = 0.031 (2X)
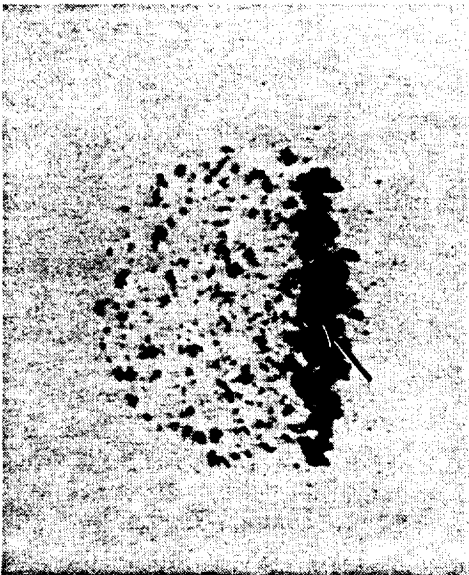
**Single-Sheet Nextel AF40 Bumper**

43.4 µs After Impact

4-1523     6.67 km/s     t/D = 0.033

**Double-Sheet Nextel AF62 Bumper**

44.1 µs After Impact

4-1525     6.59 km/s     t/D = 0.039 (2X)
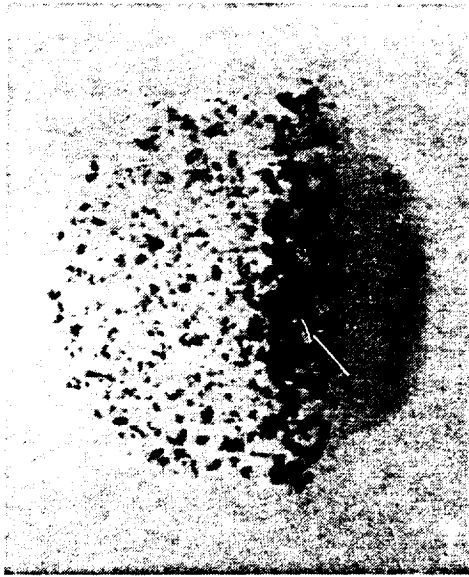
Figure 82. Late-time views of debris clouds produced by the impact of 9.53-mm-diameter, 2017-T4 aluminum spheres with single- and double-sheet aluminum and Nextel bumpers. Large central fragments are shown with arrows.

## TABLE 20

## NORMALIZED DEBRIS-CLOUD VELOCITY AND FRAGMENT DATA

Velocity data have been normalized by dividing the various measured velocities by the impact velocity of the test. All projectiles were 9.53-mm-diameter, 2017-T4 aluminum spheres.

| Shot Number | $\frac{t}{D}$ | Impact Velocity, (km/s) | Axial Debris-Cloud Velocities, | | | Spall Velocity, $V_r/V_0$ | Diametral Velocity, $V_{9\text{-}10}/V_0$ | Large Central Fragment, | |
|---|---|---|---|---|---|---|---|---|---|
| | | | $V_2/V_0$ | $V_3/V_0$ | $V_4/V_0$ | | | $d_f/D$ | $V_f/V_0$ |
| **Single-Sheet Bumpers** | | | | | | | | | |
| 4-1290 | 0.032[a] | 6.67 | 0.982 | 0.974 | 0.877 | 0.079 | 0.153 | 0.498 | 0.973 |
| 4-1359 | 0.062[b] | 6.78 | 0.968 | 0.966 | 0.785 | 0.142 | 0.327 | 0.312 | 0.968 |
| 4-1523 | 0.033[c] | 6.67 | 0.974 | 0.973 | 0.880 | 0.063 | 0.106 | 0.558 | 0.973 |
| **Double-Sheet Bumpers** | | | | | | | | | |
| 4-1286 | 0.031[d] | 6.42 | — | — | — | — | — | 0.448 | 0.919 |
| 4-1525 | 0.039[e] | 6.59 | — | — | — | — | — | 0.206[f] | 0.947 |

[a] 1100-O aluminum bumper.
[b] 6061-T6 aluminum bumper.
[c] Nextel AF40 bumper. Shown is the $t/D$ ratio based on an equivalent thickness of aluminum.
[d] Double-sheet, 1100-O aluminum bumper. Sheets were spaced 7.62 cm apart.
[e] Double Nextel AF62 bumper. Shown is the $t/D$ ratio based on an equivalent thickness of aluminum. Sheets were spaced 7.62 cm apart.
[f] Fragment not along center line of debris cloud.

of momentum, that the mass of the Nextel fabric involved in the formation of the front element was slightly larger than the mass of aluminum involved in the formation of the front element for an aluminum-sheet test. The mass of the front element, for an aluminum test with a comparable $t/D$ ratio, was equivalent to the mass of a disk of the bumper sheet whose diameter was 56 percent of the diameter of the sphere. The normalized velocity of the rear of the debris cloud, $V_4/V_0$, was slightly higher for the Nextel tests. The normalized radial expansion velocity, $V_r/V_0$, of the spall-shell fragments and the diametral expansion velocity of the center element, $V_{9\text{-}10}/V_0$, was lower for the Nextel test. The reduced expansion velocities indicated that the debris cloud for this test was more "dense" than for the single-sheet aluminum debris cloud.

The normalized diameter of the large central fragment for the single-sheet Nextel test was larger than the one produced in the single-sheet aluminum test. A single sheet of

aluminum may be slightly more effective in breaking up the sphere than an "equivalent" sheet of Nextel fabric. After the impact of the sphere with the first sheet of the aluminum and Nextel bumpers, the diameter of the large central fragment was approximately 50 and 56 percent, respectively, of the original projectile diameter. The impact of the aluminum debris cloud with the second sheet of aluminum produced an additional 20 percent reduction in the equivalent diameter of the large central fragment. The impact of the Nextel debris cloud with the second sheet of Nextel produced an additional 60 percent reduction of the diameter in the large central fragment. Each sheet of Nextel fabric was effective in reducing the size of the fragment that struck it.

The second sheet of Nextel was more effective in reducing the diameter of the large central fragment than the second sheet of aluminum because the Nextel debris cloud lacked a front element. As was shown in Figure 41, most of the material in the front element of an all-aluminum debris cloud was concentrated at the leading edge of the element. When an aluminum debris cloud encountered the second sheet of an aluminum multi-shock shield, the front element arrived at the second sheet ahead of the disk-like center element. Because the second sheet was thin, the impact of the front element with the second sheet eliminated that portion of the second sheet encountered by the front element. The center element then passed through the hole and the debris generated by this second impact. During passage through the reduced-velocity debris produced by the second impact, some erosion of center-element fragments occurred. In the case of the Nextel double-sheet bumpers, the front element was a dispersed cloud of short Nextel fibers that had little effect on the second sheet of Nextel. Consequently, the bulk of the debris cloud and the large central fragment impacted intact material, producing the significant reduction in the size of the large-central-fragment.

The radiographs, witness-plate damage patterns, and other data just presented clearly demonstrate that multicomponent shield can be more effective than single-sheet

bumpers of the same weight, provided space is available for the relatively thick wall construction required by the multi-shock system. The radiographs, etc., also illustrated some of the debris-cloud modification processes that make multicomponent shields more efficient. The primary modification processes were: (1) the reduction in projectile-fragment size, as a result of the secondary collisions with the intermediate layers and (2) the increase in the radial and axial dispersion of the debris cloud. Both of these modification processes significantly altered the temporal distribution of the load applied to the rear wall.

As indicated at the beginning of this section, a wide variety of multicomponent shields have been designed and tested. Most multicomponent-shield designs employed an aluminum bumper and rear wall. During testing, the composition, thickness, and spacing of one or more intermediate layers was varied to maximize the resistance to perforation or failure of the rear wall while keeping the overall wall thickness and weight constant. In a number of designs, a single sheet of aluminum was used as the intermediate layer. In some instances, the sheet was thinner than the bumper; in other instances, the sheet was thicker than the bumper. The thickness of the intermediate sheet must be selected with care. The size and velocity of some fragments produced by the collision of the debris cloud with the second sheet were great enough to produce unwanted perforations of the rear wall. The dimensions of these second-sheet fragments were on the order of the thickness of the second sheet, suggesting that intermediate layers composed of a sandwich of several thin sheets may be just as effective in breaking up projectile fragments as a single sheet with the same areal density, but produce much smaller "second-sheet" fragments. The trade-off between the performance of a thicker second sheet and the increased lethality of fragments produced during the disintegration of the impacted area of the sheet must be considered with care.

Nonmetallic intermediate layers made from multiple sheets of Kevlar, Nextel, and other materials or combinations of these materials were very effective in improving the

performance of multicomponent shields. Because the debris produced by the impact of the all-aluminum debris clouds with the nonmetallic intermediate layers consisted of short lengths of fibers, dangerous intermediate-layer fragments were not formed. In many cases, only widely-scattered craters produced by the impact of projectile fragments were evident on the rear wall. In general, the multicomponent-shield systems with nonmetallic intermediate layers were able to withstand impacts of larger projectiles than were all-aluminum, multicomponent-shield systems of the same weight. The mechanisms responsible for the improved performance of shield with nonmetallic intermediate layers remain to be ascertained. In a number of successful tests that employed nonmetallic intermediate layers, however, significant bulging and distortion of the bumper and rear wall occurred. During the impact process, gasses formed by the vaporization of volatile components of the intermediate-layer materials apparently increased the pressure load applied to the shield-system components. Occasional failures of the shield-system structure resulted from the application of these pressure loads.

The tests with the multi-shock shields were all performed with the bumper sheet normal to the shot-line axis. In the case of the aluminum multi-shock shield, the primary function of the second sheet was to eliminate the front element of the debris cloud. As will be shown in the next two sections of this report, the debris clouds formed by the oblique impact of spherical projectiles and the impact (at any angle) of nonspherical projectiles do not exhibit front elements or the symmetric distributions of the projectile fragments evident in the debris clouds produced by the normal impact of spheres. As a result, the use of intermediate layers in a multicomponent-shield system may prove, in general, to be more effective than indicated by the results of tests with spherical projectiles at normal incidence.

# SECTION IX. OBLIQUE IMPACTS

The description of the formation of debris clouds and the discussion of test results presented in the preceding sections of this report were confined to the simple case of a sphere impacting a thin bumper sheet at normal incidence. During the last forty years, most of the work done to evaluate the performance of spacecraft shielding has been done with the bumper normal to the flight of the projectile. Spacecraft on long-duration missions in Earth orbit will risk collision with micrometeoroids and irregularly-shaped fragments of orbital debris. The most likely collision risk for the manned space station, for example, is posed by a fragment approaching the station at an angle of about 50 degrees to the surface of the shielding and a velocity of 11 to 12 km/s [61]. Assessments of the impact-damage risks for other spacecraft yield similar threat definitions. The results of two oblique-impact tests are presented in this section. In this report, the angle of obliquity is defined as the angle the shot-line axis makes with the normal to the surface of the bumper.

Gehring [62] described a series of 18 tests in which 3.18-mm-diameter, aluminum spheres impacted 0.64-, 1.02-, and 1.60-mm-thick, 1100-O aluminum bumpers at 30-, 45-, and 60-degrees obliquity. The rear walls were 1.60-, 3.18-, and 6.35-mm-thick, 7075-T6 aluminum sheets spaced 5.08 cm behind the rear walls. Impact velocities for the tests ranged from 7.26 to 7.65 km/s. The posttest conditions of the rear wall — safe (no perforation or spall), rear spall, and perforation — were reported. Gehring stated that the major source of damage to the rear wall was due to the impact of fragments, in contrast to the very minor fragment damage observed for normal impacts of similar structures at the same impact velocities. He further stated that the amount of fragmentation damage was greatest for the tests at 45 degrees obliquity. More recently, results of several studies of oblique hypervelocity impact tests have been published. Schonberg and Taylor [63] evaluated the performance of a number of shield systems subjected to oblique, hyper-

velocity impact. Ari and Wilbeck [64] provided fragment-size distribution data for tungsten cylinders that impacted closely-spaced, double-sheet aluminum bumpers at oblique angles. Several test series were performed to determine the ballistic limits of specific space-station shield designs [65, 66]. A recent test series by Schmidt [67], examined the use of double-sheet bumpers and their effectiveness in preventing the failure of the pressure wall of a multi-sheet shield subjected to an oblique hypervelocity impact.

Little work, however, has been done to describe the structure of a debris cloud produced by the oblique hypervelocity impact of an aluminum sphere with a single- or multicomponent aluminum bumper, or to characterize the size and velocity of fragments produced by the impact. Two tests were performed, as part of the funded portion of the work described in this report, to examine the formation of debris clouds produced by oblique hypervelocity impact. In the tests, a 9.53-mm-diameter, 2017-T4 aluminum sphere was fired at a 0.508-mm-thick, 2024-T3 aluminum sheet at 30 degrees obliquity and at a 1.143-mm-thick, 6061-T6 aluminum sheet at 45 degrees obliquity. The bumper sheets were taped to a 3.18-mm-thick frame which was held in a special test fixture that was rotated to obtain the desired angle of obliquity. Witness plates (3.18-mm-thick, 5456-H116 aluminum sheets) were placed 38.1 cm behind the bumpers (spacing measured normal to the bumper) to record the damage patterns produced by the impact of the debris clouds. Orthogonal-pair radiographs were obtained for two views of the debris cloud formed by the 30-degree impact (Shot 4-1301). Three views of the debris cloud were obtained, using only the top-view x-rays, for the 45-degree impact (Shot 4-1303). The side-view x-rays were not used for this test because fragments from the ejecta veil and the debris cloud would have severely damaged the film and film cassette.

The radiographs of the debris cloud from the test at 30-degrees obliquity are shown in Figure 83. The morphological features of debris clouds produced by normal impacts were still evident in the radiographs of the debris clouds for this test. An ejecta

196

**Side-View Radiograph**



**Top-View Radiograph**

| 4-1301 | 6.54 km/s | t/D = 0.053 |

Figure 83. Orthogonal-pair radiographs of the debris cloud produced by the impact of a 9.53-mm-diameter, 2017-T4 aluminum sphere with a 0.508-mm-thick, 2024-T3 aluminum sheet at 30-degrees obliquity. Debris clouds are shown at 6.6 and 22.5 μs after impact.

veil, external bubble of bumper debris, and an internal structure with a front, center and rear element of projectile debris were formed. These features have a "normal" appearance in the side-view radiograph, but were shown to be distorted in the top-view radiograph. The front element of the internal structure had shifted from the center line of the debris cloud, "blended" with the debris bubble, and followed a line of flight that was nearly normal to the surface of the bumper. The center element and the spall shell continued to travel along the shot-line axis, although a significant number of the fragments in each of

these elements followed trajectories that caused them to move away from the shot-line axis. The center-element and spall-shell fragments for Shot 4-1301 were larger than the corresponding fragments in a debris cloud formed by the normal impact of a 9.53-mm-diameter sphere with a sheet of the same thickness and at the same velocity.

Radiographs of the debris cloud for the test at 45-degrees obliquity are presented in Figure 84. The upper radiograph contains three views of the debris cloud, at a reduced



**Top-View Radiographs**

4-1303                          6.56 km/s                          t/D = 0.120
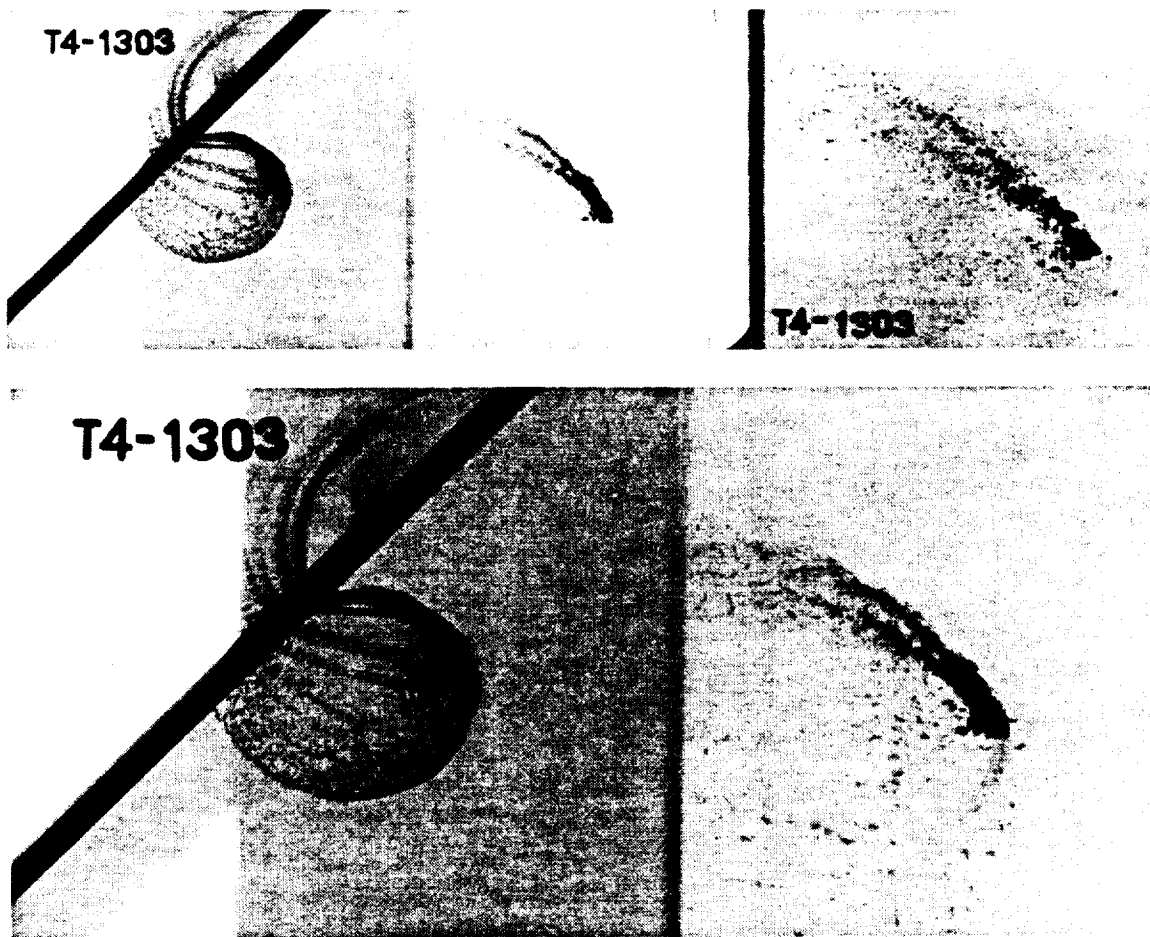
Figure 84. Radiographs of the debris cloud produced by the impact of a 9.53-mm-diameter, 2017-T4 aluminum sphere with a 1.143-mm-thick, 6061-T6 aluminum sheet at 45-degrees obliquity. Scale of the lower radiograph is the same as the radiographs shown in Figure 83. Debris clouds are shown at 6.6, 22.6, and 45.2 μs after impact.

scale. to illustrate the shape and movement of the debris produced by the impact of a 9.53-mm-diameter, 2017-T4 aluminum sphere with a 1.143-mm-thick, 6061-T6 aluminum sheet. The lower radiograph was enlarged to the same magnification used for the radiographs presented in Figure 83 for ease of comparison of the debris cloud features. The enlarged late-time view of the debris cloud is presented in Figure 85.

The morphological features of the debris clouds for Shots 4-1301 and 4-1303 were considerably different. The radiographically denser internal structure of Shot 4-1301 retained some resemblance to the normal-impact internal structure shown numerous times in earlier figures in this report. The internal structure of the debris cloud for Shot 4-1303, however, consisted of a long, slightly curved "streamer" of projectile fragments that were arranged with the largest fragments at the front of the structure. A small spall shell formed after impact and is shown in the first view of the debris cloud. The spall shell was
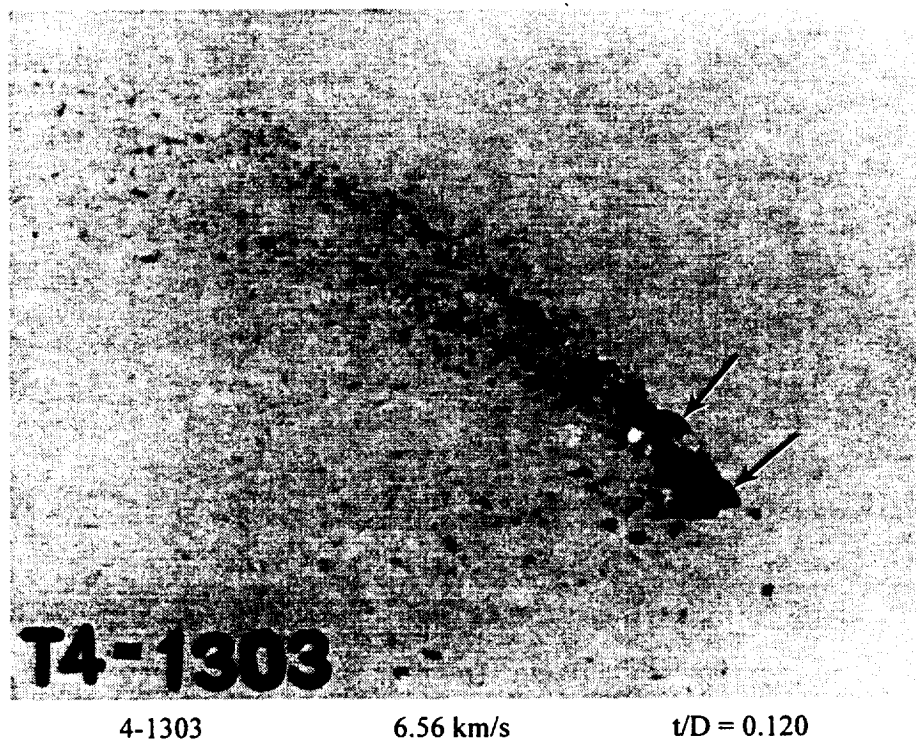


4-1303          6.56 km/s          t/D = 0.120

Figure 85. Enlarged, late-time view of debris cloud shown in Figure 84. Arrows indicate larger fragments with edges that display the original curvature of the sphere.

not evident in the later views, perhaps because it collided with the slower-moving debris above and ahead of it (as seen in the radiographs) and was assimilated by the cloud of fragments in the affected portion of the "streamer." Analysis of the radiographs of the debris clouds shown in Figures 83, 84, and 85 indicated that the axial velocities of the fragments at the front of the clouds, for the tests at 30- and 45-degree-obliquity, were 5 and 11 percent lower, respectively, than the impact velocities. The axial velocities of the center elements of debris clouds formed by normal impacts with similar structures were about 4 and 6 percent lower, respectively, than the impact velocity. The radial velocity of the dense, lower portion of the center elements was essentially the same for both tests. The analysis of the radiographs also indicated that the line of flight of these lower-portion fragments deviated about 3.6 degrees from the shot-line axis toward the normal to the bumper sheet. A comparison of the axial and radial velocities of the leading-edge fragments would indicate that the resultant velocity of these fragments will decrease rapidly as obliquity is increased above 45 degrees and impact velocity is held constant.

It was evident that the projectile fragments produced by the oblique tests were larger than those produced by comparable normal-impact tests. The debris cloud for Shot 4-1301 was too compact to make reasonable measurements of the fragments in the center element. Measurements of the length and width of the two fragments shown with arrows in Figure 85 were made and used (following procedures given in Section IV for the determination of $d_f$ of the large central fragment) to estimate the equivalent diameter of the fragments. The equivalent diameters of these fragments were 3 and 3.5 mm. It is interesting to note that both of these fragments exhibited the same curvature, along one edge, as the original projectile. It is probable that there were several more fragments in the cluster of fragments at the front of the debris cloud that were about the same size and shape as the two fragments just described. A cluster of 3- to 3.5-mm-diameter fragments traveling at a velocity of about 5.8 km/s would penetrate the rear wall of most spacecraft.

The witness-plate damage patterns produced by the debris clouds for Shots 4-1301 and 4-1303 are shown in Figures 86 and 87, respectively. In each figure, they are compared with the damage pattern produced on witness plates from normal-impact tests which used the same diameter spheres, $t/D$ ratios, and impact velocities. All four witness plates shown in Figures 86 and 87 are at the same scale to illustrate the extent of the damaged area and the differences in the damage pattern produced on each plate.

As shown in Figure 86, the cloud of projectile fragments for Shot 4-1301 produced a circular damage pattern that was slightly smaller than the circular damage pattern for Shot 4-1284. The center of the damage pattern for Shot 4-1301 was shifted about 1 cm to the right of the point where the shot-line axis intersected the witness plate. The distribution of the craters within the damaged area was uneven, however. In the top-view radiograph of Shot 4-1301 (Figure 83), the largest pieces of the fragmented projectile are shown to be on the right side of the shot-line axis. The impact of the larger fragments in this portion of the debris cloud produced a D-shaped opening in the witness plate. Widely scattered, larger fragments on the left side of the shot-line axis produced the smaller holes to the left of the large opening. A light mottled pattern of small craters and pits was evident on most of the plate to the right of the main damage area. The small craters and pits (< 0.5 mm diameter) were produced by the impact of finely-divided, molten bumper material that made up the distorted front element shown in the radiographs of Shot 4-1301.

The damage pattern for Shot 4-1303 consisted of a large, irregularly-shaped hole, several small holes in the region around the large hole, and a widely-scattered and randomly-spaced pattern of small to large craters over the rest of the plate. The "center" of the damage pattern for Shot 4-1303 was also shifted about 1 cm to the right of the point where the shot-line axis intersected the witness plate. The shape of the large hole in the plate would indicate that the large projectile fragments at the front of the "streamer" had

201
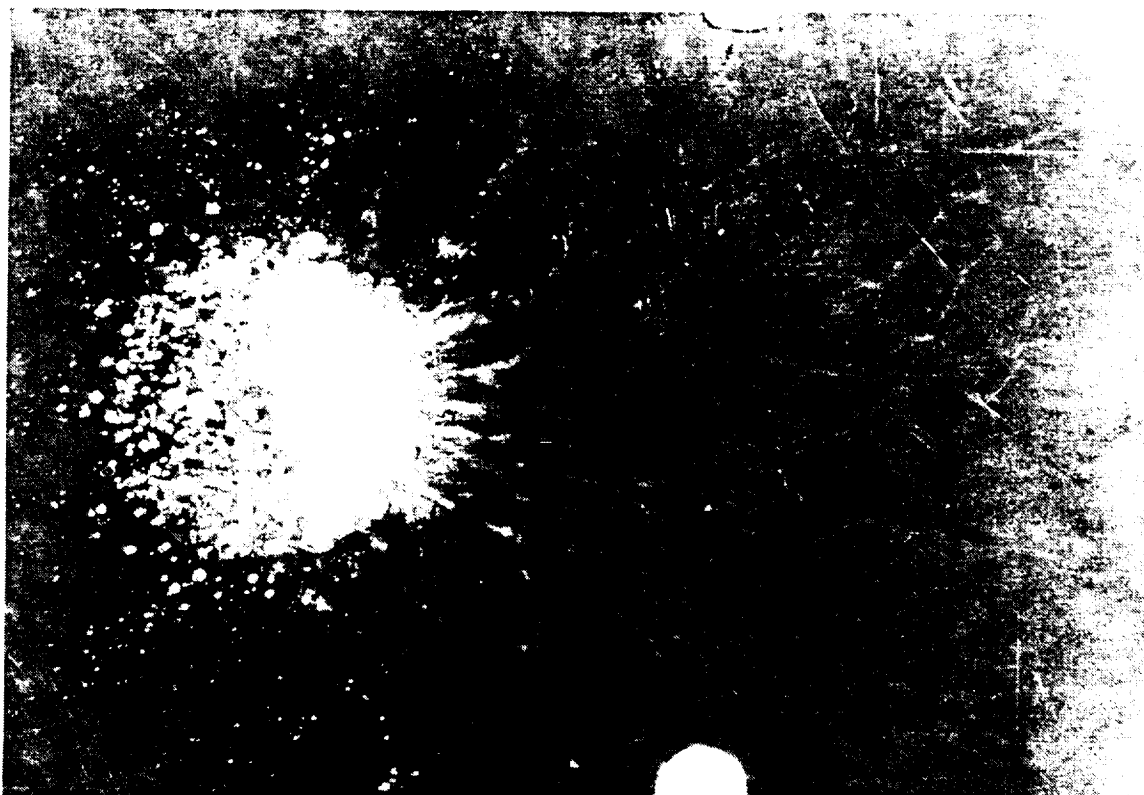
**30-Degree Obliquity** (Above)

4-1301        6.54 km/s

0.508-mm-thick, 2024-T3 Aluminum
Bumper ($t/D$ = 0.053)

3.18-mm-thick, 5456-H116 Aluminum
Witness Plate

**Normal Incidence** (Left)

4-1284        6.58 km/s

0.508-mm-thick, 2024-T3 Aluminum
Bumper ($t/D$ = 0.053)

6.35-mm-thick, 6061-T651 Aluminum
Witness Plate

Figure 86. Damage patterns produced by debris clouds formed by the impact of 9.53-mm-diameter, 2017-T4 aluminum spheres with aluminum bumper sheets having a $t/D$ ratio of 0.053. Bumpers were at 30-degrees obliquity for the upper plate and at normal incidence for the lower plate. Both plates are shown at the same scale.
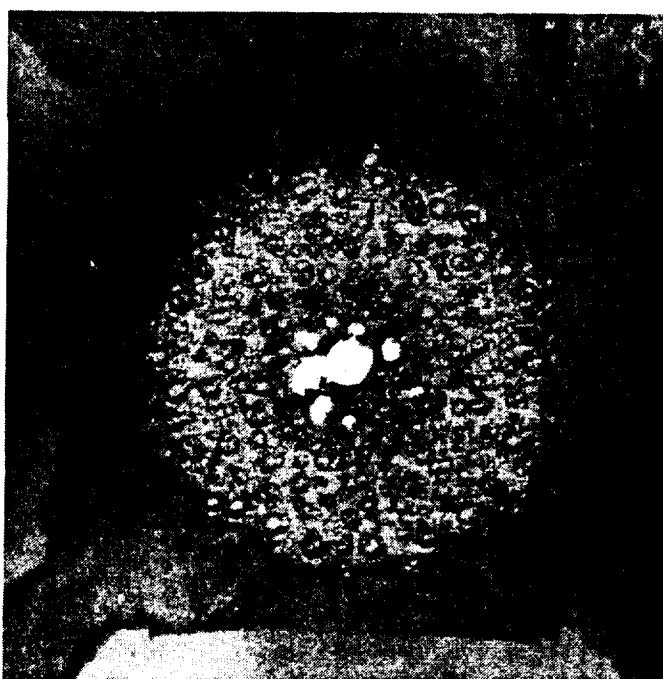
202
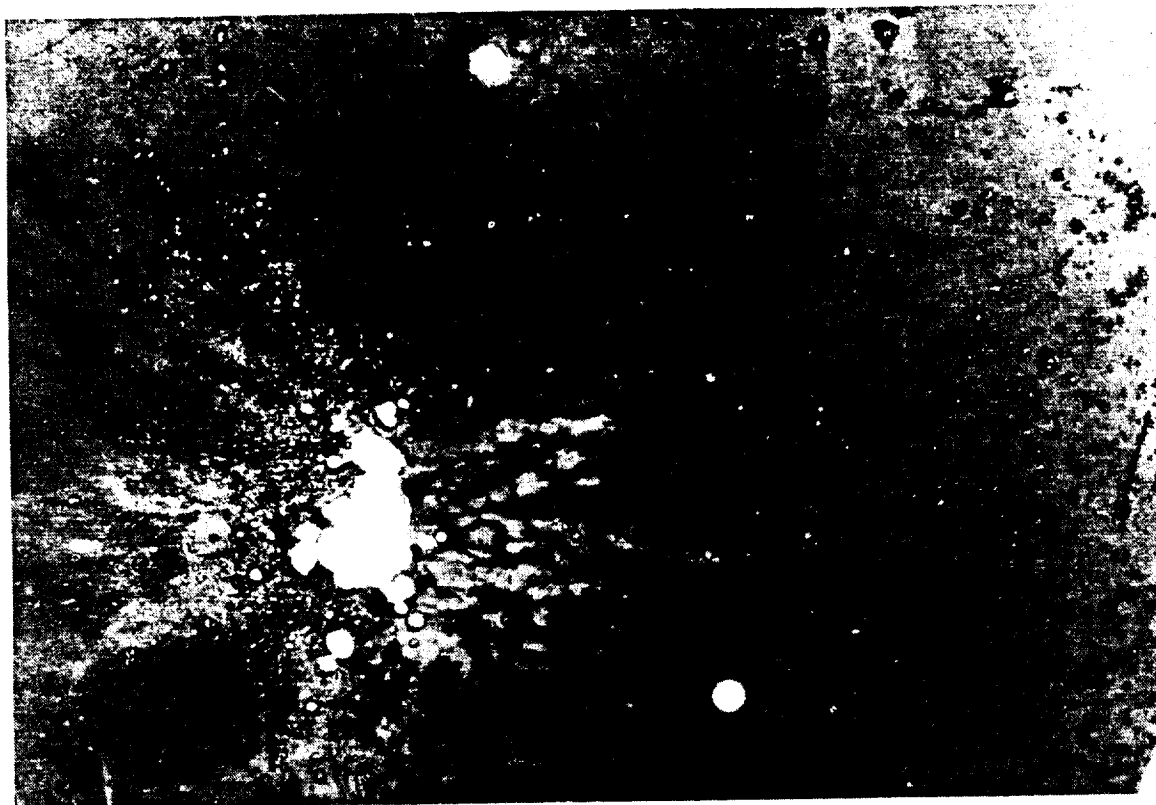
**45-Degree Obliquity**
(Above)

4-1303        6.56 km/s

1.143-mm-thick,
6061-T6 Aluminum Bumper
(t/D = 0.120)

3.18-mm-thick, 5456-H116
Aluminum Witness Plate
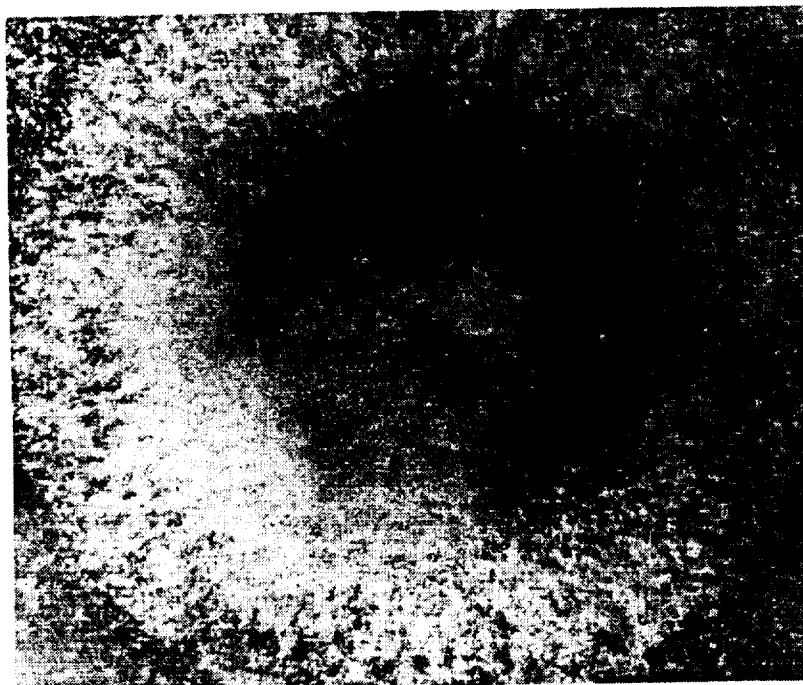

**Normal Incidence** (Left)

4-12911        6.71 km/s

1.549-mm-thick,
6061-T6 Aluminum Bumper
(t/D = 0.163)

3.18-mm-thick, 2219-T87
Aluminum Witness Plate

Figure 87. Damage patterns produced by debris clouds formed by the impact of 9.53-mm-diameter, 2017-T4 aluminum spheres with aluminum bumper sheets having similar *t/D* ratios. Bumpers were at 45-degrees obliquity for the upper plate and at normal incidence for the lower plate. Both plates are shown at the same scale.

203

some lateral dispersion (i.e., were above and below the plane of the top-view radiograph shown in Figures 84 and 85.

The irregularly-shaped damage pattern produced by Shot 4-1303 was in clear contrast to the circular pattern of uniformly-sized and evenly-distributed craters produced on the witness plate for Shot 4-1291 and for all tests done at normal incidence. In the case of a normal impact, expansion of the debris cloud, formation of the hole in the bumper, and production of the damage pattern were processes that were symmetric about the shot-line axis. Symmetry of these features occurred because the instantaneous properties of the impact-induced shock in the sphere were symmetric about the shot-line axis in planes normal to the shot-line axis. Uniform expansion of the shock in these planes resulted in a uniform response of the projectile material to the shock at all points equidistant from the shot-line axis. Axial symmetry of the shock does not occur in a sphere during an oblique impact. Shock properties were symmetric, however, in all planes normal to the plane that was perpendicular to the surface of the bumper and contained the shot-line axis and (i.e., the plane through the side-view x-rays and the range center line in Figure 83).

The kinematics of the impact of a sphere with any oblique surface are different than for an impact with a normal surface and will become increasingly different as the angle of obliquity of the impact increases. Because the bumper is inclined, the initial contact between the sphere and the bumper is a sliding contact and regions experiencing quasi one-dimensional loading may or may not develop. During penetration, the line of contact between the sphere and the bumper quickly changed from a circle to an arc that moved across the front of the sphere, away from the impact site. As the sphere embeds in the bumper, the downrange portion of the sphere may be fractured as a result of the release of shock-induced stresses produced during the its initial contact with the bumper. Most of the later stages of an oblique impact may involve the interaction of a fractured projectile with shock-disturbed bumper material. The holes in the bumpers used for the

204

oblique-impact tests were elliptical. Examination of the dimensions of the holes indicated they were larger on the downrange side than would have been expected, using an oblique projection of the hole formed by a normal impact as a standard for the hole dimensions. Expansion of the sphere during the impact could have produced the observed growth in the hole dimensions.

The downrange debris produced by an oblique impact tended to be distributed over a wider area than the debris for a normal impact. The debris clouds shown in Figures 83 and 84 were asymmetric and the projectile and bumper debris were shown to travel in two directions. The bumper debris (finer material in the "belly" of the debris cloud) moved away from the bumper, traveling along the normal to the bumper sheet; the projectile debris moved downrange, following a trajectory that deviated slightly toward the normal to the bumper, but that was generally along the shot-line axis.

When the angle of obliquity was increased from 30 degrees to 45 degrees, the size of the projectile fragments increased, even though the $t/D$ ratio of the bumper used for the 45-degree test was more than twice the $t/D$ ratio used for the 30-degree test. The increase in the $t/D$ ratio would have reduced the size of the fragments produced by impacts at normal incidence. Consequently, it would appear reasonable to assume that larger fragments would have been produced by a 45-degree impact with a bumper sheet that had the same $t/D$ ratio as the 30-degree impact (i.e., 0.053). It is clear that the processes of fracture and fragmentation of the sphere that occur during a normal impact are dominated by another process during an oblique impact.

The decrease in the axial velocity of the leading edge of the projectile fragments for the oblique impacts was greater than would have been expected for tests at normal incidence using the same bumper thicknesses. When the increase in the mass of the bumper encountered by the sphere during an oblique impact was taken into account, the observed decrease in leading-edge velocity appeared reasonable.

As the angle of obliquity increased, debris in the ejecta veil becomes more of a threat to objects on or close to the impact side of the bumper. The leading edge of the ejecta veil for the 45-degree test shown in Figure 84 was at least 50 percent further from the impact site than the leading edge of the debris cloud, indicating that some ejecta-veil fragments for this test were traveling at velocities well in excess of the impact velocity. At larger angles of obliquity, greater increases in the velocity of the ejecta-veil fragments will occur and, as shown by Schonberg and Taylor [63], present an increased threat to structures in their path. When the angle of obliquity is high, ricochet of the projectile is possible.

The results of the two tests described in this section merely provide a glimpse of a much wider spectrum of characteristics that exists for debris clouds formed by oblique impacts. A thorough examination of the effects of the angle of obliquity, impact velocity and $t/D$ ratio would require a large number of tests. The debris-cloud characteristics are expected, however, to change in an orderly fashion, although the rate of change may be rapid in some regions of the test-parameter space. Comparison of the results of the two oblique tests with the results of the test at normal incidence suggests ways in which the changes would occur. The distortion of the internal structure of a normal-impact debris cloud was evident in the debris cloud produced by the 30-degree impact. However, the distortion of the internal structure of the debris cloud that occurred for the 30-degree impact was much less than the distortion of the internal structure that occurred during the 15-degree interval between 30-degrees obliquity and 45-degrees obliquity. Conversely, very little change in the debris-cloud internal structure would be expected during the interval from normal incidence to 15 or 20 degrees of obliquity. Noticeable changes would occur during the interval from 15 or 20 degrees of obliquity to 30 degrees of obliquity.

206

# SECTION X. NONSPHERICAL-PROJECTILE IMPACTS

The preceding sections of this report have described the impact of spheres with different types of thin-sheet targets at normal and oblique angles of incidence. An aluminum sphere is commonly accepted as a standard projectile for use in evaluating the performance of spacecraft components and shields. However, it is very unlikely that micrometeoroids and fragments of orbital debris will be spherical. Morrison [68] had recognized the effect of projectile shape on the impact resistance of double-walled structures and had shown that cylinders impacting in the direction of their axis were considerably more effective penetrators than spheres of the same mass. In addition, he found that by reducing the length-to-diameter ratio of the cylinder, the mass of the cylinder required for penetration of the rear sheet of a double-walled structure could be reduced to one-seventh of the mass of the sphere required for penetration of the same structure. In another study, the inclination of right-cylinder aluminum projectiles at impact was shown to affect the level of damage inflicted on the rear wall of a double-sheet structure [69]. Cylinders that impacted with their axis aligned with the shot-line axis produced the least damage to a rear wall while cylinders inclined at approximately 45 degrees produced significantly more damage. Projectile shape and orientation at impact are critical parameters to be considered when assessing the lethality of nonspherical projectiles. Material presented in this section is intended to familiarize the reader with the effects of projectile shape on debris-cloud morphology. A detailed study of the causes of the differences in the morphologies of the debris clouds was not undertaken. Radiographs of tests that employed projectiles with regular and irregular shapes will simply be presented and significant features of the debris clouds will be described.

A series of tests performed at UDRI for Sandia National Laboratories provided radiographs of debris clouds that were produced by the impact of zinc spheres and

cylinders with zinc bumper sheets [49]. Three length-to-diameter ratios were used for the zinc cylinders. They were as follows: 0.05 (disk); 1.00 (right cylinder); and 3.55 (rod). The mass of the zinc sphere, disk, and right cylinder were the same. The mass of the rod was about 1.7 times greater than the other zinc projectiles.
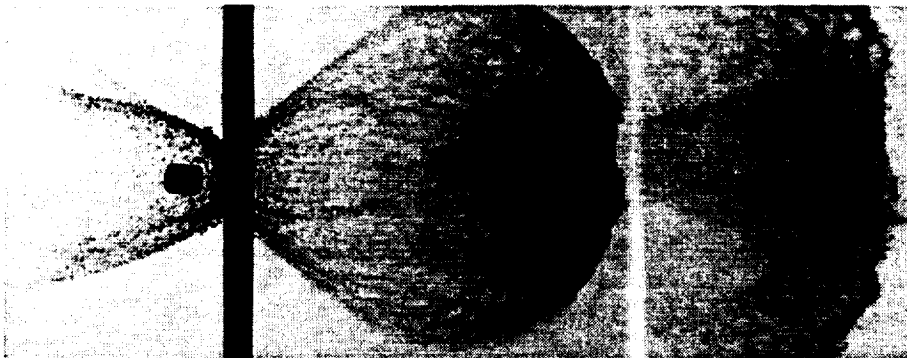
Radiographs of the debris clouds produced by the impact of a zinc sphere, right cylinder, short rod, and disk with 0.965-mm-thick zinc sheets are presented in Figure 88. Details of the projectile used for each test are provided with the radiographs. The morphological features of the debris clouds were unique for each projectile shape and the debris clouds produced different levels of damage to 2.44-mm-thick, 6061-T6 witness plates placed 15.2 cm downrange of the zinc bumpers. The features of the debris cloud for the zinc sphere were identical to the features of the $t/D = 0.16$ aluminum debris clouds described earlier in this report. The witness plate for Shot 4-1515 (sphere) was not perforated; the witness plates for the other three tests were perforated.

The right cylinder was inclined significantly ($\sim$ 20 degrees) when it struck the bumper sheet. Consequently, the debris cloud was distorted and asymmetric. As will be shown in a later figure, the timing and position (on the film) of the three post-impact x-ray views for the zinc tests was modified from the normal setup shown in Figure 3. In the modified setup, the first and third view of the debris cloud were made on the top-view film and the second view was made on the side-view film. The pre-impact view of the projectile was recorded on both pieces of film. The windows of the "unused" x-ray heads were covered with a sheet of lead. Since the top-view radiographs of the four tests provided two views of the debris clouds during their development, the top-view-radiographs were selected for use in the presentation of the series of debris clouds shown in Figure 88.

Two features observed in the debris cloud for Shot 4-1553 were also observed in the debris clouds for the tests with right-cylinder aluminum projectiles referenced earlier.

208
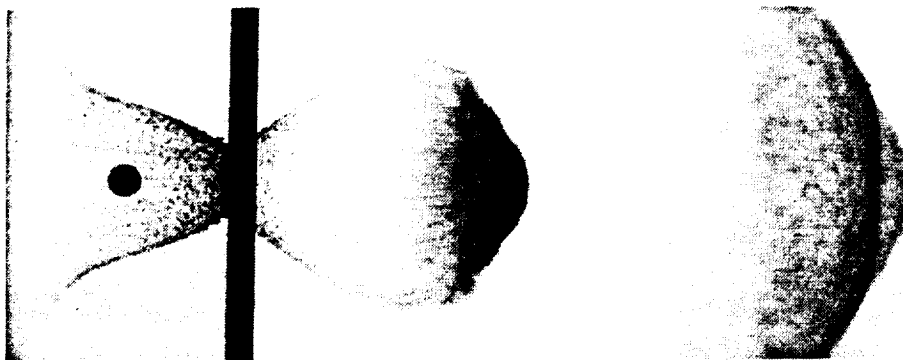
**Sphere**
5.766 mm Diameter
Mass = 0.7191 g

4-1515

4.98 km/s

**Right Cylinder**
5.055 mm Diameter,
5.055 mm Long
Mass = 0.7160 g

4-1553

5.22 km/s
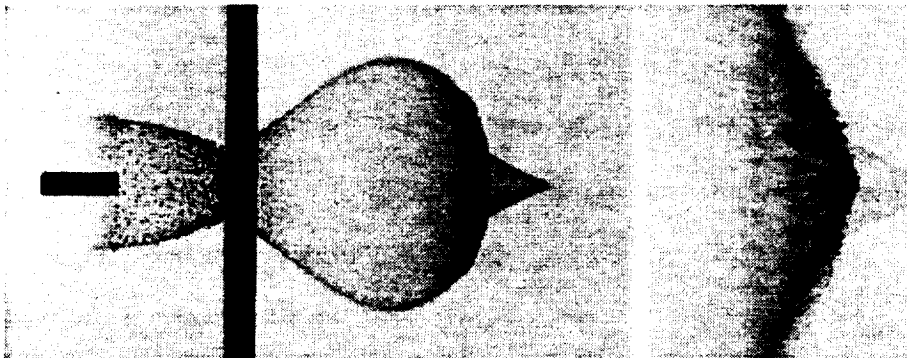
**Short Rod**
3.988 mm Diameter,
14.148 mm Long
Mass = 1.2407 g

4-1554

4.97 km/s
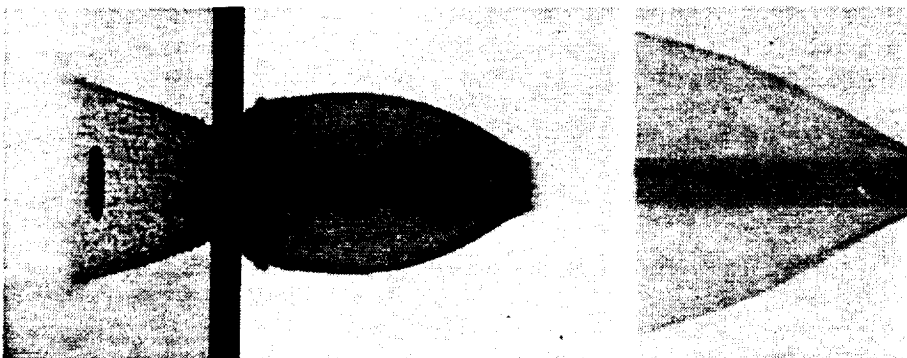
**Disk**
13.00 mm Diameter,
0.759 mm Long
Mass = 0.7314 g

4-1511

5.01 km/s

Figure 88. Radiographs of debris clouds produced by the impact of four different shapes of zinc projectiles with 0.965-mm-thick zinc bumper sheets.

These features were: (1) an inclined, conical front-element with the point towards the front of the structure and (2) a longer, denser, conical rear-element with the point at the rear of the element. The side-view radiograph showed the debris cloud to be distorted, with the conical front-element pointed down (in the direction of the inclination of the cylinder) and the conical rear-element pointed up. The conical front- and rear-elements were composed of bumper and projectile material, respectively. The witness plate for Shot 4-1553 (right cylinder) had a 5.6-cm-long tear that was promoted by a line of craters and holes formed by fragments that were located in the region of the debris cloud where the front and rear elements joined. Six large cracks ran at right angles to the tear in the witness plate and formed petals that were pushed toward the rear of the plate and formed an opening that was about 2.6 cm wide.

The short rod impacted the bumper with its axis nearly coincident with the shot-line axis. As shown in the radiograph of the debris cloud, a conical front-element of bumper debris was formed. Eroded projectile fragments formed a large, saucer-shaped structure around the conical front-element and at the front of the external bubble of debris. Approximately one-half of the rod remained intact and traveled at the original impact velocity after passing through the bumper sheet. A 3.6-cm-diameter hole was formed in the witness plate. It is likely that the hole was produced by the impact of the front element and the saucer-shaped structure of rod fragments. The rear end of the rod simply passed through the opening in the witness plate shortly after the hole was formed.

The debris cloud produced by the disk was most interesting. As shown in the views presented in Figures 88 and 89, a long columnar structure was formed inside an external bubble of debris. Several small internal features of the columnar structure elongated as the debris cloud moved downrange, indicating that the structure was composed of very small fragments and droplets. The structure, therefore, was considered to be a "porous rod" of bumper and projectile material. As shown in Figure 89, the rear

210
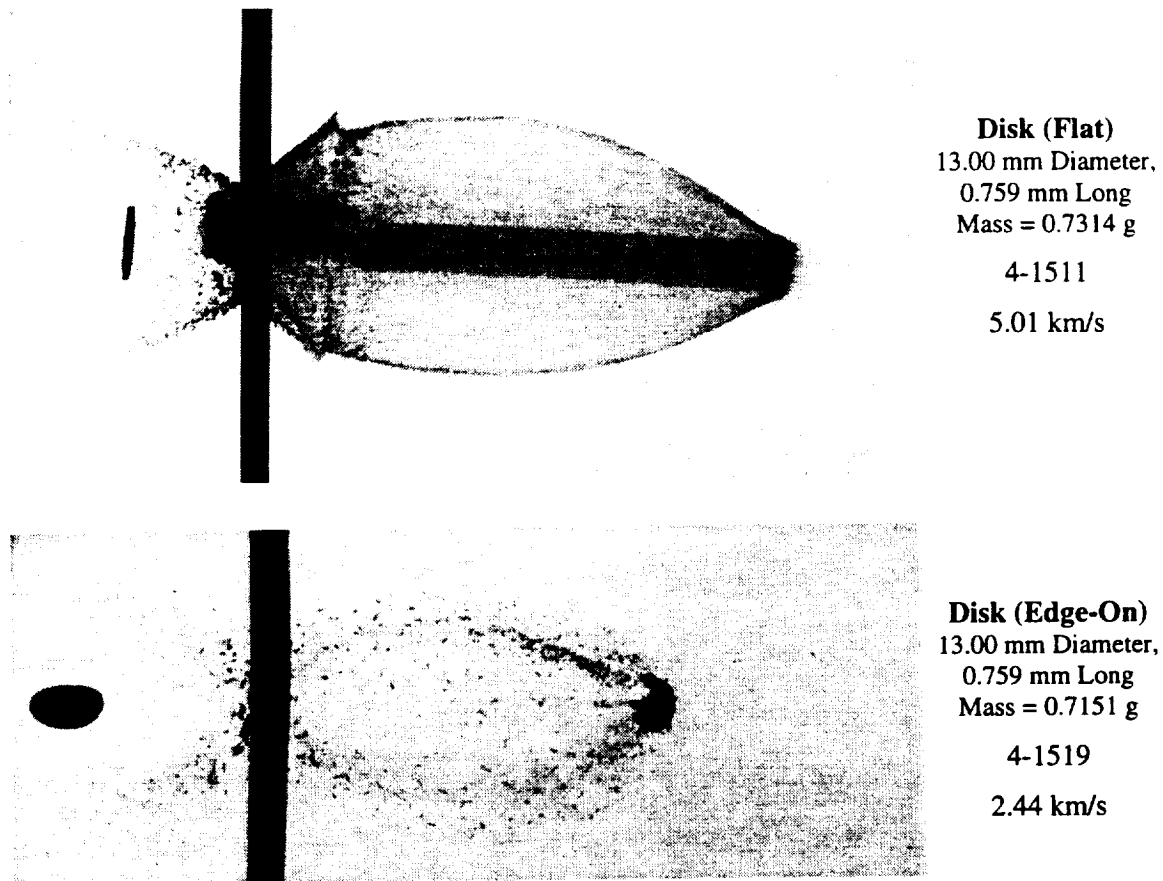
Figure 89. Views of debris clouds produced by the impact of zinc disks with 0.965-mm-thick zinc bumper sheets showing the effect of the pre-impact orientation of the disk on the fragmentation of the disk and the shape of the debris cloud.

end of the "porous rod" protruded through the hole in the bumper and moved *uprange* of the bumper (i.e., moved back toward the muzzle of the gun). The observed movement of both ends of the columnar structure was identical to the post-impact motions that are predicted for the free surfaces of two semi-infinite sheets that collide at hypervelocity. The impact of the columnar structure with the witness plate produced a 1.4-cm-diameter hole in the plate. Increasing or decreasing the spacing between the bumper and witness plate would have little effect on the damage to the plate, since the column did not display any tendency to disperse as it moved downrange.

As shown in Figure 89, the pre-impact orientation of the disk significantly affected the fragmentation of the disk and the characteristics of the debris cloud that was produced. In the case of an "edge-on" impact, only a portion of the leading edge of the disk was eroded, leaving much of the disk intact after the impact. The companion-view radiograph for Shot 4-1519 showed that the disk had rotated about 180 degrees, after impact, in the view shown in Figure 89. Although the impact velocity for Shot 4-1519 was less than one-half the impact velocity for Shot 4-1511, similar erosion of the leading edge of steeply-inclined, 2219-T87 aluminum disks was observed for impacts with Nextel sheets at 6.5 km/s.

The debris clouds shown thus far in this section, were produced by the impact of projectiles with regular shapes. Shape and orientation of the projectile at impact were shown to affect the characteristics and properties of the debris clouds. On occasion, spheres used in other tests were struck by debris from the sabot-stripper plate and were chipped or deformed prior to impact with a bumper sheet. Radiographs of debris clouds produced by the 7.2 km/s impacts of 6.35-mm-diameter, 2017-T4 aluminum spheres with nominally 0.32-mm-thick, 6061-T6 aluminum bumper sheets are shown in Figure 90. A typical debris cloud formed by the impact of a "clean" sphere is shown in the upper radiograph. The sphere in the center radiograph was heavily damaged by stripper-plate debris before it struck the bumper. A section of the upper rear of this sphere was removed and the portion that remained may have been broken into several large pieces. The debris cloud formed by the damaged sphere was considerably different than the debris cloud produced by the "clean" impact. The debris cloud formed by the damaged sphere was a cluster of randomly-spaced fragments of projectile and bumper debris, in contrast to the well-developed, symmetric structure formed by the impact of the intact sphere. As shown in the late-time-view of the debris cloud in Figure 90 (bottom radiograph), many of the damaged-sphere fragments were quite large when compared to the fragments produced

"Clean" Sphere
4-1449
t/D = 0.050
7.23 km/s

Damaged Sphere
4-1429
t/D = 0.058
7.14 km/s

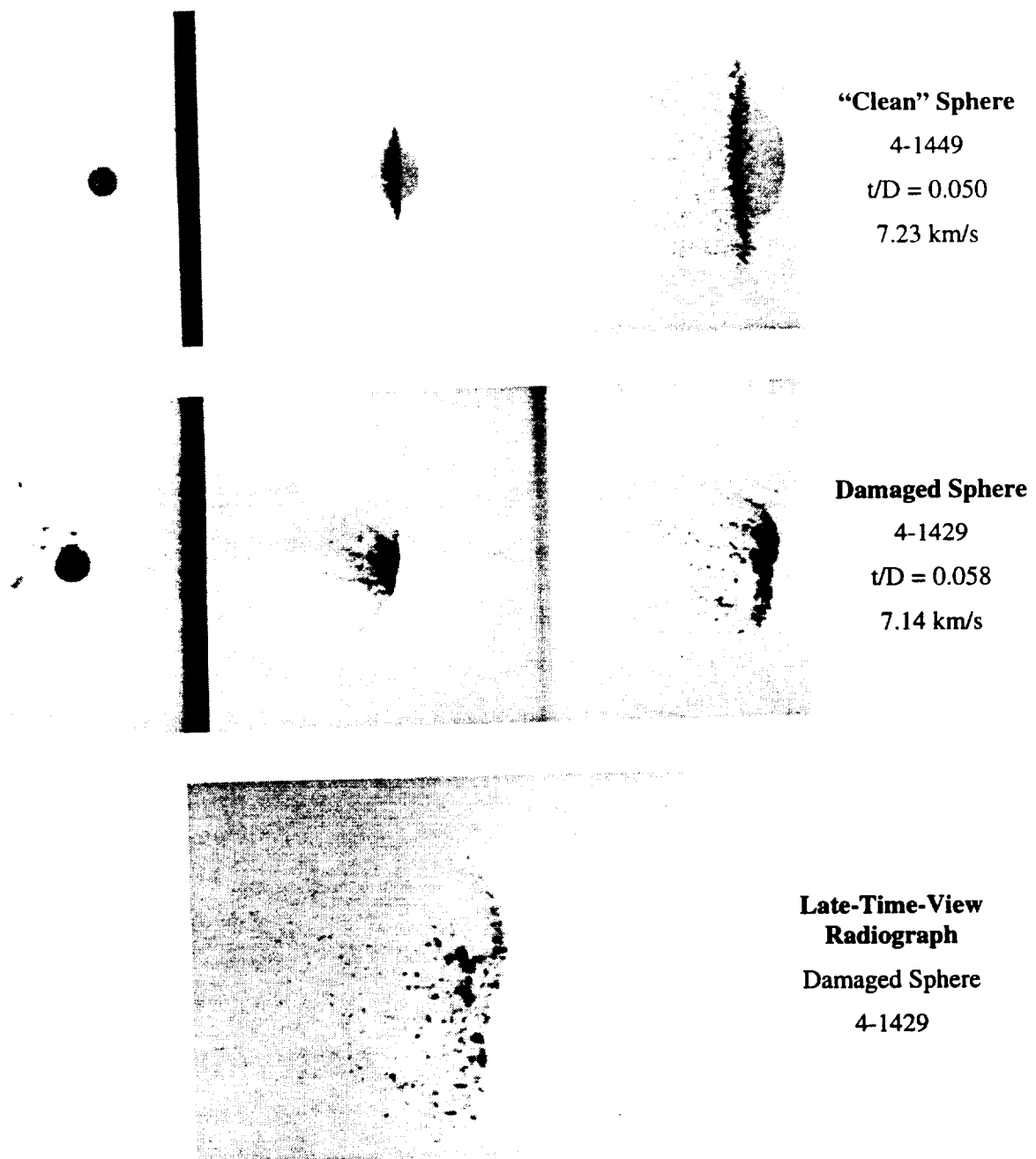Late-Time-View
Radiograph
Damaged Sphere
4-1429

Figure 90. Radiographs of debris clouds produced by the impact of 6.35-mm-diameter, 2017-T4 aluminum spheres with 0.32-mm-thick, 6061-T6 aluminum bumper sheets. The sphere shown in the middle radiograph was damaged by debris from the sabot-stripping operation.

213

by the impact of the undamaged sphere. The debris cloud formed by Shot 4-1429 may be more typical of a debris cloud produced by the impact of a large micrometeoroid or chunky fragment of orbital debris.

The debris clouds shown in the last radiographs to be presented in this report may be representative of debris clouds that would be produced by the impact of a "typical" piece of orbital debris. The pair of radiographs in Figure 91 show the debris cloud formed by the impact of a sabot insert, made of 7075-T6 aluminum, with a 0.965-mm-thick zinc bumper sheet. The insert was one of a pair that was placed inside the nylon sabot used during the launch of the short zinc rods shown in Figure 88. The sabot failed at some point during the launch process or was damaged during the sabot-stripping operation. The insert separated from the sabot and traveled to the target. The radiographs showed that it impacted the bumper sheet with its base end forward and was eroded to the
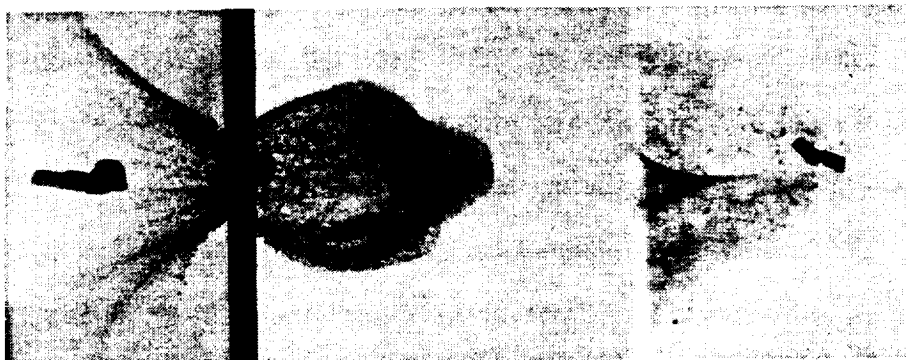


**Side-View Radiograph**
Sabot Insert
4-1549
5.03 km/s

**Top-View Radiograph**
Sabot Insert
4-1549
5.03 km/s

Figure 91. Radiographs of debris cloud produced by the impact of a sabot insert, made of 7075-T6 aluminum, with a 0.965-mm-thick zinc bumper sheet.

hole seen in the pre-impact view of the insert. The front of the debris cloud is asymmetric, with the eroded sabot insert just inside the leading edge of the cloud.

The radiographs of the debris clouds produced by the normal impact of irregularly-shaped projectiles (i.e., the edge-on disk in Figure 89, the damaged sphere in Figure 90, and the sabot insert in Figure 91) all show a large portion of the projectile intact and at the front of the leading edge of the debris cloud. By contrast, the large central fragment produced by the normal impact of a sphere with a thin sheet was always a short distance behind the front element of the debris cloud. The size and location of the large, irregularly-shaped fragment of projectile in the debris cloud, makes the fragment a serious threat to the second sheet of a double-walled structure. In many respects, the properties of the fragments in the debris clouds produced by nonspherical projectiles are similar to the properties of the fragments in debris clouds produced by oblique impacts. Evaluations of the effectiveness of spacecraft shields that are based on the results of tests that used "relatively benign" spheres as simulants of an unknown threat (unknown in mass, shape, density, impact velocity, and angle of incidence) must be tempered with the realization that the real threat is likely to more severely challenge the shield structure.

The probable cause of the reduced effectiveness of bumper shields in the promotion of the disintegration of nonspherical projectiles must be related to the nonuniform propagation of impact-induced shocks and stresses in the bumper and projectile. When a disk or short cylinder (length-to-diameter ratio of one or less) impacts a thin sheet at normal incidence, with the axis of the disk or sphere coincident with the shot-line axis, a one-dimensional shock propagates in the projectile and the bumper. The moving shock encounters undisturbed material as it travels through the projectile and bumper. After passage of the shock, all material in the planes normal to the shot-line axis will have experienced the same stress levels. Fracture and fragmentation of the projectile and the affected portion of the bumper occurred when they were released from the

shocked state. Propagation of a shock in a sphere is also an axisymmetric process and was described in detail in Section XI. During the impact of nonspherical projectiles with thin bumper sheets, propagation of the shocks in both materials was not a symmetric or predictable process. The orientation of local features of the projectile may or may not promote shock loading in the region of the feature. In many instances, a shock generated in the bumper or projectile will outrun the point of contact between their impacting surfaces. As a result, subsequent contact between the surfaces will involve interactions of previously-disturbed material. Loads generated by impacts with postshocked material may be considerably lower than loads generated by impacts with unshocked material because of microscopic changes in the structure of the previously-shocked material. Reduced impact loading of the projectile would result in the formation of larger fragments in the debris clouds.

# SECTION XI. SUMMARY AND CONCLUSIONS

Forty-three tests were performed to examine the formation of debris clouds produced by the hypervelocity impact of aluminum spheres with thin aluminum sheets. Sphere diameter (6.35 to 12.70 mm), bumper-sheet thickness (0.25 to 4.80 mm), and impact velocity (1.98 to 7.38 km/s) were the primary test variables. In several of the tests, the alloy of the spheres (2017-T4 and 1100-O) and/or sheets (1100-O, 2024-T3, and 6061-T6) was changed to evaluate the effect of material properties on the debris-cloud formation process. Except for two tests in which the bumper sheet was at an oblique angle, the tests were performed with the bumper sheet normal to the shot-line axis.

All tests provided multiple-exposure, orthogonal-pair flash radiographs of the debris clouds produced by the impacts. Measurements taken from the flash radiographs were used to determine: (1) the velocity of a number of characteristic points in the debris clouds; (2) fragment sizes; and (3) fragment-size distributions. Sufficient test data were available to permit an evaluation of the effect of $t/D$ ratio, impact velocity, scale, and material on the debris-cloud formation process. Analyses of the holes formed in the bumper sheets and the damage patterns produced on witness plates behind the bumpers complemented the analyses of the flash radiographs. Although the study described in this report was limited in terms of the range and number of test conditions, sufficient data were available to permit determination of trends and reasonable speculation on behavior in those regions where data were not available.

All debris clouds exhibited an ejecta veil, which consisted almost entirely of bumper fragments, on the impact or front side of the bumper and an expanding bubble of bumper and sphere debris on the rear side of the bumper. At the lower impact velocities, the intact or partially fragmented sphere was visible at the front of the expanding bubble of bumper debris. At the higher impact velocities, a characteristic internal structure of

217

projectile fragments developed at the front of the bubble of bumper debris. This internal structure was composed of a front, center, and rear element and was the most significant feature of the debris cloud in terms of potential for rear-wall damage. Axial and radial growth of the debris-cloud internal structure and more extensive fragmentation of the sphere were observed as $t/D$ ratio and/or impact velocity was increased.

The failure and fragmentation of an aluminum sphere that was initiated by an impact with a thin aluminum sheet was an orderly process. Several stages of failure of the sphere were observed as impact velocity was varied. When the impact velocity was low, plastic deformation of the front (impacting) surface and the development of a spall failure inside the rear surface of the sphere were the first manifestations of failure of the sphere. The onset of cracking or swelling of the rear surface of the sphere, due to the spall failure, was used to define a spall-failure-threshold velocity that was unique for each combination of impact velocity and $t/D$ ratio. At impact velocities slightly above the threshold velocity, a shell of spall fragments developed when the spall layer broke open and the spall petals separated from the back of the sphere. When the impact velocity was increased further, a cloud of projectile fragments formed and developed into a structure with the three well-defined elements mentioned in the preceding paragraph.

For impacts at the velocities and $t/D$ ratios where the debris clouds were fully developed (i.e., the internal structure consisted of a front, center, and rear element), the front element was composed of finely divided fragments and/or molten droplets of bumper and projectile. The disk-like center element was composed of solid slivers, comma-shaped, and/or chunky pieces of fragmented projectile and a single large chunky projectile fragment that was located at the center of the disk and on the debris-cloud center line. The bulk of the post-impact projectile mass appeared to be concentrated in the center element. The rear element of the internal structure was a hemispherical shell of fragments that spalled from the rear surface of the sphere.

Up to ten characteristic points were identified in the internal structures of the debris clouds. The axial and radial velocities of these points were determined using measurements taken from radiographs of the debris clouds. These point velocities were normalized by dividing them by the impact velocity of the test. Use of the normalized debris-cloud velocities to evaluate the growth of debris clouds produced by projectiles of various diameters indicated that the clouds were similar (within measurement limits) when compared on the basis of $t/D$ ratio and impact velocity. When the dimensions of debris clouds from tests using different sphere diameters, but identical $t/D$ ratios and impact velocities, were compared (at similar times after impact), the differences in these dimensions were simply the differences in the original diameters of the spheres. Most debris clouds, particularly those formed at the higher impact velocities, were symmetric about the debris-cloud center line. Debris clouds formed at the lower impact velocities tended to be slightly to significantly distorted and/or asymmetric about the debris-cloud center line.

Bumper-material alloy did not appear to affect the normalized axial and diametral velocities of most of the measurement points. However, the normalized expansion velocity of the spall-shell fragments was slightly higher for the tests with 2024-T3 aluminum bumpers than for tests with 6061-T6 aluminum bumpers. When the sphere alloy for tests with a $t/D$ ratio of 0.047 was changed from 2017-T4 aluminum to 1100-O aluminum, the expansion velocities of the center and rear elements were significantly different. The radial velocity of the periphery of the center element was slightly higher (four percent) and the spall-shell-expansion velocity was noticeably lower (fourteen percent) for the debris cloud produced by the 2017-T4 sphere.

Fragmentation of the sphere was a process that was sensitive to the intensity and the duration of the stress pulse produced by the impact with the thin bumper sheet. A comparison of spall-shell-fragment Martin's diameters from tests with the same material,

*t/D* ratio, and impact velocity, but different sphere diameters indicated that spall-shell-fragment size did not scale with the "geometry" of the test. Maintenance of similar *t/D* ratios for these comparisons required that the bumper-sheet thicknesses be different. Since the duration of the impact-induced stress pulse in the sphere was determined by the thickness of the bumper sheet, the observed difference in spall-shell-fragment size, for geometrically "similar" tests, was reasonable. The equivalent diameter of the large central fragment, however, scaled with *t/D* ratio when impact velocity was held constant. The large central fragment appeared to be a piece of the sphere that was derived from material that was near the center of the sphere but remained intact after the fracture and fragmentation phases of the debris-cloud formation process were complete.

A collection of models was developed and used to describe the formation of various debris-cloud elements. An examination of the kinematics of the impact of a sphere with a sheet showed that a portion of the sphere and bumper sheet were subjected to quasi one-dimensional loading during the initial phase of impact and that these portions formed the front element. Rapid growth of the center element was altered and/or confined by the interaction of the periphery of the center element with the edge of the evolving hole in the bumper sheet and/or the external bubble of debris. The circularity of the shell of spall fragments changed as *t/D* ratio and/or impact velocity were varied. A method for estimating the state of the material in a debris cloud was developed. Features observed in the radiographs of the debris clouds indicated that the estimation procedure was reasonable. Results of tests employing cadmium and zinc spheres and thin-sheet targets were used to infer the properties of aluminum debris clouds formed at velocities high enough to induce vaporization of the sphere and target.

Measurements of the damage done to the bumper sheets and the witness plates were analyzed. Microscopic examination of cross sections of bumper sheets, taken from the region near the edge of the hole, showed a progression of overturned flap and lip

features as $t/D$ ratio was increased. The diameters of the holes produced in the thinnest bumpers were found to be insensitive to changes in impact velocity; the diameters of the holes in the thicker bumpers were shown to be increasingly sensitive to impact velocity as $t/D$ ratio increased. Damage patterns on the witness plates were related to features observed in the debris clouds.

A description of the effect an intermediate layer of a multicomponent shield had on the debris cloud produced by the normal impact of a sphere with a thin bumper sheet was presented. In addition, radiographs of debris clouds produced by the oblique impact of spheres and the normal impact of nonspherical projectiles were shown and discussed. The properties of the debris clouds produced by these last two categories of impacts do not conform to the properties and characteristics of the debris clouds that were described for the normal impact of spherical projectiles with thin sheets. In particular, fracture and fragmentation of the projectile was significantly less for these two types of asymmetric impacts. Considerable effort and additional study will be required to adequately model and describe the features and properties of debris clouds produced by oblique impacts and the impacts of nonspherical projectiles.

The quality of the data presented in this report provided many insights into the debris-cloud formation process; however, the quantity of data for each test condition was minimal at best. While the reliability of most of the data appeared adequate (when viewed as a set or subset for particular test conditions), very few tests were actually replicated. Given the benchmark character of the data in this report, future work should first concentrate on providing additional data that would be used to strengthen statements that were made regarding trends observed in the limited data sets. Implicit in this statement is the requirement that multiple tests be performed at identical test conditions.

Data presented in this report provide a quantitative description of the formation of debris clouds produced by the normal impact of aluminum spheres with thin aluminum

sheets, for the range of impact velocities that can currently be achieved in the laboratory. These data can be used to their best advantage in the validation of models developed for use in numerical (computer) simulations of hypervelocity impacts. Ultimately, reliable models and accurate simulations will provide more information regarding the physics of the impact process, of debris cloud formation, and of the response of the main wall of a spacecraft to the impact of the debris cloud than can be obtained from impact tests. Evaluation of the response of "real" spacecraft shields to realistic threats of impact velocity and obliquity will require the use of these models and simulation techniques. These models and simulation techniques must be able to accurately reproduce all the details of the debris clouds described in this report. The inability of a model to meet this simple requirement will cause concern for the validity of the model.

When making comparisons of real and simulated debris clouds, the comparisons must focus on those conditions where experimental data are available before exploring the results of computations made using other test parameters (e.g., higher impact velocities). Particular attention should be devoted to comparisons of the shape of debris-cloud elements, the velocities and dimensions of the measurement points identified in this report, the size and distribution of fragments in the debris cloud, and the effects of a change of state on the projectile and target materials. Much work remains to be done in the development and formulation of reliable fracture and fragmentation models. Since the formation of the spall shell was an external expression of the characteristics of the stress pulse, the spall-shell-fragment data presented in this report would be most useful in the evaluation and refinement of fracture and fragmentation models. The effects of a change of state of projectile and shield material on debris-cloud formation and structure is also an area requiring much additional work. Unless realistic simulations of these aspects of symmetric impacts can be performed, credible simulations of the oblique impact of irregularly-shaped objects with debris shields will be impossible.

# REFERENCES

1.    Whipple, F. L.: Meteorites and Space Travel. *The Astronomical Journal*, No. 1161, 131, February 1947.

2.    *Proceedings, The Rand Symposium on High-Speed Impact.* Sponsored by the Rand Corporation and the Office of Scientific Research of the Air R&D Command, The Rand Corporation, Santa Monica, CA, January 31-February 2, 1955.

3.    *Proceedings, The Second Hypervelocity and Impact Effects Symposium.* Sponsored by the Naval Research Laboratory and the Air Research and Development Command, Naval Research Laboratory, Washington, DC, May 22-24, 1957.

4.    *Proceedings, The Third Symposium on Hypervelocity.* Sponsored by the US Army, Navy, and Air Force, Armor Research Foundation of IIT, Chicago, IL, October 7-9, 1958.

5.    *Proceedings, Hypervelocity Impact Fourth Symposium.* Sponsored by the US Army, Navy, and Air Force, Air Research and Development Command, Eglin AFB, FL, April 26-28, 1960.

6.    *Proceedings, Fifth Symposium on Hypervelocity Impact.* Sponsored by the US Army, Navy, and Air Force, Colorado School of Mines, Denver, CO, October 30-November 1, 1961.

7.    *Proceedings, Sixth Symposium on Hypervelocity Impact.* Sponsored by the US Army, Navy, and Air Force, The Firestone Tire & Rubber Co., Cleveland, OH, April 30-May 2, 1963.

8.    *Proceedings, Seventh Hypervelocity Impact Symposium.* Sponsored by the US Army, Navy, and Air Force, Martin Company (Orlando), Orlando, FL, November 17-19, 1964.

9.    *Proceedings, AIAA Hypervelocity Impact Conference.* American Institute of Aeronautics and Astronautics, Cincinnati, OH, April 30-May 2, 1969.

10.   Maiden, C. J.: Experimental and Theoretical Results Concerning the Protective Ability of a Thin Shield Against Hypervelocity Projectiles. *Proc. Sixth Symp. on Hypervelocity Impact,* Vol. 3, 69-156, Cleveland, OH, August 1963.

11.   Maiden, C. J., A. R. McMillan, and R. E. Sennett: Thin Sheet Impact. NASA CR-295, September 1965.

# REFERENCES
## (Continued)

12. Backman, M. E. and W. J. Stronge: Penetration Mechanics and Post-Perforation Effects in an Aluminum-Aluminum System. NWC TP 4414, October 1967.

13. Swift, H. F., J. M. Carson, and A. K. Hopkins: Ballistic Limits of 6061-T6 Aluminum Bumper Systems. AFML-TR-67-324, October 1967.

14. Nysmith, C. R. and B. P. Denardo: Experimental Investigation of the Momentum Transfer Associated with Impact into Thin Aluminum Targets. NASA TN D-5492, October 1969.

15. 1986 Hypervelocity Impact Symposium Proceedings. *Int. J. Impact Engng.* **5**, 1987.

16. 1989 Hypervelocity Impact Symposium Proceedings. *Int. J. Impact Engng.* **10**, 1990.

17. 1992 Hypervelocity Impact Symposium Proceedings. *Int. J. Impact Engng.* **14**, 1993.

18. 1994 Hypervelocity Impact Symposium Proceedings. *Int. J. Impact Engng.* **17**, 1995.

19. Piekutowski, A. J.: Properties of Largest Fragment Produced by Hypervelocity Impact of Aluminum Spheres with Thin Aluminum Sheets. *Proc. AIAA Space Programs and Technologies Conference,* Paper No. 92-1588, Huntsville, AL, March 1992.

20. Ang, J. A.: Pulsed Holography Diagnostics of Impact Fragmentation, in *High-Pressure Shock Compression of Solids II,* L. Davison, D. E. Grady, and M. Shahninpoor, Eds., 176-193, Springer-Verlag, 1995.

21. Herdan, G.: *Small Particle Statistics.* Elsevier Publishing Co., Houston, TX, 1953.

22. Grady, D. E.: Personal Communication. Sandia National Laboratory, 1992.

23. Grady, D. E.: Local Inertial Effects in Dynamic Fragmentation. *J. Appl. Phys.,* **53**, 322-325, 1982.

24. Grady, D. E.: The Spall Strength of Condensed Matter. *J. Mech. Phys. Solids,* **36**(3), 353-384, 1988.

# REFERENCES
## (Continued)

25.    Maiden, C. J. and A. R. McMillan:  An Investigation of the Protection Afforded a Spacecraft by a Thin Shield. *AIAA*. 2(11), 1992-1998, 1964.

26.    Carson, J. M. and H. F. Swift:  Hole Diameters in Thin Plates Perforated by Hypervelocity Projectiles. AFML/MAY-TM-67-9, November 1967.

27.    Hörz, F., M. J. Cintala, R. H. Bernhard, and T. H. See:  Dimensionally Scaled Penetration Experiments:  Aluminum Targets and Glass Projectiles 50 μm to 3.2 mm in Diameter. *Int. J. Impact Engng.* 15(3), 257-280, 1994.

28.    Hörz, F., M. J. Cintala, R. H. Bernhard, and T. H. See:  Cratering and Penetration Experiments in Teflon Targets at Velocities from 1 to 7 km/s. *Int. J. Impact Engng.* 17, 419-430, 1995.

29.    Piekutowski, A. J.:  Unpublished data. UDRI, 1989.

30.    Turpin, W. C. and J. M. Carson:  Hole Growth in Thin Plates Perforated by Hypervelocity Pellets. AFML-TR-70-83, April 1970.

31.    Duvall, G. E.:  Shock Waves in Solids.  In *Shock Metamorphism of Natural Materials*, B. M. French and N. M. Short, Eds., 19-29, Mono Book Corp., Baltimore, MD, 1968.

32.    Kipp, M. E., D. E. Grady, and J. W. Swegle:  Numerical and Experimental Studies of High-Velocity Impact Fragmentation. *Int. J. Impact Engng.* 14, 427-438, 1993.

33.    Alme, M. L. and C. E. Rhoades, Jr.:  A Computational Study of Projectile Melt in Impact with Typical Whipple Shields. *Int. J. Impact Engng.* 17, 1-12, 1995.

34.    Gilath, I., S.Eliezer, T. Bar-Noy, R. Englman, and Z. Jaeger:  Material Response at Hypervelocity Impact Conditions Using Laser Induced Shock Waves. *Int. J. Impact Engng.* 14, 279-289, 1993.

35.    Piekutowski, A. J.:  Characteristics of Debris Clouds Produced by Hypervelocity Impact of Aluminum Spheres with Thin Aluminum Plates. *Int. J. Impact Engng.* 14, 573-586, 1993.

# REFERENCES
## (Continued)

36.   Ang, J. A.: Impact Flash Jet Initiation Phenomenology. *Int. J. Impact Engng.* **10**, 23-33, 1990.

37.   Swift, H. F., D. D. Preonas, and W. C. Turpin: Dissection Methods for Measuring the Characteristics of Expanding Debris Clouds. *Rev. Sci. Instrum.* **41**(5), 746-751, May 1970.

38.   Rinehart, J. S.: *Stress Transients in Solids.* Hyper Dynamics, Sante Fe, NM, 1975.

39.   Hopkins, A. K., T. W. Lee, and H. F. Swift: Materials Phase Transformation Effects upon Performance of Spaced Bumper Systems. *J. Spacecraft Rockets* **9**, 342-345, 1970.

40.   Anderson, C. E. Jr., T. G. Trucano, and S. A. Mullin: Debris Cloud Dynamics. *Int. J. Impact Engng.* **9**(1), 89-113, 1990.

41.   Bjork, R. J.: Vaporization and SDI Lethality. DNA-TR-89-28, July 1990.

42.   Shockey, D. A., D. R. Curran, J. E. Osher, and H. H. Chau: Disintegration Behavior of Metal Rods Subjected to Hypervelocity Impact. *Int. J. Impact Engng.* **5**, 585-593, 1987.

43.   Lubars, W.: *Materials in Design Engineering, Materials Selector Issue* **58**(5), Reinhold Publishing Corporation, New York, NY, 1963.

44.   Chhabildas, L. C., L. M. Barker, J. R. Asay, and T. G. Trucano: Relationship of Fragment Size to Normalized Spall Strength for Materials. *Int. J. Impact Engng.* **10**, 107-124, 1975.

45.   Trucano, T. G. and J. R. Asay: Effects of Vaporization on Debris Cloud Dynamics. *Int. J. Impact Engng.* **5**, 645-653, 1987.

46.   Alme, M. L., E. L. Christiansen, and B. G. Cour-Palais: Hydrocode Simulations of the Multi-Shock Meteoroid and Debris Shield. in *Shock Compression of Condensed Matter 1991*, S. C. Schmidt, R. D. Dick, J. W. Fowles, and D. G. Tasker, Eds., 975-978, Elsevier Science Publishers B. V., Amsterdam, The Netherlands, 1992.

# REFERENCES
## (Continued)

47. Marsh, S. P. (Editor): *LASL Shock Hugoniot Data*. University of California Press, Berkeley, CA, 1980.

48. Schmidt, R. M., K. R. Housen, A. J. Piekutowski, and K. L. Poormon: Cadmium Simulations of Orbital Debris Shield Performance to Scaled Velocities of 18 km/s. *J. Spacecraft Rockets* **31**(5), 866-877, 1994.

49. Konrad, C.H., L. C. Chhabildas, M. D. Boslough, A. J. Piekutowski, K. L. Poormon, S. A. Mullin, and D. L. Littlefield: Dependence of Debris Cloud Formation on Projectile Shape, in *High-Pressure Science and Technology–1993*, American Institute of Physics AIP Conference Proceedings 309, Part 2, S. C. Schmidt, J. W. Shaner, G. A. Samura, and M. Ross, Eds., 1845-1848, AIP Press, New York, NY, 1994.

50. Mullin, S. A., C. E. Anderson, Jr., and J. S. Wilbeck: Dissimilar Material Scaling Relationships for Hypervelocity Impact, DNA-TR-89-112, February 1989.

51. Holsapple, K. A.: Hypervelocity Impact Experiments in Surrogate Materials. *Int. J. Impact Engng.* **14**, 335-345, 1993.

52. Poormon, K. L. and A. J. Piekutowski: Comparisons of Cadmium and Aluminum Debris Clouds. *Int. J. Impact Engng.* **17**, 639-648, 1995.

53. Backman, M. E. and S. A. Finnegan: A Phenomenological Investigation of Compact Projectiles Against Plates at Speeds up to 3 km/s, in *Eighth International Symposium on Ballistics*, American Defense Preparedness Association, VIII-13 - VIII-25, Orlando, FL, 1984.

54. Gehring, J.: Theory of Impact on Thin Targets and Shields and Correlation with Experiment, in *High-Velocity Impact Phenomena*, Kinslow, Ed., 105-156, Academic Press, New York, NY, 1970.

55. Richardson, A. J.: Theoretical Penetration Mechanics of Multi-sheet Structures Based on Discrete Modeling. *J. Spacecraft Rockets* **17**, 486-489, 1982.

56. Christiansen, E. L.: Evaluation of Space Station Meteoroid Debris Shielding Materials, Eagle Engineering Report 87-163, 1987.

# REFERENCES
## (Concluded)

57. Cour-Palais, B. G. and J. L. Crews: A Multi-Shock Concept For Spacecraft Shielding. *Int. J. Impact Engng.* **10**, 135-146, 1990.

58. Cour-Palais, B. G. and A. J. Piekutowski: The Multi-Shock Hypervelocity Impact Shield, in *Shock Compression of Condensed Matter 1991*, S. C. Schmidt, R. D. Dick, J. W. Fowles, and D. G. Tasker, Eds., 979-982, Elsevier Science Publishers B. V., Amsterdam, The Netherlands, 1992.

59. Cour-Palais, B. G., A. J. Piekutowski, K. J. Dahl, and K. L. Poormon: Analysis of the UDRI Tests on Nextel Multi-Shock Shields. *Int. J. Impact Engng.* **14**, 193-204, 1993.

60. *Nextel Ceramic Fiber Products.* Nextel 312 Fiber Product Data Sheets. 3M Ceramic Materials Department, St. Paul, MN.

61. Christiansen, E. L.: Personal Communication. NASA-JSC, 1994.

62. Gehring, J.: Engineering Considerations in Hypervelocity Impact, in *High-Velocity Impact Phenomena*, Kinslow, Ed., 463-514, Academic Press, New York, NY, 1970.

63. Schonberg, W. P. and R. A. Taylor: Penetration and Ricochet Phenomena in Oblique Hypervelocity Impact. *AIAA*, **25**(7), 639-646, 1989.

64. Ari, N., and J. S. Wilbeck: Debris Fragment Characterization in Oblique Hypervelocity Impact. *Int. J. Impact Engng.* **14**, 37-48, 1993.

65. Christiansen, E. L.: Unpublished Data. NASA-JSC, 1994.

66. Williamsen, J. E.: Unpublished Data. NASA-MSFC, 1994.

67. Schmidt, R. M.: Unpublished Data. Boeing Defense & Space Group, 1994.

68. Morrison, R. H.: Investigation of Projectile Shape Effects in Hypervelocity Impact of a Double-Sheet Structure. NASA TN D-6944, August 1972.

69. Piekutowski, A. J.: Debris Clouds Generated by Hypervelocity Impact of Cylindrical Projectiles with Thin Aluminum Plates. *Int. J. of Impact Engng.* **5**, 509-518, 1987.

# APPENDIX

This appendix contains the raw spall-fragment data taken from enlarged prints of the late-time-view radiographs of 13 tests. Two data sheets are presented for one of the tests, Shot 4-1621. For this test, Martin's diameter measurements were made parallel *and* perpendicular to the shot-line axis. Details of the analytical treatment of this data were given in Section IV, Part C. A brief description of the procedures used to prepare the prints for the analysis of the fragments is presented in this appendix. This description and the illustrations of the process provide the information needed for interpretation of the sets of data that are presented with the fragment-size-distribution data tables that follow.

Enlarged photographs (approximately 2.5X) of the late-time view radiographs were prepared and marked for analysis by scribing a set of lines and circles into the print, as shown in Figure A1. First, an arc that circumscribed the shell of spall fragments was
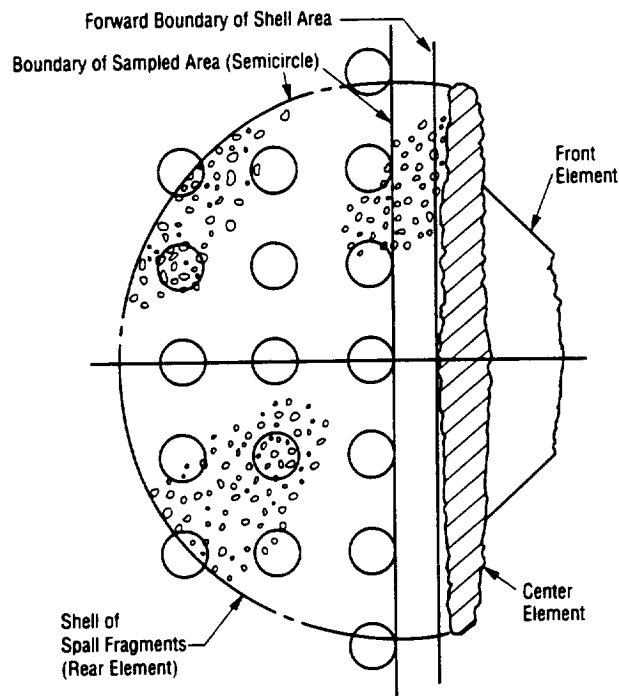


Figure A1. Illustration of the lines and circles scribed on the prints of radiographs used for the analysis of spall-shell fragments.

scribed on the photograph. Next, lines were drawn parallel and perpendicular to the shot-line axis of the debris cloud, through the center of the arc describing the spall shell. The forward boundary of the spall shell was defined by a line that was drawn perpendicular to the shot-line axis and just touched the rear of the center element. Finally, a template was used to scribe a series of 0.50-inch-diameter circles in the area to be sampled. The template was made so that one field circle was drawn for each square inch of area to be examined. After each print was scribed, the field circles were numbered and the fragments in each field circle were identified before their measurements were taken. The number of field circles (and the total field area) are given for each test. The number of field circles listed on the data sheets included all full and partial field circles within the sampled area. For two of the tests, Shots 4-1395 and 4-1622, additional field circles were used in the analysis. These additional circles filled the spaces in each *row* of field circles (i.e., the added circles filled the rows shown parallel to the shot-line axis in Figure A1).

In eight of the tests, the center of the arc that formed the boundary of the spall-shell area was behind the line defining its forward boundary. For these eight tests, the leading edge of the pattern of field circles, or the sampled area, was drawn tangent to the vertical center line of the arc as shown in Figure A1. For the other five tests, the center of the arc was in front of the forward boundary of the spall-shell area and the sampled area was coincident with the spall-shell area. The field-circle pattern was drawn with its leading edge tangent to the forward boundary of the sampled area.

The spall shell had grown to be too large to be confined to the 4-inch-wide x-ray film for five of the tests. For these tests, the sampled area was "clipped" at the top and/or bottom. An illustration of the possible combinations of sampled and shell areas is shown in Figure A2. In this figure, the forward edge of the spall-shell area is shown as a dashed line. In the data sheets that follow, the sampled area, sampled area type, and shell area are provided for each test. The total number of fragments in the spall shell, $N_T$, was estimated
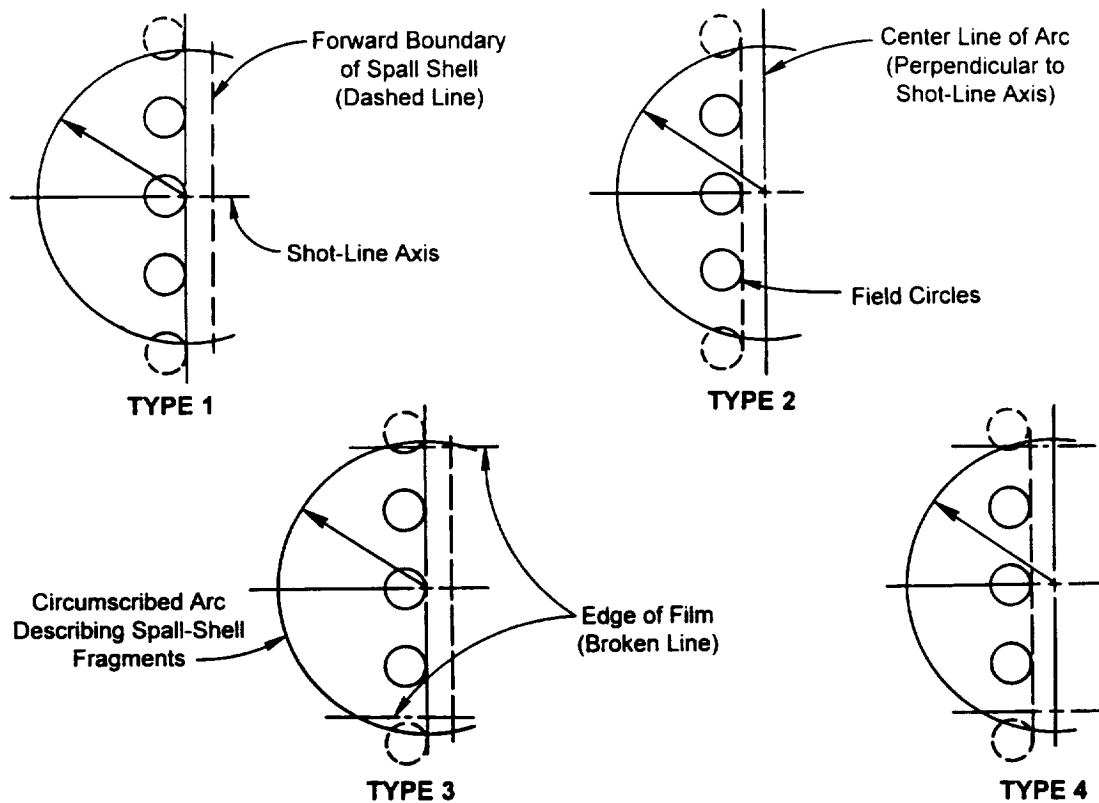
230

Figure A2. Illustration of the four types of spall-shell and sampled areas encountered during the analysis of spall-shell fragments.

by multiplying the number of fragments in the field circles, $N_F$, by the ratio of the spall-shell area to the field area.

A film magnification factor was determined for each photograph. This factor was used to adjust the raw fragment, Martin's-diameter measurements for the magnification of the fragment shadow due to the relationship of the x-ray source, the fragment, and the film when the film was exposed and from the enlargement of the x-ray image during the print-making process. The diameters listed in the data table are the Martin's diameters of the fragment images *on the print*. These diameters and the field, sample, and shell areas must be multiplied by the film magnification factor shown on the data sheets to obtain their true size. The fragment-size distribution data presented in each table were obtained by sorting the raw measurements by fragment diameter.

231

**Shot Number: 4-1283** (Shadows of fragments were too faint to get reliable measurements)

Number of 0.50-inch-diameter Circular
   Fields in Sampled Area: 41.5

Field Area: 8.148 in$^2$
   (Number of fields x Area of circle)

Sampled Area: 38.961 in$^2$ (Type 3)

Shell Area: 70.733 in$^2$

Number of Fragments in Field Area, $N_F$: 418

Ratio of Shell Area to Field Area: 8.680

Film Magnification Factor (must be applied to raw data in table below): N/A

### Fragment-Size Distribution Data (Raw measurements)

| Diameter, (mm) | Number, (−) | Diameter, (mm) | Number, (−) | Diameter, (mm) | Number, (−) | Diameter, (mm) | Number, (−) | Diameter, (mm) | Number, (−) |
|---|---|---|---|---|---|---|---|---|---|
| 0.6 | N/A | 1.5 | N/A | 2.4 | N/A | 3.3 | N/A | 4.2 | N/A |
| 0.7 | " | 1.6 | " | 2.5 | " | 3.4 | " | 4.3 | " |
| 0.8 | " | 1.7 | " | 2.6 | " | 3.5 | " | 4.4 | " |
| 0.9 | " | 1.8 | " | 2.7 | " | 3.6 | " | 4.5 | " |
| 1.0 | " | 1.9 | " | 2.8 | " | 3.7 | " | | |
| 1.1 | " | 2.0 | " | 2.9 | " | 3.8 | " | | |
| 1.2 | " | 2.1 | " | 3.0 | " | 3.9 | " | | |
| 1.3 | " | 2.2 | " | 3.1 | " | 4.0 | " | | |
| 1.4 | " | 2.3 | " | 3.2 | " | 4.1 | " | | |


**Shot Number: 4-1289**

Number of 0.50-inch-diameter Circular
   Fields in Sampled Area: 35.9

Field Area: 7.049 in$^2$
   (Number of fields x Area of circle)

Sampled Area: 34.643 in$^2$ (Type 3)

Shell Area: 63.338 in$^2$

Number of Fragments in Field Area, $N_F$: 222

Ratio of Shell Area to Field Area: 8.985

Film Magnification Factor (must be applied to raw data in table below): 0.40079

### Fragment-Size Distribution Data (Raw measurements)

| Diameter, (mm) | Number, (−) | Diameter, (mm) | Number, (−) | Diameter, (mm) | Number, (−) | Diameter, (mm) | Number, (−) | Diameter, (mm) | Number, (−) |
|---|---|---|---|---|---|---|---|---|---|
| 0.6 | -- | 1.5 | 17 | 2.4 | 1 | 3.3 | 1 | 4.2 | -- |
| 0.7 | 6 | 1.6 | 11 | 2.5 | -- | 3.4 | -- | 4.3 | -- |
| 0.8 | 8 | 1.7 | 15 | 2.6 | -- | 3.5 | -- | 4.4 | -- |
| 0.9 | 17 | 1.8 | 5 | 2.7 | -- | 3.6 | -- | 4.5 | -- |
| 1.0 | 30 | 1.9 | 5 | 2.8 | -- | 3.7 | -- | | |
| 1.1 | 18 | 2.0 | 2 | 2.9 | -- | 3.8 | -- | | |
| 1.2 | 39 | 2.1 | 5 | 3.0 | -- | 3.9 | -- | | |
| 1.3 | 18 | 2.2 | 1 | 3.1 | 1 | 4.0 | -- | | |
| 1.4 | 19 | 2.3 | 3 | 3.2 | -- | 4.1 | -- | | |

**Shot Number: 4-1358**

Number of 0.50-inch-diameter Circular
   Fields in Sampled Area: 23.4

Field Area: 4.594 in$^2$
   (Number of fields x Area of circle)

Sampled Area: 21.737 in$^2$ (Type 1)

Shell Area: 24.708 in$^2$

Number of Fragments in Field Area, $N_F$: 142

Ratio of Shell Area to Field Area: 5.378

Film Magnification Factor (must be applied to raw data in table below): 0.37931

### Fragment-Size Distribution Data (Raw measurements)

| Diameter, (mm) | Number, (–) | Diameter, (mm) | Number, (–) | Diameter, (mm) | Number, (–) | Diameter, (mm) | Number, (–) | Diameter, (mm) | Number, (–) |
|---|---|---|---|---|---|---|---|---|---|
| 0.6 | -- | 1.5 | 13 | 2.4 | 5 | 3.3 | 1 | 4.2 | 1 |
| 0.7 | 1 | 1.6 | 4 | 2.5 | 9 | 3.4 | 1 | 4.3 | 2 |
| 0.8 | 2 | 1.7 | 5 | 2.6 | 1 | 3.5 | 2 | 4.4 | -- |
| 0.9 | 4 | 1.8 | 5 | 2.7 | 4 | 3.6 | -- | 4.5 | 1 |
| 1.0 | 13 | 1.9 | 5 | 2.8 | -- | 3.7 | 2 | 4.7 | 1 |
| 1.1 | 5 | 2.0 | 5 | 2.9 | -- | 3.8 | -- | 5.0 | 3 |
| 1.2 | 3 | 2.1 | 2 | 3.0 | 6 | 3.9 | -- | 5.6 | 1 |
| 1.3 | 5 | 2.2 | 5 | 3.1 | -- | 4.0 | 5 | 6.5 | 1 |
| 1.4 | 12 | 2.3 | -- | 3.2 | 6 | 4.1 | 1 | | |

**Shot Number: 4-1359**

Number of 0.50-inch-diameter Circular
   Fields in Sampled Area: 42.5

Field Area: 8.345 in$^2$
   (Number of fields x Area of circle)

Sampled Area: 40.202 in$^2$ (Type 3)

Shell Area: 50.124 in$^2$

Number of Fragments in Field Area, $N_F$: 238

Ratio of Shell Area to Field Area: 6.006

Film Magnification Factor (must be applied to raw data in table below): 0.36858

### Fragment-Size Distribution Data (Raw measurements)

| Diameter, (mm) | Number, (–) | Diameter, (mm) | Number, (–) | Diameter, (mm) | Number, (–) | Diameter, (mm) | Number, (–) | Diameter, (mm) | Number, (–) |
|---|---|---|---|---|---|---|---|---|---|
| 0.6 | -- | 1.5 | 21 | 2.4 | 6 | 3.3 | -- | 4.2 | -- |
| 0.7 | -- | 1.6 | 15 | 2.5 | 3 | 3.4 | 1 | 4.3 | -- |
| 0.8 | 1 | 1.7 | 22 | 2.6 | 3 | 3.5 | 2 | 4.4 | -- |
| 0.9 | 10 | 1.8 | 17 | 2.7 | 2 | 3.6 | -- | 4.5 | 1 |
| 1.0 | 8 | 1.9 | 5 | 2.8 | 3 | 3.7 | 1 | | |
| 1.1 | 12 | 2.0 | 8 | 2.9 | 2 | 3.8 | -- | | |
| 1.2 | 21 | 2.1 | 11 | 3.0 | 5 | 3.9 | 1 | | |
| 1.3 | 20 | 2.2 | 7 | 3.1 | 3 | 4.0 | -- | | |
| 1.4 | 21 | 2.3 | 5 | 3.2 | 1 | 4.1 | -- | | |

**Shot Number: 4-1360**

Number of 0.50-inch-diameter Circular
  Fields in Sampled Area: 23.1

Field Area: 4.536 in$^2$
  (Number of fields x Area of circle)

Sampled Area: 21.157 in$^2$ (Type 1)

Shell Area: 24.815 in$^2$

Number of Fragments in Field Area, $N_F$: 164

Ratio of Shell Area to Field Area: 5.471

Film Magnification Factor (must be applied to raw data in table below): 0.40346

### Fragment-Size Distribution Data (Raw measurements)

| Diameter, (mm) | Number, (−) | Diameter, (mm) | Number, (−) | Diameter, (mm) | Number, (−) | Diameter, (mm) | Number, (−) | Diameter, (mm) | Number, (−) |
|---|---|---|---|---|---|---|---|---|---|
| 0.6 | -- | 1.5 | 19 | 2.4 | 2 | 3.3 | 2 | 4.2 | -- |
| 0.7 | 1 | 1.6 | 8 | 2.5 | 2 | 3.4 | 1 | 4.3 | -- |
| 0.8 | 2 | 1.7 | 8 | 2.6 | 1 | 3.5 | -- | 4.4 | -- |
| 0.9 | 6 | 1.8 | 7 | 2.7 | 4 | 3.6 | 1 | 4.5 | -- |
| 1.0 | 15 | 1.9 | 2 | 2.8 | 2 | 3.7 | 2 | | |
| 1.1 | 9 | 2.0 | 5 | 2.9 | 1 | 3.8 | -- | | |
| 1.2 | 15 | 2.1 | 6 | 3.0 | 2 | 3.9 | -- | | |
| 1.3 | 13 | 2.2 | 8 | 3.1 | 1 | 4.0 | -- | | |
| 1.4 | 12 | 2.3 | 3 | 3.2 | 4 | 4.1 | -- | | |


**Shot Number: 4-1394**

Number of 0.50-inch-diameter Circular
  Fields in Sampled Area: 13.9

Field Area: 2.729 in$^2$
  (Number of fields x Area of circle)

Sampled Area: 11.574 in$^2$ (Type 2)

Shell Area: 14.612 in$^2$

Number of Fragments in Field Area, $N_F$: 61

Ratio of Shell Area to Field Area: 5.354

Film Magnification Factor (must be applied to raw data in table below): 0.40264

### Fragment-Size Distribution Data (Raw measurements)

| Diameter, (mm) | Number, (−) | Diameter, (mm) | Number, (−) | Diameter, (mm) | Number, (−) | Diameter, (mm) | Number, (−) | Diameter, (mm) | Number, (−) |
|---|---|---|---|---|---|---|---|---|---|
| 0.6 | -- | 1.5 | 6 | 2.4 | 1 | 3.3 | 1 | 4.2 | -- |
| 0.7 | -- | 1.6 | 2 | 2.5 | 1 | 3.4 | -- | 4.3 | -- |
| 0.8 | -- | 1.7 | 4 | 2.6 | 2 | 3.5 | 2 | 4.4 | -- |
| 0.9 | 1 | 1.8 | 2 | 2.7 | -- | 3.6 | 1 | 4.5 | -- |
| 1.0 | 3 | 1.9 | 1 | 2.8 | -- | 3.7 | -- | 5.1 | 1 |
| 1.1 | 4 | 2.0 | 6 | 2.9 | 1 | 3.8 | -- | 5.7 | 1 |
| 1.2 | 4 | 2.1 | 4 | 3.0 | 1 | 3.9 | -- | | |
| 1.3 | 3 | 2.2 | 2 | 3.1 | 3 | 4.0 | -- | | |
| 1.4 | 4 | 2.3 | -- | 3.2 | -- | 4.1 | -- | | |

**Shot Number: 4-1395**

Number of 0.50-inch-diameter Circular
    Fields in Sampled Area: 17.8

Sampled Area: 8.601 in² (Type 1)

Number of Fragments in Field Area, $N_F$: 84

Field Area: 3.495 in²
    (Number of fields x Area of circle)

Shell Area: 9.997 in²

Ratio of Shell Area to Field Area: 2.860

Film Magnification Factor (must be applied to raw data in table below): 0.36611

### Fragment-Size Distribution Data (Raw measurements)

| Diameter, (mm) | Number, (-) | Diameter, (mm) | Number, (-) | Diameter, (mm) | Number, (-) | Diameter, (mm) | Number, (-) | Diameter, (mm) | Number, (-) |
|---|---|---|---|---|---|---|---|---|---|
| 0.6 | -- | 1.5 | 3 | 2.4 | -- | 3.3 | 2 | 4.2 | -- |
| 0.7 | -- | 1.6 | 2 | 2.5 | 2 | 3.4 | 1 | 4.3 | 1 |
| 0.8 | 2 | 1.7 | 7 | 2.6 | 4 | 3.5 | 3 | 4.4 | -- |
| 0.9 | -- | 1.8 | 5 | 2.7 | 3 | 3.6 | -- | 4.5 | 2 |
| 1.0 | 4 | 1.9 | 2 | 2.8 | 1 | 3.7 | -- | 4.8 | 1 |
| 1.1 | -- | 2.0 | 5 | 2.9 | 1 | 3.8 | 2 | 5.0 | 2 |
| 1.2 | 2 | 2.1 | 5 | 3.0 | 4 | 3.9 | -- | 5.1 | 1 |
| 1.3 | 4 | 2.2 | 2 | 3.1 | 1 | 4.0 | 3 | 5.2 | 1 |
| 1.4 | 3 | 2.3 | 2 | 3.2 | -- | 4.1 | -- | 5.3 | 1 |

**Shot Number: 4-1433**

Number of 0.50-inch-diameter Circular
    Fields in Sampled Area: 7.6

Sampled Area: 6.169 in² (Type 2)

Number of Fragments in Field Area, $N_F$: 43

Field Area: 1.492 in²
    (Number of fields x Area of circle)

Shell Area: 6.169 in²

Ratio of Shell Area to Field Area: 4.135

Film Magnification Factor (must be applied to raw data in table below): 0.39809

### Fragment-Size Distribution Data (Raw measurements)

| Diameter, (mm) | Number, (-) | Diameter, (mm) | Number, (-) | Diameter, (mm) | Number, (-) | Diameter, (mm) | Number, (-) | Diameter, (mm) | Number, (-) |
|---|---|---|---|---|---|---|---|---|---|
| 0.6 | -- | 1.5 | 2 | 2.4 | -- | 3.3 | -- | 4.2 | 1 |
| 0.7 | -- | 1.6 | -- | 2.5 | 4 | 3.4 | -- | 4.3 | -- |
| 0.8 | 3 | 1.7 | 2 | 2.6 | 2 | 3.5 | -- | 4.4 | -- |
| 0.9 | 1 | 1.8 | 3 | 2.7 | 3 | 3.6 | 1 | 4.5 | -- |
| 1.0 | 2 | 1.9 | 1 | 2.8 | 1 | 3.7 | -- | 4.8 | 1 |
| 1.1 | 3 | 2.0 | 1 | 2.9 | -- | 3.8 | -- | 5.0 | 1 |
| 1.2 | 1 | 2.1 | 1 | 3.0 | 3 | 3.9 | -- | 5.3 | 1 |
| 1.3 | -- | 2.2 | 1 | 3.1 | -- | 4.0 | 1 | 5.5 | 1 |
| 1.4 | 2 | 2.3 | -- | 3.2 | -- | 4.1 | -- | | |

**Shot Number: 4-1601**

Number of 0.50-inch-diameter Circular
    Fields in Sampled Area: 24.5

Sampled Area: 22.922 in² (Type 1)

Number of Fragments in Field Area, $N_F$: 232

Field Area: 4.810 in²
    (Number of fields x Area of circle)

Shell Area: 28.540 in²

Ratio of Shell Area to Field Area: 5.933

Film Magnification Factor (must be applied to raw data in table below): 0.42752

### Fragment-Size Distribution Data (Raw measurements)

| Diameter, (mm) | Number, (–) | Diameter, (mm) | Number, (–) | Diameter, (mm) | Number, (–) | Diameter, (mm) | Number, (–) | Diameter, (mm) | Number, (–) |
|---|---|---|---|---|---|---|---|---|---|
| 0.6 | 1 | 1.5 | 13 | 2.4 | 1 | 3.3 | 1 | 4.2 | 1 |
| 0.7 | 27 | 1.6 | 6 | 2.5 | 6 | 3.4 | 1 | 4.3 | -- |
| 0.8 | 22 | 1.7 | 11 | 2.6 | 3 | 3.5 | 1 | 4.4 | -- |
| 0.9 | 15 | 1.8 | 13 | 2.7 | 2 | 3.6 | -- | 4.5 | 1 |
| 1.0 | 22 | 1.9 | 2 | 2.8 | 1 | 3.7 | -- | 4.9 | 1 |
| 1.1 | 12 | 2.0 | 9 | 2.9 | -- | 3.8 | -- | 5.0 | 1 |
| 1.2 | 12 | 2.1 | 3 | 3.0 | 6 | 3.9 | -- | 5.1 | 1 |
| 1.3 | 13 | 2.2 | 8 | 3.1 | 1 | 4.0 | -- | | |
| 1.4 | 12 | 2.3 | 3 | 3.2 | -- | 4.1 | -- | | |

**Shot Number: 4-1621**

Number of 0.50-inch-diameter Circular
    Fields in Sampled Area: 23.6

Sampled Area: 21.617 in² (Type 2)

Number of Fragments in Field Area, $N_F$: 82

Field Area: 4.634 in²
    (Number of fields x Area of circle)

Shell Area: 23.419 in²

Ratio of Shell Area to Field Area: 5.054

Film Magnification Factor (must be applied to raw data in table below): 0.38130

### Fragment-Size Distribution Data (Raw measurements)

| Diameter, (mm) | Number, (–) | Diameter, (mm) | Number, (–) | Diameter, (mm) | Number, (–) | Diameter, (mm) | Number, (–) | Diameter, (mm) | Number, (–) |
|---|---|---|---|---|---|---|---|---|---|
| 0.6 | -- | 1.5 | 6 | 2.4 | 3 | 3.3 | -- | 4.2 | 1 |
| 0.7 | 1 | 1.6 | 6 | 2.5 | 1 | 3.4 | 1 | 4.3 | -- |
| 0.8 | -- | 1.7 | 6 | 2.6 | 2 | 3.5 | -- | 4.4 | 1 |
| 0.9 | 2 | 1.8 | 3 | 2.7 | 3 | 3.6 | -- | 4.5 | 1 |
| 1.0 | 5 | 1.9 | 1 | 2.8 | 1 | 3.7 | -- | 6.0 | 1 |
| 1.1 | 5 | 2.0 | 2 | 2.9 | 1 | 3.8 | -- | | |
| 1.2 | 5 | 2.1 | 2 | 3.0 | 1 | 3.9 | -- | | |
| 1.3 | 8 | 2.2 | 1 | 3.1 | 1 | 4.0 | -- | | |
| 1.4 | 7 | 2.3 | 4 | 3.2 | -- | 4.1 | -- | | |

**Shot Number: 4-1621** (Measurements made in direction perpendicular to shot-line axis)

Number of 0.50-inch-diameter Circular
Fields in Sampled Area: 23.6

Field Area: 4.634 in²
(Number of fields x Area of circle)

Sampled Area: 21.617 in² (Type 2)

Shell Area: 23.419 in²

Number of Fragments in Field Area, $N_F$: 82

Ratio of Shell Area to Field Area: 5.054

Film Magnification Factor (must be applied to raw data in table below): 0.38130

### Fragment-Size Distribution Data (Raw measurements)

| Diameter, (mm) | Number, (-) | Diameter, (mm) | Number, (-) | Diameter, (mm) | Number, (-) | Diameter, (mm) | Number, (-) | Diameter, (mm) | Number, (-) |
|---|---|---|---|---|---|---|---|---|---|
| 0.6 | -- | 1.5 | 5 | 2.4 | 2 | 3.3 | 2 | 4.2 | 1 |
| 0.7 | 1 | 1.6 | 3 | 2.5 | 2 | 3.4 | 1 | 4.3 | -- |
| 0.8 | 1 | 1.7 | -- | 2.6 | -- | 3.5 | -- | 4.4 | -- |
| 0.9 | 3 | 1.8 | 6 | 2.7 | 3 | 3.6 | -- | 4.5 | 1 |
| 1.0 | 12 | 1.9 | -- | 2.8 | 1 | 3.7 | -- | 5.5 | 1 |
| 1.1 | 3 | 2.0 | 3 | 2.9 | 1 | 3.8 | 1 | | |
| 1.2 | 6 | 2.1 | 2 | 3.0 | 2 | 3.9 | -- | | |
| 1.3 | 9 | 2.2 | 2 | 3.1 | 1 | 4.0 | -- | | |
| 1.4 | 6 | 2.3 | -- | 3.2 | 1 | 4.1 | -- | | |

**Shot Number: 4-1622**

Number of 0.50-inch-diameter Circular
Fields in Sampled Area: 17.8

Field Area: 3.495 in²
(Number of fields x Area of circle)

Sampled Area: 9.005 in² (Type 2)

Shell Area: 9.005 in²

Number of Fragments in Field Area, $N_F$: 53

Ratio of Shell Area to Field Area: 2.576

Film Magnification Factor (must be applied to raw data in table below): 0.38358

### Fragment-Size Distribution Data (Raw measurements)

| Diameter, (mm) | Number, (-) | Diameter, (mm) | Number, (-) | Diameter, (mm) | Number, (-) | Diameter, (mm) | Number, (-) | Diameter, (mm) | Number, (-) |
|---|---|---|---|---|---|---|---|---|---|
| 0.6 | -- | 1.5 | 5 | 2.4 | 1 | 3.3 | -- | 4.2 | 2 |
| 0.7 | -- | 1.6 | -- | 2.5 | 2 | 3.4 | -- | 4.3 | 2 |
| 0.8 | -- | 1.7 | 2 | 2.6 | 1 | 3.5 | -- | 4.4 | 1 |
| 0.9 | -- | 1.8 | -- | 2.7 | 1 | 3.6 | -- | 4.5 | 1 |
| 1.0 | 2 | 1.9 | 2 | 2.8 | 1 | 3.7 | 1 | 5.1 | 1 |
| 1.1 | 2 | 2.0 | 1 | 2.9 | 1 | 3.8 | -- | 5.5 | 1 |
| 1.2 | 6 | 2.1 | -- | 3.0 | 1 | 3.9 | 1 | 6.0 | 1 |
| 1.3 | 2 | 2.2 | 5 | 3.1 | 1 | 4.0 | -- | 6.6 | 1 |
| 1.4 | 2 | 2.3 | 1 | 3.2 | 1 | 4.1 | 1 | | |

**Shot Number: 4-1716**

Number of 0.50-inch-diameter Circular
    Fields in Sampled Area: 42.0

Field Area: 8.247 in²
    (Number of fields x Area of circle)

Sampled Area: 39.078 in² (Type 4)

Shell Area: 48.668 in²

Number of Fragments in Field Area, $N_F$: 185

Ratio of Shell Area to Field Area: 5.901

Film Magnification Factor (must be applied to raw data in table below): 0.38807

### Fragment-Size Distribution Data (Raw measurements)

| Diameter, (mm) | Number, (–) | Diameter, (mm) | Number, (–) | Diameter, (mm) | Number, (–) | Diameter, (mm) | Number, (–) | Diameter, (mm) | Number, (–) |
|---|---|---|---|---|---|---|---|---|---|
| 0.6 | -- | 1.5 | 12 | 2.4 | -- | 3.3 | 1 | 4.2 | -- |
| 0.7 | -- | 1.6 | 8 | 2.5 | 3 | 3.4 | -- | 4.3 | -- |
| 0.8 | 3 | 1.7 | 12 | 2.6 | 1 | 3.5 | -- | 4.4 | -- |
| 0.9 | 12 | 1.8 | 6 | 2.7 | 6 | 3.6 | -- | 4.5 | -- |
| 1.0 | 14 | 1.9 | 5 | 2.8 | -- | 3.7 | -- | | |
| 1.1 | 15 | 2.0 | 7 | 2.9 | 1 | 3.8 | -- | | |
| 1.2 | 32 | 2.1 | 3 | 3.0 | 4 | 3.9 | -- | | |
| 1.3 | 17 | 2.2 | 3 | 3.1 | 1 | 4.0 | -- | | |
| 1.4 | 9 | 2.3 | 9 | 3.2 | 1 | 4.1 | -- | | |

**Shot Number: 4-1744**

Number of 0.50-inch-diameter Circular
    Fields in Sampled Area: 37.8

Field Area: 7.422 in²
    (Number of fields x Area of circle)

Sampled Area: 33.926 in² (Type 3)

Shell Area: 42.630 in²

Number of Fragments in Field Area, $N_F$: 200

Ratio of Shell Area to Field Area: 5.743

Film Magnification Factor (must be applied to raw data in table below): 0.36446

### Fragment-Size Distribution Data (Raw measurements)

| Diameter, (mm) | Number, (–) | Diameter, (mm) | Number, (–) | Diameter, (mm) | Number, (–) | Diameter, (mm) | Number, (–) | Diameter, (mm) | Number, (–) |
|---|---|---|---|---|---|---|---|---|---|
| 0.6 | -- | 1.5 | 19 | 2.4 | -- | 3.3 | 1 | 4.2 | -- |
| 0.7 | -- | 1.6 | 12 | 2.5 | 3 | 3.4 | -- | 4.3 | -- |
| 0.8 | -- | 1.7 | 13 | 2.6 | 3 | 3.5 | 2 | 4.4 | -- |
| 0.9 | 9 | 1.8 | 8 | 2.7 | 3 | 3.6 | -- | 4.5 | -- |
| 1.0 | 19 | 1.9 | 6 | 2.8 | 1 | 3.7 | -- | | |
| 1.1 | 11 | 2.0 | 7 | 2.9 | 1 | 3.8 | 1 | | |
| 1.2 | 38 | 2.1 | 3 | 3.0 | -- | 3.9 | -- | | |
| 1.3 | 21 | 2.2 | 3 | 3.1 | -- | 4.0 | -- | | |
| 1.4 | 12 | 2.3 | 3 | 3.2 | 1 | 4.1 | -- | | |

# INDEX
## FIGURE CONTENT BY SHOT NUMBER

This index was designed to assist the reader locate radiographs of debris clouds or photographs of bumper sheets, witness plates, etc., that appear in the figures presented in this report. It should be mentioned that not all of the available radiographs of debris clouds and photographs of test articles were used in the preparation of the report. When radiographs of debris clouds were shown, the index indicated which radiograph of the orthogonal pair (i.e., side or top) was presented. Each radiograph contained up to four views. The four views were designated as follows: P - pre-impact view of projectile and 1, 2, and 3 - the first, second, and third views of the debris cloud, respectively. The times of the individual exposures, with respect to impact, were given in Table 3 (page 26) for most of the tests. When photographs of witness plates were presented, the front of the plate was shown, unless noted otherwise in the figures. Details of the materials used in the tests were given in Table 1 (page 7). The availability of various types of data was shown in Table 2 (page 15). Impact velocities and $t/D$ ratios were provided in nearly all of the tables presented in this report. However, Table 4 (page 29) and Table 9 (page 73) provide the most comprehensive listing of these test variables.

In the index, tests employing aluminum projectiles and targets were listed first; tests employing other projectile and target materials were listed under separate subheadings. In the listing of tests using aluminum spheres and bumper sheets, four tests that were listed were not included in the set of 43 tests that comprised the data set examined in this study. Data and/or results of these four tests were used in the report because of some unique aspect of the test or its results. The information for these four tests is shown in italics in the index. The listing in each subheading of the index was arranged, in ascending order, by shot number.

239

# INDEX

# INDEX
## (Continued)

# INDEX
## (Continued)

# INDEX
## (Continued)

# INDEX
## (Continued)

# INDEX
## (Concluded)